ISSN 0915-6348

NATIONAL INSTITUTE FOR FUSION SCIENCE

Physics of High Energy Density Plasmas Produced by Pulsed Power

H. Akiyama (Ed.)

(Received - June 10, 1994)

NIFS-PROC-18 June 1994

RESEARCH REPORT
NIFS-PROC Series

NAGOYA, JAPAN

Physics of High Energy Density Plasmas Produced by Pulsed Power

Edited by Hidenori Akiyama

Keywords: High Energy Density Plasma, Pulsed Power, Z-Pinch, Plasma Focus, Opening Switch, Pulsed Ion Beam, Pulsed Electron Beam, Vircator, BWO, Railgun

PREFACE

This publication is a collection of papers presented at the research meeting on "Physics of High Energy Density Plasmas Produced by Pulsed Power" held at National Institute for Fusion Science in December 17-18, 1993, in which forty two persons attended from the seventeen organizations, and twenty seven papers were given orally.

The high energy density plasmas are able to be produced by pouring an extremely large power into a small space for a short time. These high energy density plasmas have many fields of applications - z-pinch, plasma focus, opening switch, pulsed ion beam, pulsed electron beam, vircator, BWO, railgun, thermal gun and high energy flowing plasma, for example.

The researchers from different kinds of fields gathered to discuss the high energy density plasmas, which are one of common research targets to all attendants, and then came to know their physics better.

Hidenori Akiyama
Kumamoto University

CONTENTS

LIST OF ATTENDEETS

H.Akiyama	Kumamoto University
R.Ando	Kanazawa University
T.Fujimi	Nihon University
M.Fukao	Shizuoka University
S.Furuya	Tokyo Institute of Technology
M.Han	Gunma university
Y.Hashimoto	Himeji Institute of Technology
K.Hirano	Gunma University
N.Hisatome	Gunma University
K.Horioka	Tokyo Institute of Technology
T.Hoshide	Tokyo Institute of Technology
S.Ihara	Saga University
K.Ikuta	Japan Steel Works,Ltd.
K.Imasaka	Kumamoto University
S.Ishii	Tokyo Institute of Technology
S.Kato	Nissin Electric Co.,Ltd.
S.Katsuki	Kumamoto University
M.Kimura	Shizuoka University
H.Kitaoka	Gunma University
S.Kohno	Kumamoto University
K.Kurashina	Niigata University
K.Masugata	Nagaoka University of Technology
M.Masuzaki	Kanazawa University
H.Matsuzawa	Yamanashi Institute of University
S.Miyamoto	Osaka University
K.Moriyama	Nihon University
Y.Naha	Shizuoka University
Y.Nakagawa	Osaka City University
K.Sato	National Institute for Fusion Science
M.Sato	Himeji Institute of Technology
N.Shimomura	The University of Tokushima
N.Shirai	Osaka University
A.Shlyaptseva	Nihon University
T.Tajima	National Institute for Fusion Science
Y.Takahama	Gunma University

K.Takasugi	Nihon University
T.Yanagidaira	Gunma University
T.Yamamoto	Gunma University
K.Yasuike	Osaka University
K.Yatsui	Nagaoka University of Technology
M.Yatsuzuka	Himeji Institute of Technology
A.Yoshida	Gunma University

Resistivity Variation of Fuse as an Opening Switch

Naoyuki Shimomura, Masayoshi Nagata and Hidenori Akiyama*

Faculty of Engineering, The University of Tokushima

*Faculty of Engineering, Kumamoto University

ABSTRACT

Resistance variation of thin copper wires in water as an opening switch was studied to obtain the basic data for design of an inductive energy storage pulsed power generator. The dimensions of a wire influence not only wire resistance but the relation between the resistivity and the energy deposited in the wire of unit mass. The dependence of the changing rate of wire resistivity on the resistivity was obtained using the energy balance equation about exploding wires, as a result, the phases of wire explosion were clearly confirmed and the influence of the dimension was removed from the relation between the resistivity and the deposited energy in early phase of the wire vaporization.

§1. INTRODUCTION

Pulsed power generators with an inductive energy storage system[1]-[3] can be designed compactly and economically. Opening switches[4][5] are indispensable to pulsed power generators using the inductive storage system. Fuses[5]-[10] of metal foil or thin wires placed in tamper have been used as opening switches because of their simplicity and reasonable high performance.

Here, resistance variation of thin copper wires in water as an opening switch was studied to obtain the basic data for design of an inductive storage

pulsed power generator. The dimensions of a wire influence the relation between the resistivity and the energy deposited in the wire of unit mass. Nevertheless, it is desirable that the relation is represented regardless the wire dimensions. We observed the relation between the resistivity and the energy deposited in the wire of unit mass, and attempted to remove the influence of the wire dimensions from its relation.

§2. EXPERIMENTAL CONFIGURATION

Figure 1 shows the equivalent circuit of the pulsed power generator used in experiments. The pulsed power generator consists of a capacitor(10μF) as a primary energy source, a triggered gap switch, an energy storage inductor(84μF) and a fuse opening switch. The explosion of copper wire in water[10] is used as fuses, and the dimensions of wire are 0.05mm in diameter and 5 to 30cm in length. The initial charging voltage is 10kV. The voltage across the wire and the current through it were observed by digitizing oscilloscopes and their waveforms were processed by a personal computer after low-pass filtering.

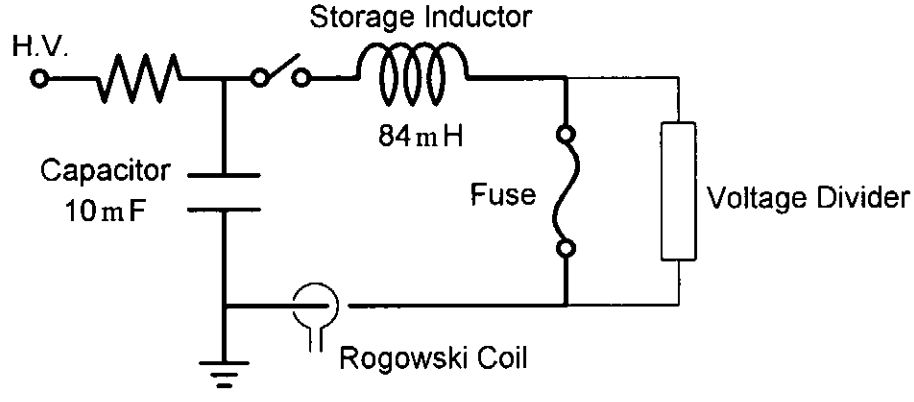

Fig.1 Equivalent circuit of the experimental apparatus.

§3. EXPERIMENTAL RESULTS

The typical waveforms of the voltage across the wire, V, and the current through it, I, are shown in Figure 2. In this case, the output voltage was reached near 80kV, as a result, the voltage multiplication ratio was about 8 owing to the initial charging voltage of 10kV. The lower three waveforms in Fig.2, which represent the resistance, R, the power, P, and the energy deposited in wire, W, were calculated from V and I.

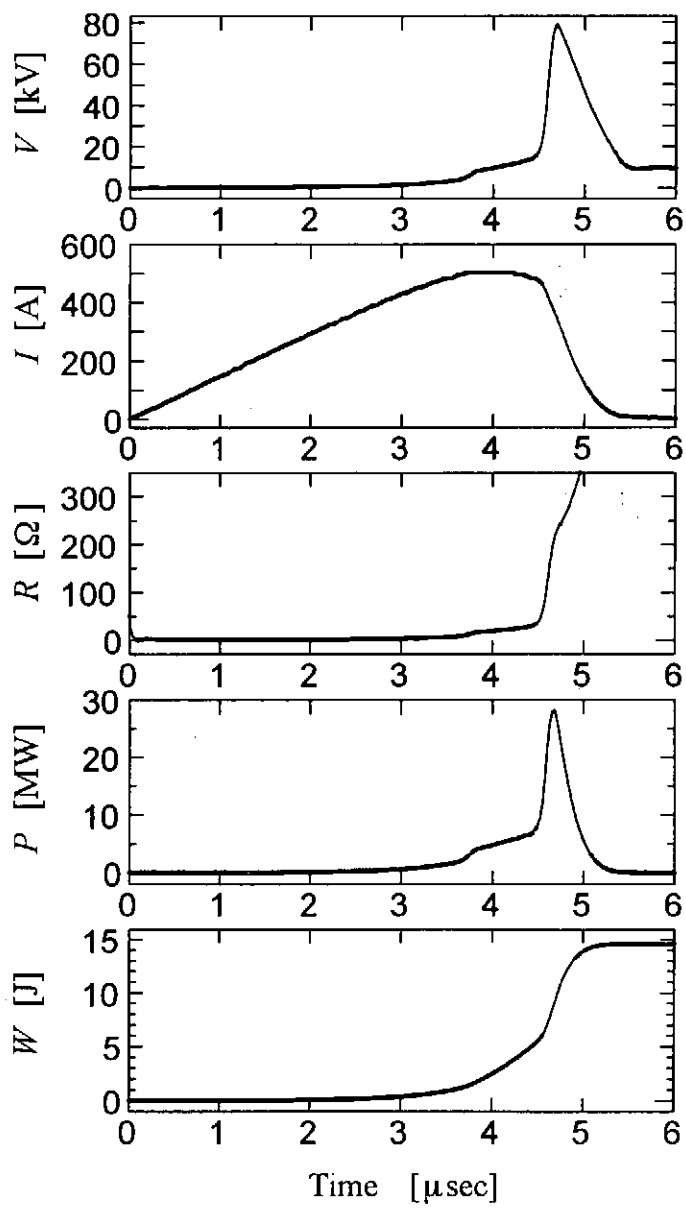

Fig.2 Typical Waveforms

In consideration of dimensions of wires, the dependence of copper wire resistivity(ρ) on energy(E) deposited in it of unit mass is able to obtained, shown in Figure 3, where the parameter is the length of wires. Even if the length of wire is chaneged, there is no effect on resistivity from 0 to 2kJ. The resistivity curves changed in region over 2kJ, where the wires are in a phase of vaporization. Figure 4 shows the relation between the wire resistivity and $d\rho/dE$, which is the changing rate of resistivity on energy deposited in wire of unit mass, and calculated from Figure 3. In Figs.3 and 4, each relation are influenced by the wire length, although both resistivity and the energy are normalized from dimension.

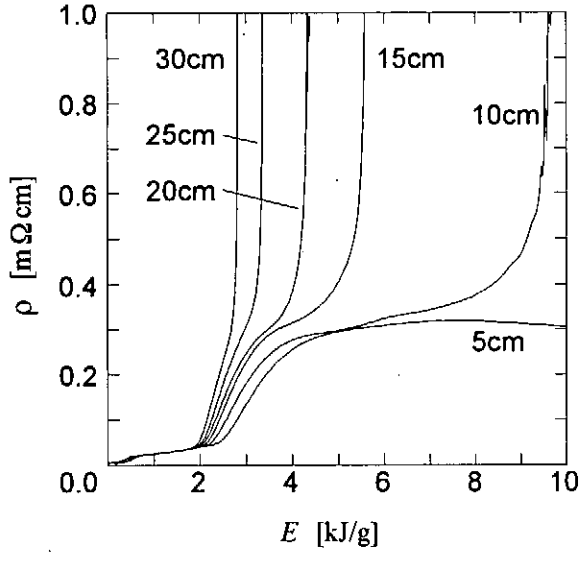

Fig.3 Dependence of resistivity on energy deposited in wire with unit mass.

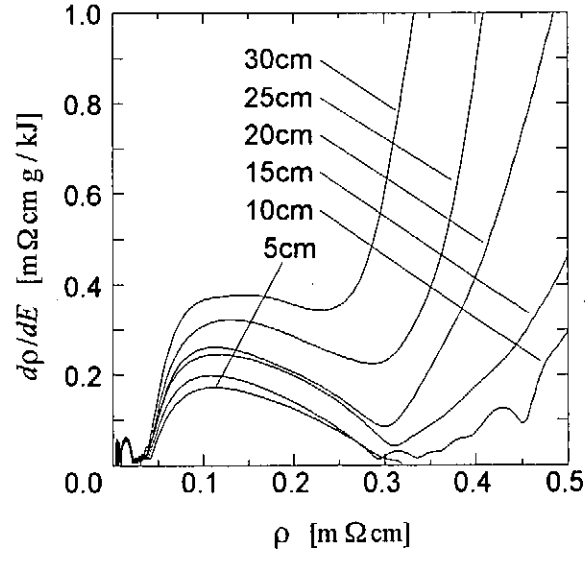

Fig.4 Dependence of resistivity differentiated by energy on wire resistivity

§4. DISCUSSION

Since the resistivity is estimated from the initial dimension of wire here, its transformation is ignored. When the data of resistivity variation will be applied to designing pulsed power generators or loads, it is rather convenient that the transformation is disregarded. Nevertheless, the transformation has to be

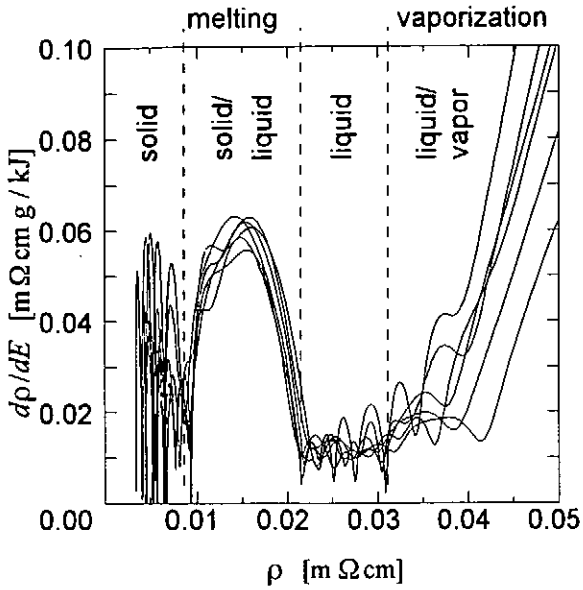

Fig.5 Dependence of resistivity differentiated by energy on wire resistivity

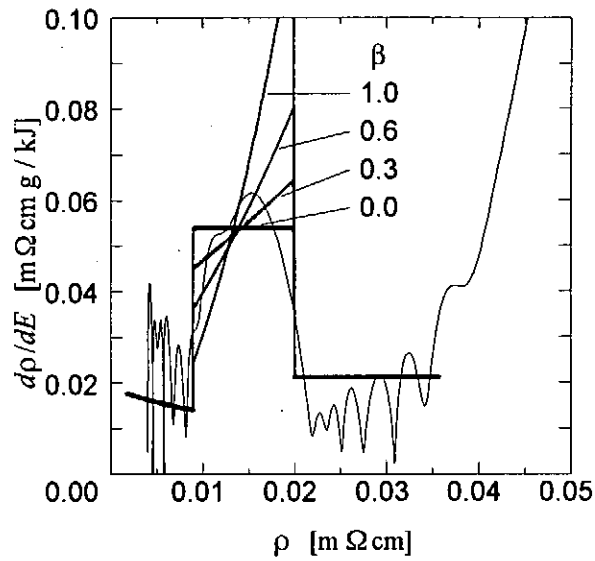

Fig.6 Calculated dependence of Fig.5.

considered to understand the influence of wire dimension on wire resistivity.

Figure 5 represents the low-resistivity region in Fig.4. The data have many noise under 0.01mΩcm, and they are trimmed in very low-resistivity region under 5μΩcm. The melting phase can be distinguished from other phases in Fig. 5, since curves of $d\rho/dE$ form a mountain-shape in melting phase. In consequence, we can discriminate between regions, where are in phases of solid, melting and liquid, though it is difficult to discriminate in Fig.3[6][7]. It seems that the melting essentially progresses in axial or radial directions of wire, as a result. We assume the melting model whose process consists of a mixed propagation both in axial and radial directions. The averaged resistivity, ρ_a, is shown as,

$$\rho_S = \frac{\rho_S \rho_l (1-\alpha)}{(1-\alpha\beta)\{\rho_S \alpha\beta + \rho_l (1-\alpha\beta)\}} + \frac{\rho_l \alpha (1-\beta)}{1-\alpha\beta}, \quad \cdots\cdots\cdots\cdots\cdots\cdots (1)$$

in the phase of melting process. Here, ρ_s and ρ_l are the resistivities of solid and

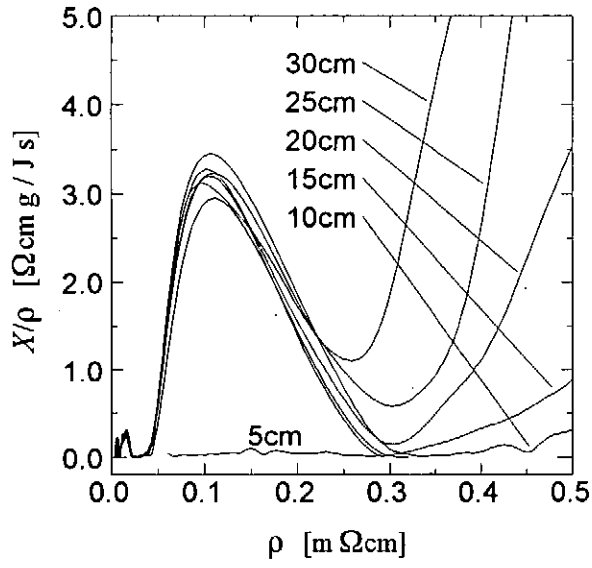

Fig.7 Dependence of X/ρ on wire resistivity

liquid copper, respectively, α is the ratio of liquid copper in wire, and β is the ratio of melting-propagation to axial direction in a total melting. Figure 6 shows the resistivity variation calculated from eq.(1). The curve of β=0.3 fits for the experimental data better than any other curves, which suggests that the propagation in axial direction dominates a melting process to some extent.

The process in a vaporization phase is more complicated, because the transformation of wire and partial or whole breakdowns in wire happen. L.Vermij discussed the transformation of wire into spherical shape[8]. We should evaluate the resistivity normalized by the initial dimension of wire as stated above. Here, we assume that the resistivity in vaporization phase is represented by

$$\rho = \rho_0(E)\mathrm{f}(t) \quad \cdots\cdots (2)$$

where $\rho_0(E)$ is a function of essential copper resistivity on deposited energy and $\mathrm{f}(t)$ expresses the function meaning the wire shape and its transformation. And we define X following equation,

$$X = \frac{\partial \rho}{\partial E} \cdot \frac{\partial \rho}{\partial t} \quad \cdots\cdots (3)$$

Eqs.(2) and (3) lead to

$$X / \rho \cong \frac{d\rho_0(E)}{dE} \cdot \frac{d\,\mathrm{f}(t)}{dt} \quad \cdots\cdots (4)$$

Though it is difficult to obtain ρ_0, f and X from the experimental data, X/ρ can be calculated easily, thus Figure 7 is obtained. The curves of X/ρ in Fig.7 coincide with each other below about 0.3mΩcm. The influences of wire dimension is removed from the resistivity variation in this region. The right side of this region, where is over about 0.3mΩcm, corresponds to the phase after producing a maximum output voltage.

§5. CONCLUSION

The wire resistivity was calculated from the experimental data and the influences of wire dimension were removed from the resistivity to a certain degree. The obtained variation of resistivity is normalized by the initial dimension of wire, so that the effect of the wire transformation is not directly included. But the resistivity variation is rather convenient for applications of the design of generator and its loads. Taking the results of processes of both melting and vaporization into consideration, the output waveforms of pulsed power generators can be calculated.

REFERENCES

[1] J.N.Dimarco and L.C.Burkhardt, "Characteristics of a Magnetic Energy Storage System Using Exploding Foils", *J.Appl. Phys.*, **41**, 3894 (1970)

[2] N.Shimomura, H.Akiyama and S.Maeda, "Compact Pulsed Power Generator by an Inductive Energy Storage System with Two-Staged Opening Switches", *IEEE Trans.Plasma Sci.*, **PS-19**, 6 (1991)

[3] G.Cooperstein, et al., "Inductive Energy Storage System at NRL", *Proceedings of the 6th International Conf. on High-Power Particle Beams*,

843 (1986)
[4] A.Guenther, M.Kristiansen and T.Martin, "OPENING SWITCHES", ADVANCES IN PULSED POWER TECHNOLOGY Vol.1 ,PLENUM PRESS, (1987)
[5] Ihor M. Vitkovitsky: "HIGH POWER SWITCHING", Van Nostrand Reinhold Company, 1987.
[6] V.A.Burtsev, V.N.Litunovskii and V.F.Prokopenko, " Electrical explosion of foils. I," *Sov.Phys.Tech.Phys.*, **22**, 8 (1977)
[7] V.A.Burtsev, V.N.Litunovskii and V.F.Prokopenko, " Electrical explosion of foils. II," *ibid*, **22**,8 (1977)
[8] L.Vermij, "The Voltage Across a Fuse During the Current Interruption Process", *IEEE Trans.Plasma Sci.*, **PS-8**,4 (1980)
[9] Irvin R.Lindemuth, et.al.,"A computational model of exploding metallic fuses for multimegajoule switching", *J.Appl.Phys.*, **57**,1 (1985)
[10] N.Shimomura, H.Akiyama and S.Maeda, "Improvement of a Pulsed Power Generator by Fuses in the Liquid Nitrogen," Trans. of the Institute of Electrical Engineers of Japan, vol.109-A, p.323, 1989.

Beam divergence characteristic of Two-Stage Ion Diode

Nobutake Shirai, Kazuhito Yasuike,
Genji Takahashi, Norihisa Shomoto, Kazuhiro Yamamoto,
Kazuo Imasaki*, Chiyoe Yamanaka*,
Shuji Miyamoto, and Sadao Nakai

Institute of Laser Engineering, Osaka University
*Institute for Laser Technology

Abstract

The improvement of beam divergence by Two-Stage Diode is being studied at ILE Osaka University. We measured 750keV carbon beam divergence by Shadow-Box with CR-39. We used the track analizer (LUZEX III) that could measure and digitize position of tracks, track diameter and shape of tracks to count a number of tracks on CR-39 and got results of beam divergence at first stage and second stage with track diameter resolution.

1.Introduction

Two stage, extraction geometry insulated ion diode (Reiden-SHVS) for Inertial Confinement Fusion Drivers has been studied at ILE Osaka University for the past several years. Light ion beam for ICF drivers requires an intensity at the target of the order of 100TW/cm^2 to ignition. Focused beam intensity is proportional to both the particle energy and the beam current and a reciprocal of square of the beam divergence. We can see from this what improvement of beam divergence is necessary to get high intensity at the target. Simulation of two stage ion diode forecasts that the improvement factor of beam divergence by post acceleration is a function of (V1/V2), V1 and V2 are first and second stage diode voltage, respectively [1].

2.Experiment

We measured first and second stage divergences to observe improvement of beam divergence by using a two stage diode. We used Reiden-SHVS (4MV, 40kA, 100ns) induction adder accelerator that consists eight induction cavities and diode as a two stage diode[2]. The cathode electrode has a magnetic field coil to insulate the diode. The Anode electrode has a passive ion source (parafin or epoxy) or plasma gun to produce proton or carbon beam. Figure 1 shows a schematic diagram of a Reiden-SHVS Applied B ion diode with beam diagnostics. Diagnostics for the experiments include: various voltage and current measurements, Thomson Parabola baem energy detector, Biased Charge Collector, and Shadow box for measurements of beam divergences. In this experiment, SHVS produced 750 keV (the first stage accelarated ions to 400keV, and the second stage to 350 keV) carbon annular beams, and ion current was 90 A/cm^2. Anode-ground gap (AK1) and ground-

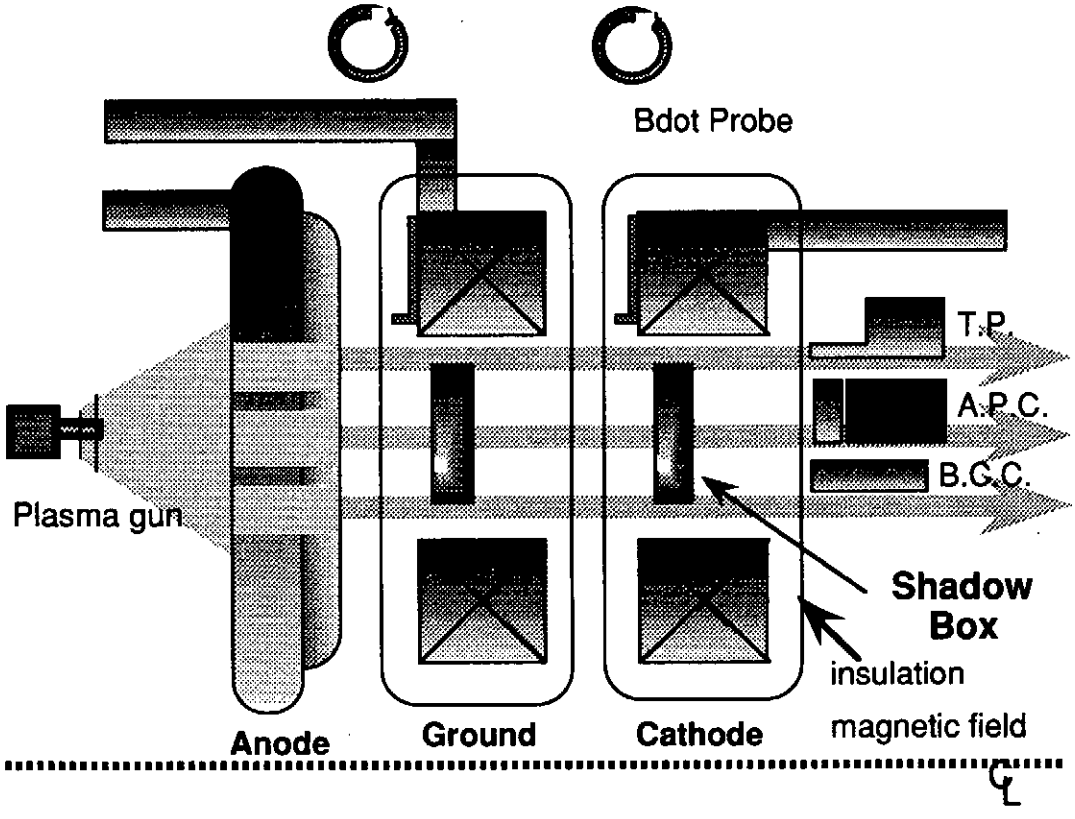

Figure 1. Schematic diagram of the Reiden-SHVS two stage diode and diagnostics.

cathode gap (AK2) was 8mm, 9mm, respectively, and the ground electrode length was 41mm.

We measured the ion beam divergences of first stage accelarator and second stage accelarator at once by shadow boxes placed at the ground electrode (S.B.#1, #2) or cathode electrode (S.B.#3, #4). Shadow boxes had a three 1mmϕ apertures array, a Ta Rutherford scatterer, a 100μm (S.B.#2 and #4) or a 300 μm (S.B.#1 and #3) pinhole, and a CR-39 nuclear detector to record beam images on Ta scatterer. After shot, track analyzer, LUZEX III saw a surface of CR-39 with optical microscope and CCD camera, and measured ion track etchi-pits position, diameter, ellipticity, and other shape parameters. Track densities distributions were made from these data -we counted tracks that had same diameter in a given area on CR-39 and plotted track densities at each position. Figure 2. shows ion track densities on CR-39

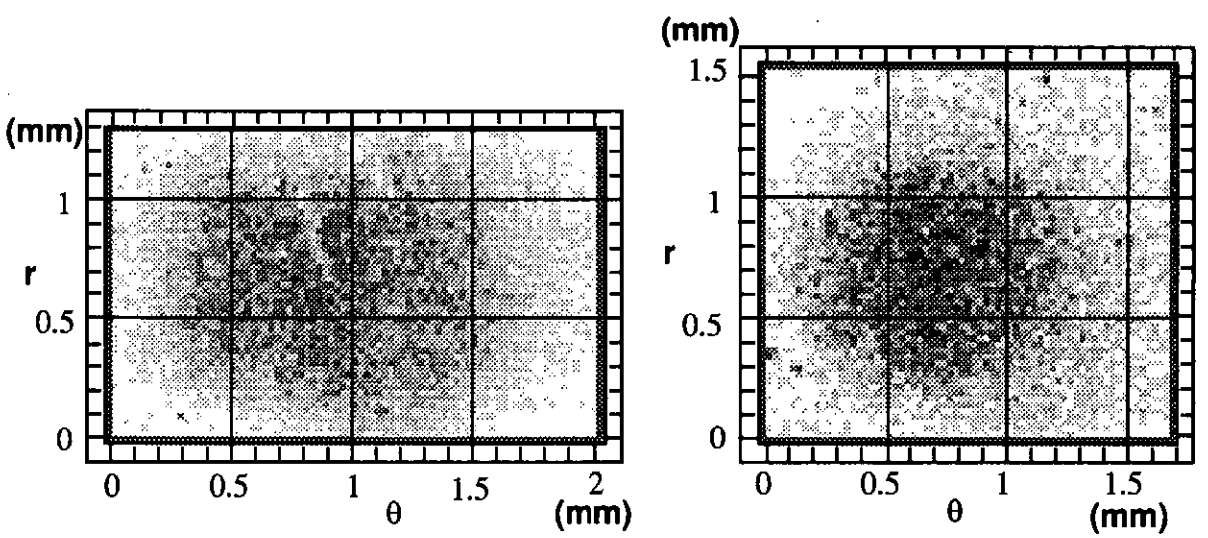

Figure 2. Ion track densities distributions on CR-39 of shadow box that were calclated by track analyzer.

for first stage (S.B.#2) and second stage (S.B.#4). The former is the aperture image of 0.4MeV proton and carbon beams that were accelarated through the first accelaration gap, and ion track distribution is spread in θ direction. This can be

explained by that insulation magnetic field bent ion tranjections. The latter is of 0.75Mev beams that were accelarated through the first and second accelaration gap, and shows less spread than the former.

3. Divergence analysis

We can get the beam divergences after the first stage accelaration and the second stage accelaration by analyzing these track density images. Figure 3. shows that difference of analysis method between shadow box and pinhole camera. Because

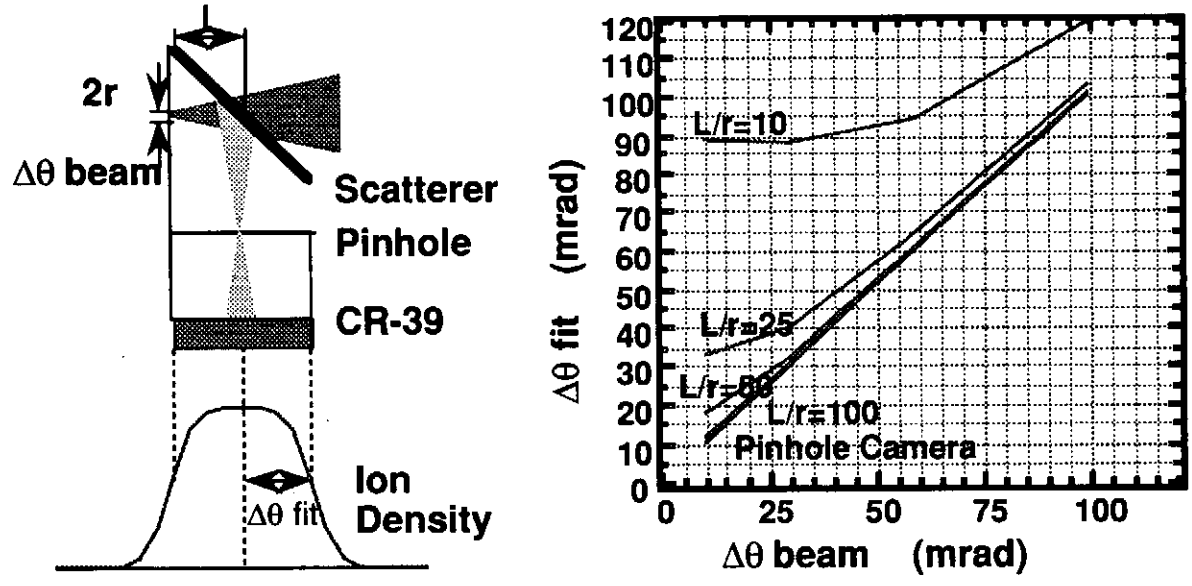

i) Schematic diagram of shadow box and calculated ion track density distribution.

ii) Appearance divergence of shadow box as a pinhole camera

Figure 3. Difference of analysis methode between shadow box and pinhole camera

shadow box has finite diameter aperture, beam image on a target is essentialy different from pinhole camera. We defined the shadow box parameter L/r, L was the length between the aperture and the target (Ta scatterer) and r was the radius of the aperture. If ion beam was uniform, we calculated beam image curves of a given divergence and shadow box parameter L/r by gaussian convolution (Figure 3. i)). We can see the difference of shadow box with L/r from pinhole camera, when we get divergences by HWHM of the curve (Figure 3. ii)). In this experiment, we used

shadow boxes of L/r=10, then we had have to make fitting shadow box data by calculated curves.

In order to get beam divergences of first and second stages, we integrated the track densities distribution data over θ direction for smoothing, because of energy spreaded for θ direction, and analyzed this integrated curve. The following results were obtained: in #c117 shot, shadow box #2 measured first stage divergences, 0.50~1.00μm tracks image was calculated as 30mrad, 1.25~2.00μm tracks image was caluclated as 40mrad, and 2.25~3.00μm tracks image was calculated as 50mrad. Shadow box #4 measured post accelaration beam divergence, 0.50~1.00μm, 1.25~2.00μm, and 2.25~3.00μm tracks images were calculated as 40mrad. Our results did not agree with those obtained by two stage diode theories.

4. Discussion

We shall discuss this results in detail. In this experiment, the Reiden-SHVS produced mainly low energy (750keV) carbon beams, and it was too hard for those beams to propagate through the 41mm length ground electrode without beam expansion. Suppose we inject a 400keV, 90A/cm^2 cylindrical (radius is 12.5mm) C^+ beam into the ground electrode, and the envelope angle is 30~50mrad at injection. We calculate angles that beams envelopes have at 1mm from beam center line at the end of ground, as 30mrad [3]. This expansion makes second stage divergence 30~50mrad. When carbon beams are ununifom, we consider filamentation instability. These C^+ beams can not propagate up to 5mm in vacuum without filamentation instability. The diagram for the experiment result and these calculations would look something like figure 4. In short, we can not observe improvement of beam divergence by using ground electrode with insulation magnetic coil. In recent SHVS experiment, i-series, we use a thin ground board (1mm punch board), but simulation says insulation magnetic field can not insulate up to 600kV voltage. Then we must make an Anode with insulation magnetic coil. We may use time resolution pinhole camera (Arrayed pinhole camera) to measure divergences of early high energy proton beams.

We can select high energy proton tracks on CR-39, when CR-39 tracks of

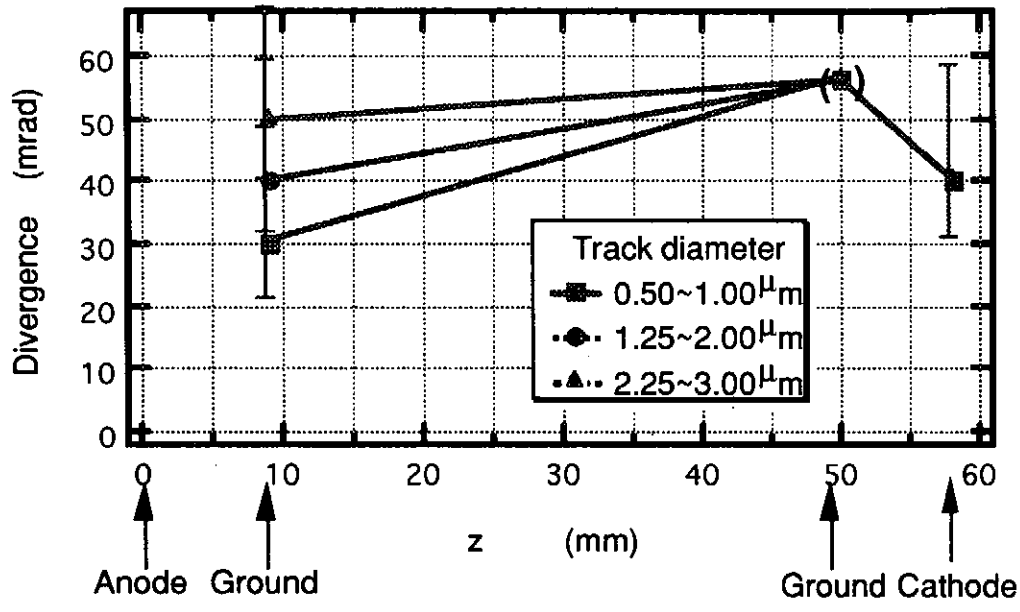

Figure 4. The diagram for the experiment result and effect of beam expansion through the ground electrode.

Thomson parabola are analyzed by LUZEX III. CR-39 of #c117 is not clearly separated carbon tracks and proton tracks. We must consider etching conditions that can make a distinction between desireble ion tracks and others, and scatterer of shadow box. S.B.#1~#4 have Ta bulk scatterer, that make energy spreads of scattered ion. Then shadow boxes must have thin (sub micron) Ta or Au scatterer.

5. Conclusion

In this SHVS experiment, we measured beam divergences after first accelaration and after post accelaration by compact shadow boxes with CR-39, and ion tracks on CR-39 are counted by track analyzer,LUZEX III. The result of the divergence analysis was that beam divergence at second stage was not smaller than divergence at first stage, but we get the improvement point of two stage diode of Reiden-SHVS (we must make an anode electrode with insulation magnetic coils and thin ground electrode.), and get the possibility of the divergence measurement with energy and ion species resolution by using compact shadow box with CR-39.

6. References

[1] S.A.Slutz and M.P.Desjarlais, J.Appl.Phys., vol.67, no.11, pp.6705-6717(1990).

[2] Y.Yasuda, S.Miyamoto, etc., Proceedings of the Twelfth Symposium on Ion Sources and Ion-Assisted Technology, June5-7, (1989) Tokyo, pp217-220

[3] S.Humphries, Jr., Charged Particle Beams., John Wiley & Sons, Inc., (1990)

New multi-dimensional diagnostics method for intense ion beams

Kazuhito YASUIKE, Nobutake SHIRAI, Genji TAKAHASHI, Norihisa SHOUMOTO, Kazuhiro YAMAMOTO, Kazuo IMASAKI, Chiyoe YAMANAKA, Shuji MIYAMOTO and Sadao NAKAI

Institute of Laser Engineering, Osaka University
Institute for Laser Technology

Abstracts

We have developed a new diagnostic method for intense ion beams, named arrayed pinhole camera (APC). An arrayed pinhole camera can measure spatial distributions of beam divergence and flux with time resolution. We measured proton and carbon beams of energy about 0.2 MeV, generated by beam-extraction type applied-B diode. Achieved performances of this APC are a spatial resolution on anode of 1 mm, an effective divergence resolution of better than 10 mrad and a time resolution of 10 ns.

§1. Introduction

In an ion beam inertial confinement fusions, high intensity ion beams of more than 5000 TW/g (100 TW/cm^2) are required on a target to achieve a "hohlraum" temperature about 300 eV[1-6]. Beam parameters for ion beam fusion reactor are estimated to be 30 beamlets of lithium beams of 30 MeV, 0.3 MA (several kA/cm^2 at diode) with beam divergence of 7 up to 4 mrad. A focused beam intensity is proportional to the beam power and to the inverse square of the beam divergence. Thus, the improvement of beam divergence is effective to get the high intensity focus. Simulations of ion diodes say that beam divergence may change with time as a result from growth of instabilities in a diode [7]. Theoretical studies predict that non-uniformity of beam degrades the beam quality due to its filamentation[8]. These results from simulations and theories are have not all verified in experimentally. Measurement of beam divergence with time and spatial resolution is necessary to understand the diode physics, to clear the origin of beam divergence and to generate high brightness beam. However, spatial distribution of both beam divergence and beam flux are not able to acquired by conventional methods.

There are some methods of divergence measurements. Figure 1 shows four different methods to measure the beam divergence. Shadow boxes (Fig. 1.a) and single pinhole cameras (Fig. 1.b) are used in conventionally. Both method measures spatially averaged divergence. These conventional

methods require assumption of beam source uniformity in observing area. Existent beams have non-uniformity in space. We can acquire spatial resolved divergence by a collimeter array as shown in Fig.1.c. In order to measure a spatial distribution of divergence by this method, we must move a collimeter array throughout the measuring region. This method is usually applied for stationary beams or high repetitive beams.

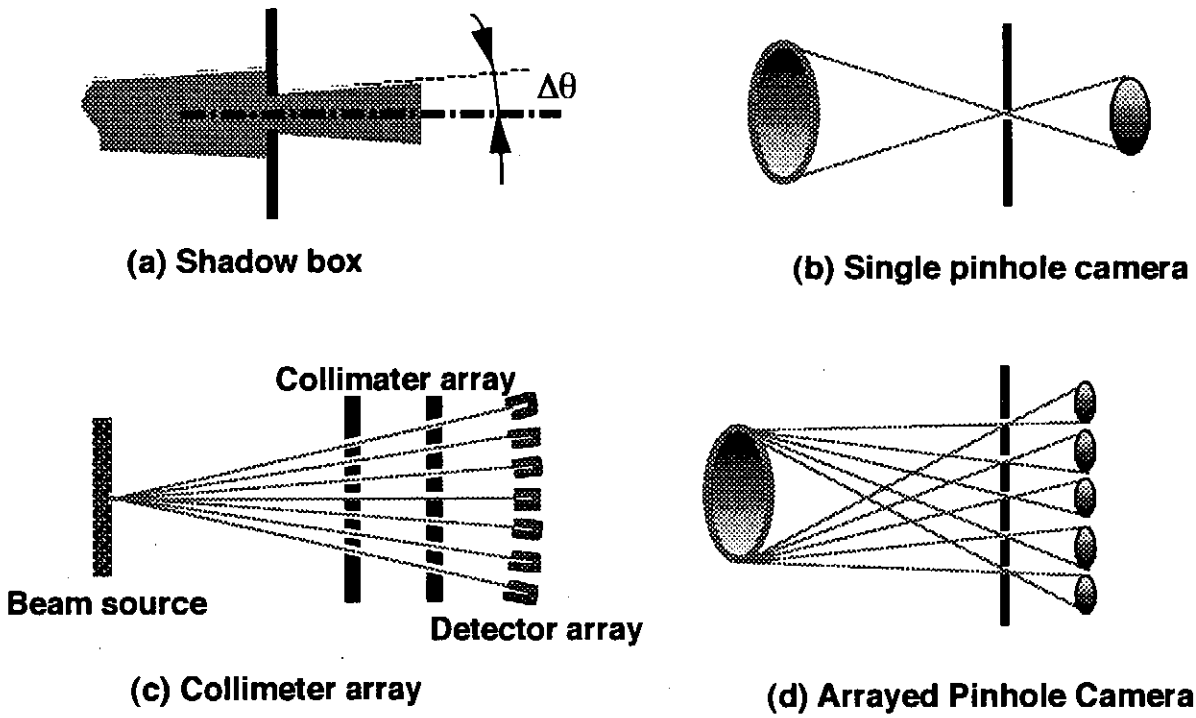

Fig. 1. Some divergence measurements methods.
(a) Shadow-box and (b) Single pinhole camera measurements require an assumption of beam uniformity. (c) collimator array can discriminate an object point, but it cannot acquire divergence distribution. (d) Arrayed Pinhole Camera works like a collimator array, but can be acquired divergence distribution.

We have developed an arrayed pinhole camera (APC) to overcome these disadvantages of conventional methods. By this method, we can measure beam divergence and its flux simultaneously with spatial distribution. Figure 1.d shows a schematic configuration of arrayed pinhole camera. The principle of APC is observing same anode area from some different observation angles. An arrayed pinhole camera is consist of pinhole cameras in a row, and each pinhole camera sees same object area. Spatial profile of the angular distribution of the beam can be obtained. An APC is able to have a time resolution by using a time resolved ion detector.

§2. Arrayed Pinhole Camera

2.1. Principle of measurement of beam divergence distribution by APC

Figure 2 shows analysis procedure to obtain spatial distribution of divergence from measured APC images. Fig. 2.a is a profile of measured image taken by each pinhole camera of APC.

In order to evaluate the beam divergence by a single figure of merit parameter, we assumed that beams have Gaussian angular distributions[10], and evaluated the divergence $\Delta\theta$ by half width half maximums (HWHM) of fitted angular distribution.

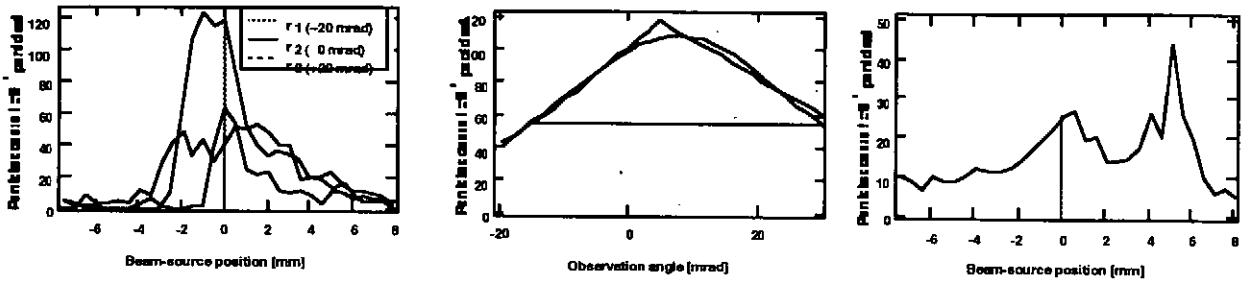

(1) Intensity distribution of APC's each image. (2) Angle distribution of incident beam at point r=0. (3) Divergnece vs. Beam source position.

Fig. 2. Data processing sequence of acquired APC image into divergence distribution. (1) Intensity distribution of APC image. Each curve correspond each pinhole image. (2) Mapping intensity of images at X = 0 (Corresponding to "Beam source position" X = 0 on (1))to get angle distribution. (3) Divergence at X = 0 is corresponding to HWHM of fitted curve of (2).

2.2. Angular and spatial resolutions

Figure 3 shows a definition of dimensional parameters of the arrayed pinhole camera. Geometrical angular resolution Δ is defined by a minimum pinhole separation d_1 and a distance between object and pinhole array L_1, $\Delta = d_1/L_1$. Smaller pitch results better geometrical angular resolution. When we determined to avoid overlapping each image, we must diminish magnification factor of the arrayed pinhole camera and diminished area of each image on the image plane. Diminishing image area degrade spatial resolution of images. Thus, spatial resolution and angular resolution are incompatible terms. We derive design parameters of the arrayed pinhole camera for required spatial resolution, angular resolution and observing area, with following given conditions.

A magnification factor M_{ag} of pinhole camera is, $Mag = L_1 / L_2$, where L_1 and L_2 are distances between object and pinhole array, and pinhole array and image plane, respectively.

Pinhole images should not be overlapped each other. A separation of image d_2 is defined by L_1, L_2 and d1 as $d_2 = (L_1 + L_2)\, d_1 / L_1$.

In order to avoid overlapping images, following condition $a_1 < (L_1 + L_2)\, d_1 / L_2$ is required, where a_1 is a size of observing area. When geometrical angular resolution Δ and observing area a_1 are given, L_1, L_2 and Mag will be determined by following relations.

$$\frac{a}{\Delta} Mag < (L_1 + L_2) \qquad (1)$$

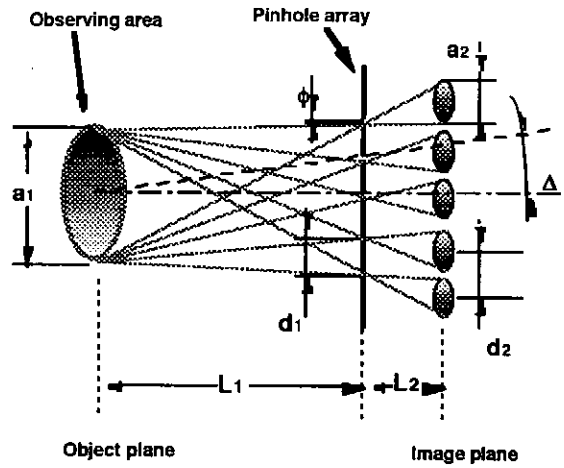

Figure 3 Definition of dimensional parameters of the arrayed pinhole camera.

2.3. Assumption of gaussian distribution

It can be assumed that the angular distribution of ion beams from magnetically insulated ion diodes has gaussian profile, because several different fields in the diode affect the beam to scatter statistically.

The distribution function of beam at source is expressed as,

$$f(r,\theta) = N_0(r) \cdot \exp\left\{-\left(\frac{\theta}{\Delta\theta(r)}\right)^2 \cdot \ln 2\right\} \ [\text{particles} \cdot \text{cm}^{-2} \cdot \text{sr}^{-1}], \qquad (2)$$

where $N_{0(r)}$ is flux distribution of ion beam, r is two dimensional position vector, θ is direction of main robe and $\Delta\theta(r)$ is spatial distribution of beam divergence.

When we measured ion beams by APC, our observed data are intensity distribution of each pinhole camera image of the APC, which depend on source position. In an assumption of gaussian distributed beam profile, f(r) can be reconstructed from discrete observation angle of pinhole image distributions. We labeled each pinhole image of APC as $g_k(r')$ numbered k for different observation angle. Observed images $g_k(r)$ on an image plane is expressed as

$$g_k(r) = f(r', \theta_k) \cdot d\Omega \cdot \left(\frac{1}{Mag}\right)^2 \ [\text{particles} \cdot \text{cm}^{-2}], \qquad (3)$$

$$\theta_k = K(r',k),\ k = 1,\ 2,\ \ldots,\ n\ , \tag{4}$$

where dW is solid angle of pinhole viewed from object and r' is position on image plane. We can obtain divergence distribution $\Delta\theta(r)$ by fitting g1(r) ... gk(r) to gaussian for each r that is calculated backward from r'. We also obtain a beam flux distribution $N_0(r)$ from these fittings. A distribution of current density $J_i(r)$ is calculated from distribution of ion flux $N_0(r)$ as,

$$J_i(r) = \frac{e \cdot Z}{\tau} \frac{4\pi \cdot N_0(r)}{\ln 2} \Delta\theta^2(r)\ [A \cdot cm^{-2}]\ , \tag{5}$$

where t is pulse width e· Z is ion charge.

Better resolution than geometrical resolution Δ can be obtained by the analysis of gaussian fitting.

Fitting is performed using four unknown parameters k_0, k_1, k_2 and k_3 as

$$G(k_0, k_1, k_2, k_3) = k_0 + k_1 \cdot \exp\left[-\left(\frac{x - k_2}{k_3}\right)^2\right], \tag{6}$$

where G is fitted results function. The parameter k_0 means uniform noise flour of profile. The parameter k_1 correspond to function $N_0(r)$ of each position. The parameter k_3 correspond to divergence $\Delta\theta$. The parameter k_2 means direction of robe or direction of beam in macroscopic. When more than two peaks are exist, single gaussian fitted results $\Delta\theta$ have rather large values particularly in each peak have nearly equal value, and apart from each other.

§3. Measurements of time resolved divergence distribution

We have designed a compact, time resolving APC. We used a micro channel plate with phosphor screen (MCP) as ion detectors.

We analyze only radial spatial resolution, because of the azimuthal spread of beam due to penetration of insulating magnetic field into the anode in our experimental condition.

3.1 Specific design and demonstration of a time resolved APC

We measured ion beam divergence with 1 mm spatial resolution and 10 ns time resolutions simultaneously. We use single stage applied-B type ion diode using with four plasma guns. Ion beam is generated by single stage diode driven by Reiden-SHVS an induction adder 2 MV, 40 GW pulsed power supply. Figure 12 shows single stage ion diode driven by Reiden-SHVS and measuring instruments. Beam parameters are shown in Table I. From thomson parabola measurements, a main particle form plasma guns is carbon C^+ of about 140 keV.

We use gated micro channel plate with phosphor screen for time resolving ion detector of APC. Ion images of APC are directly come into micro channel plate (MCP). A diameter of micro channel limits spatial resolutions. Resolving distance on MCP is about five times of micro channel diameter corresponded to 0.07 mm.

The detection efficiency of MCP for high energy ions is about 5 %. A gain of MCP we used was about 1000 (at 1000 V applied gate pulse). Micro channels of MCP have bias angle to perpendicular to MCP incident face of 15 degree, and they are oriented in azimuthal direction to avoid some pass through ions.

We applied a gate pulse simultaneously both a MCP and a phosphor screen. A dividing ratio of gate pulse in the MCP assy, is about 1 : 4.7 for the MCP and the phosphor screen. We use a gate pulse of 10 ns, 3.5 kVp-p (about 750 V for MCP).

In order to eliminate stray light noise images, we employed metal filter. It installed 0.5 mm prior to MCP face to minimize the effect of scattering. We use 3000 Å. aluminum film. Resultant of this metal filter, noise images are almost eliminated.

Table I

Ion beam parameters and requirements for a designing an APC (time resolved measurements).

Diode Parameters		
Anode-cathode gap	11 mm	
Applied-B field at cathode		0.8 T
Critical insulating voltage		2.2 MV
Operating region		$V / V_{crit} < 0.5$
		$J_i / J_{child\text{-}Langmuir} < 1$
$J_{child\text{-}Langmuir} = 14\ A/cm^2$, at 1 MV, 10 mm anode-cathode-gap		
Beam Parameters		
Particle species		Carbon
Ion energy in main		0.7 MeV
Ion current density		$J_i = 2 - 10\ A/cm^2$
Pulse duration	60 ns	
Specifications of APC		
Spatial	Observation area	a1 > 10 mm diameter
	Spatial resolution	Dx = 1 mm on the anode
Angular	observation range	± 100 mrad
	Angular resolution	D < 20 mrad
Time resolution		10 ns

3.2. Experiments

Figure 4 shows experimental apparatus. Timings of MCP gate pulse are monitored. Figure 5 shows typical APC image and its processed divergence distribution.

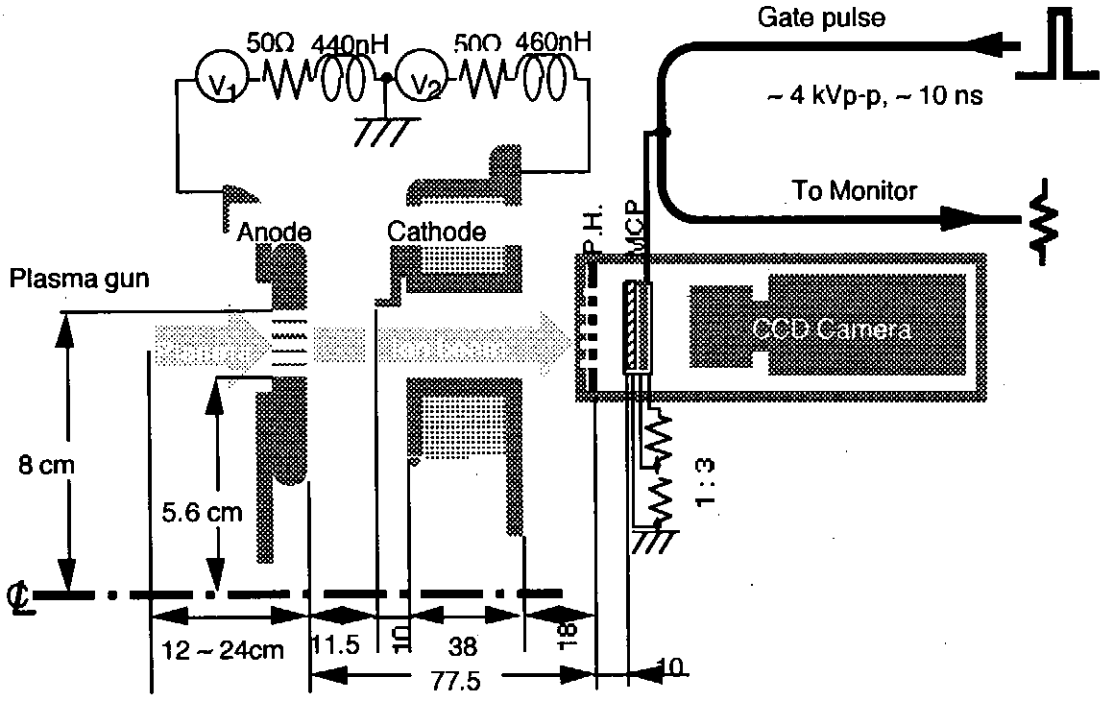

Fig. 4. Experimental apparatus.

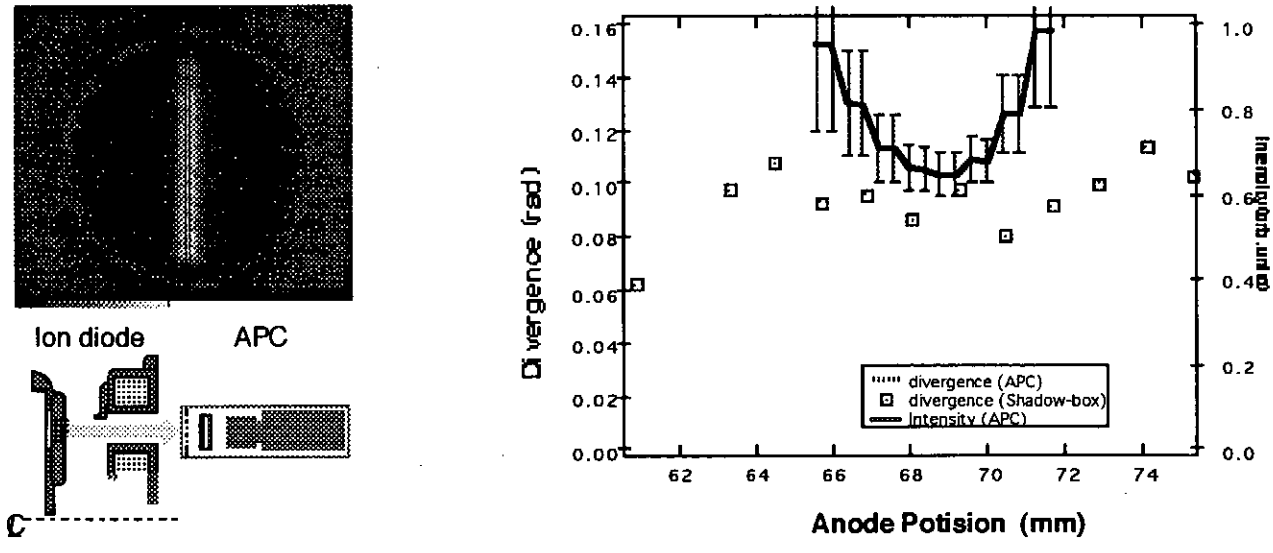

Fig. 5. Typical APC image (upper left) and its processed divergence distribution.

3.3. Results and analysis

We acquire spatial distribution of divergence for several timings from start of diode applied voltage. Driving condition is the same for each shot. Figure 6 shows time dependence of averaged beam divergence.

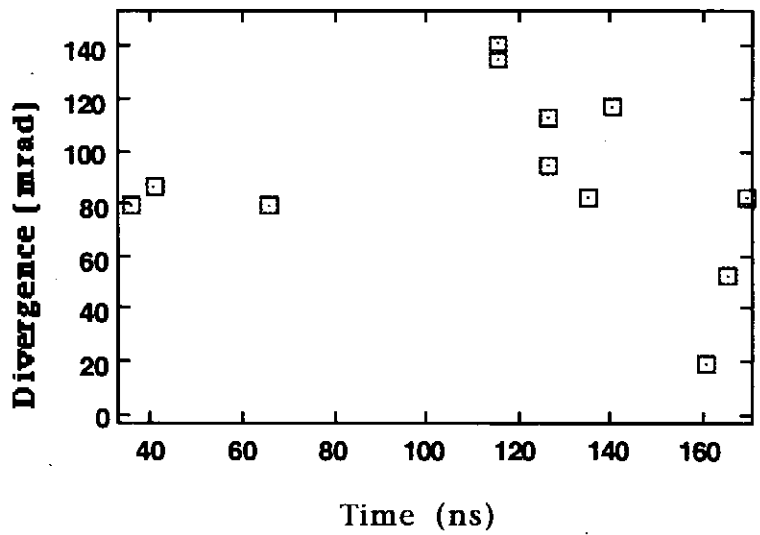

Fig. 6. Time dependence of divergence.

We considered that measured divergence $\Delta\theta_{measured}$ is sum of several origins of divergence. It can be expressed as

$$\Delta\theta^2_{measured} = \Delta\theta^2_{source} + \Delta\theta^2_{diode} + \Delta\theta^2_{transport}, \qquad (7)$$

where $\Delta\theta_{source}$, $\Delta\theta_{diode}$ and $\Delta\theta_{transport}$ are source divergence, degradation by diode and degradation by transport, respectively. Source divergence is determined by ion source itself. Divergence degradation is caused by ion mode coupling to diode instabilities. Degradation by transport is caused by space charge expansion, filamentation caused from spatial non uniformity of beam and growth of filamentation instability in weak magnetic field [ref.].

We calculated deflections by diode insulating magnetic fields. From calculations of 200 keV 200A/cm^2 carbon(C^+) beam, displacements in radial direction are less than 0.1 mm and a variance of radial displacements (rotations) are less than 0.05 mm. Azimuthal deflections are from 6.5 to 10 mrad. From these calculations, trajectory distortions effect slightly to ambiguities and they are nonessential.

We assume spatially uniformed background noises for time resolved APC. If there is non-uniformity background noise, some errors are included in divergence. We can avoid these effects caused from light noises by using filters or employing nuclear reaction detector methods.

§4. Conclusion and future developments

We have developed the arrayed pinhole camera a new beam divergence measurements method. It can measure beam divergence with spatially continuous distribution and its flux simultaneously. We performed testing of time resolved type arrayed pinhole camera to prove its measurements abilities. Our developed APC has 1 mm spatial resolution, 17 mrad observation angle separation and 10 ns time resolution. Its observing area is 10 mm.

Our next step is diode parameter survey for good diode operation and unveil diode physics. We can acquire 2-dimensional (plane) divergence distribution using with several one dimensional APC's. Data form APC's can be reconstructed by tomographic methods. We can also reconstruct beam information (divergence) along a beam propagation (z-direction) from applying with tomographic methods to APC data. Difference in designing APC is only pinhole separation. A smaller pinhole separation suitable for better angular resolution, on the contrary, larger its separation gains spatial resolution along a beam propagation. In rough estimations, we obtain 2 mm resolution in z-direction at pinhole separation = 10 mm, L_1 = 30 mm. We will discriminate main region of divergence growing in the ion diode by tomographic methods from APC data.

Reference

[1] M. M. Basko and J. Meyer-Ter-Vehn, NUCLEAR FUSION, **33**, 601 (1993).

[2] R. R. Peterson, "Ballistic Focus Light Ion Beams for an Inertial Confinement Fusion Reactor", Beams '92, 25-29 May 1992, Washington D.C., 909.

[3] D. L. Cook, R. G. Adams, J. H. Aubert, L. D. Bacon, J. E. Bailey, D. D. Boolmquist, J. D. Boyes, G. A. Chandler, et al., "LIGHT-ION-DRIVEN INERTIAL CONFINEMENT FUSION", 14th Int'l Conf. on Plasma Phys. and Controlled Nuclear Fusion Research, würzburg, Germany,

[4] K. Imasaki, S. Miyamoto, S. Higaki, T. Ozaki, S. Nakai and C. Yamanaka, JPN. J. of Appl. Phys., **23**, L83 (1984).

[5] T. A. Mehlhorn, L. D. Bacon, J. E. Bailey, D. D. Bloomquist, G. A. Chandler, R. S. Coats, D. L. Cook, M. E. Cuneo, et al., "PROGRESS IN LITHIUM BEAM FOCUSING AND BEAM-TARGET INTERACTION EXPERIMENTS AT SANDIA NATIONAL LABORATORIES", Beams '92, 25-29 May 1992, Washington D.C., 31.

[6] J. P. Quintenz, R. G. Adams, G. O. Allshouse, L. D. Bacon, J. E. Bailey, D. D. Bloomquist, G. A. Chandler, R. S. Coats, et al., "PROGRESS IN LIGHT ION FUSION", JPQ Pulsed Power Sciences,

Sandia National Laboratories.

[7]M. P. Desjarlais, T. D. Pointon, D. B. Seidel, R. S. Coats, M. L. Kiefer, J. P. Quintenz and S. A. Slutz, Phys. Rev. Lett., **67**, 3094 (1991).

[8] S. A. Slutz, Phys. Fluids B, **4**, 2645 (1992).

[10] J.D. Jackson, "Classical Electrodynamics 2nd ed." John and Wiley Sons; inc..

Evaluation of Dynamic Pressure of Ablation Plasma Produced by Intense, Pulsed, Ion Beam

Xiangdong Kang, Katsumi Masugata and Kiyoshi Yatsui

Laboratory of Beam Technology and Department of Electrical Engineering, Nagaoka University of Technology, Nagaoka, Niigata 940-21, Japan

ABSTRACT

Basic characteristics of an ablation plasma produced by an intense, pulsed, ion beam have been evaluated from the measurement of ion-flux density by using a biased-ion collector. The target mass loss is detected by the measurement of the weights of the target before and after the shot. An one-dimensional hydrodynamic model is introduced by assuming a high-power, light-ion beam-driven expansion and the following adiabatic expansion into vacuum. Using this model, it is possible to deduce the pressure from the data of the ion flux and the mass loss of the target. This method is also applicable to other intense pulsed energy sources such as lasers or electron beams.

1. Introduction

Intense, pulsed, light-ion beam (LIB) has been successfully applied for materials science. Particularly, various thin films have been effectively prepared by an intense, pulsed, ion-beam evaporation technique (IBE).[1-4] If a target is irradiated by the LIB, an extremely high-power density will be achieved near the surface of the target since the range of the LIB is quite short in

it, hence resulting in the production of high-density, high-temperature "ablation" plasma. The ablation plasma will be deposited on the substrate placed nearby the target, preparing thin films very quickly even without heating the substrate. The deposition characteristics of the IBE have been found to be different from other methods such as vacuum depostion or sputtering. Principally, the IBE is similar to a pulsed-laser evaporation (PLE), but the mechanism of the energy deposition is quite different. A lot of works have been carried out on the evaporated-particle characteristics for the PLE.[5,6] However, the phyical process of the IBE has not been made clear. To study the behavior of the ablation plasma in the IBE is of interests not only from basic physics but also from technological applications.

The purpose of this paper is to investigate the behavior of the ablation plasma produced by the IBE. For this purpose, one-dimensional hydrodynamic model for the IBE is introduced with the assumption of high-power, LIB-driven expansion and the following adiabatic expansion into vacuum, and the analytic solutions are given to deduce the pressure using the data of the ion flux and the mass loss of target determined experimentally.

2. Experiment

Figure 1 (a) shows the experimental setup of the IBE process together with several arrangement to observe the behavior of the ablation plasma. An intense, pulsed, charged-particle beam generator, "ETIGO-II",[7] was used in the experiments. Figure 1 (b) shows the setup to observe the patterns by the LIB-damage on target (Ti) and by evaporation-particle deposition on substrate (glass). The distance between the target and substrate is 37 mm. The ion flux of the ablation plasma was measured by a biased-ion collector (BIC)[8] placed at the same position as the substrate (see Fig. 1 (c)). Furthermore, the mass loss of the target was measured by the comparison of the weights of the target before and after the shots (see Fig. 1 (d)).

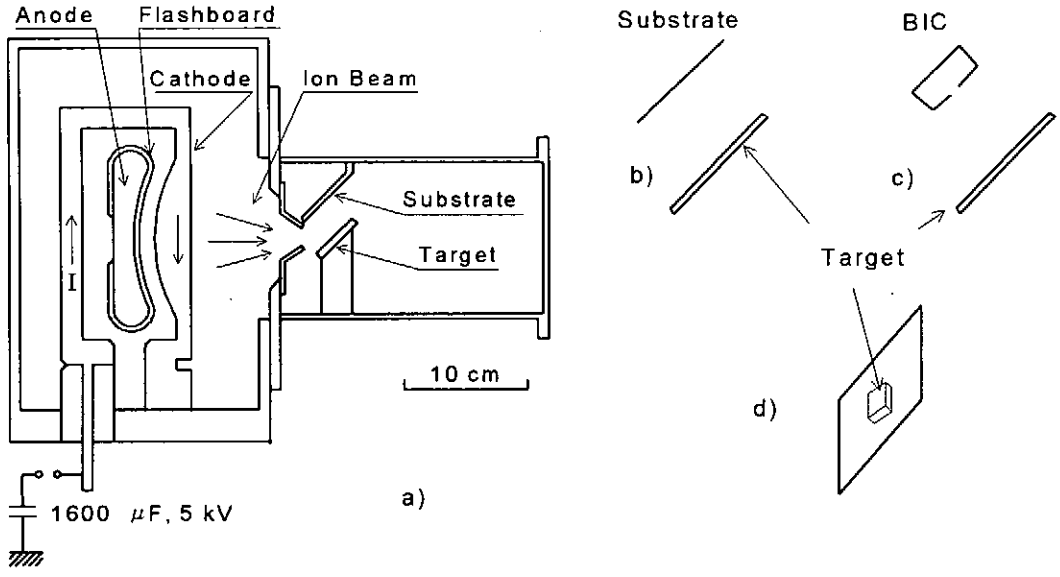

Fig. 1 (a) Experimental setup of the IBE, together with several scheme to measure (b) the patterns of LIB damage on target and evaporation–particle deposition on substrate, (c) the ion flux of the ablation plasma, and (e) the target mass loss.

Figure 2 shows the typical waveforms of diode voltage (V_d), diode current (I_d), diode power ($P_d = V_d I_d$) and ion-current density (J_i) measured at z = 140 mm downstream from the anode. From Fig. 2, we see the peaks to be $V_d \sim 1$ MV, $I_d \sim 80$ kA, $P_d \sim 80$ GW, $J_i \sim 1$ kA/cm^2 and τ (pulse width of J_i) ~ 70

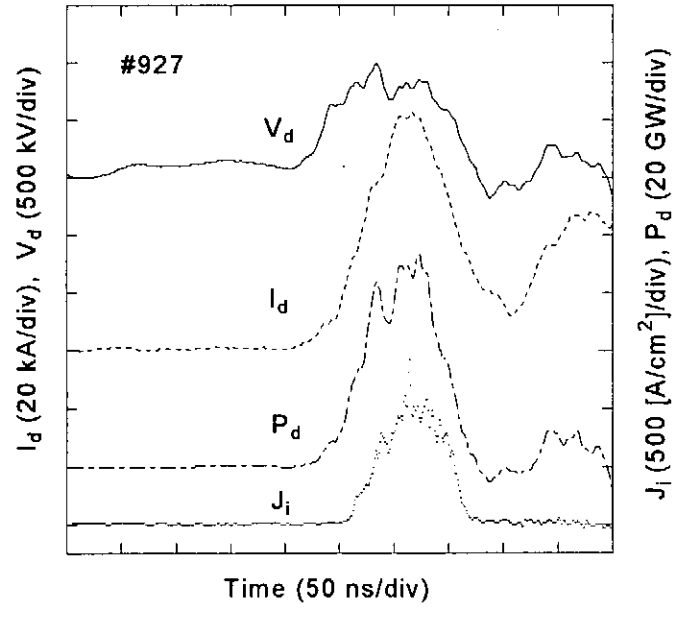

Fig. 2 Waveforms of V_d, I_d, P_d and J_i, where J_i was measured by BIC with the potential of – 1 kV at z = 140 mm downstream from the anode.

ns (FWHM).

3. Model and Analytic Solutions[9-11]

To investigate the behavior of the ablation plasma produced by the IBE, we separate the process of the IBE into two stages. The first stage (a) is the high-power, LIB-driven expansion. It includes the LIB interaction with the target, resulting in the evaporation of the surface, and the interaction of the evaporated material with the incident LIB. Thus, a plasma is produced, and subsequently the expansion takes place. Since, in the stage (a) the surface layer (~ several μm) is heated quickly, the time derivative of the mass of the evaporated material per unit area is asummed to be zero, M = constant. For the second stage (b) after the LIB termination, an adiabatic expansion of the plasma into vacuum takes place, which leads to the deposition of thin films. For the stage (a), we assume spatial uniform but time varying power deposition per unit mass. Since M = constant, the following solutions solved analytically for a planar foil[12] are introduced to this case for $x \geq 0$ and $0 \leq t \leq \tau$:

$$v = \frac{(3+\alpha)}{2}\frac{x}{t} \quad , \tag{1.a}$$

$$e = \frac{2(1+\alpha)\varepsilon t^{1+\alpha}}{(3+\alpha)\gamma + \alpha - 1} \quad , \tag{1.b}$$

$$\rho(\sigma_1(t), x) = \frac{2M}{\sqrt{2\pi\sigma_1(t)^2}} \exp\left\{-\frac{x^2}{2\sigma_1(t)^2}\right\} \tag{1.c}$$

where

$$\sigma_1(t) = \sqrt{\frac{t^{3+\alpha}}{2\theta}} \quad , \tag{1.d}$$

$$\theta = \frac{(3+\alpha)\{(3+\alpha)\gamma + \alpha - 1\}}{16(\gamma - 1)\varepsilon} \, . \tag{1.e}$$

Here, ρ, v, p, e, x, t, τ and γ represents the mass density, velocity, pressure, specific energy, length coordinate, time, pulse width and specific heat constant, respectively. A power-law driving source term, $\varepsilon(1+\alpha)t^{\alpha}$, has been used in

the energy equation. The case $\alpha = -1$ corresponds to the adiabatic expansions, whereas the energy deposition rate is constant in time at $\alpha = 0$. Equation (1c) of the mass density represents a half Gaussian function. Here, to represent the size of the expanding plasma in the x direction, we introduce $\sigma_1(t)$, the distance at which the plasma density decreases to 61 % of the maximum density. After the LIB termination, the plasma is subject to the adiabatic expansion. For a nonzero initial internal energy, the solution of the adiabatic expansion is same as that of LIB–driven expansion given by eq. (1) but setting $\alpha = -1$. During the adiabatic expansion ($t \geq \tau$), we assume v, e, and ρ to be given by

$$v(t,x) = A(t)x \,, \tag{2.a}$$

$$e(t,x) = e(t) \,, \tag{2.b}$$

$$\rho(t,x) = \frac{2M}{\sqrt{2\pi\sigma_2(t)^2}} \exp\left\{-\frac{x^2}{2\sigma_2(t)^2}\right\} \,, \tag{2.c}$$

where, $\sigma_2(t)$ is the plasma edge in the stage (b). Substituting eq. (2) into adiabatic hydrodynamic equations, we have

$$A(t) = \frac{1}{\sigma_2(t)} \frac{d\sigma_2(t)}{dt} \,, \tag{3.a}$$

$$e(t) = e_0 \left\{\frac{\sigma_0}{\sigma_2(t)}\right\}^{\gamma-1} \,, \tag{3.b}$$

$$\sigma_2(t) \frac{d^2\sigma_2(t)}{dt^2} = e_0(\gamma - 1)\left\{\frac{\sigma_0}{\sigma_2(t)}\right\}^{\gamma-1} . \tag{3.c}$$

In the above, we used $e(\tau) = e_0$, and $\sigma_2(\tau) = \sigma_1(\tau) \equiv \sigma_0$.

As the plasma expands toward the substrate at $t >> \tau$, $\sigma_0 / \sigma_2(t)$ will be very small. From eq. (3) together with condition that $\frac{d\sigma_2}{dt}|_{t=\tau} = \frac{d\sigma_1}{dt}|_{t=\tau}$, the plasma–expansion velocity, $u_0 = \frac{d\sigma_2}{dt}$, can be approximately given by

$$u_0 = \sqrt{e_0\left\{2 + \frac{(\gamma-1)(3+\alpha)}{1+\alpha}\right\}} \,. \tag{4.a}$$

The plasma edge (σ_2) is thus given by

$$\sigma_2(t) = u_0 t \quad . \tag{4b}$$

Substituting eq. (4b) into eqs. (2) and (3), and assuming the data of BIC responses as $J_{BIC} \propto \rho v$, we obtain J_{BIC} as

$$J_{BIC} = \frac{x}{t^2} Q_0 \exp\left\{-\frac{(x/t)^2}{2u_0^{\,2}}\right\} \quad , \tag{5}$$

where Q_0 is the constant. From eq. (5), u_0 is expressed by

$$u_0 = \frac{x}{\sqrt{2}t_{max}} \quad , \tag{6}$$

where t_{max} means the time at which the BIC data attains the peak.

From eqs. (2), (3) and (4), the dynamic pressure, $p_d = \frac{1}{2}\rho v^2$, and the static pressure, $p = (\gamma - 1)\rho e$, are given by

$$p_d = \frac{Mx^2}{\sqrt{2\pi}t^3 u_0} \exp\left\{-\frac{(x/t)^2}{2u_0^{\,2}}\right\} \quad , \tag{7.a}$$

and

$$p = \frac{2M(\gamma-1)(\frac{\sigma_0}{u_0 t})^{\gamma} u_0^{\,2}}{\sqrt{2\pi}\left\{2 + \frac{(\gamma-1)(3+\alpha)}{1+\alpha}\right\}\sigma_0} \exp\left\{-\frac{(x/t)^2}{2u_0^{\,2}}\right\} \quad . \tag{7.b}$$

From eqs. (1d), (1e), and (4b), σ_0 is obtained by

$$\sigma_0 = \frac{2u_0\tau}{(3+\alpha)\sqrt{1 + \frac{2(1+\alpha)}{(3+\alpha)(\gamma-1)}}} \quad . \tag{7.c}$$

4. Results and Discussions

We have measured the patterns of the LIB–damage on Ti target and evaporation–particle deposition on glass substrate in the diameter to be ~ 3.5 cm and 4 cm, respectively. Since the above two patterns are seen to be almost the same size, the IBE process seem to be considered as one–dimensional.

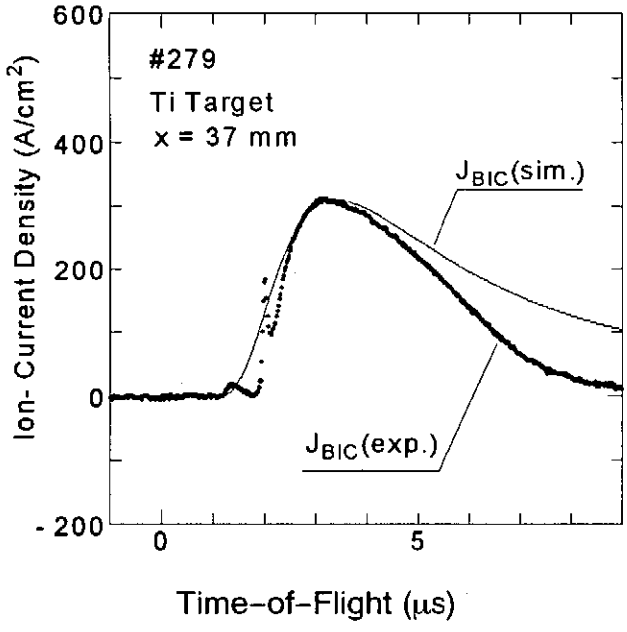

Fig. 3 BIC data of the experiment (dots) compared with the simulation (solid line) for Ti target at V_d ~ 1 MV.

The dots in Fig. 3 show the BIC data for Ti target. The expansion velocity of the plasma of $u_0 \sim 0.8$ cm/μs was estimated by eq. (6), and the corresponding theoretical curve of J_{BIC} was plotted in Fig. 3 (solid line) by using eq. (5).

To detect the mass loss of the target, the target weights were measured before and after the shot by using an electronic balance. The data of the measurements are summarized in Table I. The mass loss (M) is estimated to be ~ 1.4 mg/cm^2/shot.

From the mass-loss data of Table I ($M \sim 1.4$ mg/cm^2) and BIC data of Fig. 3 ($u_0 \sim 0.8$ cm/μs), the dynamic pressure of the ablation plasma estimated by eqs. (6) and (7a), $p_d = \frac{1}{2}\rho v^2$, at $x \sim 3$ cm (the distance from the target) is plotted in Fig. 4 by a solid line. We see p_d (peak) ~ 1.4 ×10^7 Pa and its pulse width is ~ 2.4 μs.

Table I. Mass loss for Ti target

Target: Ti	Sample 1	Sample 2	Sample 3
Area [mm²]	10.4 × 9.7	10.4 × 10.5	10.2 × 9.6
Weight before shot [mg]	277	291	259
Shots	3	2	3
Weight after shot [mg]	273	288	255
Mass loss [mg/(cm²·shot)]	1.3	1.4	1.4
Mass loss depth [μm/shot]	2.9	3.1	3.0

In general, $\alpha > 0$ and $\alpha < 0$ corresponds to the cases that the beam power rises and falls in time, respectively.[9] To estimate the static pressure, $p = (\gamma - 1)\rho e$, $\alpha = 0$ is assumed in the stage (a).[9-11] Since the temperature of the ablation plasma is high, we expect high degree of excitation or ionization. For the unexcited monoatomic gas, $\gamma = 5/3$, but for the excited or

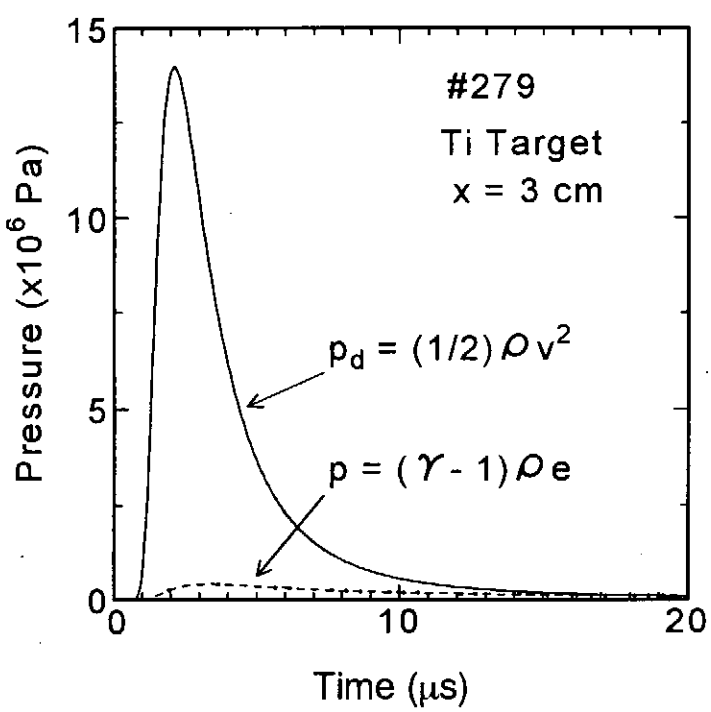

Fig. 4 Culculated curves of dynamic (p_d) and static (p) pressures as a function of time at x = 3 cm for Ti target at V_d ~ 1 MV.

ionized monoatomic species, $\gamma = 1.2 \sim 1.3$. [13] Using eqs. (6), (7b) and (7c), the static pressure (p) at $x \sim 3$ cm is also plotted in Fig. 4 by a dashed line. We see p is much smaller than p_d in the IBE. In other words, the kinetic energy of the ablation plasma is much larger than the themal energy.

5. Summary

The characteristics of the ablation plasma produced by the IBE can be easily determined by the measurement of the ion flux density and the target mass loss. An one-dimensional hydrodynamic model in the IBE process has been introduced to understand the physical process of the ablation plasma by assuming an LIB-driven expansion and the following adiabatic expansion into vacuum. The analytic solutions are given to deduce the temperature and pressure reached in the ablation using the experimental data of BIC ($u_0 \sim 0.9$ cm/μs) and the target mass loss measurement ($M \sim 1.4$ mg/cm^2/shot), yielding $p_d \sim 1.4 \times 10^7$ Pa and the pulse width of ~ 2.4 μs (at $x \sim 3$ cm) for Ti target at $J_i \sim 1$ kA/cm^2 and τ (pulse width) ~ 70 ns. The present method will be sufficiently applicable to the ablation plasma such as produced by intense lasers or electron beams.

REFERENCES

1. Y. Shimotori, M. Yokoyama, S. Harada, H. Isobe, K. Masugata and K. Yatsui: *J. Appl. Phys.* **63** (1988) 968.
2. Y. Shimotori, M. Yokoyama, S. Harada, K. Masugata and K. Yatsui: *Jpn. J. Appl. Phys.* **28** (1989) 468.
3. K. Yatsui: *Laser and Particle Beams* **7** (1989) 733.
4. T. Takaai, T. Hatsushika, T. Susuki, K. Masugata and K.Yatsui: "*Surface Engineering*", ed. by S. A. Meguid (Elsevier Sci. Pub. Ltd., 1990), p. 188.
5. P. E. Dyer, R. D. Greenough, A. Issa and P. H. Key: *Appl. Phys. Lett.* **53** (1988) 534.
6. J. P. Zheng, Z. Q. Huang, D. T. Shaw and H. S. Kwok: *Appl. Phys. Lett.* **54** (1989) 280.
7. K. Yatsui, A. Tokuchi, H. Tanaka, H. Ishizuka, A. Kawai, E. Sai, K. Masugata, M. Ito and M. Matsui: *Laser and Particle Beams* **3** (1985) 119.
8. C. Eichenberger, S. Humphries, Jr. and J. Maenchen: *J. Appl. Phys.* **48** (1977) 1447.
9. X. Kang, K. Masugata and K. Yatsui: *Jpn. J. Appl. Phys.* **33**, #2 (1994) (in press).
10. K. Yatsui, X. Kang, T. Sonegawa, T. Matsuoka, K. Masugata, Y. Shimotori, T. Satoh, S. Furuuchi, Y. Ohuchi, T. Takeshita and H. Yamamoto: *Phys. Plasmas 1*, #5, Pt.2 (1994) (in press).
11. X. Kang, K. Masugata and K. Yatsui: "Evaluation of Ablation Plasma Characteristics of Intense, Pulsed, Ion-Beam Evaporation", *Laser and Particle Beams* (1993) (submitted for publication).
12. A. V. Farnsworth, Jr., M. M. Widner, M. J. Clauser, P. J. McDaniel and K. E. Lonngren: *Phys. Fluids* **22** (1979) 859.
13. Ya. B. Zeldovich and Yu. P. Raiser: "*Physics of Shock Wave and High Temperature Hydrodynamic Phenomena*" (Academic Press, 1968), Vol.II, p. 573.

A Study on Successive Generation of Intense Pulsed Ion Beams by the Inverse Pinch Ion Diode

Yoshiyuki HASHIMOTO, Mitsuyasu YATSUZUKA and Sadao NOBUHARA

Department of Electrical Engineering, Faculty of Engineering, Himeji Institute of Technology, 2167 Shosha, Himeji, Hyogo 671-22

Abstract

Successive generation of intense pulsed ion beams was studied experimentally by the inverse pinch ion diode. When the anode of metals or plastics is used as an ion source, the diode impedance and the ion beam current were changed with every shots of operation. In case of a copper anode, the ion current at the tenth shot was reduced to one half or one third than that at the first shot. Using soda-lime glass ($Na_2O{\cdot}CaO{\cdot}5SiO_2$) surface of which vacuum oil or Aquadag was coated as the ion source, the diode impedance and the ion current remained constant during 25–30 shots. Using the vacuum oil ion source, the most dominant species in the ion beam was C^{3+} which has energy in the range of 150–200 keV. The current density of the ion beam at 120 mm behind the anode was about 100 A/cm^2.

1. Introduction

Recently, generation of an intense pulsed ion beam (IPIB) using a pulsed power machine has been studied for the application to material development. Yatsui et al. have reported the production of thin films using the IPIB.[1,2] Pogrebnjak et al. have showed the increasing microhardness of metal samples by irradiating the IPIB.[3,4] Hashimoto et al. have achieved the focusing of the IPIB using an inverse pinch ion diode (IPD)[5,6] with a flat anode[7] and improved quality of the IPIB by successive operation.[8] Generally, metals or plastics such as aluminum, copper, acrylic resin or Teflon have been used to generate the IPIB as an ion source for application of the material development. However, these ion source materials are easily vaporized by electron bombardment, leading to change in diode characteristics with each shot of operation.

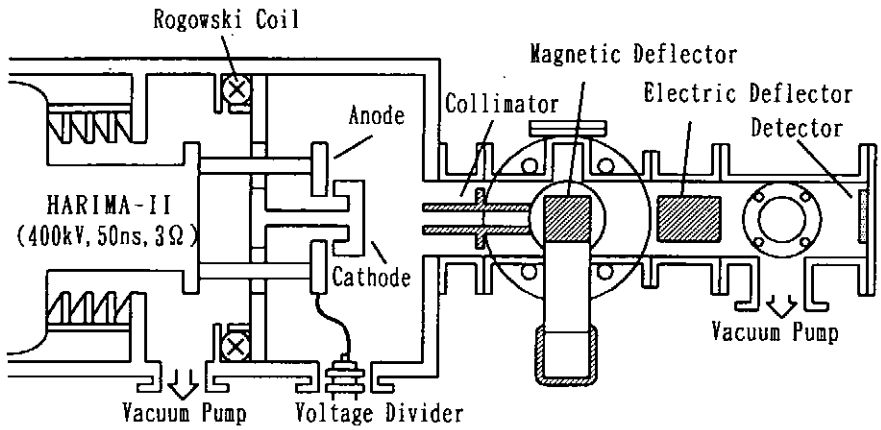

Fig. 1 Schematic configuration of the experimental setup.

In this paper, we report on a stable generation of an IPIB using a glass anode whose surface was coated with vacuum oil or Aquadag. The diode impedance and the ion beam current obtained with the glass anode are compared with those solid ion sources. In § 2, the apparatus and methods are introduced. Experimental results and some discussions are described in § 3, and some conclusions are presented in § 4.

2. Apparatus and Methods

A drawing of the experimental setup is shown in Fig. 1. The pulsed power machine "HARIMA-II" (400 kV, 3 Ω, 50 ns) at Himeji Institute of Technology was used. The inverse pinch diode (IPD) was located at the end of the "HARIMA-II." The inner and outer diameters of the anode were 12 mm and 50 mm, respectively. Two types of the anode were used. One was the metal or plastic anode such as aluminum, copper, acrylic resin or Teflon. Another was the glass anode of which surface vacuum oil and Aquadag was coated as an ion source. The inner and outer diameters of the cathode were 12 mm and 16 mm, respectively. The anode-cathode (A-K) gap length was 3 mm. A diode chamber was evacuated by an oil diffusion pump to $2.0\text{–}8.0\times10^{-5}$ Torr.

Diode voltage was measured using a resistive divider at closely the anode plate. Diode current was measured using a Rogowski coil at the end of the pulsed power generator. Ion current was estimated using a biased ion collector (BIC) located on the downstream side of the diode. In this experiment, two types of BIC were used: one was a single pinhole BIC and the other was a multi pinhole BIC. The single pinhole BIC consisted of a ground

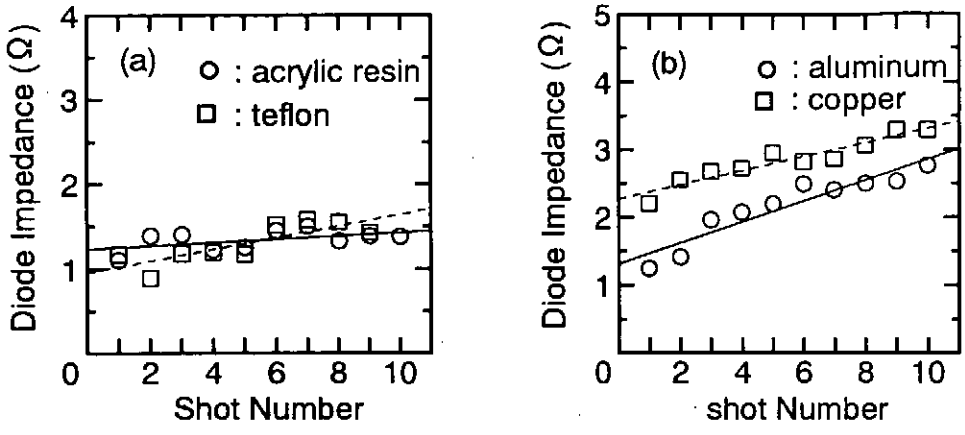

Fig. 2 The diode impedance as a function of shot number for (a) the plastics and (b) the metals as an ion source, respectively, where the A-K gap length is 3 mm and thickness of each ion source is 2 mm.

plate with a small aperture of 0.5 mm in diameter and an ion collector located behind the ground plate. The single pinhole BIC was movable in the axial and radial directions and was used to measure the current density of ion beams. The multi pinhole BIC consisted the ground plate with a mesh (transparency = 2.8 %) and an ion collector, was used to measure the total current of ion beams. The collectors of both BICs were biased at a voltage of −450 V to remove accompanying electrons. Species and energy distribution of ion beams were diagnosed using a Thomson-parabola ion spectrometer. The Thomson-parabola ion spectrometer consists of a collimator, electric and magnetic deflectors, and an ion detector. The collimator has two pinholes of 0.2 mm and 0.5 mm in diameter. The maximum value of magnetic and electric field are 0.5 T and 6 kV/cm, respectively. Here, a solid-state track detector (CR-39) was utilized as an ion detecting film.

3. Experimental Results and Discussion

3.1 Ion beam generation with solid ion sources

Diode characteristics during successive shots was studied with the ion source material of aluminum, copper, acrylic resin and Teflon. The thickness of these materials was 2 mm.

The characteristics of the ion beam during successive shots were studied using the anode of plastics or metals as an ion source. The ion beam was generated at intervals of 5 minutes at each shot. Figure 2(a) and 2(b) show the diode impedance as a function of

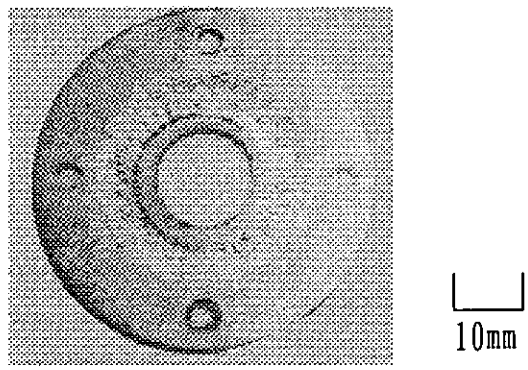

Fig. 3 A photograph of the copper plate attached to the anode after 10 shots.

shot number for the plastic ion sources and the metal ones, respectively, where the A-K gap length was 3 mm and the residual gas pressure in the diode chamber was 5×10^{-5} Torr. Here, the diode impedance was defined as the ratio of the maximum diode voltage to the maximum diode current. As seen in Fig. 2, the diode impedances at each ion source increase almost linearly with shot number. The increase in the diode impedance results from dissipation of the solid ion sources by electron bombardment to the anode surface, that is, the resultant extension of the A-K gap length. The degree of increased impedance for the metal ion sources is larger than that for the plastic anode as shown in Fig. 2(a) and 2(b). This is ascribed to the fact that the metal anodes dissipated more easily by electron bombardment than the plastics did.

A photograph of the copper plate after 10 shots is shown in Fig. 3. The damage of the copper plate by electron bombardment is the most severe at a slightly outside of the cathode as seen in Fig. 3. After 10 shots, the thickness of the copper plate, which was 2 mm in the thickness at the first, was decreased by 1 mm.

The ion beam current as a function of shot number for the plastic ion sources and the metal ones are shown in Fig. 4(a) and 4(b), respectively. In both cases, the ion beam current is decreasing with increasing shot number. The decrease in ion beam current is caused by the increase in the diode impedance as mentioned above. The amount of ion beam current is found to be different with each ion source materials as seen in Fig. 4(a) and 4(b). The dominant component of the ion beam species for acrylic, Teflon, aluminum and copper plates were found to be H^+, C^{3+}, Al^+ and Cu^{3+} ions using the Thomson parabola ion spectrometer, respectively.

From these results, it was found that the diode impedance were varied with each shot

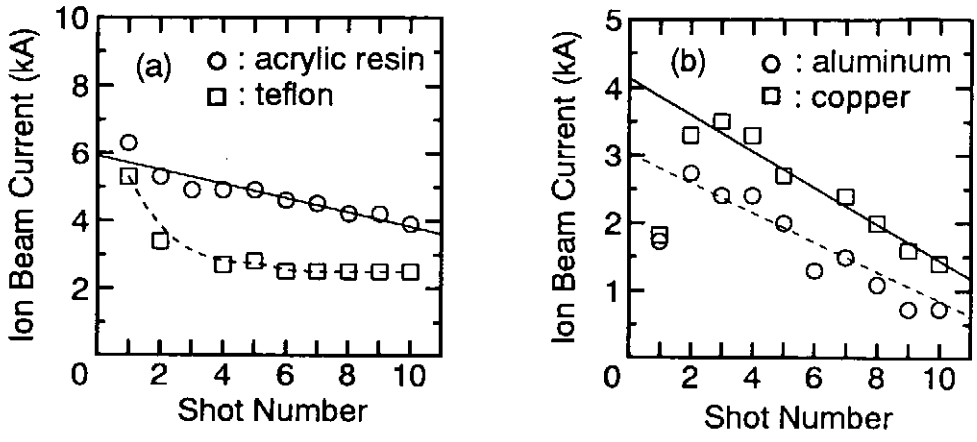

Fig. 4 Ion current as a function of shot number for (a) the plastics and (b) the metals as an ion source, respectively, where the A-K gap length is 3 mm.

of operation for the metal and plastic anode. As a result, the energy and current of ion beams were varied with every shots. Although ions are easily extracted using the ion source of plastics and metals, these ion sources are not good for stable ion beam generation. Generation of a stable ion beam by successive shots needs to tough materials against electron bombardment.

3.2 Ion beam generation with a glass anode

Instead of plastics or metals, a soda-lime glass ($Na_2O{\cdot}CaO{\cdot}5SiO_2$) was attached to the anode surface to prevent the anode from dissipating by electron bombardment. The glass anode comprises an aluminum ring and a glass plate of 2 mm in thick. The aluminum ring and the glass plate are fixed with a synthetic resin glue. Vacuum oil or Aquadag solution as an ion source were applied on the surface of the glass anode. The thickness of vacuum oil or Aquadag solution was negligible compared with A-K gap length.

Typical time histories of diode voltage, diode current, ion beam current and ion beam current density are shown in Fig. 5, where the vacuum oil is coated on the surface of the glass anode as an ion source. The current and current density of the ion beam were measured at 120 mm behind the anode using the single and the multi pinhole BIC, respectively. As seen in Fig. 5, the maximum diode voltage is found to be about 200 kV, and the pulse width is about 80 ns (FWHM). The diode current rises in 10 ns after the diode voltage is started and reaches its peak value of 90 kA within 70 ns. The peak value

of the ion beam current is found to be 2.5 kA. As seen in Fig. 5(d), the maximum density of the ion beam is 120 A/cm^2.

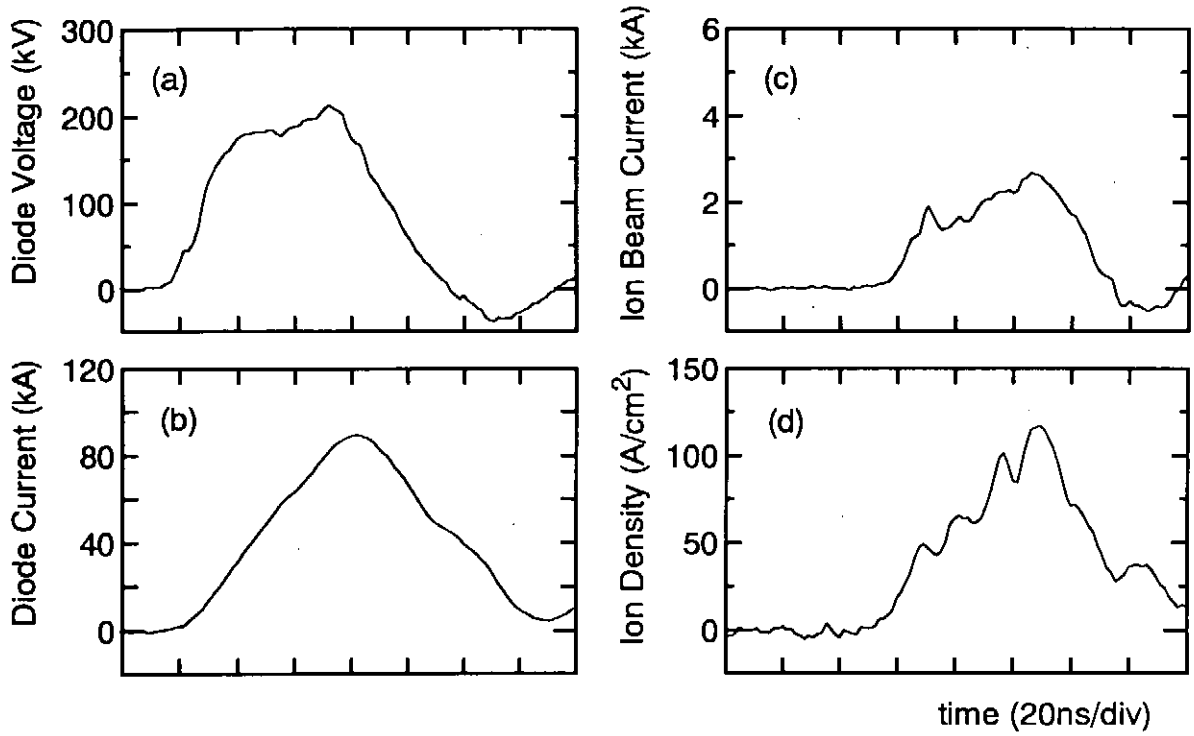

Fig. 5 Typical time history of (a) diode voltage, (b) diode current, (c) ion current and (d) current density of ion beam, where the vacuum oil is coated on the glass attached to the anode as an ion source.

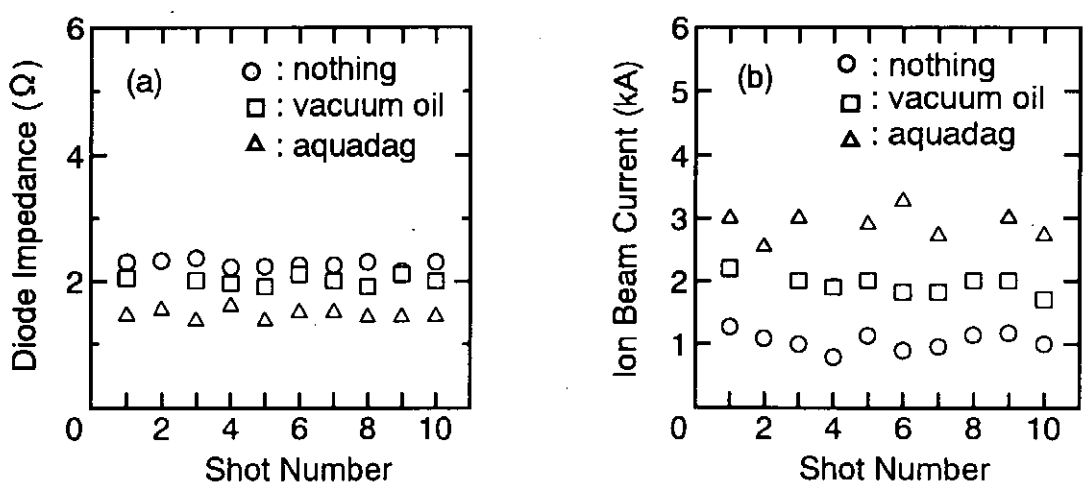

Fig. 6 (a) Diode impedance and (b) ion current as a function of shot number for a glass anode.

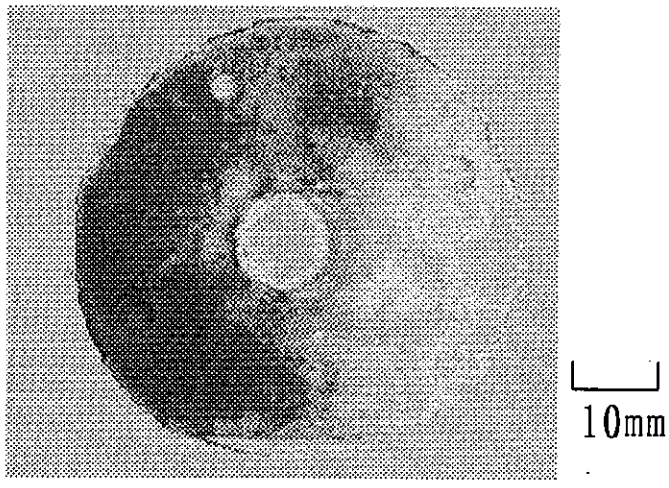

Fig. 7 A photograph of the glass anode after 20 shots.

The ion beam was generated by successive shots at the intervals of 5 minutes in each shot, where the A-K gap length was 3 mm and the residual gas pressure in the diode chamber was 5×10^{-5} Torr. Figure 6(a) and 6(b) show the diode impedance and the ion current as a function of shots number, respectively, where a solid circle indicates for no ion source, a solid square for the vacuum oil ion source and a solid triangle for the Aquadag solution. The diode impedance is the same as that defined in § 3.1. The ion beam current was measured with the multi pinhole BIC located at 120 mm behind the anode. As seen in Fig. 6(a), the diode impedance for various ion sources remains constant during successive operation. This result implies that the glass is more tough against dissipation by electron bombardment than aluminum, copper, acrylic resin or Teflon. In Fig. 6(a), we see the largest diode impedance for no ion source on the glass, while the smallest diode impedance appears for the Aquadag ion source. This result is due to difference in the surface resistance of each ion source. As seen in Fig. 6(b), the ion currents are almost constant for each shot. The ion currents for the Aquadag and vacuum oil ion sources were about 3 kA and 2 kA, respectively, in Fig. 6(b). The ion current of 1 kA is obtained even for no ion source on the glass. In this case, ions arises from adsorbed matter on the glass surface.[6)]

Figure 7 is a photograph of the glass anode after 20 shots, showing less damage of the glass surface by electron bombardment. Then, in this experiment, no change of the A-K gap length and the diode impedance is observed at each of successive shots.

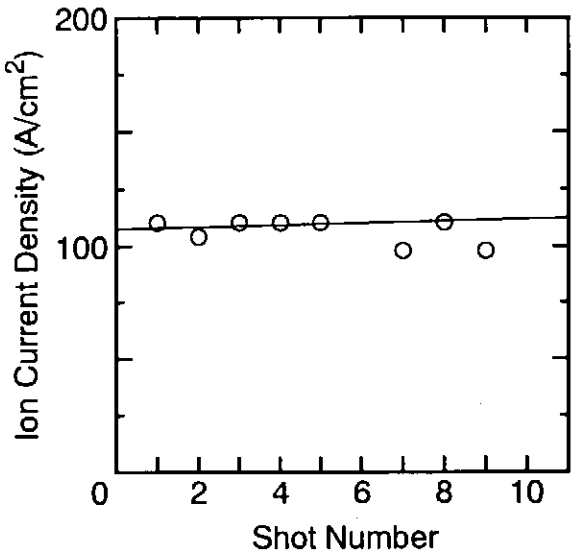

Fig. 8 Current density of ion beam on the diode axis, where the vacuum oil is used as an ion source.

The current density of the ion beam on the diode axis for the vacuum oil ion source is shown in Fig. 8, the data of which was obtained by the single pinhole BIC located at 120 mm behind the anode. As seen from Fig. 8, the current density of the ion beam was found to be almost constant during successive operation. In Fig. 8, the maximum current density of the ion beam is about 100 A/cm^2.

Figure 9 shows photographs of the film, CR-39, indicating the mass and energy distributions of ion beams obtained by the Thomson-parabola ion spectrometer, where the upper (a) is for the vacuum oil ion source and the lower (b) is for the Aquadag ion source. As seen in Fig. 9(a) and 9(b), the main components of the ion beam are found to be C^+, C^{2+} and C^{3+} in both cases. In Fig. 9, we see low and high energy components of ions. The low energy component has the energy in range of 150– 200 keV, which energy is in good agreement with the diode voltage measured with the voltage divider. The high energy components of ions are two to four times larger than that of low energy ones. These high-energy ions can be produced through the charge exchange process in the diode region.

As mentioned above, using the glass anode, the diode impedance as well as the ion beam current remains constant during 25–30 shots under the present experimental conditions. The anode with the harder materials such as quarts glass or ceramics instead of the soda-lime glass might improve the diode characteristics during successive operation.

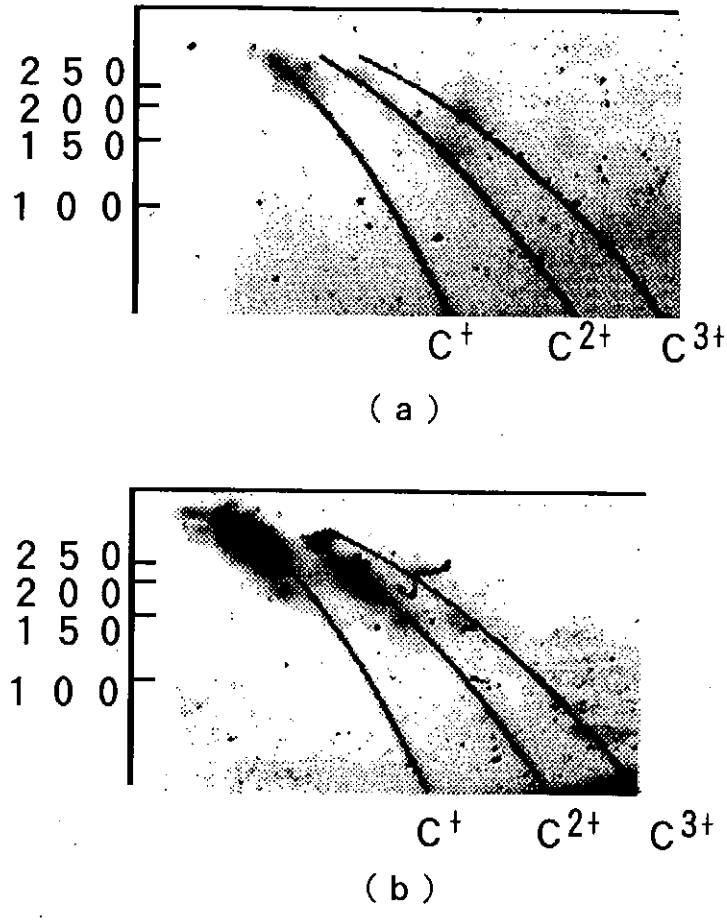

Fig. 9 Photographs of the CR-39 film which show the mass and energy distribution of the ion beam measured by the Thomson- parabola ion spectrometer, where (a) the upper picture indicates for the vacuum oil ion source, (b) the lower one for the Aquadag solution ion source, and the magnetic and the electric fields were 0.15 T and 3 kV/cm, respectively.

4. Conclusions

Successive generation of intense pulsed ion beams has been studied. When aluminum, copper, acrylic resin or Teflon was attached to the anode as an ion source, the diode impedance increased with increasing shot number. After 10 shots, the ion current was reduced to one half or one third than that at the first shot. When the soda-lime glass ($Na_2O{\cdot}CaO{\cdot}5SiO_2$) was attached to the anode, on the other hand, the diode impedance and the ion current remained constant during 20–30 shots. In the case of applying a

vacuum oil to the glass anode as an ion source, the most dominant species of the ion beam was C^{3+} which has energy in the range of 150–200 keV. The current density of the ion beam at 120 mm behind the anode was about 100 A/cm^2.

References

1) Y. Shimotori, M. Yokoyama, S. Harada, H. Isobe, K. Masugata and K. Yatsui : J. Appl. Phys. **63** (1988) 968.

2) K. Yatsui : Laser & Particle Beams **7** (1989) 733.

3) A. D. Pogrebnjak and Sh. M. Ruzimov : Phys. Lett. A **120** (1987) 259.

4) A. D. Pogrebnjak, I. F. Isakov, M. S. Opekunov, Sh. M. Ruzimov, A. E. Ligachev, A. V. Nesmelov and I. B. Kurakin : Phys. Lett. A **123** (1987) 410.

5) J. P. VanDevender, J. P. Quintenz, R. J. Leeper, D. J. Johnson and J. T. Crow : J. Appl. Phys. **52** (1981) 4.

6) S. Miyamoto, A. Yoshinouchi, T. Ozaki, S. Higaki, H. Fujita, K. Imasaki, S. Nakai and C. Yamanaka : Jpn. J. Appl. Phys. **22** (1983) L703.

7) Y. Hashimoto, M. Sato, M. Yatsuzuka and S. Nobuhara : Jpn. J. Appl. Phys. **31** (1992) 1922.

8) Y. Hashimoto, M. Yatsuzuka and S. Nobuhara : Jpn. Appl. Phys. **32** (1993) 4838.

Measurements of 20 GHz High-Power Microwaves Output from a Large Diameter Plasma Filled Backward Wave Oscillator

Ken-ichi kurashina, Wonsop Kim, Kazuo Ogura, Kazuo Minami,
Tsuguhiro Watanabe*, and Syouji Sugito*

Department of Electrical Engineering, Faculty of Engineering,
Niigata University
and
*National Institute for Fusion Science

ABSTRACT

A large diameter plasma filled backward wave Oscillator(BWO) is investigated experimentally. The parameters of slow wave structure are chosen so that the oscillation frequency is about 20 GHz at 60 keV beam energy. Plasma is produced by the beam and it has favorable effects on beam propagation and Cerenkov oscillation. The output power of the BWO with plasma is observed to be 3-6 times that of vacuum BWO. The power level of several kW and efficiency is about 0.01% are obtained. The output power strongly enhanced when the guiding magnetic field approaches to the fundamental electron cyclotron resonance. The maximum power of 490 kW with an efficiency of 4% is achieved even for a relatively low beam energy of 60 keV.

1. INTRODUCTION

In large scale fusion devices, microwave sources of the order of 100 MW for the purposes of non-inductive current drive, current profile control and plasma heating are expected to be indispensable.[1] For such purposes, high power microwave sources utilizing intense electron beams (IREB's) are a hopeful candidate. Backward wave oscillators (BWO's) driven by IREB are one of these devices. BWO's reached output power levels 1GW/cm at wavelengths near 1 cm[2)~3)] and they are one of the most promising microwave sources for future plasma heating. They can be driven by an axially injected electron beam without initial perpendicular velocity. A metallic slow wave structure (SWS) with periodically corrugated wall is not charged up harmfully by the beam and can carry large beam currents compared with dielectric SWS's. The improvements in efficiency were observed, when BWO's were operated in the presence of background gases with adequate pressure[4)] or of plasma with moderate density[5)]. We present experimental results of a large diameter plasma filled BWO with an oscillation frequency around 24GHz. The diameter is much larger than the free space wavelength of generated microwaves. The large diameter enables us to attain high power TM oscillation which withstands microwave breakdown inside the SWS. An optimal design study was made by our linear analysis.[6)~8)]

The outline of this paper is as follows. In section 2, we discuss the design of the large diameter BWO. Experimental set-up is shown in section 3. The experimental results and operation mode in the large diameter BWO are presented in section 4. The summary is given in section 5.

2. LARGE DIAMETER BWO DESIGN

The purpose of our experiment is to investigate the microwave generation from a large diameter plasma filled BWO. The BWO consists of SWS with sinusoidally varying metallic wall and an annular beam propagating in the SWS as shown in Fig. 1. The dimensions of SWS are chosen so as to get the oscillation frequency about 24 GHz for the beam energy 100 keV. In Fig.2, the dispersion curves of two structure mode, TM and TM , are depicted. The investigation of the structure TM mode with 100 keV beam line gives the oscillation frequency about 24 GHz. The average diameter of this SWS is about 4 times larger than the free space wavelength of output wave. The interaction between the beam and the structure mode is inherently weak. For low energies down to 30 keV, the frequency is expected to be around 20 GHz or less. The interactions of beam mode with higher structure modes such as TM are much weaker than that with fundamental TM mode.

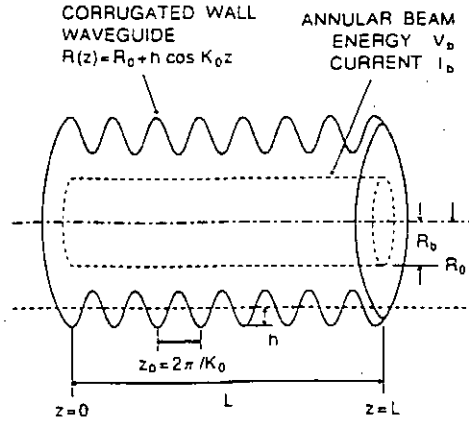

Fig.1

Oversized slow wave structure and an Annular Beam

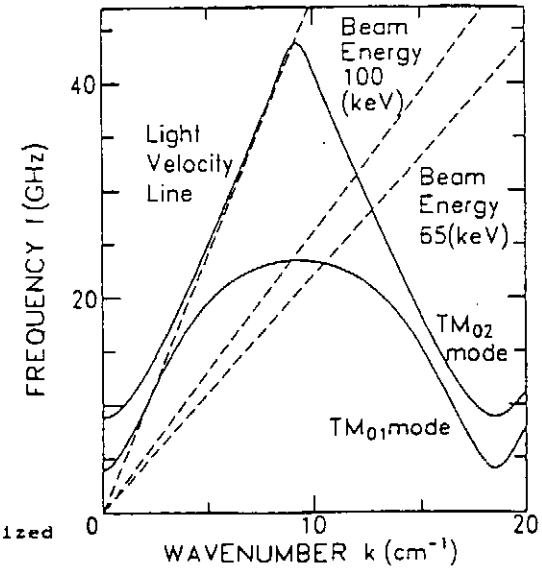

Fig.2

Dispersion Relation of Oversized Slow Wave Structure

3.EXPERIMENTAL SETUP

The schematic diagram of experimental setup is shown in Fig.3. The Marx generator drives the pulse forming line (PFL) with high voltage up to 130 kV. PFL consists of a coaxial line with the characteristic impedance of 50 ohm. The electron beam is generated by a beam diode that consists of an aluminum cathode with circular sharp edge and foiless stainless steel anode. The PFL output voltage up to 65 kV is applied to the cold cathode through a gap switch. In order to get relatively uniform electron beam at average electric fields around 70 kV/cm, the axisymmetric emitting edge of the cathode is wrapped with velvet. The beam collector is inversely tapered aluminum pipe, connected to the SWS. On the end with small diameter, the microwave output window is installed. The electron beam diode, the large diameter SWS and the beam collector are installed in a stainless steel pipe which is evacuated to a pressure $2\text{-}4\times10^{-5}$ Torr. There is a helium gas injection port near the output window. Applied guiding axial magnetic field is uniform over the extent from the cathode to the end of SWS.

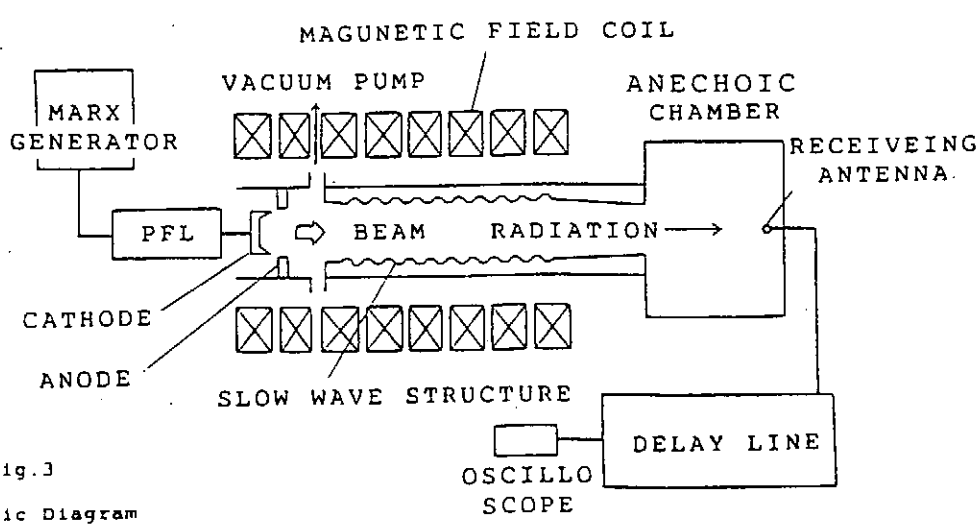

Fig.3
Schematic Diagram of Experimental Setup

The diagram of microwave diagnostic system is shown in Fig.4. The microwaves generated in SWS are radiated from the output window into anechoic chamber which is covered with microwave absorber. The pick up horn is placed at 10 cm away from the output window. The received signal is split into two branches by a multi-hole directional coupler. One branch consists of a short waveguide which forms a prompt signal. The other is a delay line waveguide 8 m long and results in a delayed signal. The delay time depends on the frequency and directly correlates to the frequency spectrum of the microwave.

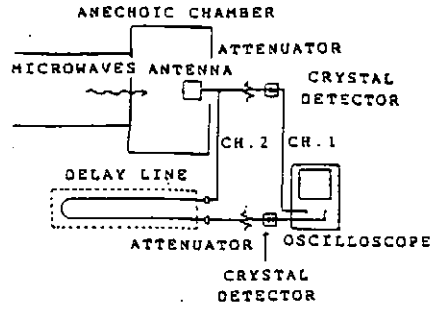

Fig.4
Schematic Diagram of Microwave Diagnostic System

4.EXPERIMENTAL RESULTS

a) Beam Propagation

The electron beam propagation is monitored by thermal damage patterns taken with thermally sensitive paper mounted on a stainless steel plate. Figure 5 shows the changes in the axial positions of cross-sectional thermal damage patterns of the beam.

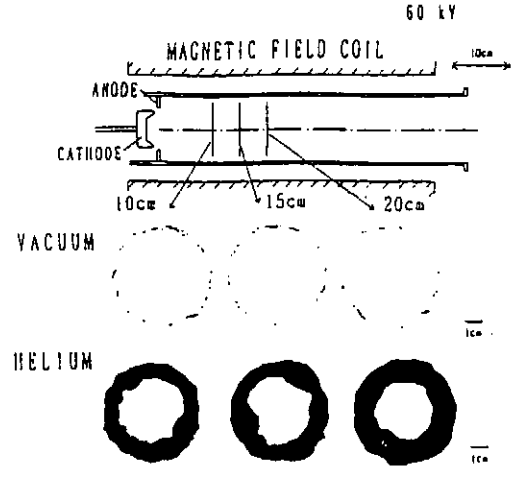

Fig.5
Thermal Damage Patterns of Electron Beam for Velvet-Wrapped Cold Cathode in High Vacuum and in Helium Gass

All patterns represent an overlay of 10 shots. In vacuum case, the damage patterns are a broken thin circle. The electron beam is annular but the uniformity is considerably poor. In helium gas at the pressure 40 mTorr, the damage patterns are much denser and thicker than those in vacuum case. This drastic change of the damage patterns shows that helium plasma is produced by the beam. The stainless steel plate without the thermally sensitive paper is used to measure the beam current wave form at various axial positions. Inside the interaction region between the beam and the structure wave, the beam current is about 200 A in vacuum and increases to about 250 A in helium gas. Plasma produced by the beam improves significantly the beam propagation inside the SWS.

b) Microwave Measurements

Figure 6 shows a typical microwave signal from the large diameter plasma filled BWO. The beam energy and current are 55 keV and 200 A, respectively. The frequency is about 19 GHz and roughly coincides with the predicted value in our linear analysis.The output frequencies were ranging from 17.4 to 21 GHz. The frequency spectrum lower than 17.3 GHz cannot be measured because of the presence of cutoff frequency of the delay line waveguide. In many shots, only the prompt signal (CH1) was observed and there are no

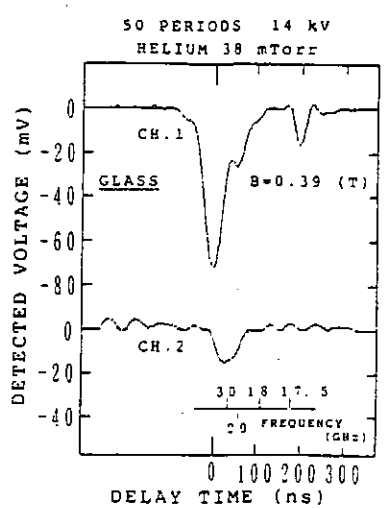

Fig.6
Frequency Spectrum for Large Diameter Plasma-Filled BWO

delayed signals. In these cases, output frequency was estimated to be from 14.5 GHz to 17.4 GHz.

The output power increases with increasing anode-cathode voltage as shown in Fig. 7. The peak microwave power is the order of 1 kW and the efficiency is around 0.01%. Figure 8 shows the dependence of the output power on the normalized structure length. In the plasma filled BWO, the output power increases with increasing the length of structure,L. However, in vacuum BWO, the power keeps a low level and start to increase at $L=70z_0$. The large diameter BWO might not work well at the conditions which we adopted.

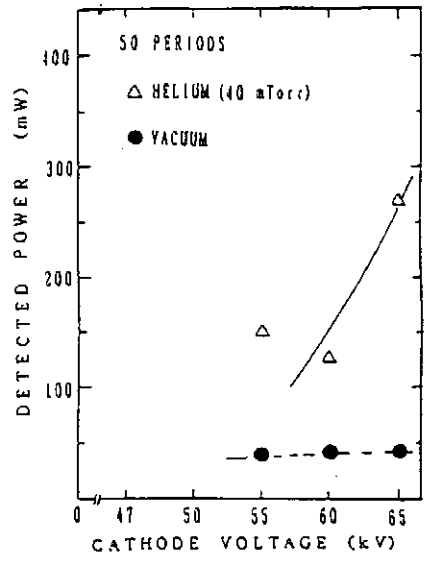

Fig.7

Dependence of the Output on Cathode Voltage

c) Operation Mode of a Large Diameter BWO

Regarding the dependence of BWO output on guiding magnetic field, the conflicting results have been reported previously. Near electron cyclotron resonance (ECR), the microwave power even decreased resonantly. On the other hand, there were some reports that the output power increased resonantly near ECR.[4), 9), 10)]

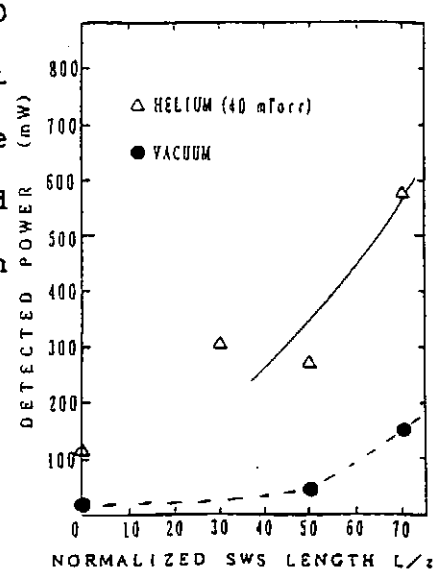

Fig.8

Dependence of the Output on Total Length of SWS

In our experiment, a large diameter SWS was used. The Cerenkov interaction was very weak up to about 65 keV beam energy. The fundamental ECR is at 0.64 T and second ECR is at 0.32 T. The microwave power increased drastically with approaching to the fundamental ECR. The maximum power is about 490 kW. It is emphasized that the beam energy was about 60 keV. The corresponding maximum efficiency was about 4 %. In vacuum case, the similar magnetic dependence was obtained. The maximum power and efficiency were about 300 kW and 3 %, respectively. A small hump was observed at the second ECR.

5.SUMMARY

We have investigated a large diameter plasma filled BWO experimentally. The parameters of slow wave structure are designed to oscillate at 24 GHz with 100 keV beam energy and 20 GHz with 60keV. Average diameter 60 mm is four times larger than space wavelength at 20 GHz. The BWO is driven by annular beam with radius 26.3 mm, typical current 200 A and typical energy 60 keV. Plasma is produced by the beam and improved beam propagation is observed. The good effects of plasma on Cerenkov oscillation is confirmed. The output power of plasma filled BWO is 3-6 times that of vacuum BWO. Both output powers of plasma filled BWO and vacuum BWO are strongly enhanced, when the guiding magnetic field approaches to the fundamental electron cyclotron resonance. The maximum power of 490 kW with the efficiencyof 4% is obtained with relatively low beam energy 60 keV.

REFERENCES

1) W.Lindquist, F.Casci, N.Fujisawa, et at., Plasma Physics and Controlled Nuclear Fusion Research 1990 (Proc. 13th Int. Conf. Washington D.C.), Vol.1, IAEA-CN-53/F-III-5.

2) S.P.Bugaev, V.A.Cherepenin, V.I.Kanavets, et al., IEEE Trans. Plasma Sci., Vol. PS-18, (1990) 518.

3) S.P.Bugaev, V.A.Cherepenin, V.I.Kanavets, et al., IEEE Trans. Plasma Sci., Vol. PS-18, (1990) 525.

4) K.Minami, W.R.Lou, W.W.Destler, et al., Appl. Phys. Lett. Vol.53, (1988) 559.

5) Y.Carmel, K.Minami, R.A.Kehs, et al., Phys. Lev. Lett., Vol.62, (1989) 2389.

6) K.Minami, Y.Carmel, V.L.Granatstein, et al., IEEE Trans. Plasma Sci., Vol.PS-18, (1990) 537.

7) M.M.Ali, K.Ogura, K.Minami, et al., Phys. Fluids B, Vol.4, (1992) 1023.

8) K.Minami, M.M.Ali, K.Ogura, et al., J. Phys. Soc. Jpn., Vol.61, (1992) 3566.

9) S.Yu.Galuzo, V.L.Kanavets, A.I.Slepkov and V.A.Pletyushkin, Sov. Phys. Tech. Phys., Vol.27, (1982) 1030.

10) A.N.Didenko, A.R.Borisov, G.P.Fomenko, et.al., Sov. Tech. Phys. Lett., Vol.9, (1983) 572.

Plasma Effects on Electron Beam Dynamics in a Virtual Cathode Oscillator

Mitsuyasu Yatsuzuka, Kenji Nagakawa, Yoshiyuki Hashimoto,

and Sadao Nobuhara

Department of Electrical Engineering, Faculty of Engineering, Himeji Institute of Technology

Abstract

High-power microwave generation in an axially-extracted virtual cathode oscillator has been studied experimentally. The microwave emission of 1.2 GW at frequencies in the range of 15 GHz is observed in the presence of annular electron beam operated at a 330 kV and 20 kA. The electron beam current in the diode region is well characterized by the electron space-charge-limited current in bipolar flow, which is well below the critical current defined for diode pinching. The observed microwave emission is accompanied by the strongly pinched electron beam which is resulted from the formation anode plasma. Essential feature of such a pinching effect for the microwave generation is confirmed by the absence of emission when the pinch of electron beam is suppressed by the application of the axial magnetic field.

I. INTRODUCTION

The virtual cathode oscillator (vircator) has become one of the most promising high-power microwave sources, because of conceptional simplicity, high-output-power capability, and possible wide bandwidth with tunable character [1]. Tunability of radiation frequencies can be achieved by changing anode-cathode (A-K) gap separation, cathode dimension, and cathode shape. Recent experiments showed the maximum microwave power as large as several gigawatts in the frequency

range from 0.5 to 17 GHz [1-3]. More recently, Yatsuzuka et al. [4] observed higher frequencies in range of 20-35 GHz with the peak power of 350 MW by the use of a point pinch diode which is capable of producing a high electron beam density. Benford et al. [5,6] showed that the microwave generation begins when the diode current characterized by the electron space-charge-limited current, I_{SC}, exceeds the critical current, I_C, which is defined as a current whose self-magnetic field turns electrons 90 degrees in the diode gap. Burkhart [7] showed that the diode current and voltage at microwave turn-on are much larger than those at the point where $I_{SC} = I_C$. There are a number of phenomena occurring simultaneously in vircator diodes such as beam pinching, ion generation on the anode [7], and the interaction between the vircator and magnetically insulated transmission line [8]. The exact importance and sequence of these phenomena related to the microwave generation are not yet well understood.

In this report our experimental study is focused on the electron beam behavior at the time of microwave generation from an axially-extracted vircator with an annular cathode and aluminum-foil anode. In order to see the overall picture of electron beam behavior, electron beam current at just upstream and downstream of the anode is measured while observing beam traces on the anode. We observed pinching of electron beam accompanied by microwave generation for the condition $I_{SC} < I_C$, contrary to the earlier observation by Benford and others [5,6]. The experimental setup and microwave diagnostic system are described in Section II. In Section III experimental results of microwave emissions are presented and some conditions for microwave emission are discussed. Conclusions are given in Section IV.

II.EXPERIMENT

Experiments were performed using the pulsed power generator "HARIMA-II" (maximum output voltage: 400 kV, output impedance: 3 Ω, and pulse duration: 50 nsec) at the Himeji Institute of Technology. The schematic diagram of the experimental arrangement is shown in Fig. 1. The electron beam diode consists of an annular cathode (typically radius $R_c = 1 - 1.5$ cm and thickness x

= 1.0 mm) and an aluminum foil anode of 15 μm in thickness. The electron beam emitted from the annular cathode passed through the anode foil and was injected into a cylindrical waveguide (radius R = 2.25 cm and 2 m in length) located at just downstream of the anode. The A-K gap separation d was varied from 0.2 to 0.7 cm. Electron beam currents were measured using a nsec-response Rogowskii coil at the upstream (1.1 cm from the anode) and downstream (0.1 cm from the anode). The diode voltage was measured by a resistive divider at the location close to the anode. The radiation microwave propagated along the circular waveguide to a matched termination. The microwave signals were extracted from a probe (0.05 cm in diameter and 0.1 cm in length) located on the wall of the cylindrical waveguide. The outputs of the probe were split into two parts via a power divider or a directional coupler. The signal from one leg of the divider was attenuated and detected by a crystal diode for microwave power measurement. The signal from another leg propagated in a long waveguide dispersive delay line (WRJ-10, cutoff frequency f_c = 6.55 GHz, and length L = 105.7 m) to determine microwave frequency. The probe was calibrated for a TM_{01} mode which was excited in the cylindrical waveguide by a TM_{01} mode launcher, allowing us to determine the coupling coefficient of the probe for power measurement. The network for diagnostics was calibrated at low powers using a network analyzer (HP8510B).

III. RESULTS AND DISCUSSION

A. Microwave generation

Typical time history of the diode voltage, upstream electron beam current, downstream electron beam current, and microwave emission is shown in Fig. 2, where the A-K gap separation is d = 0.49 cm, the cathode radius is R_c = 1.5 cm, the maximum diode voltage is 330 kV, and the maximum diode current is 23 kA at the upstream. As seen in Fig. 2, the microwave emission occurs approximately 75 nsec after the start of the beam current. The microwave pulse rises in 10 nsec and pulse duration of 15 nsec is much shorter than the beam pulse width of 80 nsec. Frequency measurements were performed using the waveguide dispersive delayed line. The propagation time τ of the microwave through the waveguide is given by

$$\tau = \frac{L}{c\,[\,1 - (f_c / f)^2\,]^{1/2}} \qquad (1)$$

where c is the speed of light, L is the length of the waveguide, f is the microwave frequency and f_c is the cutoff frequency of the waveguide. Typical initial pulse of the microwave emission and delayed pulse through the waveguide are shown in Fig. 3. Since the propagation time τ = 437 nsec in Fig. 3, the frequency is found to be 11.1 GHz from (1). The microwave pulse widths before and after propagating through the dispersive delay line remain unchanged, so that the radiation frequency is considered to be a single frequency.

The dependence of microwave power and frequency on the A-K gap separation is shown in Fig. 4 for the cathode radius R_c = 1 cm. The largest emission of microwave power 1.2 GW at frequency 15 GHz is observed at d = 0.4 cm. No microwave emission occurs in the region of d $>$ 0.5 cm and d $<$ 0.33 cm as is expected from the consideration of expanding plasma as will be discussed in the next section. A beam-to-microwave power conversion efficiency at the peak microwave emission is 18 % for the microwave peak power of 1.2 GW when the typical diode voltage is 330 kV and beam current is 20 kA.

B. Electron beam behavior

In order to clarify beam flow in the vircator diode, we measured electron beam currents at the upstream of the anode and at the downstream of the anode. Figure 5 shows the beam currents as a function of diode voltage which changes with time as shown in Fig. 2. The arrow in the figure indicates the time history. The characteristic of current-voltage changes its slope at a point A (310 kV, 19 kA) as shown in Fig. 5(a). Even when the diode voltage is increased above 310 kV, the electron beam current at the upstream remains constant, indicating a sudden increase of the diode impedance. Such a sudden increase of the impedance is a manifestation of electron beam pinching. The microwave emission starts right after pinching of electron beam as indicated by the solid circle

"ON" in Fig. 5, which is followed by the maximum microwave power (shown by the solid triangle "PEAK") and the termination of the emission marked by the solid square "OFF".

Our observation may well be described by a simple model for the electron space-charge-limited current in the presence of expanding plasma on the anode surface as well as on the cathode surface. Both anode plasma and cathode plasma are assumed to expand with velocity v_p to cause gap closure. The time-dependent gap separation d_g is then given by

$$d_g = d - 2v_p t. \tag{2}$$

Ion beams ejected from the anode plasma propagate in the A-K gap region. In the presence of ion beams, electron beam current becomes 1.86 times of the electron space-charge-limited current, I_{SC}, i.e., the electron current in the bipolar space-charge-limited flow, I_{BSC}, is known to be [9]

$$I_{BSC} = 1.86 I_{SC}, \tag{3}$$

where I_{SC} is the one-dimensional space-charge-limited current in the absence of plasmas at both electrodes and is approximated as [10]

$$\gamma_0 = 1 + \frac{e\phi_0}{mc^2} \tag{4}$$

whereas the non-relativistic Child-Langmuir current is given by

$$I_{sc} = \frac{4\pi\sqrt{2}}{9}\frac{\varepsilon_0 mc^3}{e}\left(\frac{r_c}{d_g}\right)^2(\gamma_0 - 1)^{3/2}$$

Here m and -e are the mass and charge of electron, respectively, c is the speed of light, $\varepsilon_0 = 8.85 \times 10^{-12}$ F/m, $r_c = [R_c^2 - (R_c - x)^2]^{1/2}$ is an effective radius of the cathode, γ_0 is the relativistic factor evaluated at the anode and is given by

$$I_{SC} = 2\pi\frac{\varepsilon_0 mc^3}{e}\left(\frac{r_c}{d_g}\right)^2(\sqrt{\gamma_0} - 0.8471)^2 = 8.52\left(\frac{r_c}{d_g}\right)^2(\sqrt{\gamma_0} - 0.8471)^2 \quad (\text{kA}), \tag{5}$$

with ϕ_0 as a potential at the anode (zero potential at the cathode is assumed).

The critical current for diode pinching may be defined as a current whose induced azimuthal magnetic field is strong enough to make the cyclotron radius of an electron equal to the gap separateion, or [9]

$$I_c = 2\pi \frac{m\varepsilon_0 c^3 R_c}{e\ d}(\gamma_0^2 - 1)^{1/2} = 8.52\ \frac{R_c}{d}(\gamma_0^2 - 1)^{1/2} \qquad \text{(kA)}. \tag{6}$$

On the other hand, the electron space-charge-limited current propagating through a cylindrical drift tube of radius R is written for a thin annular beam as [9]

$$I_L = \frac{4\pi\ \varepsilon_0 mc^3 / e}{2\ \ln\ (R / r_b)}\ (\gamma_0{}^{2/3} - 1\ )^{3/2} = 8.52 \frac{(\gamma_0^{2/3} - 1)^{3/2}}{\ln(R/r_b)} \qquad \text{(kA)}, \tag{7}$$

where r_b is the beam radius.

In Fig. 5(a), electron space-charge-limited current in bipolar flow, I_{BSC} (given by (3) supplemented by (4) for the plasma expansion velocity $v_p = 2 \times 10^4$ m/sec), and critical current, I_c, given by (6) are shown to compare with the experimental results. As a reference, I_{BSC} in the absence of plasma expansion ($v_p = 0$) is also shown. As seen in Fig. 5(a), the upstream beam current less than the critical current is in good agreement with electron space-charge-limited current in bipolar flow modified for gap closure due to expanding anode and cathode plasmas. On the other hand, the beam current at the downstream almost equals to or slightly larger than the electron space-charge-limited current of the drift tube as shown in Fig. 5(b), suggesting virtual cathode formation.

From the results mentioned above, the time evolution of charge flow in the vircator diode will be outlined as follows: When a high voltage is applied to the cathode, the electron beams are emitted from the many whiskers on the cathode surface, producing a cathode plasma. The intense electron beam emitted from the cathode plasma follows the space-charge-limited flow. When the intense electron beam hits the anode, an anode plasma will be produced. Then ions from the anode plasma propagate the A-K gap region, resulting in the bipolar flow. When the beam current increases, weak pinch of electron beam occurs due to the self-magnetic field of the electron beam.

Furthermore, there is no electric field in the anode plasma, then electrons drift radially inward due to $v \times B$ drift. As a result, the electron beam is strongly pinched. The microwave emission occurs at the time of strongly-pinched electron beam formation. We confirmed this model by applying an external axial magnetic field to the diode region as will be discussed in the next section.

C. Effect of external magnetic field

Figure 6 shows the microwave peak power as a function of external magnetic field strength together with the radiation frequency. As seen in Fig. 6(a), an increase in magnetic field strength decreases microwave power. No microwave emission occurs in the magnetic field when it exceeds 0.14 T. The radiation frequency is independent on the external axial magnetic field up to 0.14 T.

The trace of beam bombardment on the anode was observed using a X-ray pinhole photograph as shown in Fig. 7. The upper trace (a) is with no magnetic field and the lower one (b) is with B = 0.14 T as shown in Fig. 6(b). The dark part in the center in Fig. 7(a) indicates the pinching of electron beam. In this shot we observed the microwave emission. On the other hand, when the axial magnetic field of 0.14 T is applied, there is no pinching evidence of electron beams as seen in Fig. 7(b), and no microwave emission is observed in this case. In our experiment a SUS-mesh anode was also used instead of aluminum foil. Figure 8 is the photograph of the mesh anode after 3 shots (a) with no magnetic field and (b) with the axial magnetic field of 0.2 T. As shown in Fig. 8(a), we observe a hole in the center of the mesh which indicates strong pinching of the electron beam.

From these results described above, the strong electron pinching due to the anode plasma formation is found to be essential for microwave generation.

IV.CONCLUSION

High-power microwave radiations from an axially-extracted virtual cathode oscillator have been studied experimentally. The microwave emission of 1.2 GW in the frequency range of 15 GHz is observed using the 330 kV, 20 kA annular electron beam of radius 1 cm. The electron

beam current in the diode region is in good agreement with the electron space-charge-limited current in bipolar flow, indicating that the anode plasma is produced by electron beam bombardment to the anode. As a result, the electron beam is strongly pinched, leading to microwave emission. The electron beam current in the diode region is well below the critical current for diode pinching at the time of microwave emission, which is different from the earlier observation [5,6]. The microwave emission is suppressed by the axially-applied magnetic field, because the magnetic field inhibits pinching of electron beams. The X-ray trace radiated from the anode and the photograph of the SUS-mesh anode after microwave emission confirm the formation of strongly-pinched electron beam.

ACKNOWLEDGEMENT

This work was supported by the Grant-in-Aid for Scientific Research, The Ministry of Education, Science and Culture of Japan and Himeji City Fund for Development of Science and Industry.

REFERENCES

[1] V. L. Granatstein and I. Alexeff, *High-Power Microwave Sources.* Boston: Artech House, 1987, chs. 13 and 14.

[2] J. Benford and J. Swegle, *High-Power Microwaves.* Boston: Artech House, 1992, ch. 9.

[3] C. S. Hwang and M. W. Wu, IEEE Trans. Plasma Sci., vol. 21, 239, 1993.

[4] M. Yatsuzuka, Y. Hashimoto, M. Sato, I. Ohta, T. Kaneko, S. Nobuhara, and T. Tazima, *J. Phys. Soc. Jpn.*, vol. 60, 352, 1991.

[5] J. Benford, H. Sze, W. Woo, and B. Harteneck, *Phys. Rev. Lett.*, vol. 56, 344, 1986.

[6] H. Sze, J. Benford, W. Woo, and B. Harteneck, *Phys. Fluids,* vol. 29, 3873, 1986.

[7] S. Burkhart, *J. Appl. Phys.*, vol. 62, 75, 1987.

[8] D. Price, D. Fittinghoff, J. Benford, H. Sze, and W. Woo, *IEEE Trans. Plasma Sci.*, vol. 16, 177, 1988.

[9] R. B. Miller, *An Introduction to the Physics of Intense Charged Particle Beams.* New York: Plenum Press, 1982, ch. 2.

[10] H. R. Jory and A. W. Trivelpiece, *J. Appl. Phys.*, vol. 40, 3924, 1969.

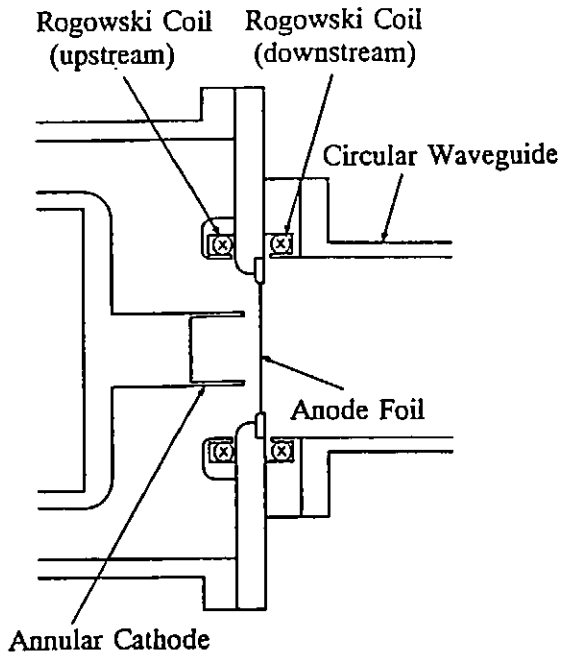

Fig. 1 The schematic of vircator diode.

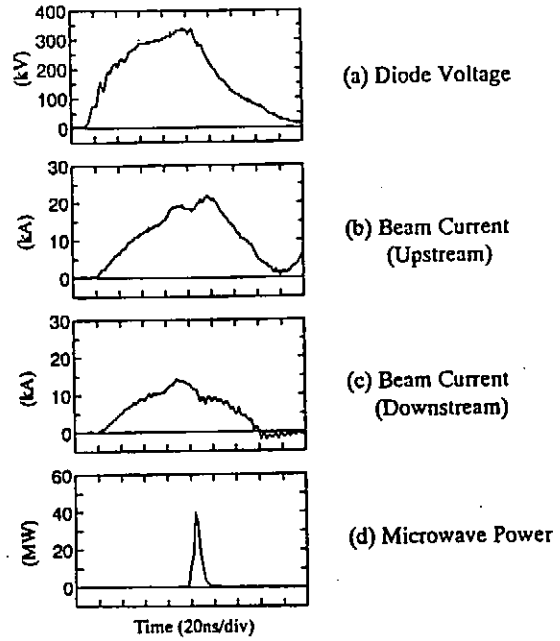

Fig. 2 The time history of diode voltage, upstream electron beam current, downstream electron beam current, and microwave emission for A-K gap separation of d = 0.49 cm and cathode radius of R_c = 1.5 cm.

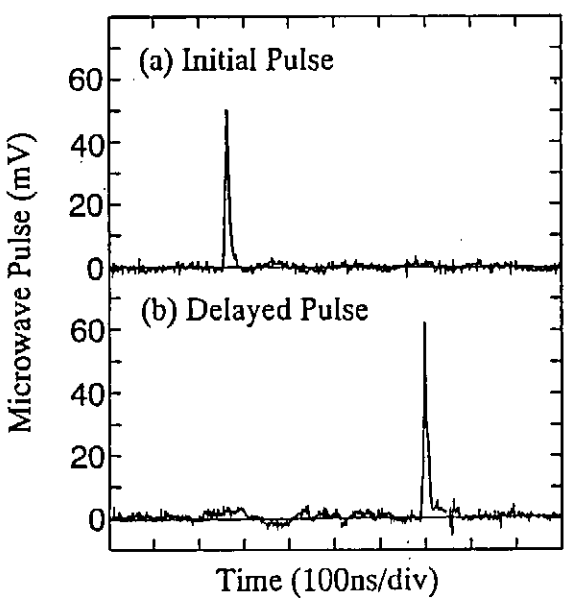

Fig. 3 Initial pulse of microwave emission and delayed pulse through the waveguide.

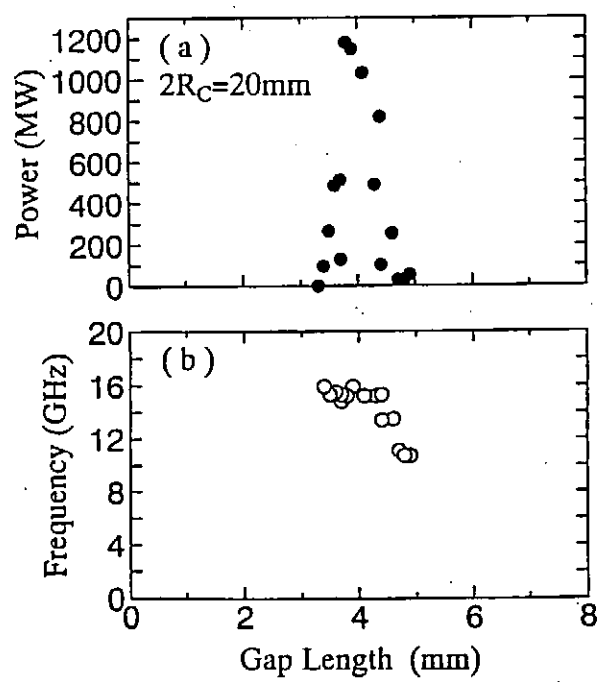

Fig. 4 Microwave power and frequency as a function of A-K gap separation for cathode radius of R_c = 1 cm.

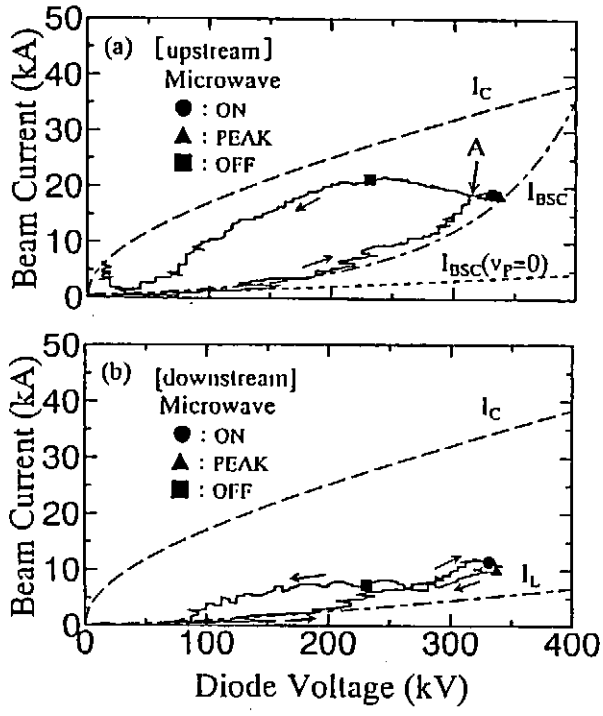

Fig. 5 Beam current, upstream (a) and downstream (b), as a function of diode voltage. Arrows show the time history. For the upstream current, the electron beam pinching starts at A followed by the turn-on of microwave emission (●). After the maximum power of the microwave emission at the maximum diode voltage (▲), the emission turns off (■). The critical current, Ic, is given by (6), while the electron-space-charge-limited current in bipolar flow, I_{BSC}, is given by (3). The plasma expanding speed is $v_p = 2 \times 10^4$ m/sec , while I_{BSC} with the vanishing expanding speed is also drawn as a reference. Space-charge-limited current in the drift tube, I_L, is given by (7).

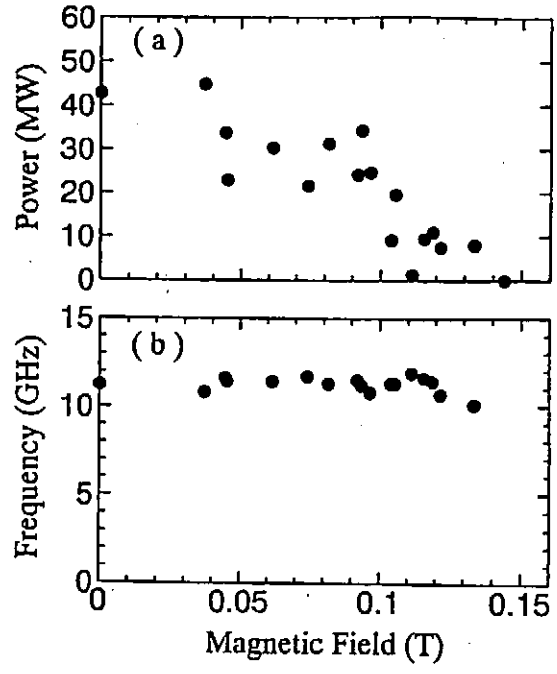

Fig. 6 Effect of the external axial magnetic field on microwave power and frequency. Cathode radius R_C = 1.5 cm and A-K gap separation d = 0.49 cm.

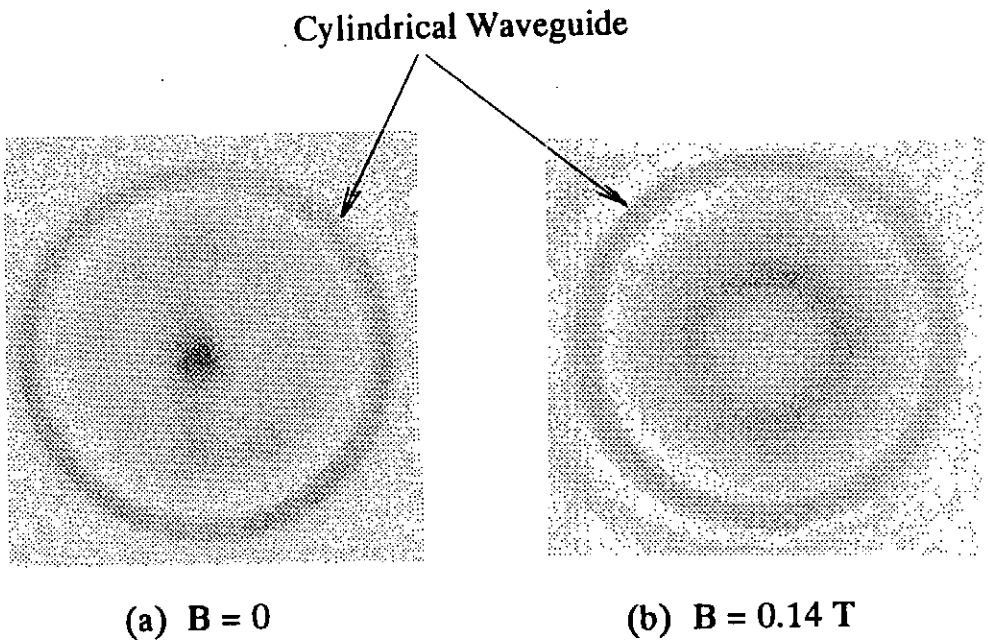

Fig. 7 X-ray pinhole photograph of trace of beam bombardment (a) for no magnetic field and (b) for B = 0.14 T.

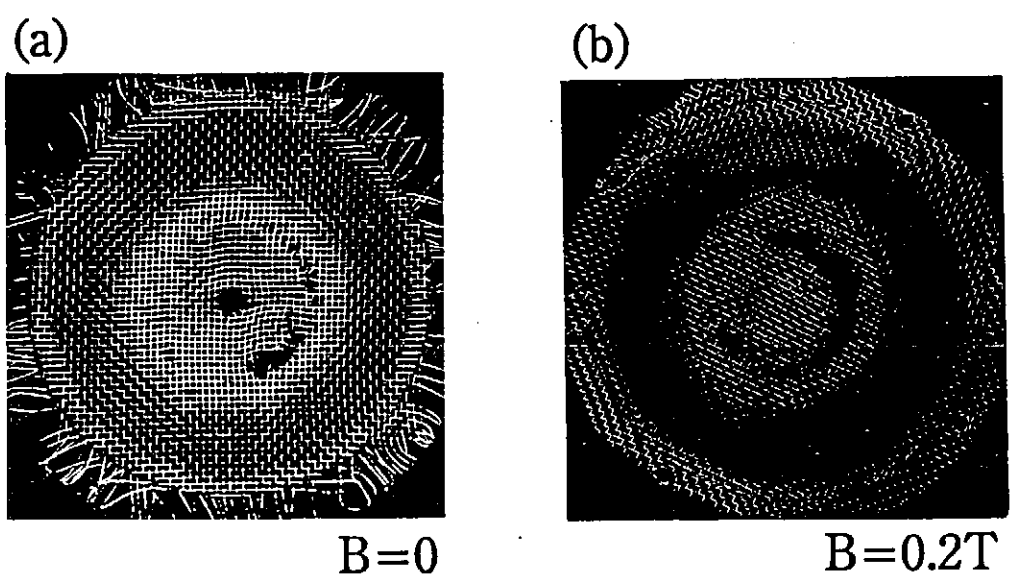

Fig. 8 The photograph of SUS-mesh anode after 3 shots for (a) no magnetic field and (b) magnetic field of 0.2 T.

Study on Surface Treatment by Pulsed Electron Beams

Shigeru Kato , Kenta Naito , Satoru Senbayashi, Yuu Kawakita and Musuhi Hakoda

Nissin Electric Co.,Ltd.

ABSTRACT

We developed a pulsed electron beam system for surface treatment use. It features high peak power density and broad area beams, which result in the possibility of the advanced surface treatment. We experimentally demonstrated surface hardening, amorphizing and alloying with this system. A description of the performance of the system and results of surface treatment experiments are presented.

§1. INTRODUCTION

At present, the surface treatment by cw CO_2 laser beams or cw electron beams is actively studied. High power density of those beams is made use of in the treatment. We developed a new pulsed electron beam system which produces still higher (peak) power density than those conventional beams, based on our pulsed power technology, and are researching on advanced surface treatment using this system.

§2. PULSED ELECTRON BEAM SYSTEM (FLASHTRON- 150EX)

2-1. Outline of FLASHTRON-150EX

A schematic diagram and an equivalent circuit of the developed pulsed electron beam system (named FLASHTRON-150EX) are shown in Figs.1 and 2, respectively. Performance specifications are shown in Table 1.

FLASHTRON was designed to be simple, inexpensive and compact as a first proto-

type of a future industrial pulsed EB processing system. Thus, spark gap switches are adopted as switching devices and a pulse transformer is used for stepping-up voltage. Furthermore, the pulse forming network(PFN) consists of commercial door-knob type ceramic capacitors connected in series and parallel. In spite of that the output pulse duration of this PFN is 100ns, its effective length is about 0.5m and considerably shorter than 1.7m, that of PFL with water capacitor, which contributes to system compactness. The distance between the each stage of PFN capacitors is also variable as a new idea, so that the output waveform is controllable by its ajustment. Intense EB extraction is caused by the explosive emission from a cold cathode. Electron beams pass through an anode made of multi-aperture plate (aperture ratio which means a ratio of apertures area to total area of the plate is about 70%) and then irradiate a taget. Figures 3 (a) and (b) are photographs of FLASFTRON-150EX.

2-2.Performance of FLASHTRON-150EX

Load voltage waveform with an impedance matched dummy load is shown in Fig.4. It indicates that the expected output could be successfully obained by the new type PFN. Typical voltage and current waveforms of FLASHTRON with EB diode are shown in Fig.5. The ratio of detected electron beam current passing through an anode to diode current is lower than the anode geometrical aperture ratio. This is considerd to be due to pinch effect, which prevents electron beams going straight.

Although significant surface treatment results were obtained with this EB diode as shown in §4, the temporal diode impedance change was severe. Much better EB diode, especialy a cathode featuring rapid turn-on characteristics should be developed.

§3. CHARACTERISTICS and EFFECT of PULSED ELECTRON BEAM SURFACE TREATMENT

Characteristics of pulsed EB and its surface treatment is summarized in Table 2. Conventional cw CO_2 laser beams or cw electron beams are used, being focused to very

small area (~1mm^2) in order to achieve high power density. On the other hand, pulsed electron beams can give us higher (peak) power density than conventional ones over large area (1cm^2~100cm^2) due to their short pulse duration and high current. This beam feature can realize energy deposition only on desired surface layers, keeping substrate low temperature, which leads to efficient surface treatment without serious thermal influence to the substrate. Consequently, very rapid heating and cooling are arisen in the treated layers. And then, this very rapid cooling yields advanced treatment effects of amorphization, formation of metastable phase and so on. Additionally, pulsed EB treatment being done quickly over large area, high throughput could be also obtained.

By ajusting beam intensity,pulsed electron beams are expected to bring useful effects in each process of heating, melting, vaporization and ionization, as shown in Table 3. Not only solid but also gaseous materials can be irradiated. Recently flue gas treatment by EB is attracted through increasing social concern of environmental issues.

§4.EXPERIMENTAL RESULTS of SURFACE TREATMENT

4-1 Surface hardening of carbon steel (S45C)

First of all, we carried out surface hardening experiments of carbon steel from a viewpoint of proof of principle. Typical results are shown in Fig.6. Surface microhardness (Hv) was increased from 300 for unirradiated state to 900 by single shot irradiation. The hardened depth was about 20μm. But the surface roughness was degraded. This reason was considered to be the melting of the surface thin layers, because of concentrated and local surface heating by low energy component of electron beams and their nonuniformity. Then, the following two modifications were carried out.

The first one was reducing low energy component by magnetic switch divertor show in Fig.7. For metal surface treatment, FLASHTRON-150EX was designed to be relatively low voltage(~150kV), high current(~50kA). In such low impedance system,

generation of low energy beams is unavoidable at the diode collapse. So, we invented to divert unwanted current compulsively, connecting magnetic switch(MS) in parallel with EB load. Since the switching (saturating) time of MS is controllable, energy component below any desired level can be reduced. Typical results are shown in Fig.8. Energy component below about 70keV is effectively reduced. Figure 9 shows a S45C irradiation result with EB reduced low energy component. Surface hardening without degradation of surface roughness was realized, increasing Hv to 600, which was a little bit lower than the former result. The effect of reducing low energy component was confirmed by a numerical calculation of a temperature distribution in a target irradiated by pulsed EB. Calculated results are shown in Fig10. Figures 10 (a) and (b) show temperature distributions without and with a MS divertor, respectively. In contrast to surface temperature reaching the melting point for the scheme without MS, surface temperature for the scheme with MS is below the melting point.

The second modification to obtain the result of Fig.9 was improving beam propagation characteristics leading to the uniform distribution of beam intensity by using a "ceramic beam guide" shown in Fig.11. Improved results are shown in Fig.12 and Fig.13. Considering that the beam uniformity is improved by overlaps of many beamlets, each of which has a certain divergence angle, it is understood that the beam uniformity bacame better as the beam propagation length increased. The beam guide effect was also observed with a rod-shape guide as same as a pipe-shape guide shown in Fig.11. Besides, the degree of vacuum in a beam drift chamber was below 4×10^{-4} Torr both with and without a beam guide. The mechanism of this beam guid effect hasn't been explained yet, and is being investigated.

4-2 Amorphization of Fe-Si-B alloy

We tried to amorphize Fe-Si-B alloy as a typical glazing process which used rapid cooling after melting caused by beam irradiation. Amorphization can greatly improve suface corrosion resistance, magnetic characteristics and so on.

The results are shown in Fig.14. While several peaks corresponding to the

crystal structure of the alloy are observed in the X ray diffraction spectrum before beam irradiation in Fig.14 (a), almost all peaks disappears after beam irradiation in Fig.14 (b), which indicates that the alloy was amophized. Because FLASHTRON-150EX is capable of amorphizing over about 5㎠ for single shot, a quick and large area amorphization processing would be expected using step & repeat method, if the repetition rate could be increased much more than 1pps at present.

4-3 Elementary experiments of surface alloying.

Surface alloying is one of the most attractvie melting processes for industrial use. Its purpose is to reinforce a weakpoint of a substrate material by the formation of alloy only in surface layers, keeping original advantages of the substrate mterial.

Nb substrate coated about 3μm thick Ni was irradiated by pulsed EB as a elementary experiments of surface alloying. Cross-sectional EPMA images before and after single shot irradiation are shown in Fig.15. Potential of pulsed EB alloying was approved, being observed the formation of mixing layers of Nb and Ni.

§5.CONCLUSION

We developed a new pulsed electron beam system FLASHTRON-150EX for surface treatment and demonstrated its capability of useful surface treatment through irradiation experiments.

In recent years, similar attempts have been increased in America and Russia[1),2)], but generally, little interest is taken in pulsed EB material processing. We expect that the potential of pulsed EB material processing will be recognized by many researchers both in the field of pulsed power technology and material processing, and new ideas and technologies will be developed, in the near future.

§6.REFERENCES

1) K.W.Struve, et al., 9th Inter. Conf. on High-Power Paritcle beams, P1960 (1992)

2) V.I.Engelko, et al., 9th Inter. Conf. on High-Power Particle Beams,P1935 (1992)

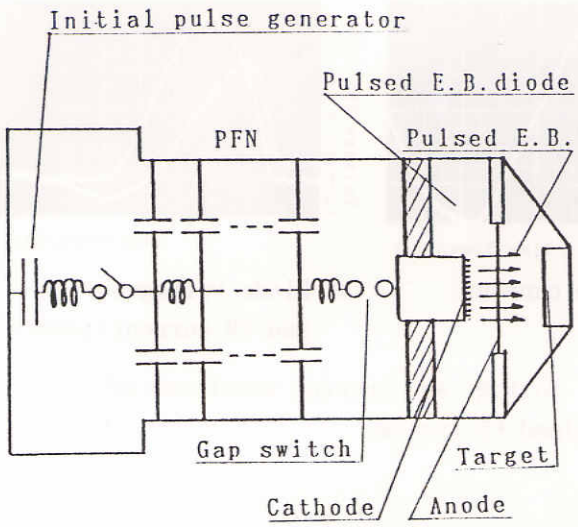

Table.1 Specifications of FLASHTRON-150EX

EB energy	150kV
EB current	50kA
Pulse duration	100ns
Repetition rate	1pps

Fig.1 Schematic diagram of a pulsed EB system developed.

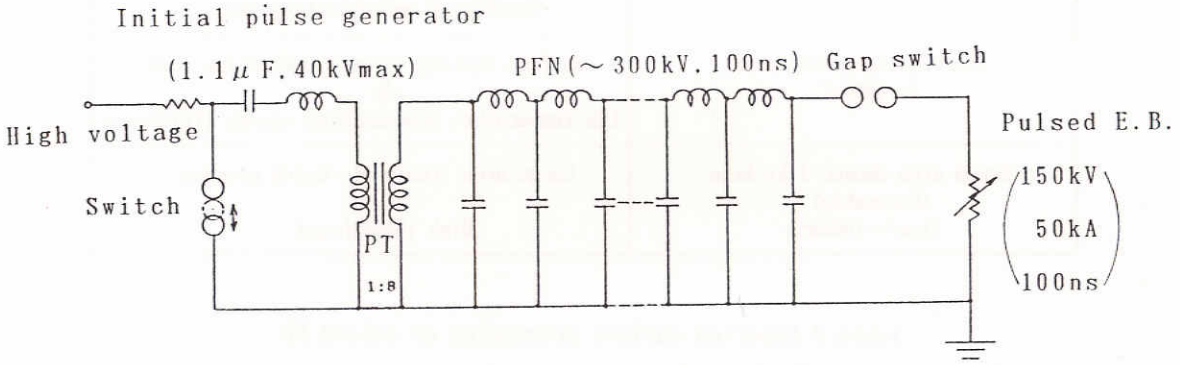

Fig.2 Equivalent circuit of a pulsed EB system developed.

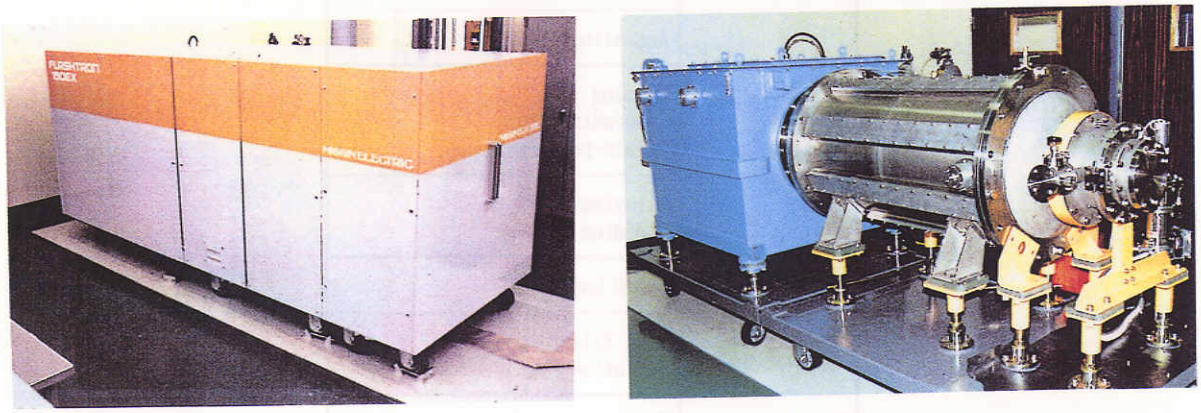

a) Package. b) Inside the package.

Fig.3 Photographs of a pulsed EB system developed.

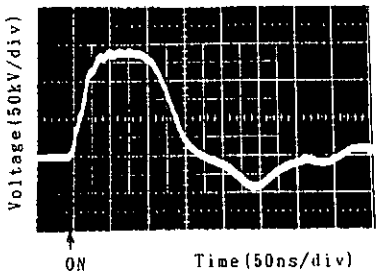

Fig.4 Voltage waveform on the load. (load impedance R=3Ω).

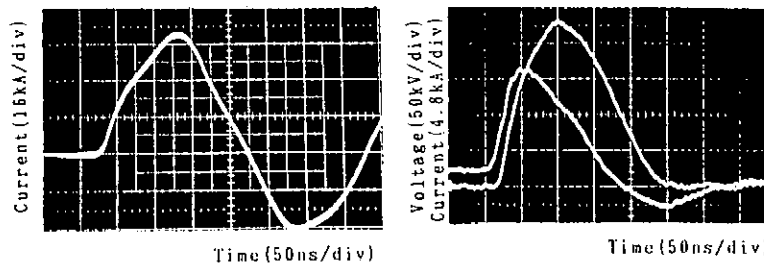

a) Diode current.

b) Diode voltage (upper) and EB current (lower).

Fig.5 Voltage and current waveforms of the pulsed EB system.

Table.2 Characteristics of pulsed EB processings

Beam characteristics	Process characteristics
High peak power density · High current (10^7~10^9W/cm^2, ~50kA)	Very rapid surface heating and cooling ⇩ Capable of amorphization etc.
Short pulse duration (~100ns)	Surface heating without conduction loss ⇩ Low temperature process·High energy efficiency
Broad area shower-like beam (Focusable) (1cm^2~100cm^2)	Large area treatment · Quick process ⇩ High through-put

Table.3 Expected surface processing of pulsed EB

Heating process	Surface cleaning Surface activation
	Transformation hardening
	Annealing
Melting process	Glazing (Amorphization, grain-refining)
	Alloying Cladding
Vaporization process	Shock hardening
	Thin film formation (ablation PVD)
Excitation· ionization process	Excitation or ionization of gas (laser oscillation, removal of SOx and NOx)

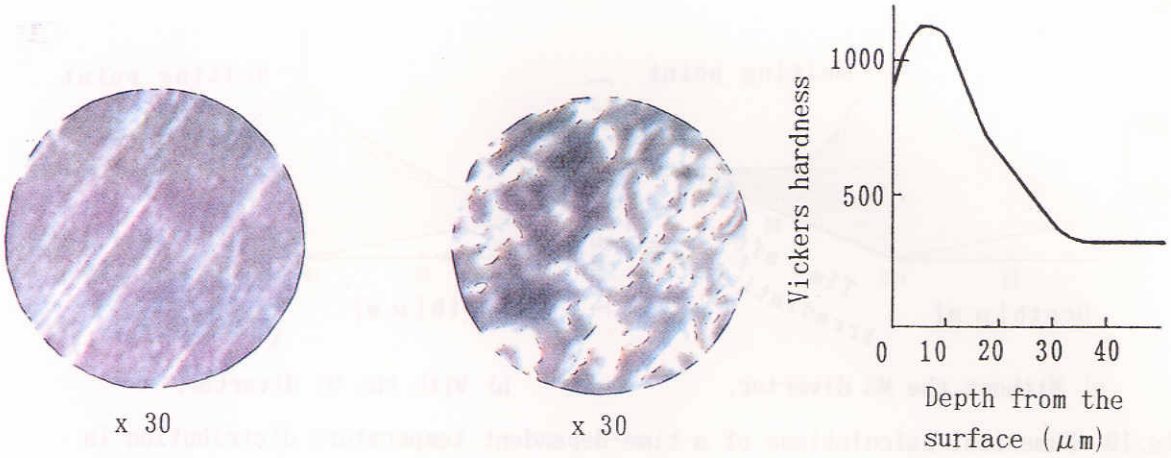

a) Before irradiation.
Hv=300.

b) After irradiation.
Hv～900.

Fig.6 Change in microhardness of the surface layer of the target (S45C plate). Photographs show the surface of the sample observed by a microscope.

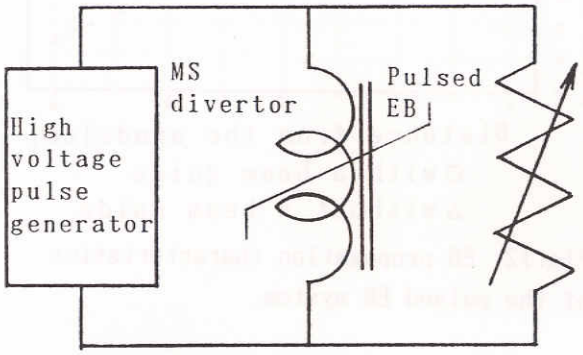

Fig.7 Equivalent circuit of a pulsed EB system using a magnetic-switch (MS) divertor.

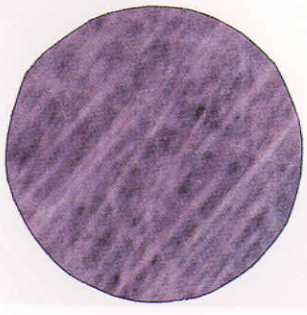

Fig.9 Photograph of the surface of the sample irradiated by the pulsed EB using the MS divertor which reduces low-energy component of the beam.

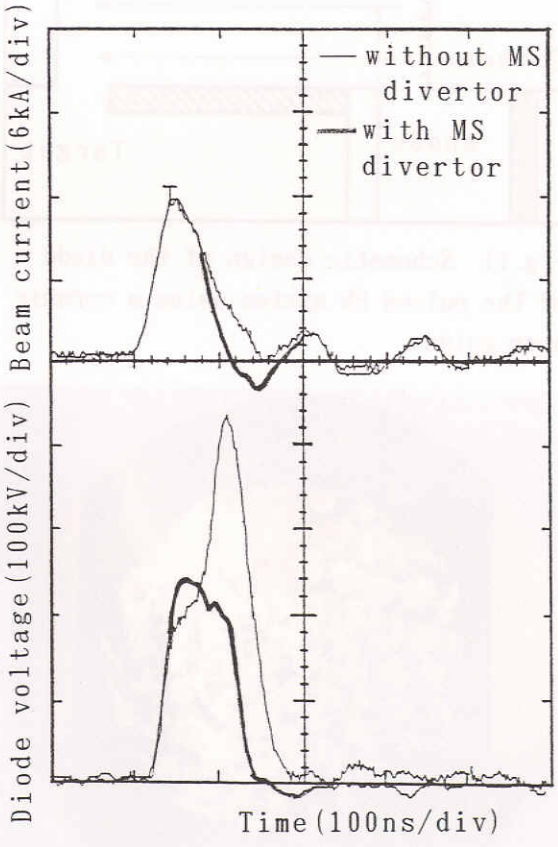

Fig.8 Comparison of the diode voltage (upper 2 traces) and the beam current (lower 2 traces) waveforms of the diode with or without the MS divertor.

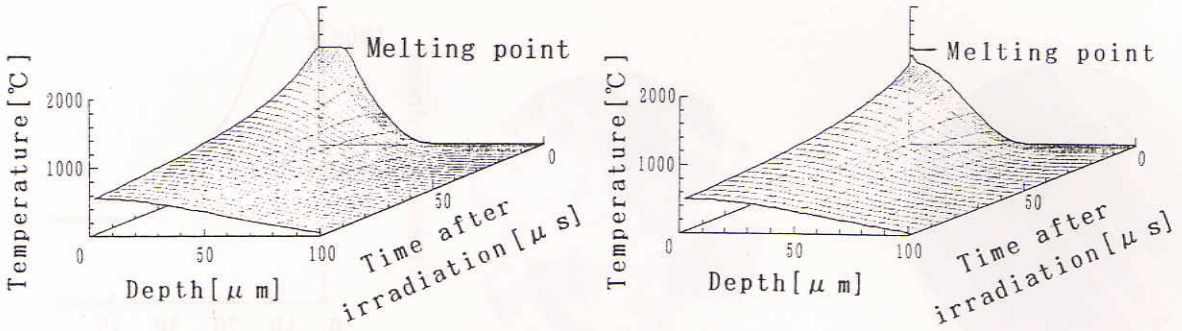

a) Without the MS divertor.　　b) With the MS divertor.

Fig.10 Numerical calculations of a time-dependent temperature distribution in the target irradiated by the pulsed EB.

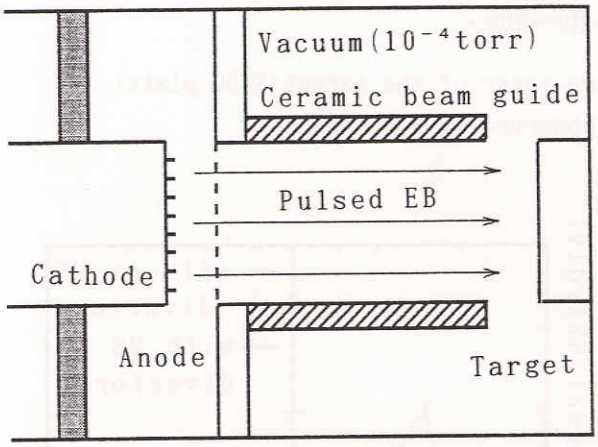

Fig.11 Schematic design of the diode of the pulsed EB system using a ceramic beam guide.

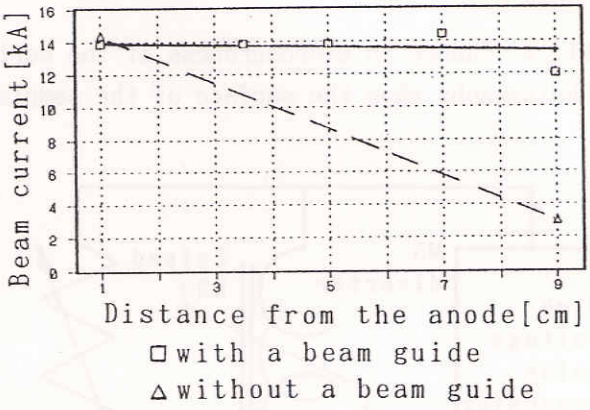

Fig.12 EB propagation characteristics of the pulsed EB system.

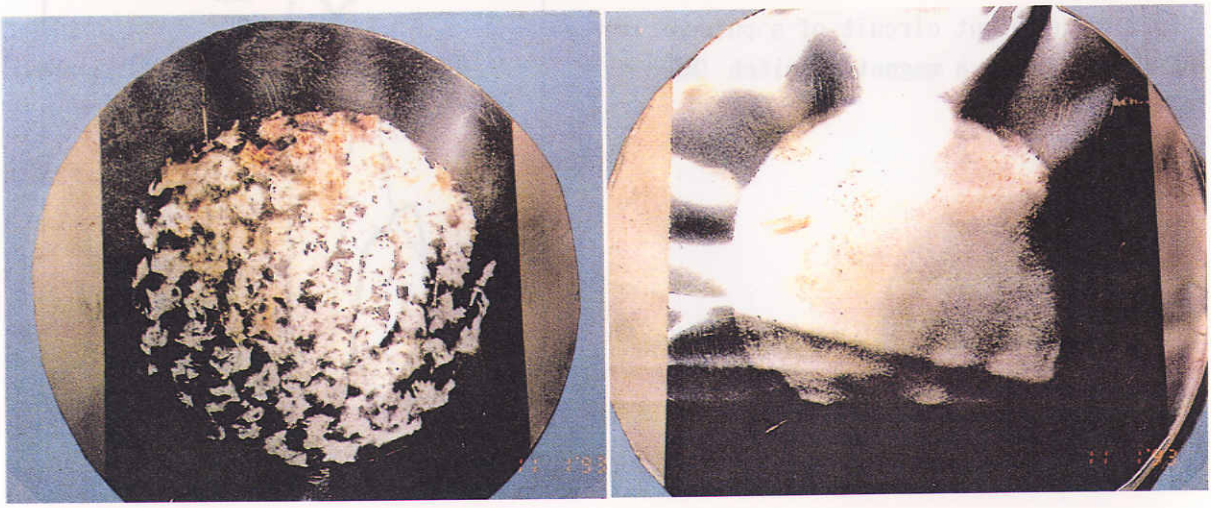

a) Without a beam guide (D=10mm).　　b) With a beam guide (D=60mm).

Fig.13 Comparison of the beam patterns. Photographs show the surface of the copper plates irradiated by the pulsed EB with or without a ceramic beam guide (D:distance from the anode).

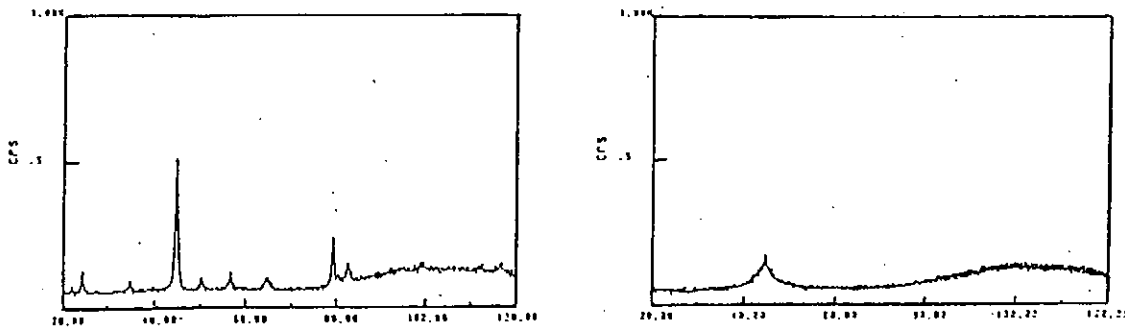

a) Before irradiation.　　b) After irradiation.

Fig.14 Comparison of X-ray diffraction spectra of Fe-Si-B samples before and after irradiation of the pulsed EB.

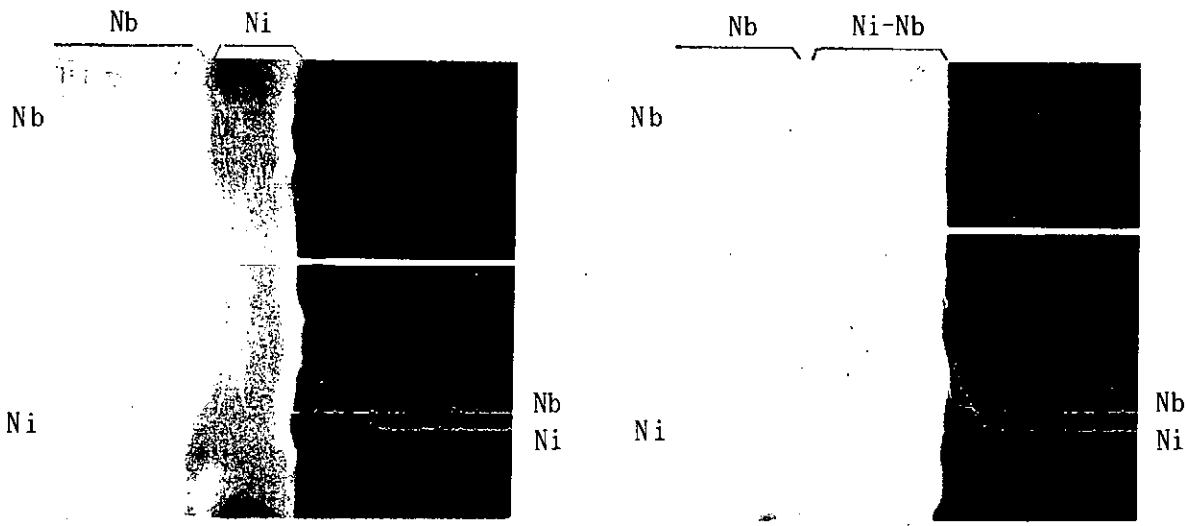

a) Before irradiation.　　b) After irradiation.

Fig.15 EPMA across Ni-coated Nb-plate before and after irradiation of the pulsed EB. Nb and Ni distributions in the sample are also traced in each photographs.

Present Status of Ohmic Ignition Chemical Launcher Experiment

K.Ikuta, Y.Aso, K.Fujioka, Y.Uehara, S.Nakamura and K.Yamamoto
The Japan Steel Works,Ltd
Takanodai 1-3, Yotsukaido, Chiba, Japan 284

Abstract

This paper describes the first successful demonstration of centrifugal mass separator packaged in a cartridge of the ohmic ignition chemical(OIC) gun in order to extract hot hydrogen from the reaction products of OIC interaction between water and aluminum.

Introduction

The ohmic ignition chemical(OIC) launcher is a version of light gas gun which accelerates a bullet by centrifugally extracted hot hydrogen pressure from the reaction products of OIC interaction between water and aluminum[1]. The reaction products generated by OIC interaction is initially injected through a nozzle into the centrifuge chamber packaged in the cartridge to separate Al_2O_3 and hydrogen. Because of the large mass ratio between hydrogen and Al_2O_3, the hot hydrogen is concentrated near the axisymmetric axis of the chamber where the breech of the gun tube is located. The projectile is accelerated by this hot hydrogen along the gun tube to high velocity.

Apparatus

We employed OIC cartridge developed by ourselves[1] for the demonstration experiment of the centrifuge. Four cartridges are simultaneously used to generate the OIC reaction products which are injected into the cyclone chamber. Every cartridge has its own nozzle for the injection. The injected products are 90° reflected by the reflector to induce the vortex in the chamber. A schematic of the cyclone chamber with four cartridges is shown in Fig.1.

Results

The electric energy of about 100kJ are fed into the four cartridges to ignite the water-aluminum reaction. The working voltage of the capacitor bank was 10kV and the each mass of the water and the aluminum loaded in the cartridges was about 13.5 grams respectively. Since the phase transition of Al_2O_3 gas is around 3000°C, the wall of the chamber worked effectively to solidify the gas. Fig.2 shows the picture of the cyclone chamber where the wall surface is covered by lava-like Al_2O_3.

The most important point to notice was that the inner bore of the gun barrel was barely contaminated by Al_2O_3 lava-like ash. More than 90% of the Al_2O_3 gas seems to be trapped by the cyclone chamber, though we need to investigate this percentage further more.

An interesting results was the velocity attained by this experiment. In the case of no cyclone chamber with barrel length being 1 meter the velocity of the projectile with the weight of 100 grams was about equal to 10^3m/s. The velocity obtained was also about 10^3m/s with both the cyclone chamber and the barrel having the length of 2 meters. In both case the same amount of water and

aluminum was loaded. This clearly shows the effecient acceleration of the projectile by the light gas even though one quarter of the molecule was taken off from the reaction products by the cyclone chamber.

We conclude, therefore, that the cyclone chamber in OIC cartridge can work as a mass filter.

Acknowledgments

The authors would like to express their deep thanks to Mr. K.Shimo of JSW for his supports.

Reference

1) K.Ikuta, "Ohmic Ignition Chemical Launcher as a Version of the Light Gas Gun", Proc.43rd ARA Meeting, Report No.24

Figure Caption

Fig.1 Schematics of OIC launcher with a cyclone

Fig.2 A picture of the cyclone chamber with lava-like Al_2O_3

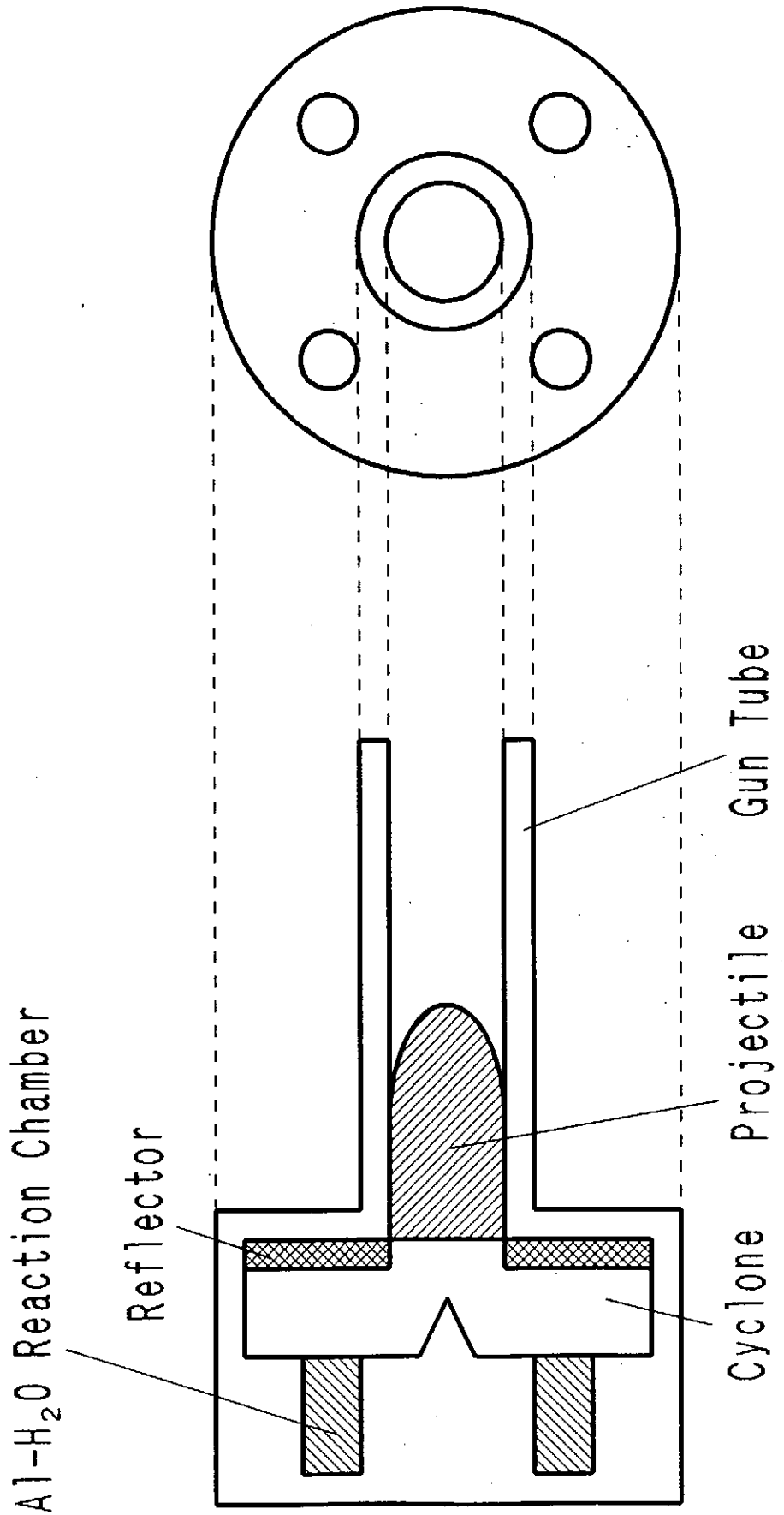
Al-H_2O Reaction Chamber
Reflector
Gun Tube
Projectile
Cyclone

Fig. 1

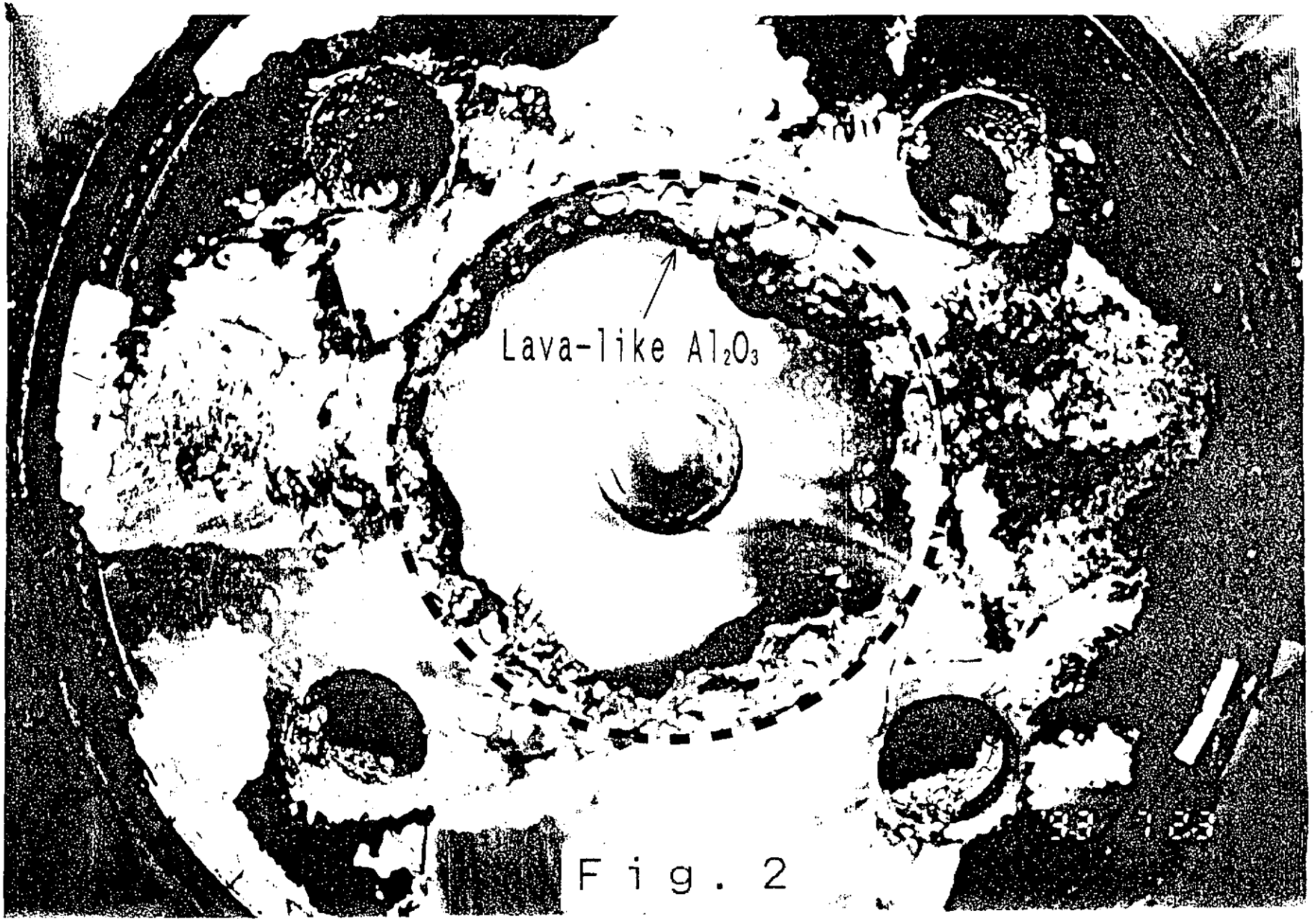

Fig. 2

Gas-Puff Z-Pinch driven by Inductive Energy Storage Pulsed Power Generator ASO-II

K. Imasaka, K. Hasegawa, H. Akiyama and S. Maeda

Department of Electrical Engineering and Computer Science

Kumamoto University, Kumamoto 860, Japan

ABSTRACT

Inductive energy storage pulsed power generator ASO-II with two-staged opening switches, which had been developed in our laboratory was used as a power source of a gas-puff z-pinch and was compared with a fast bank with the same energy. A uniform discharge and a z-pinch implosion occurred at higher driving current than that of fast bank. The intensity of soft x-ray driven by ASO-II with only one-staged opening switch (copper wire fuses) was much increased in comparison with that driven by the fast bank. From the observation of hot spots by a pin-hole camera, the spatial positions of the hot spots did not much move shot to shot. These results are very important to the applications of the gas-puff z-pinch to industry.

1. Introduction

To increase an intensity of a soft x-ray emitted from a gas-puff z-pinch implosion and a reproducibility of hot spots is very important to the application of a compact intense soft x-ray source[1],[2] to industry such as x-ray lithography, x-ray microscopes, x-ray laser[3]-[6]. A Conventional gas-puff z-pinch has been driven by a fast bank, with which it is difficult to obtain a uniform discharge because of a slow rise time of a

driving current. On the other hand, the gas-puff z-pinch plasma produced by a pulsed power generator with a fast rise time of driving current emits a intensive soft x-ray. Generally, a capacitive energy storage pulsed power generators have been used as a power source of a gas-puff z-pinch[7],[8]. However, it is a large machine. The inductive energy storage pulsed power generator, which has the opening switches, is compact and lightweight.

In this paper, a gas-puff z-pinch is driven by an inductive energy storage pulsed power generator, which is named ASO-II and has been composed in our laboratory. The obtained results are compared with those obtained with a fast bank with a same energy as ASO-II. The ASO-II has two-staged opening switches. The opening switches are composed of a plasma opening switch (POS) and parallel wires placed in a water vessel. By these switches, a long conduction time and a short opening time can be achieved. In the experiments, only one-staged opening switch (parallel wires) is used.

2. Experimental Apparatus

A schematic diagram of a gas-puff z-pinch placed on the pulsed power generator ASO-II and its equivalent circuit are shown Figs.1 and 2. The ASO-II has a coaxial configuration with a height of about 2.3m and a maximum diameter of 1.5m. The capacitor has a capacitance of 14.9μF and a maximum storage energy of 27kJ. After charging the capacitor, the triggered spark gap switch is operated. The energy of the capacitor is transferred to the storage inductor, Ls, of about 0.7μH and

compressed by a opening switch. The opening switch consists of copper wire fuses which are placed radially in the water vessel. The fuse length and number are able to be varied from 5cm to 66cm and from 1 to 24. A spark gap is placed between the fuses and z-pinch sections to prevent the current from flowing into z-pinch before the fuses have been completely opened. As the fuses vaporize, the induced voltage across the fuses increases and the breakdown of the spark gap occurs, and then a current is transferred to the gas-puff z-pinch section.

The operated gas is Ar which is injected from the hollow-shaped anode to cathode through a fast opening valve. Both electrodes are made of brass and the spacing between them is 10mm. The diameter of the annular gas ϕ is 5mm or 18mm. The charging voltage V_{ch} of the capacitor is 20kV or 25kV. The delay time Δt, which is the differential times when the coil current of the fast opening valve and the fuse current begin to flow, is varied in the experiments. The coil current is measured with a B-dot probe. The source and load currents are measured with Rogowski coils shown in Fig.1. The soft x-ray is detected by a pin-photo diode with Al filter of 3μm thickness. A pin-hole(the diameter of 400μm) camera with 3μm Al filter is used to obtain the shape of hot spots. The pin-hole camera is placed in the discharge chamber shown in Fig.3. The Fuji super HR-A medical x-ray film is used for it.

3. Experimental Results and Discussions

Fig.4 and 5 show the typical waveforms of current and a soft x-ray signal measured with the pin-photo diode in the case

of driven by a first bank and ASO-II. The parameters of copper wire fuses are the number of 8, the diameter of 0.2mm and the length of 20cm. The values of ϕ and Vch are 5mm and 20kV, respectively. From Fig.4, it is found that a rise time of the current is slow and an intensity of the soft x-ray is small. On the other hand, from Fig.5, it is found that the faster rise time of a load current ,I_L, is obtained and the larger soft x-ray emission is observed at the higher current than that of the fast bank shown Fig.4.

Fig.6 shows the dependence of a soft x-ray intensity on the delay time Δt,where ● and ○ are the results for ASO-II and fast bank, respectively. The soft x-ray emission from the pinched plasma produced by ASO-II is larger than that by fast bank. Fig.7 shows the current versus the delay time. These results indicate that the pinched plasma by ASO-II is produced at a higher current than that by the fast bank.

Fig.8 show the spatial distribution image of hot spots for 10 shots taken by the pinhole camera with 3μm Al filter. Here, V_{ch} and ϕ are 25kV and 18mm, respectively. Figs.8 (a) and (b) are the pin-hole photographs in the cases driven by the fast bank and ASO-II, respectively. In the case of the fast bank, the hot spots distribute spatially into the radial direction at around the center of the electrodes shot to shot. In the case of ASO-II, there are the hot spots at around the center of the z-axes. These results indicate that the pinched plasmas produced by ASO-II are reproducible in comparison with those by the fast bank.

The reasons why the soft x-ray emission from the pinched plasma by using ASO-II increases and the positions of hot spots are in a small area are considered as follows: a pinched plasma is able to be produced at a larger current than that of fast bank by supplying a driving current which has a first rise time. Another reason is that an inductive energy storage pulsed power generator can supply a high voltage with a fast rise time and short pulse wide to the initial phase of the discharge. Therefore, the more uniform discharge occurs in comparison with that by the fast bank.

4. Conclusion

A gas-puff z-pinch plasma is driven by the inductive energy storage pulsed power generator ASO-II with two-staged opening switch, and is compared with that by a fast bank with the same energy. Only one-staged opening switch (copper wire fuses) is used. The implosion of the gas-puff z-pinch driven by ASO-II occurred at the larger current than that driven by the fast bank, and the soft x-ray intensity was large in comparison with that driven by the fast bank. From the observation of the hot spots by a pin-hole camera, it is found that the spatial positions of the hot spots produced by ASO-II do not much move shot to shot, that is, are reproducible. These results are very important in the applications of the gas-puff z-pinch. Further experiments will be done by using the two-staged opening switch.

REFERENCES

(1) P.Choi. et. al. : "Temporal developmentof hard and soft x-ray emission from a gas-puff Z-pinch", Rev.Sci. Imstrum., Vol.57, No.8, pp.2162-2164 (1986)

(2) J. H. W.Lau, et. al. : "Submillimeterhigh brightness pulsed x-ray source", Appl. Phys. Lett., Vol.52, No.25, pp.2111-2113 (1988)

(3) J. Kirz, and H. Barback : "Soft x-ray microscopes", Rev. Sci. Instrum., Vol.56, No.1, pp.1-13 (1985)

(4) I.Okada, et. al. : "A plasma x-ray source for x-ray lithography", J.Vac. Sci, Techol, Vol. B4, No.1, pp.243-247 (1986)

(5) Irving N. Weinberg, et. al. : "Elementalimaging of biological speciments using a z pinch", Appl. Phys. Lett., Vol.47, No.10, pp.1116-1118 (1985)

(6) G.D.Lougheed, et. al. : "Solenoid gas puff imploding liner x-ray source", J. Appl. Phys., Vol.65, No.3, pp.978-992 (1989)

(7) G. Mehlman: "Quantitativex-ray spectroscopy of neon Z-pinch plasmas", J. Appl. Phys., Vol. 60, No. 10, pp.3427-3432 (1986)

(8) K.Takaugi. et. al. : "X-ray generation from a gas-puff z-pinch driven by a pulsed power generator with a self-crowbar switch", Rev. Sci. Instrum., Vol.64, No.8, pp.2403-2404 (1993)

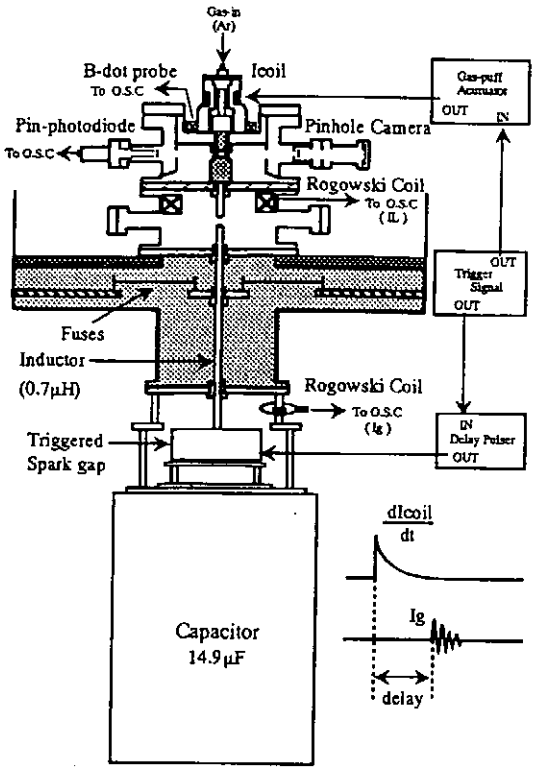

Fig.1 Experimental setup.

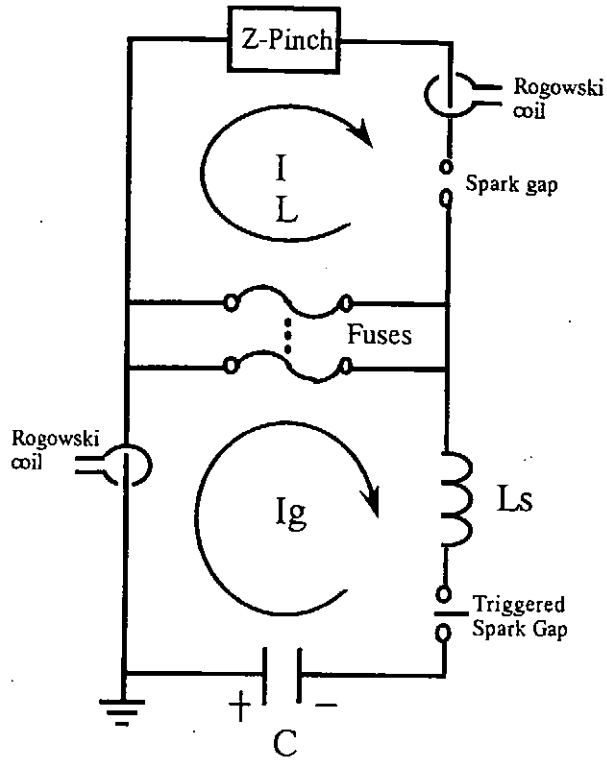

Fig.2 Equivalent circuit of Fig.1.

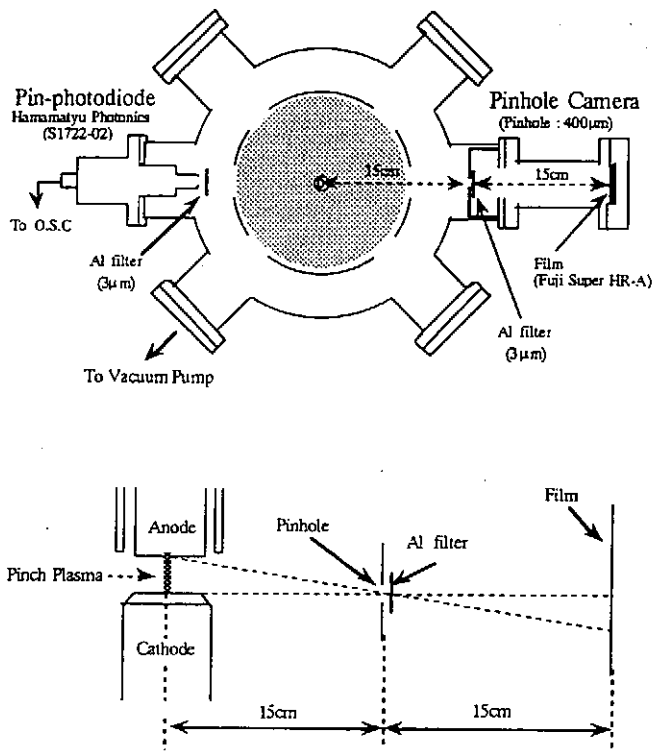

Fig.3 Arrangement of the pin-hole camera.

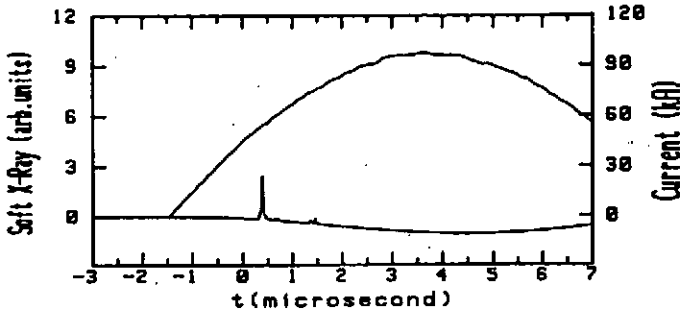

Fig.4 Typical wave forms of current and soft x-ray driven by a fast bank. (Vch=20kV, ϕ=5mm)

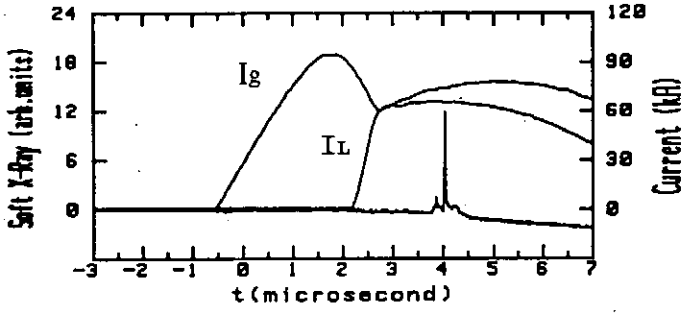

Fig.5 Typical wave forms of generator current I_g, load current I_L and soft x-ray driven by ASO-II. (Vch=20kV, ϕ=5mm)

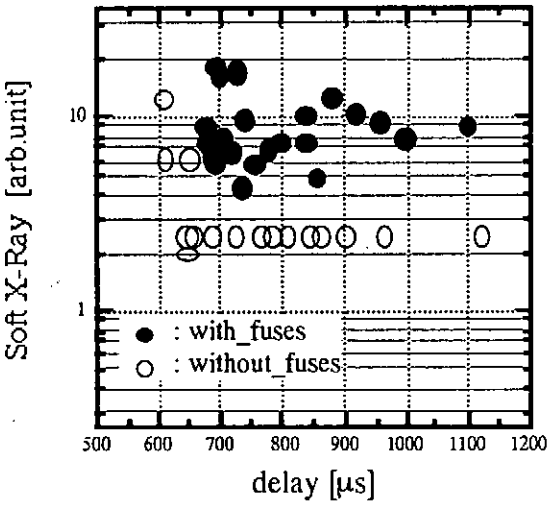

Fig.6 Relation between the intensity of soft x-ray and delay. (Vch=20kV, ϕ=5mm)

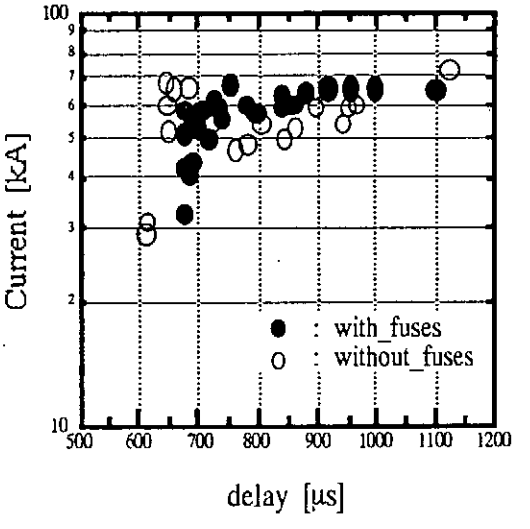

Fig.7 Relation between the current when the soft x-ray is emitted and delay. (Vch=20kV, ϕ=5mm)

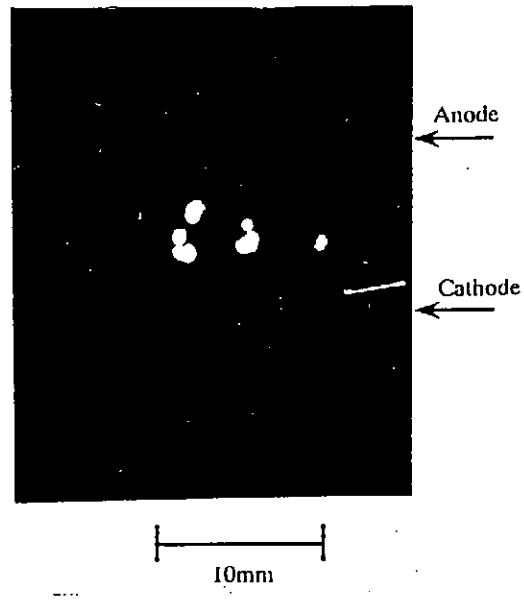

(a)

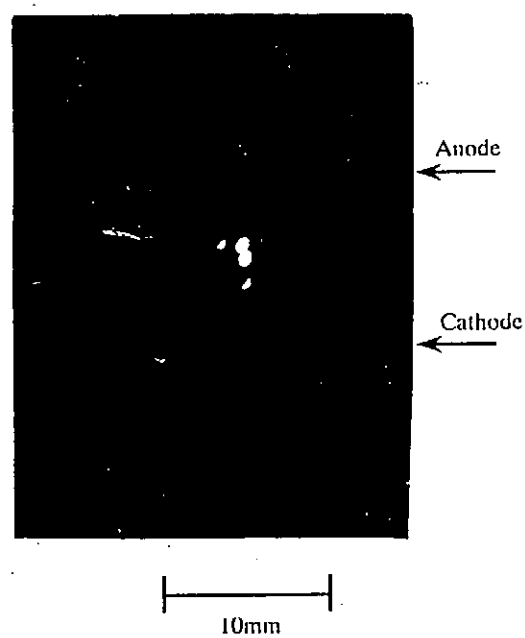

(b)

Fig.8 Pin-hole photograph:
(a) driven by a fast bank
(b) driven by ASO-II
(Vch=25kV, ϕ=18mm, 10shots)

Contraction Phase of a Gas-puff Z-pinch

Kinya Moriyama[+], Keiichi Takasugi,

Tetsu Miyamoto and Koichi Sato[++]

Atomic Energy Research Institute, Nihon University

[+]College of Science and Technology, Nihon University

[++]Plasma Science Center, Nagoya University

Abstract

The dynamics of a gas-puff z-pinch plasma was investigated using a Kerr-cell camera. A large amplitude Rayleigh-Taylor instability was observed develop during the contraction of the plasma. Two types of gas nozzles were examined to reduce axial nonuniformity, and it was confirmed that the uniform z-pinch was produced by the choice of the nozzle.

I. Introduction

The implosion dynamics and the stability of z-pinch plasmas have been major subjects in the nuclear fusion research.[1] Those are also important in view of application to x-ray emission source. The dynamic behavior of the z-pinch implosion was investigated using a Kerr-cell camera, and wavelength and growth rate of the observed instability were measured.

The gas distribution between the electrodes is a key parameter for the z-pinch plasma generation. The gas

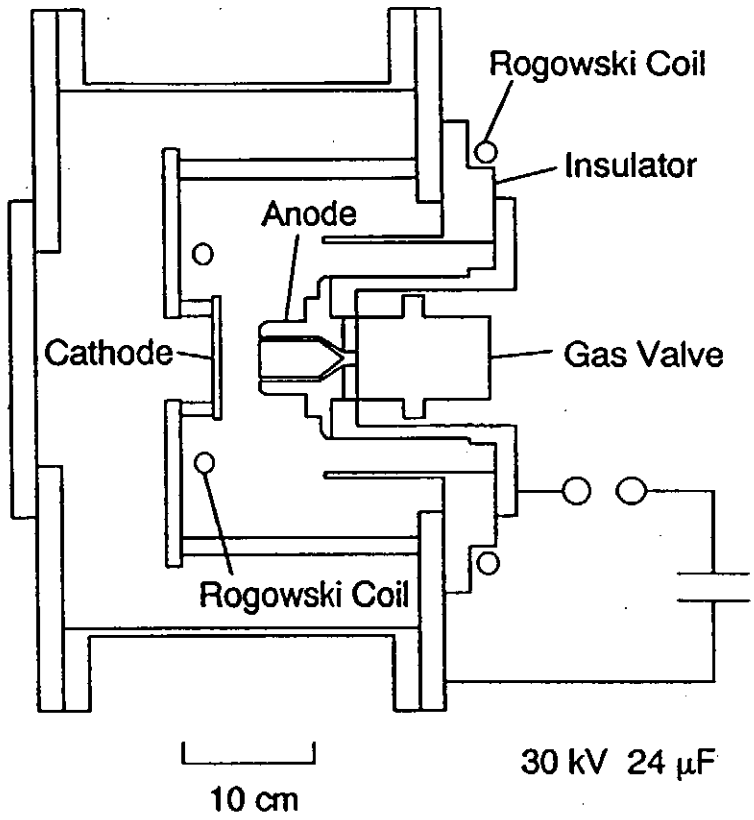

Fig. 1. Experimental setup of the SHOTGUN z-pinch device.

distribution has been measured by a pressure probe in the SHOTGUN device,[2] and the formation of hollow gas distribution has been confirmed. The naturally expanding gas distribution causes a nonuniform compression of the pinch. The uniformity of the plasma has been improved by the choise of the gas-puff nozzle.[3] And the uniformity of the z-pinch plasma column is also improved by applying a longitudinal magnetic field.[4] Here it is again demonstrated that the uniformity of z-pinch on the contraction was improved by the choice the gas-puff nozzle. And the characteristics of large amplitude instability that occur on the contraction was investigated.

II. Experimental Setup

Figure 1 shows the experimental setup of the SHOTGUN z-pinch device.[2] The gas is injected through a hollow nozzle mounted on the anode of discharge section. The inner diameter of the nozzle is 28 mm, and the spacing of the electrodes is 40 mm. The capacitor is charged to 20 kV and the storage energy is 4.8 kJ. The plasma currents are measured by Rogowski coils wound on both electrodes. Extreme UV light is detected by a vacuum x-ray diode without filter. Soft x-ray signal is detected by a scintillation probe filtered by a 5 μm berylium foil.

Macroscopic behavior of the plasma in visible light is monitored by a Kerr-cell camera. The shutter time of the camera is 20 nsec, which is sufficiently shorter than the macroscopic motion of the plasma.

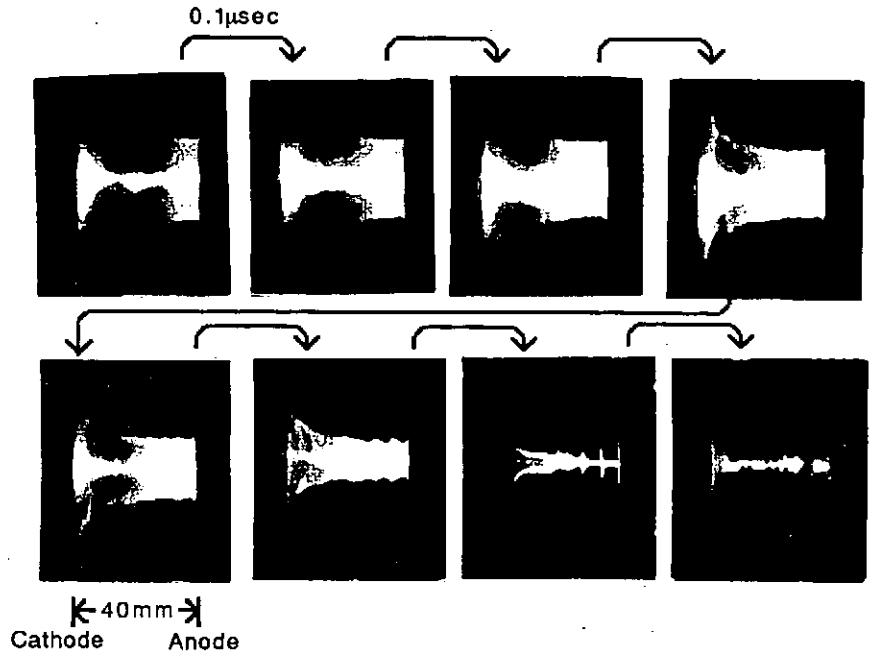

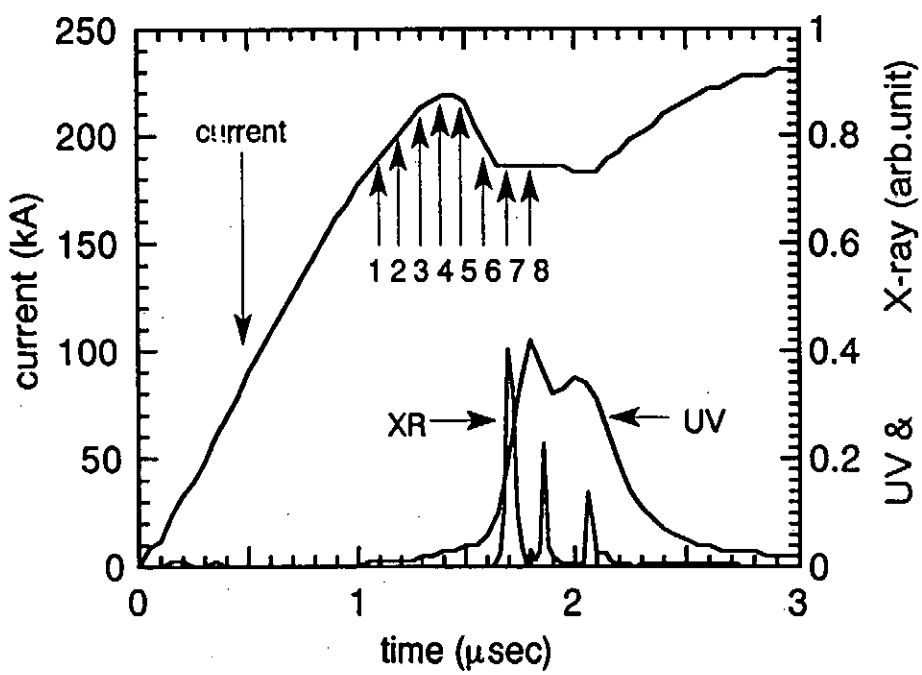

Fig. 2. Kerr-cell photographs of the z-pinch plasmas. The shuttering time of each frame is shown in the plasma current trace.

III. Experimental Results

Sequential motion of the plasma in the compression phase is shown in Fig.2 assuming its reproducibility. The light column on the axis seen in the frames 1 - 5 is the light from recombining plasma after maximum pinch which could not be avoided. The plasma current, the UV light and the x-ray signal are also shown in the figure. The radial motion at the beginning of the discharge is very slow (1 - 4). A small ripple on the surface of the plasma is observed in this phase. After the frame 5, the plasma current begins decreasing. This is due to rapid increase of plasma inductance. The amplitude of the ripple comes to increase as its radius becomes smaller. A simple mode and very large amplitude instability is observed in the frame 7. Strong x-ray emission is observed at this moment. The distance between each node is about 5 mm, which corresponds to a kind of wavelength of the instability. At the frame 8 the axially averaged pinch of the plasma occurs. The UV signal peaked at this phase.

The maximum pinch occurs from the anode to the cathode. In order to minimize the nonuniformity of the pinch along z-axis, two types of gas nozzle were examined, a) normal straight nozzle and b) 5 degrees inward directed nozzle. Figure 3 compares the radial motion of the plasma with these nozzles. The axial position Z is measured from the anode. With a straight nozzle the plasma column spreads from the anode to the cathode. The plasma is still diverged when the maximum pinch occurred. (0.6 μsec) This divergence is recovered by the use of the inward directed nozzle. And the almost uniform plasma column is formed

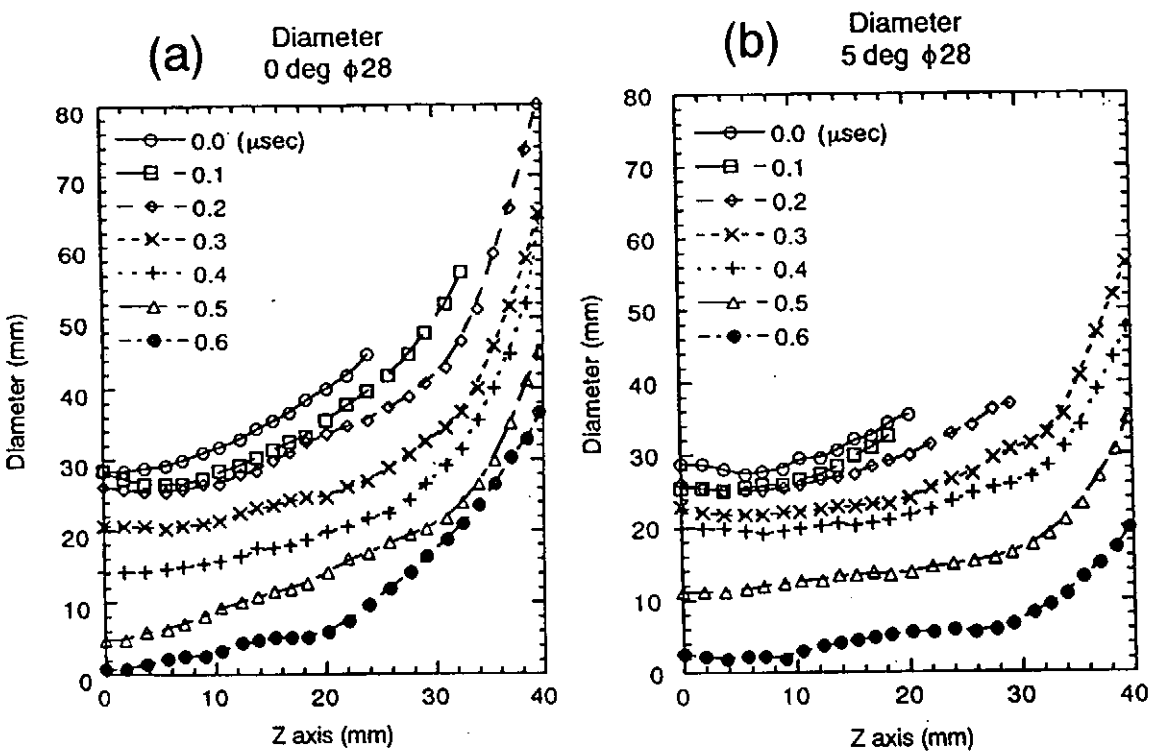

Fig. 3. Radial contractions of z-pinch plasmas using (a) normal straight nozzle and (b) 5 degrees inward directed nozzle.

at the maximum pinch.

IV. Discussion

The observed average radius r is plotted in Fig.4 as a function of time t. The solid line in the figure shows the calculated radius using the hollow gas shell model with measured plasma current. The averaged radial equation of motion is

$$M\frac{d^2r}{dt^2} = -\frac{\mu_0 I^2}{4\pi r}$$

where M is the initial line mass and I is the plasma current. In the calculation the initial line density $N = 1.6\times10^{20}$ m^{-1} was assumed. The observed radial motion agrees well with the calculation. The radius remains almost constant for initial 1 μsec, then collapses rapidly. This is a typical hollow gas-puff z-pinch, and the maximum pinch is enhanced by the increasing current.

The azimuthally uniform (m = 0 mode) instability was observed in the Kerr-cell photographs of Fig.2. The growth of the amplitude of the ripple is plotted in Fig.5. From the gradient of the fitted line the growth rate of the ripple is γ_{obs} = 5.0×10^6 sec^{-1}. The growth rate of Rayleigh-Taylor instability is roughly $\gamma = \sqrt{gk}$. The radial acceleration g is calculated from radial equation of motion as $g = 1.7\times10^9$ m/sec^2 at t = 1 μsec, when the ripple becomes observable. Using the observed wavelength λ = 5 mm, the growth rate is calculated as $\gamma = 1.4\times10^6$ sec^{-1}. Although there is some factor of difference between them, the ripple is thought to be originated from Rayleigh-Taylor instability. The wavelength must be determined by some

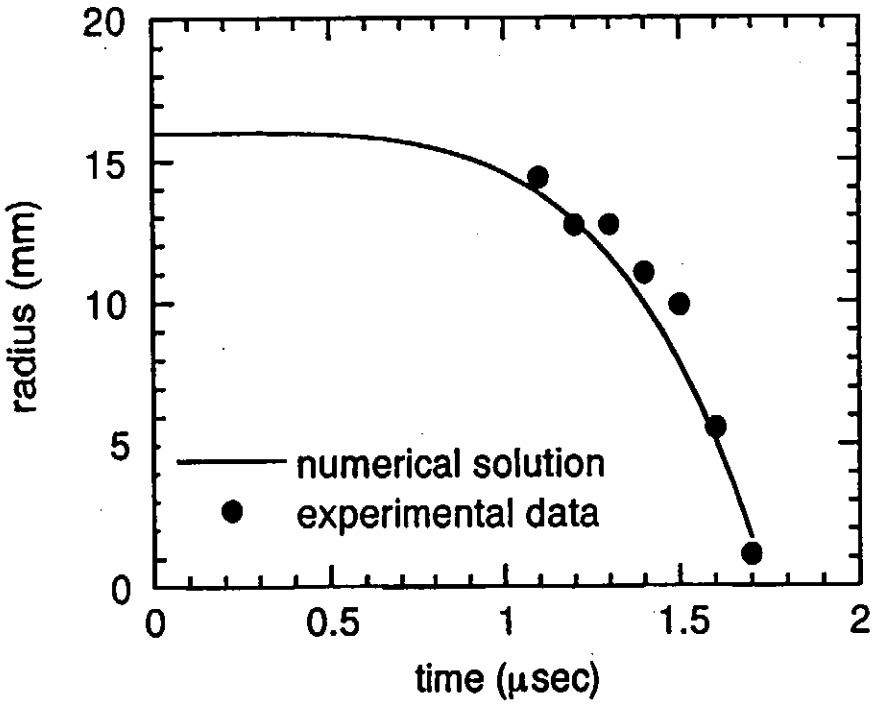

Fig. 4. Contraction of average plasma radius. The solid line shows calculated radius using measured plasma current.

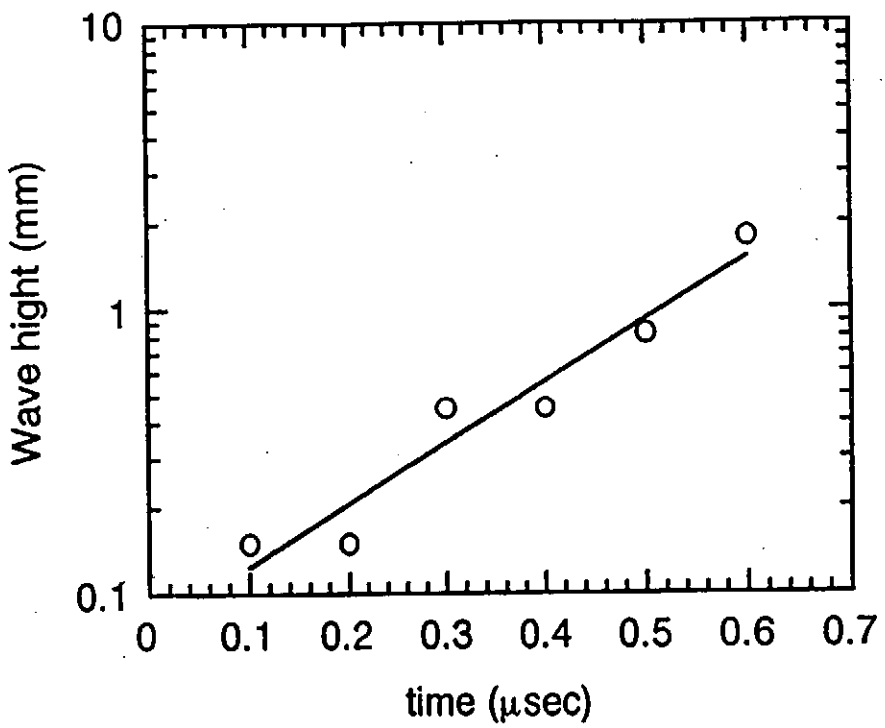

Fig. 5. Growth of amplitude of the ripple observed on the surface of the contracting plasma.

stabilization mechanism such as finite Larmor radius effect, and the instability selectively develops at the wavelength of maximum growth rate.

V. SUMMARY

The dynamic behavior of the SHOTGUN gas-puff z-pinch plasma was investigated using a Kerr-cell camera. A large amplitude instability was observed to develop during the contraction of the plasma. The observed wavelength, the acceleration and the growth rate were consistent with Rayleigh-Taylor instability. The observation of this large amplitude ripple is owing to relatively slow pinch formation for its initial radius.

Two types of gas nozzles were examined to reduce axial nonuniformity of the plasma. And the uniformity of the pinch column was improved by the use of 5 degrees inward directed gas nozzle.

REFERENCES

[1] F.L. Curzon, A. Folkierski, R. Latham and J.A. Nation, Proc. Roy. Soc. 257A, 386 (1960).

[2] K. Takasugi, A. Takeuchi, H. Takada and T. Miyamoto, Jpn. J. Appl. Phys. 31, 1874 (1992).

[3] C. Deeney, P.D. LePell, F.L. Cochran, M.C. Coulter, K.G. Whitney and J. Davis, Phys. Fluids B5, 992 (1993).

[4] S.A. Sorokin, A.V. Khachaturyan and S.A. Chaikovskii, Sov. J. Plasma Phys. 17, 841 (1991).

Control of Initial Mass on Metal Vapor Puff Z-Pinch

Seizo Furuya, Kenji Arai, Eiji Goto, and Shozo Ishii

Tokyo Institute of Technology

Abstract

The high energy density Z-pinch plasma created by injecting metal vapor between the electrodes has been examined experimentally. In the metal vapor puff Z-pinch, an initial mass of metal vapor greatly affects the pinch characteristics. To control the metal vapor spatial distribution and the puffed vapor velocity, the discharge current to produce the metal vapor with a square wave is employed. We have constructed the LC ladder discharge circuit which can generate the current pulse with 10μs in pulse width. Ag metal vapor is ejected by the discharge through a small hole drilled at the center of the electrode.

§1.Introduction

High-density and high-temperature Z-pinch plasmas are used as a high intensity pulsed soft x ray source and a soft x ray laser. High pressure gas or solid fiber is commonly used to creat high energy density Z-pinch plasmas. Since handling of thin fiber is troublesome, the fiber pinch with the high repetition rate is impossible. To overcome this drawback, we have proposed the metal vapor puff Z-pinch reported at the last workshop[1]. In this paper, we report the control of metal vapor generating process.

§2.Metal vapor puff Z-pinch

The experimental setup is shown in Fig.1(a). The lower electrode has a structure to produce metal vapor as shown in Fig.1(b). The metallic grains placed in a small cavity are vaporized by a pre-discharge. The principle of metal vapor puff Z-pinch is similar to that of gas puff Z-pinch. When the metal vapor reaches the other electrode, the main Z-discharge is fired. The main

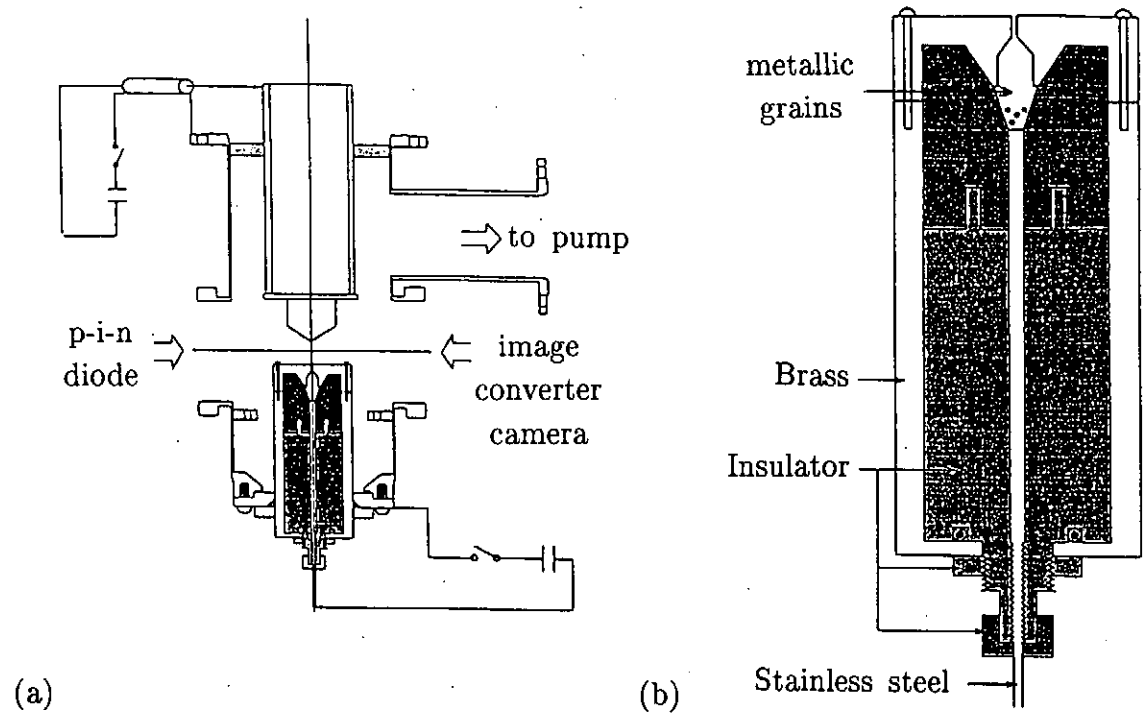

Fig.1: Metal vapor puff Z-pinch apparatus

discharge is powered by a 27μF capacitor bank charged to 20kV. For single metal vapor puffing, the pre-dishcharge is driven by a pulsed current with the first half cycle of sinusoidal wave as shown in Fig.4(a) obtained by clamping the capacitor discharge circuit. A 4.45μF capacitor charged to 10-20kV is used to produce metal vapor. Spectral behaviors of visible radiation from metal vapor was investigated by a monochromator. The line spectra from metallic atom were observed, which confirmed the metal vapor puffing. The main discharge current, the x ray output signal measured by Si p-i-n photo diode, and the streak photograph taken by an image converter camera are shown in Fig.2. The plasma column length was 20mm. The initial radius of hollow Cu metal vapor was 10mm. When the maximum pinch was established, the peak of soft x ray output was observed. At the same time, the discharge current dip was observed, which implies that the inductance of the plasma column increased. As the delay time τ between the onset of metal vapor puff and that of main discharge was increased, the peak value of the soft x ray output increased as shown in Fig.3. However, the pinch time did not vary drastically. The reproducibility of the pinch time and the soft x ray signal was poor, since the velocity and the total mass of puffed metal vapor were not equal for each shot. It is important to control these quantities in metal vapor puff Z-pinch.

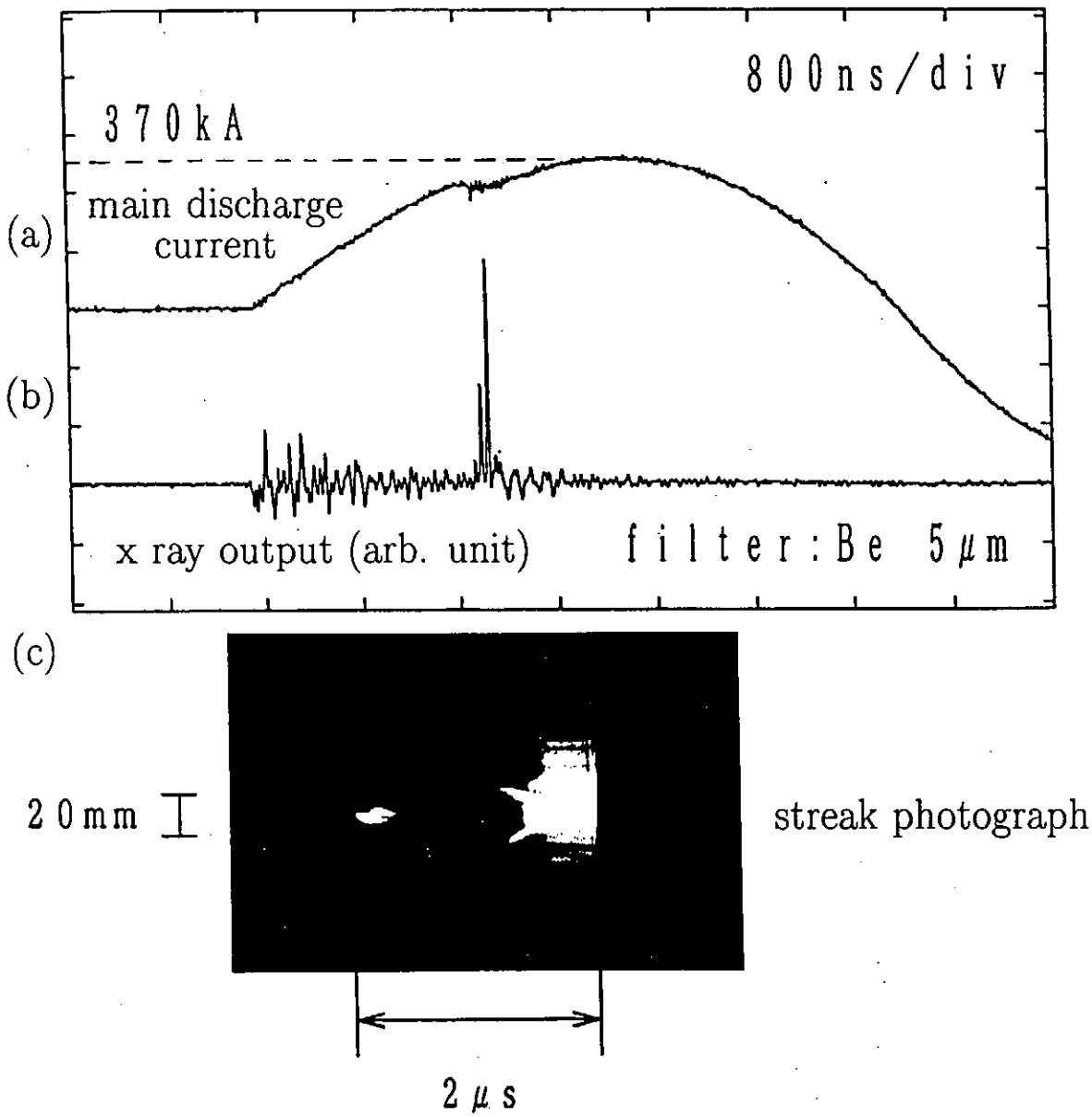

Fig.2 Hollow Cu metal vapor puff Z-pinch(τ:40μs)
(a) main discharge current (b) x ray signal
(c) streak photograph of radial profile

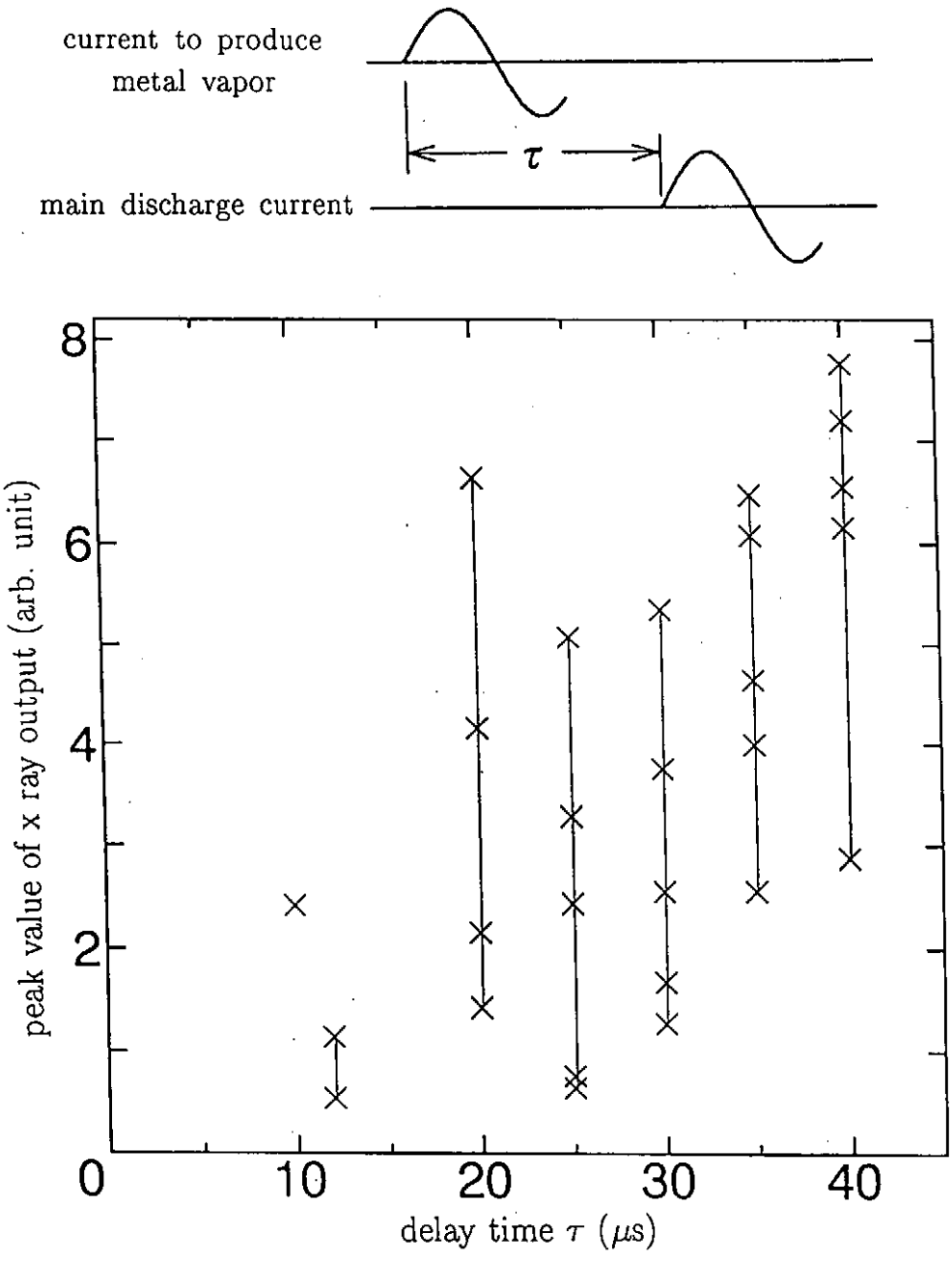

Fig.3 Peak value of x ray radiation vs. delay time τ

§3.Control of initial mass

The initial mass of metal vapor greatly affects the pinch characteristics, as seen in the change in the peak value of the soft x ray output when the delay time τ is increased. The generation processes of metal vapor, namely, heating, vaporizing, and ejecting through the electrode hole, are complicated. Since it takes some time for these processes, a square wave discharge current is desirable to control the metal vapor generation processes. We have constructed LC ladder discharge circuit as shown in Fig.5. The pulsed current shown in Fig.4(b) has 10μs in pulse width and 5kA in amplitude. Injecting Ag metal vapor through a single hole of 2.5mm in diameter, we created Z-pinch plasma of 10mm in length and 5mm in radius. Fig.6 shows typical main discharge current and the streak photograph. The reproducibility observed in streak photographs and main discharge currents is fairly good. However, the current dip and the soft x ray emission were not observed. Since the Z-pinch did not have the implosion process, the plasma temperature did not go up high enough to emit soft x ray.

§4.Conclusion

We could not compare the effect on the metal vapor generation processes given by difference of current waveforms. The square wave has much more supiority in control of the metal vapor generation.

Reference

[1] Y.Hoshina et al.:Soft x-ray radiation from metal vapor puff Z-pinch plasmas NIFS-PROC-14 89 (1993)

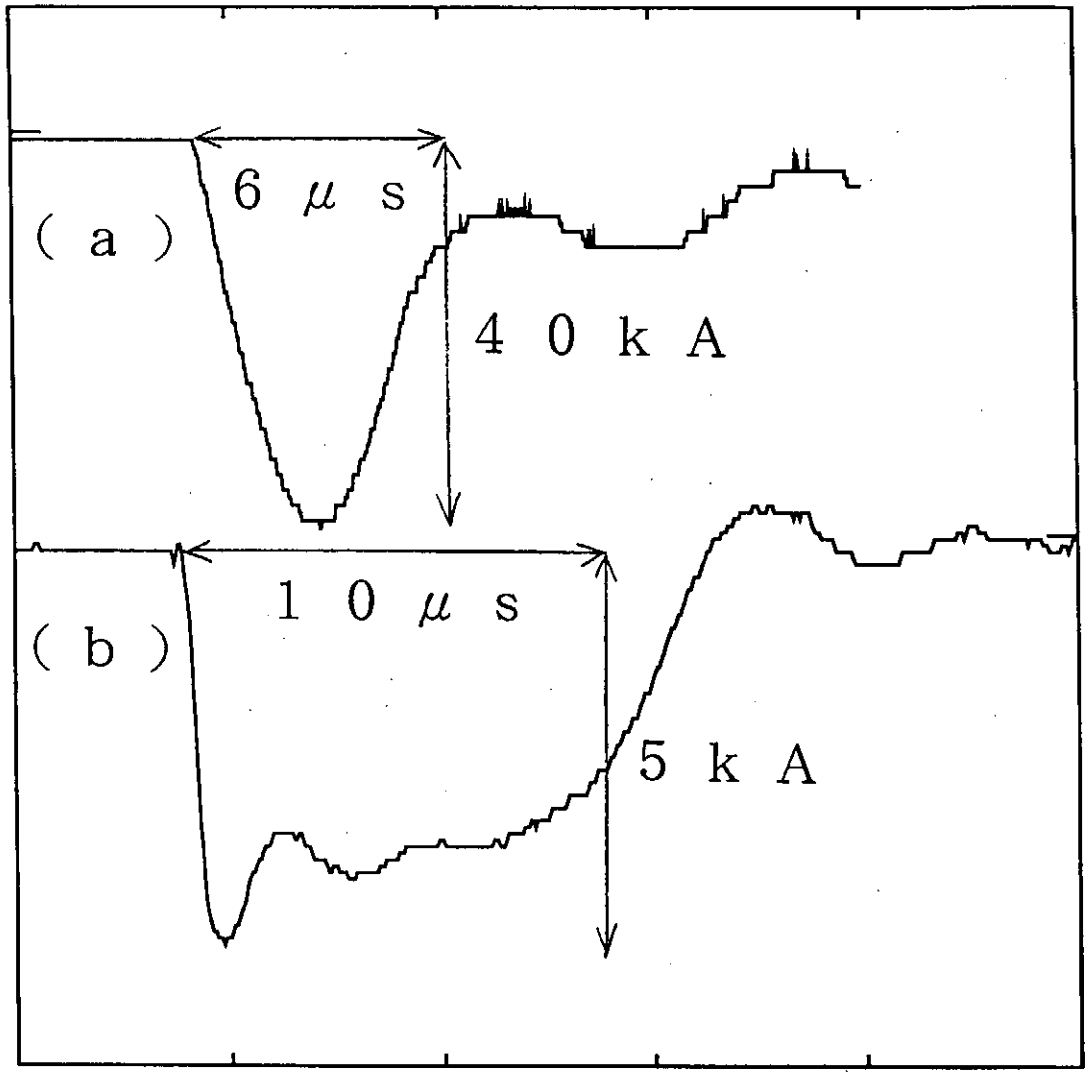

Fig.4 Current for production of metal vapor
(a) 4.45μF capacitor (b) LC ladder discharge circuit

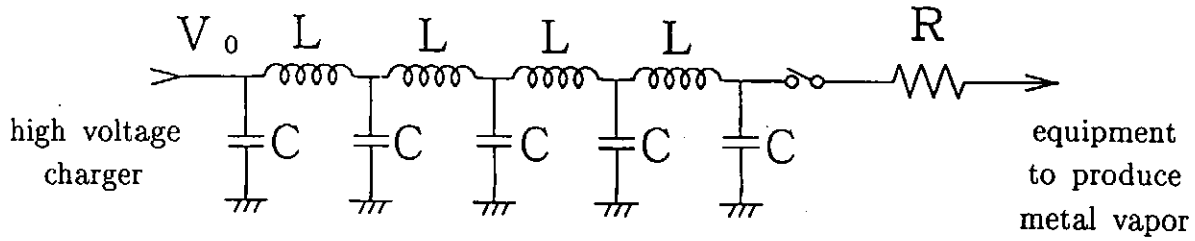

characteristic impedance : $\sqrt{(L/C)} \equiv Z$

width of pulsed current : $2n\sqrt{LC}$

amplitude (with matched resistance R) : $V_0/(2Z)$

(without R) : V_0/Z

design : $V_0 \leqq 20$ kV, $n = 5$, $L = 2$ μs, $C = 0.5$ μF

characteristic impedance : 2 Ω

width of pulsed current : 10 μs

amplitude (with R) : $\leqq 5$ kA

(without R) : $\leqq 10$ kA

Fig.5 LC ladder discharge circuit and its characteristics

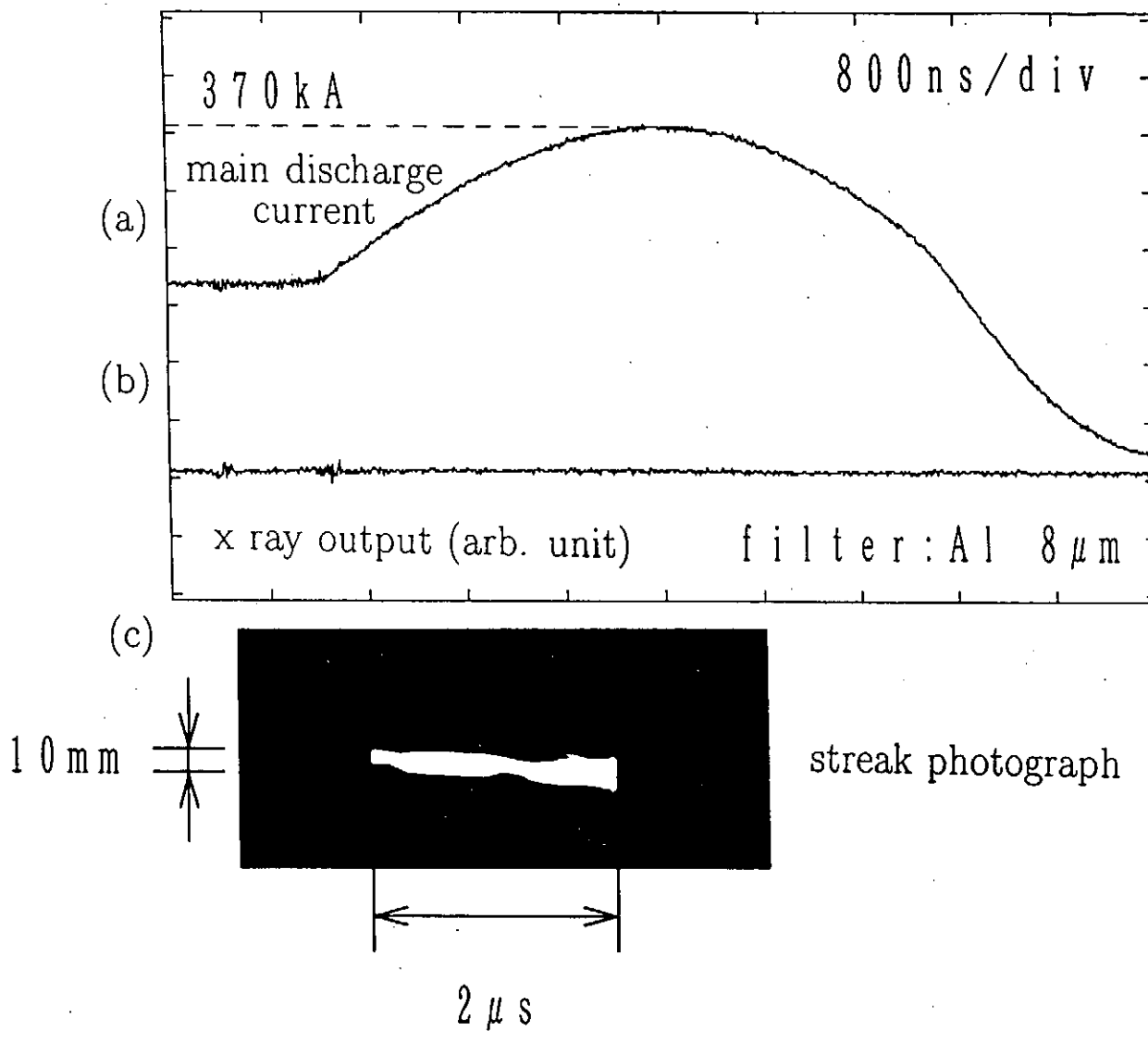

Fig.6 Cylindrical Ag metal vapor puff Z-pinch(τ:10μs)
(a) main discharge current (b) x ray signal
(c) streak photograph of radial profile

Z-pinch plasma by solid fine particle injection

Takahiro Hoshide, Qing-Pin Ai, Daiju Itagaki and Shozo Ishii

Tokyo Institute of Technology

Abstract

We have proposed Z-pinch plasma by solid fine particle injection to creat high energy density plasma. This scheme is superior in high repetition rate operation. It is possible to control the plasma point that radiate intense soft X-ray when the mass and the injection method of fine particle are chosen properly. The solid fine particles are injected through a small hole drilled at the center of the main electrode. The particles are accelerated by pulsed electrostatic field which is applied between the electrodes placed under the main electrode. Injection characteristics are experimentally examined for Cu particles of 1μm in diameter.

§1. Introduction

Gas puff Z-pinch and Z-pinch created from solid fiber or solid thin film liner are widely used as conventional methods to produce high energy density plasma. The former with gases, for example Ar, He and metal vapor, is easy to operate and can be used with high repetition rate. The later, for example fiber pinch or imploding liner, can creat high density plasmas. In this paper we report the Z-pinch by solid fine particle injection which has both advantages. This scheme is expected to have various applications of intense soft X-ray and UV radiation source, and thin film deposition of materials with the high melting point. It is possible to control the plasma point that radiate intense soft X-ray when the mass and the injection method of fine particle are chosen properly.

The particle with the diameter less than 100μm is defined as fine particles, for example, pollen ($10 \sim 100\mu$m), cigarette smoke (0.01μm), toner for photocopy machine ($1 \sim 10\mu$m), and cluster with dozens of atoms. The smaller the diameter of particle is, relatively the larger its surface area and the number of atoms on its surface are [1].

The issue on plasmas and fine particles has been studied in surface science, space science : space dust, and thin film technology : plasma CVD and plasma jet deposition. However, the plasmas created from fine particles have never been reported so far.

The solid fine particles are injected through a small hole drilled at the center of the main electrode. The particles are accelerated by pulsed electrostatic field which is applied between the electrodes placed under the main electrode. Injection characteristics are experimentally examined for Cu particles of 1μm in diameter.

§2. Experimental setup

The concept of experimental setup is shown in Fig.1. There are three electrodes which are separated to two sections. The upper pair of electrodes is for main discharge and the lower pair of electrodes is for particle acceleration.

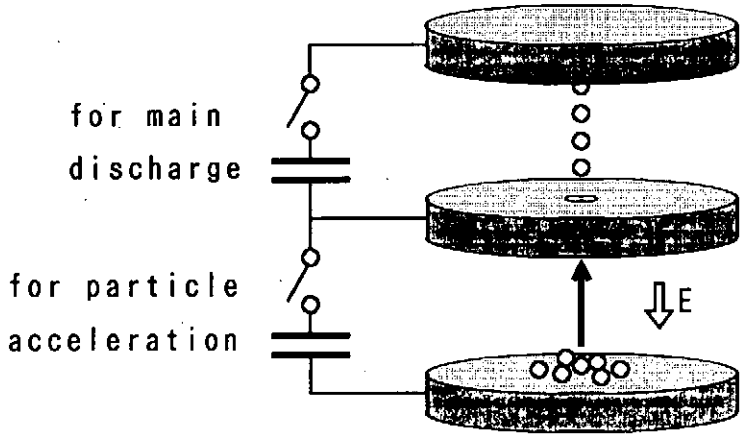

Fig.1: The concept of experimental setup

As comparing with the gases, it is rather difficult to supply fine particles between the discharge electrodes. The fine particles must be accelerated to have enough velocity for injection. Following particle acceleration method can be applicable, namely, pressure acceleration as in gas puff Z-pinch, electrostatic acceleration, magnetic acceleration, and electromagnetic acceleration as in rail gun. In this work, the particles accelerated by electrostatic field are supplied between the discharge electrodes. The electrostatic acceleration method requires a simple apparatus and is easy to operate.

The configuration for particle acceleration electrodes is shown in Fig.2. Spherical Cu particles of 1 μm in diameter are put on the lower electrode. When pulsed

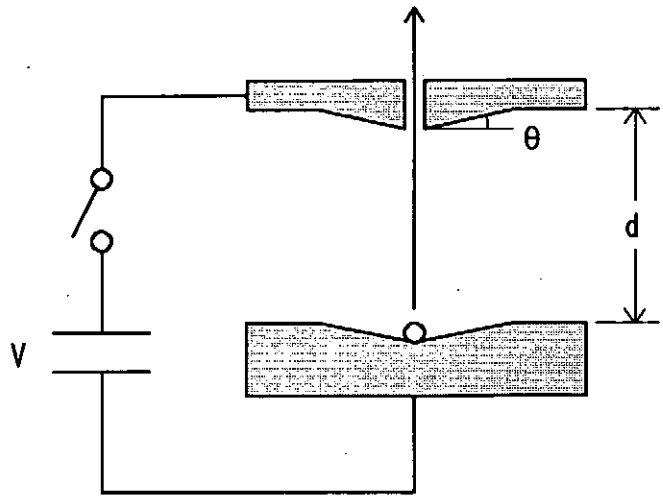

V = 16 [kV]
d = 10 [mm]
θ = 5 [deg]

Fig.2: The particle acceleration electrodes

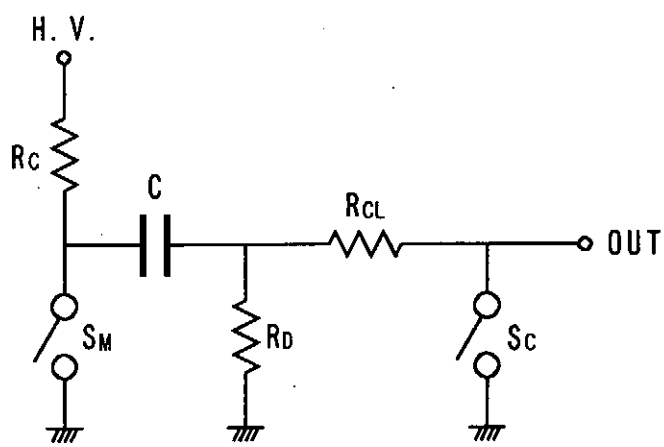

C = 0.441 [μF]
Rc = 10 [MΩ]
RD = 250 [kΩ]
RcL = 50 [Ω]

Fig.3: The equivalent circuit of power supply

high voltage is applied between the electrodes, the particles are charged to the same polarity as that of the lower electrode. The charge q appearing on the particle surface is

$$q = 1.65 \times 4\pi\varepsilon_0 r^2 E_0 \tag{1}$$

where ε_0 is the permittivity in vacuum, r the radius of the particle, and E_0 the average applied electric field, respectively. The particles are pulled up by electrostatic force, then they are injected into the space between main electrodes through the 2mm diameter hole in the middle electrode [2],[3].

In order to concentrate particles to the hole of the electrode, the shape of the middle electrode is convex and that of the lower electrode is concave. The equivalent circuit of pulsed high voltage power supply for particle acceleration is shown in Fig.3. The accelerating voltage is 16kV and 3ms in pulse width. The particle acceleration behaviors have been observed with optical measurement by using a He-Ne laser.

§3. Results

The particle behaviors in the accelerating phase have been observed by the measuring setup as shown in Fig.4.

When the particles are pulled up and scatter the He-Ne laser light, detected intensity will decrease. The particles started to move from the electrode at 200 μs after voltage application. This time delay is caused by Van-der-Waals force which keeps the particles being on the surface of the electrode. To reduce this time delay, it is necessary to prevent coherence of particles. One solution for this problem is vibrating the particles by applying a supersonic wave oscillator to the lower electrode.

The calculated dependence of the amount of charge and the particle velocity at the middle electrode on the particle size are shown in Fig.5, and 6, respectively. The amount of charge is in proportion to the square of particle size. The particle velocity is in inverse proportion to the square root of particle size. As considering troublesome handling of the fine particle, the optimum diameter of particles is $1 \sim 10\mu$m.

Injected particle behavior above the middle electrode is observed from scattered He-Ne laser beam which is expanded to about 2cm diameter beam by a beam expander. The scattered light is taken by time integrated photographs. The particle injection has not been observed in case of applied voltage with the pulse width less than 1ms.

We confirmed the injection of the fine particles between the main electrodes. The designed experimental Z-pinch apparatus is shown in Fig.7.

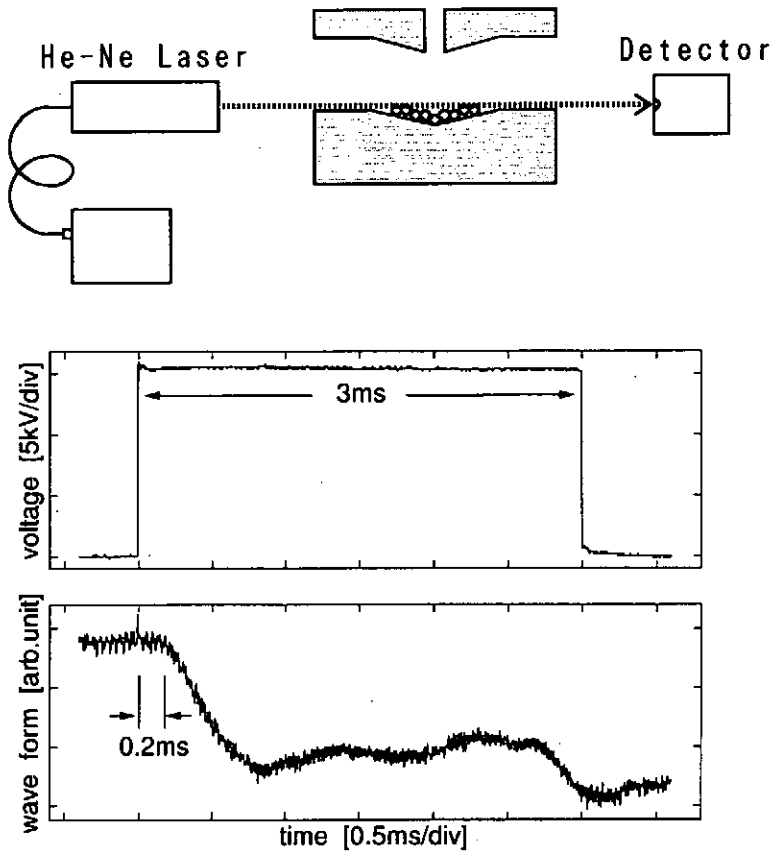

Fig.4: The measurement of delay time

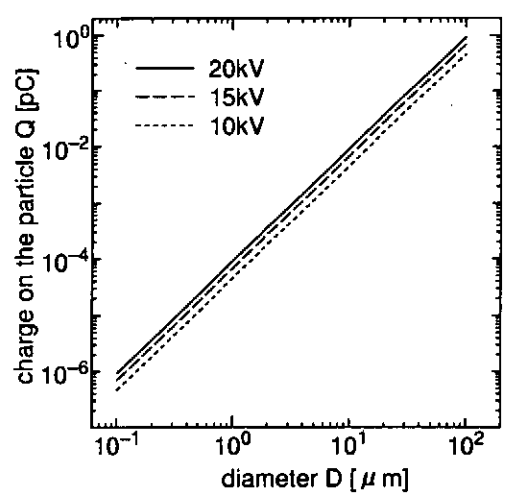

Fig.5: The charge on the particle

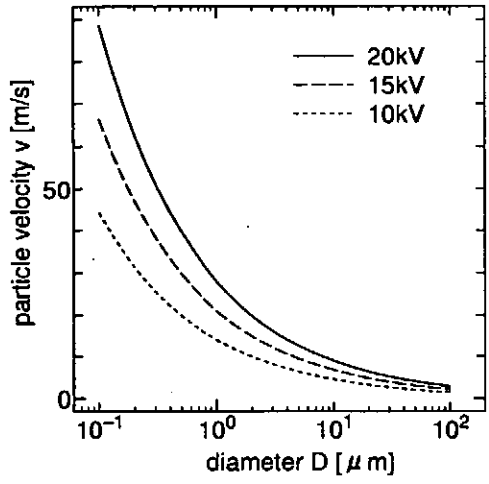

Fig.6: The particle velocity at the middle electrode

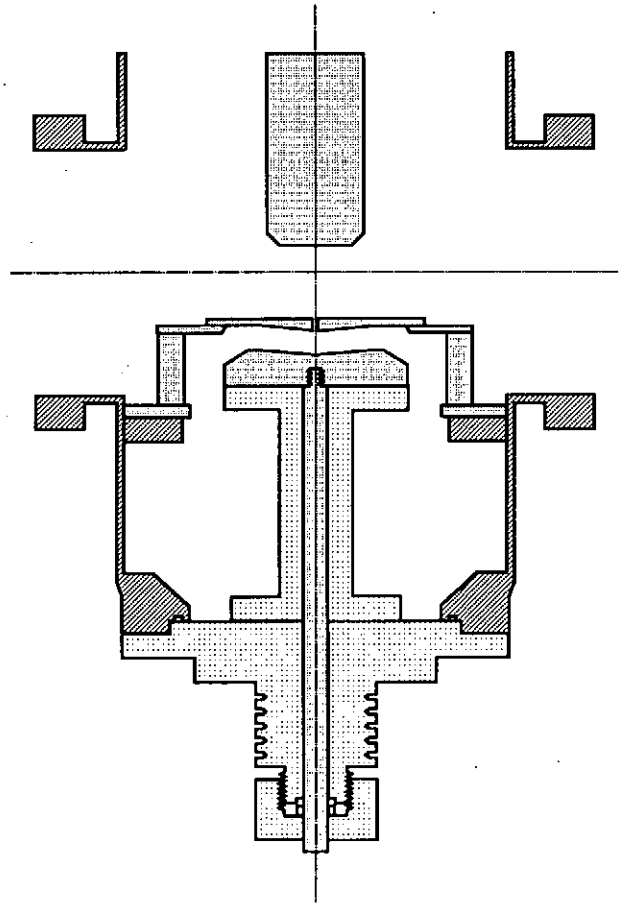

Fig.7: The disigned experimental Z-pinch apparatus

§4. Conclusion

We have proposed Z-pinch plasma by solid fine particle injection to create high energy density plasma. The Cu fine particles of 1μm in diameter injection has been established by electrostatic acceleration. There exists the time delay between the initiation of particle move and the application of pulsed acceleration voltage. This delay is caused by Van-der-Waals force. The dependence of the amount of charge and the particle velocity at the middle electrode on the particle size are calculated to estimate the optimum size of particles. The proposed Z-pinch scheme is useful for new applications in material science.

References

(1) T.Yokota : Purazuma kakuyugo gakkaisi, 6,69,1 (1993)
(2) H.Shelton, C.D.Hendricks, and R.F.Wuerker : J.Appl.Phys., 1243,31,7 (1960)
(3) A.Y.H.Cho : J.Appl.Phys., 2561,35,9 (1964)

Monochromatic x-ray imaging in plasma focus experiment

N. Hisatome, J. Du, T. Yamamoto, K. Shimoda and K. Hirano

Dept. of Electronic Engineering, Gunma University

Kiryu, Gunma 376, Japan

Abstract

A imaging spectrometer for monochromatic in soft X-ray is designed and examined using a plasma produced by a plasma focus device. In this spectrometer, a pinhole image is recorded simultaneously with monochromatic image. This provides identification of the wavelength if the soft X-ray source fluctuates from shot to shot such as in Z pinch or plasma focus. The monochromatic image of the Argon K-lines are successfully obtained and displayed in 3D. The resolution power and dispersion is obtained in-situ and compared with calculation.

§ 1 Introduction

The monochromatic X-ray imaging technique with two dimensional spatial resolution is one of a powerful diagnostic tool in pinch and laser-plasma experiment. The wavelengths ranging from 1 to 50 Å are of interest for the dense plasmas which are produced by various z-pinch devices including plasma focus. Various schemes for the soft X-ray imaging have been proposed using diffraction from a flat single- or double crystal, a curved crystal, or a layered synthetic microstructure [1, 2].

High spatial and spectral resolution are required to observe an intense soft X-ray emitting core in rapid z-pinch or plasma focus experiment. The core is sometimes considered as a result of the radiation collapse of the pinched plasmas.

Here we present a monochromatic 2-dimensional imaging system using a flat crystal spectrometer with a slit. The results are compared with that of filtered pinhole camera which enables to obtain a quantitative image intensity measurement with a

data acquisition system. Simultaneous measurement of the soft X-rays using the flat crystal imaging system and the filtered pinhole camera makes possible to obtain a time resolved-and 2-dimensional imaging by the monochromatic soft X-rays generated by the rapid pinch experiment.

§ 2 Experimental

2-1 Imaging spectrometer concept

The spectrometer described here is substantially identical with the one designed in a previous paper [3]. In order to obtain an adequate dispersion an RAP (Rubidium Acid Phtalate) flat crystal whose 2d length is 26.12 Å is employed. The use of an entrance slit (100 μm and 7 mm in width and length) made it possible to spatially resolved the X-ray source in two dimension. The slit was so mounted at the long side of the slit was in the direction of the dispersion of wavelength. A pinhole of 100 μm ϕ was placed at 1 mm from the slit end as shown in Fig. 1. The magnification of the spectral analyzed image is determined by the ratio of L_1 to L_2 + R in the axial direction of the electrode. For the radial direction, the image is same size of the source. The spectrometer in this experiment was designed that the magnification is unity. To cut off uninteresting emissions from the source, a 50 μm thick foil was adopted at the pinhole and the slit.

After being reflected on the crystal, the soft X-rays from the source were projected on to the photographic film (Kodak TRI-X). The film was mounted on a 1/4 circle which was centered at the axis of the rotation of the crystal. This spectrometer was designed to make a mark (a small spot) by a flash of an LED which can be used for measuring the wavelength on the film. To avoid absorption of the soft X-ray, He gas at an appropriate pressure was embedded in the spectrometer.

When the imploding plasma such as plasma focus and z pinch are adopted as soft X-ray sources, location of the pinched plasma always fluctuates from shot to shot. This makes any measurement of the wavelength ambiguous, because normally

we obtain only spectral lines on the photographic film. Deviation of the source brings some shift of the spectral lines on the film, and so identification of the wavelength is nearly impossible. To solve this difficulty, the pinhole which is installed on the slit plane in the spectrometer was used for making a pinhole picture on the same film. The pinhole picture provides a standard to measure the wave length of the soft X-rays.

In Fig. 1, O is the origin of the coordinate system which is at the point on the electrode axis of the plasma focus facility. A photographic film is mounted along the arc $\widehat{O'O''}$ whose center is at T, where O' is on the extension of TO. Q' (x_1, y_1) is the intersection of the arc and the extension of OP. The location of the soft X-ray source is S which fluctuates around O form shot to shot. When S is generated at (0, δ) the pinhole image of S appears at I (x_2, y_2). The crystal for spectral analysis is mounted so as to locate the axis of the rotation is at T (-L, 0).

If we fix the crystal at angle α, a spectral line projected at Q which satisfies the Bragg's condition,

$$\lambda = 2d\sin\theta \tag{1}$$

Therefore, $\widehat{IQ}$ ($\equiv \ell$) is a function of α, δ and λ (or θ). Here we should obtain λ by measuring ℓ_1 and ℓ_2, where $\ell_1 = \widehat{O'Q}$, $\ell_2 = \widehat{O'I}$ R and $\ell \equiv \ell_1 - \ell_2$. The location of O' can be determined from the spot by the LED. With respect to the crystal surface Q and Q' are symmetric, and so

$$\angle O'TQ' \equiv \Theta = \beta - 2\alpha \tag{2}$$

Therefore the coordinate of Q' (x_1, y_1) are given

$$x_1 = -\{R\cos(\beta - 2\alpha) + L\} = -\left\{R\cos\left(\frac{\ell_1}{R} - 2\alpha\right) + L\right\} \tag{3}$$

$$y_1 = -R\sin(\beta - 2\alpha) = -R\sin\left(\frac{\ell_1}{R} - 2\alpha\right) \tag{4}$$

On the other hand, the equation which pass through S and Q' is written as

$$y = \{\tan(\theta - \alpha)\}x - \delta \tag{5}$$

Substituting (3) and (4) into (5), and rearranging with respect to θ

$$\theta = a + \tan^{-1}\left(\frac{y_1 + \delta}{x_1}\right)$$

$$= a + \tan^{-1}\left\{\frac{R\sin\left(\frac{\ell_1}{R} - 2\alpha\right) - \delta}{R\cos\left(\frac{\ell_1}{R} - 2\alpha\right) + L}\right\} \tag{6}$$

From Eq. (1) and (6), we have finally

$$\lambda = 2d\sin\left[a + \tan^{-1}\left\{\frac{R\sin\left(\frac{\ell_1}{R} - 2\alpha\right) - \delta}{R\cos\left(\frac{\ell_1}{R} - 2\alpha\right) + L}\right\}\right] \tag{7}$$

where

$$\ell_1 = \ell + \ell_2 \tag{8}$$

$$\ell_2 = R\gamma = R\tan^{-1}\left(\frac{y_2}{|x_2 + L|}\right) \tag{9}$$

$$x_2 = \frac{-(L - a\delta) - \sqrt{(L - a\delta)^2 - (1 + a^2)(L^2 + \delta^2 - R^2)}}{1 + a^2}$$

$$y_2 = a\,x_2 - \delta$$

and

$$a = -\frac{h + \delta}{L}$$

2-2 Resolution and Dispersion

In Eq. (7), the fluctuation in λ is caused from ambiguity of ℓ , α , δ . Therefore, the incremental change in λ is described as

$$\Delta\lambda = \left(\frac{\partial\lambda}{\partial\ell}\right)_{\alpha,\delta}\Delta\ell + \left(\frac{\partial\lambda}{\partial\alpha}\right)_{\ell,\delta}\Delta\alpha + \left(\frac{\partial\lambda}{\partial\delta}\right)_{\ell,\alpha}\Delta\delta \tag{10}$$

where, $\Delta\ell$, $\Delta\alpha$ and $\Delta\delta$ are ambiguities in measuring of locations in pinhole

images, the spectral lines and fluctuation of the soft X-ray source, respectively. We can easily obtain the dispersion, $\frac{\partial \lambda}{\partial \ell}$ and the resolution power, $\frac{\lambda}{\Delta \lambda}$ for the spectrometer from Eqs. (7) and (8). The calculated results of the partial differentials by λ by ℓ , α and δ around Ar K lines are given in Fig. 2.

2-3 Pinhole camera and soft X-ray source

For comparison a filtered soft X-ray pinhole system was employed. The system consisted of a pinhole camera, microchannel plate-phosphor screen combination, a CCD camera, image memory board and a personal computer. To make a quantitative, and time resolved measurement of the soft X-ray intensity possible, observation of the phosphor screen current are carried out in conjunction. Performance of the pinhole camera system is described in a previous paper [4] .

The time evolution of the plasma was observed with an image converter camera in streak mode. The hard X-rays was monitored by a scintillator and photomultiplier combination which was located at 6.5 m from the source and 90 ° from the electrode axis. The soft X-rays were also observed by a scintillation detector mounted at the vacuum vessel. The arrangement of the diagnostic tools are shown in Fig 3. A simultaneous measurement provides that the soft X-ray image with time resolution.

The imaging spectrometer was examined by using the soft X-rays which were generated by a plasma focus facility with a capacity bank of 4.24 μ F. The facility is described in detail elsewhere. The experiment was carried out at a bank voltage of 55 kV and a filling pressure of 4 Torr H_2 and 6 % of Ar admixture.

§ 3 Experimental Results

3-1 Spectrograph and pinhole images

An example of the pinhole-and the monochromatic image are shown in Fig. 4. In this figure, (a) is a pinhole photograph which was taken with the filtered pinhole camera. It can be recognized that there are four intense soft X-ray emissions (hot

spots) in the photograph. The spectral lines indicated (b) correspond to four emissions in which each spot in the pinhole photograph ①, ②, ③ and ④ are analyzed and appear at ①', ②', ③' and ④' respectively. The broadening of the lines means spatially resolved images of the soft X-ray source. Using Eq. (7), we can obtain the wavelength of the lines. An L-shaped pattern overlapped partially on the pinhole image is caused by the direct exposure from the soft X-ray without being reflected by the crystal.

By means of a microphotodensitometer we measured the location of the spectral lines the results are also described in Fig. 4.

3-2 Dispersion and resolution

Using Eq. (10) we can obtain the dispersion and the resolution power of the spectrometer of calculated results. Each term in the right hand of Eq. (10) is shown in Fig. 2. In our case, $\Delta \ell$, the error caused by measurement of distance is less than 0.1 mm, and we have 5' = 1.454 x 10^{-3} rad for $\Delta \alpha$ at Ar XVII. It is estimated that δ = 1 mm in average discharge. Then we have $(\partial \lambda / \partial \ell)\Delta \ell$ = 2.60862 x 10^{-3}, $(\partial \lambda / \partial \alpha)\Delta \alpha$ = 1.5468 x 10^{-2} and $(\partial \lambda / \partial \delta)\Delta \delta$ = 6.52 x 10^{-4}. However, $(\partial \lambda / \partial \alpha)\Delta \alpha$ and $(\partial \lambda / \partial \delta)\Delta \delta$ do not affect the resolution power of the spectrometer because those are the errors which appear in the process to identify the wavelength. Therefore, we obtain the dispersion as $(\partial \lambda / \partial \ell)$ = 0.6062 x 10^{-2} Å /mm and the resolution power $\lambda / \Delta \lambda \fallingdotseq$ 1500.

3-3 Monochromatic images

The hot spots detected by various method mentioned above are shown in Figs. 5 (a),(1),(2) and (3). We can easily obtain the images with identifying their wavelength using the proposed spectrometer as seen (3). The FWHM of the first peak of the phosphor current, that is (b),(1) corresponds to the emitting duration of the soft X-ray. The second is caused by the hard X-rays emitted from the electrode surface after plasma disruption

Spatial distribution of the soft X-ray brightness between the pinhole images

and the spectral analyzed image are compared in Fig. 6. Argon ions which emit K-lines are concentrated near the electrode axis. The surrounding region emit mainly the soft X-ray by the Bremsstrahlung whose spectral band is accepted by the Be filter and the 1photographic film combination.

References

1. S. A. Pikuz, A. I. Erko, A. Ya. Faenov: Conference program of 3rd Int. Conf. on Dense Z-Pinches, London, 1993 (Imperial College, London, 1993) p. 54.
2. A. J. Cole, M. H. Key, A. Ridgeley, D. A. Brown, P. A. Norreys, E. R. Wooding and T. W. Barbee: Opt. Commun. 62 (1987) 1.
3. K. Shimoda, T. Yamamoto, S. Takada, H. Sone and K. Hirano: Jpn. J. Appl. Phys. 26 (1987) 451.
4. Y. Takahama, J. Du, T. Yanagidaira and K. Hirano: to be published in Rev. Sci. Instrum.

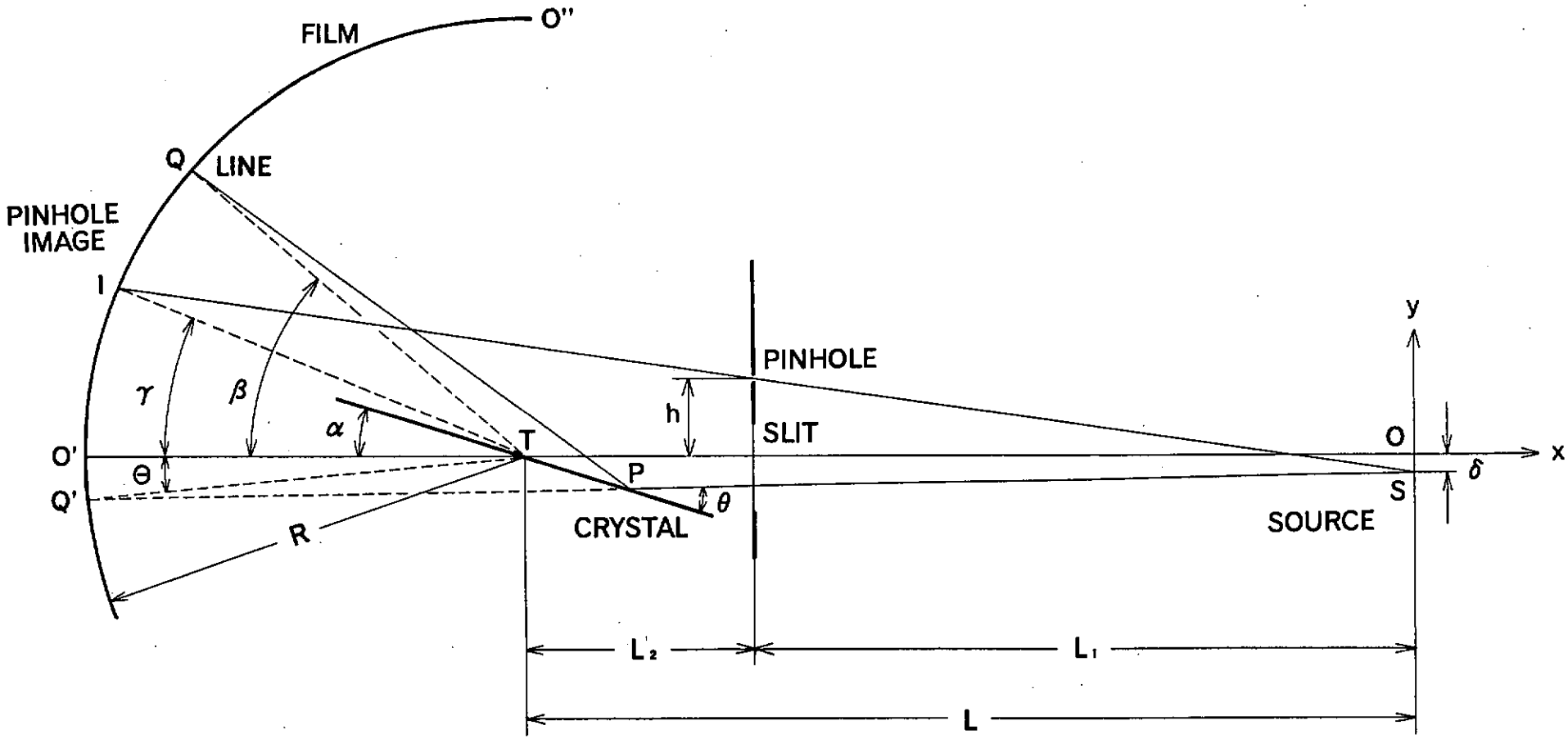

Fig. 1 Schematic diagram of the spectrometer and the soft X-ray source.

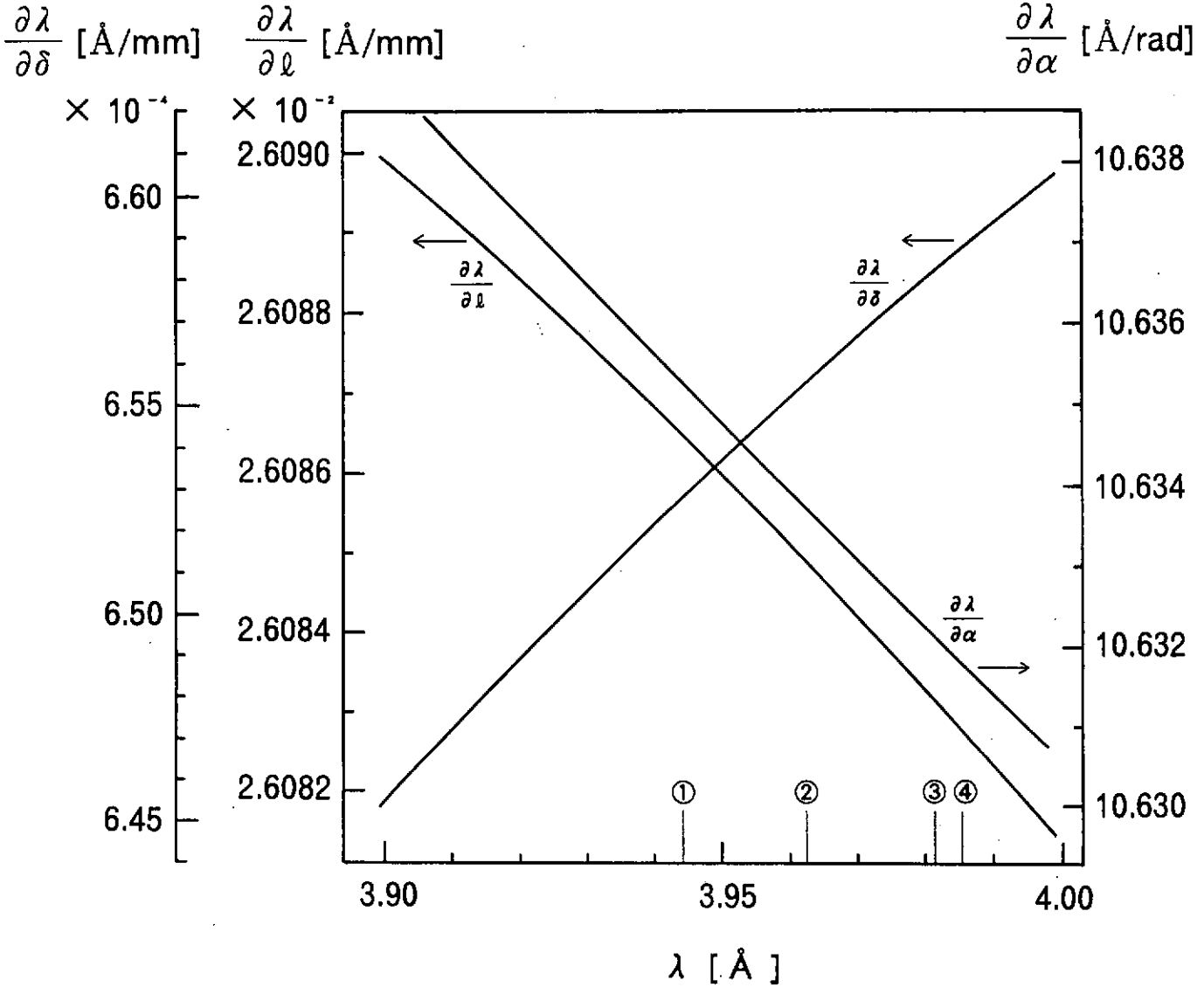

Fig. 2 Ambiguity calculation in the spectral band from 3.90 to 4.00 Å. Ar K-lines; ① Ar XVII 3.944 Å, ② ArXVII 3.962Å, ③ Ar XVI 3.981Å

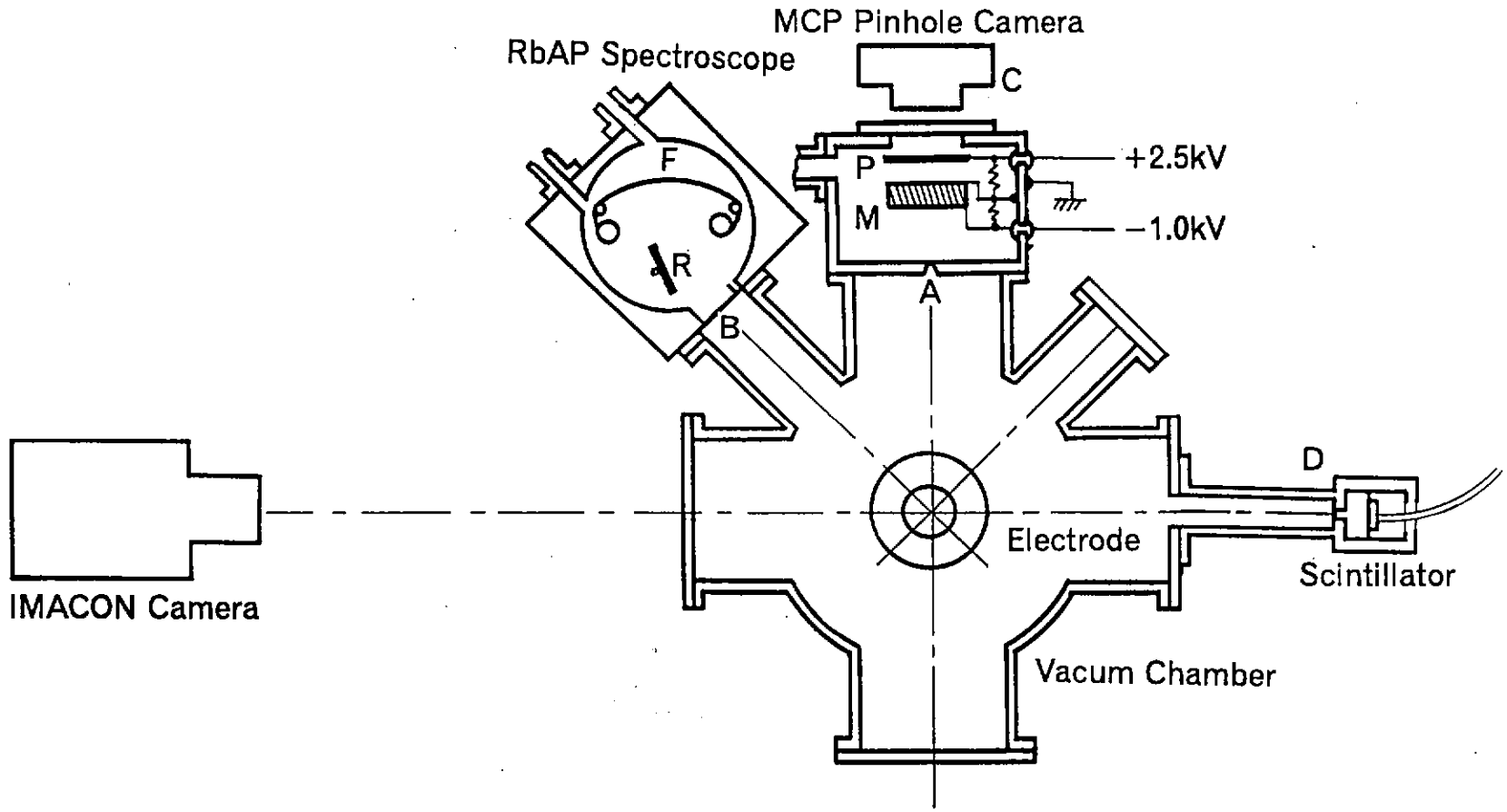

Fig. 3 Experimental arrangement of the plasma focus device and diagnostic tools.

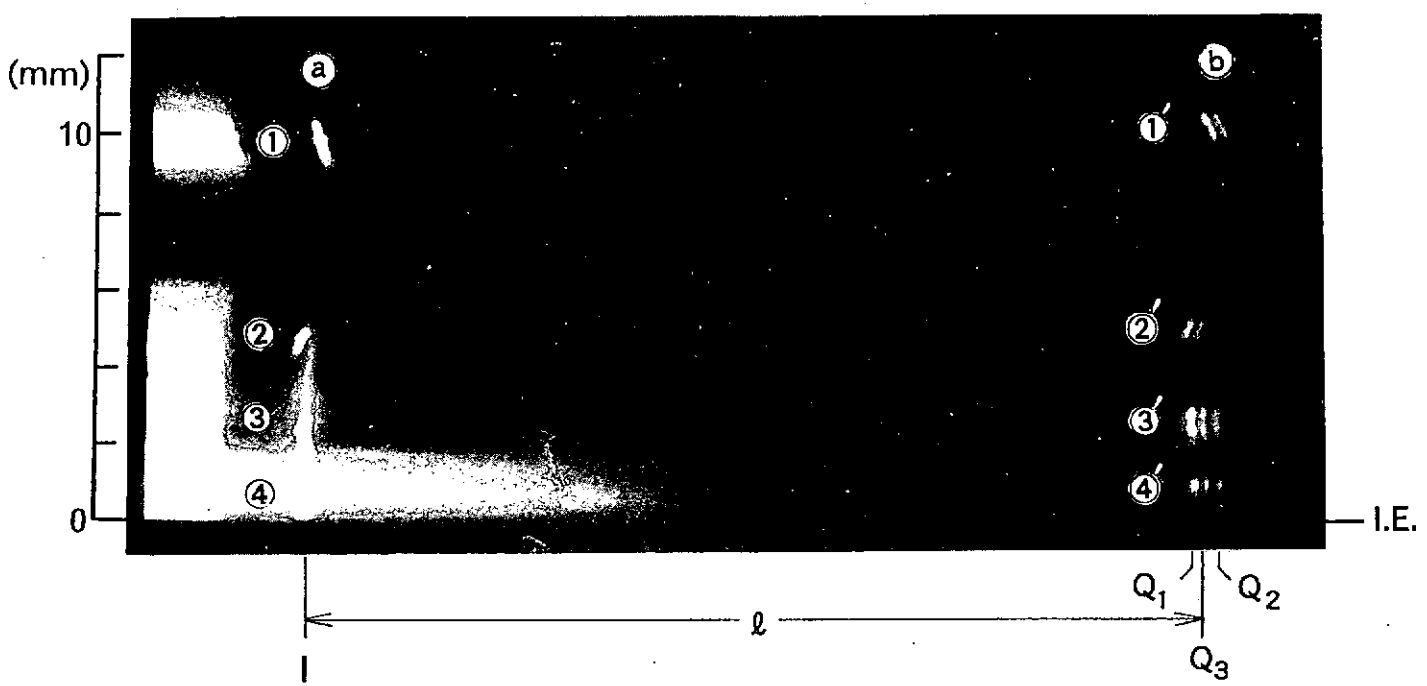

Fig. 4 Example of the pinhole photograph ⓐ and monochromatic images of the soft X-ray source ⓑ.
Q_1 : Ar XVII 3.944 Å , Q_2 : ArXVII 3.962 Å ,
Q_3 : Ar XVI 3.981 Å

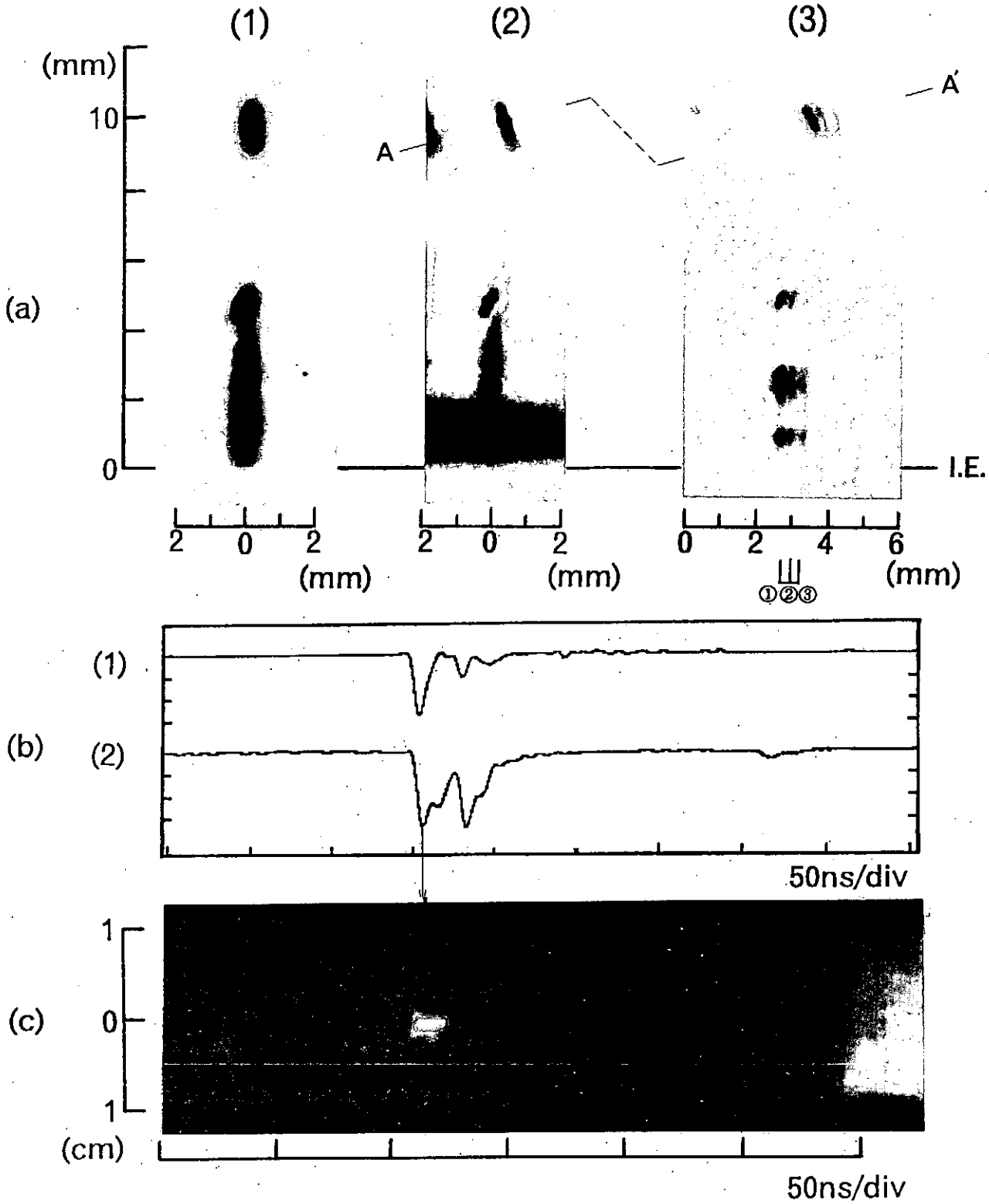

Fig. 5 Time correlation between the macroscopic plasma behavior and soft X-ray emission in the plasma focus.
(a) pinhole image and monochromatic image of Ar K-lines.
(b) monitors; (1) phosphor current and (2) soft X-ray signal by a scintillation detector. (c) dynamic behavior of the plasma observed with the image converter camera in streak mode.

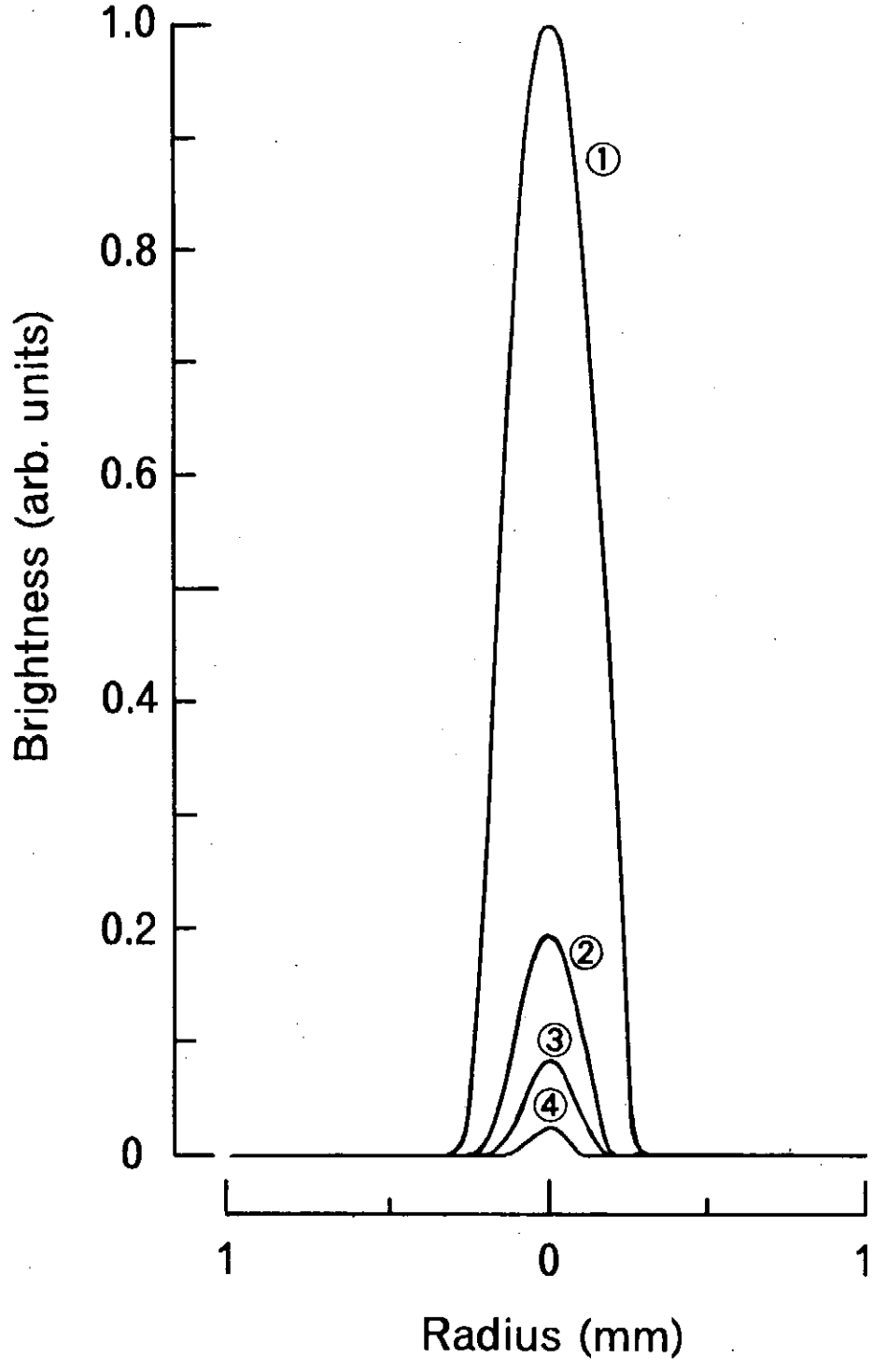

Fig. 6 Relative brightness of soft X-rays drawn along A-A' in Fig. 5 (a). ① pinhole image, ② Ar XVII 3.944 Å, ③ ArXVII 3.962Å, ④ Ar XVI 3.981Å.

Hot Spots Observation in a Dense Plasma Focus

Yoshio Takahama, Min Han※, Takeshi Yanagidaira and Katsumi Hirano

Dept. of Electronic Engineering, Gunma University

Kiryu, Gunma 376, Japan

※Gas Discharge and Plasma Laboratory, Tsinghua University

Beijing, China 100084

Abstract

Hot spots in a dense plasma focus are investigated with a time-resolved and filtered pinhole camera system through Ar k-lines. A Moire Schlieren technique is used to observe the macroscopic plasma behavior conjunctly. The hot spots are generated at the disruption of the plasma column by growing of macroscopic instabilities. On the both sides of the disrupted region, the hot spots appear and emit intense K-lines of argon nearly for 15 ns. A spatial distribution of Ar K-line emission with calibration is obtained using the pinhole camera system. The maximum intensity, $\sim 2 \times 10^{13}$ (photons/(s • mm^2 • mrad^2 • 0.01%BW)) is observed when 6 % of argon is added to the 4 Torr hydrogen.

§ 1 Introduction

Intense, small size soft X-ray sources are required in the fields such as high density lithography, X-ray microscopy and laser excitation. It is rather easy to produce the sources by generating hot spots or micropinches in the dense plasma focus or the Z pinch which were first observed by Cohen et al.[1] When high Z material is admixed into hydrogen or deuterium, the soft X-ray emission mainly comes from a small region known as the hot spots or the micropinches. They are defined as points or a fiber-shaped region which emit intense soft X-rays. Their typical density and temperature have been estimated to be 10^{19} cm^{-3} and several hundred eV. The sizes are sub-mm and mm ranges in diameter and length, respectively.

These hot spots were not observed in discharges with pure hydrogen or deuterium,

but with heavy element admixture. Several models are proposed to explain formation of the hot spot and the micropinch. Namely, they are beam plasma interaction and radiative collapse. However, the mechanisms has not been understood well, in spite of many studies.

Vikhrev et al [2] described that a radiative collapse occurred when a certain condition among the discharge current, the plasma diameter and the line density of the column is satisfied. Choi et al [3] inferred that the interaction between the electron beam and small, cold and dense plasma generates hot spots.

Here we present the results obtained by simultaneous measurement of macroscopic behavior with Moire Schlieren method and the time resolved imaging by a filtered soft X-ray pinhole camera.

§ 2 Experimental

2-1 Plasma focus device as a soft X-ray generator

A Mather type plasma focus device with a squirrel cage outer electrode was employed to generate soft X-rays. The coaxial electrode diameters are 35 and 80 mm, respectively. The length of electrodes was 80 mm. A quartz insulator extended 40 mm along the inner electrode which was anode. The condenser bank consisted of 4×1.06 μ F, 100 kV capacitors. Each capacitor was switched by a pressurized air gap. The device was operated at the bank voltage of 55 kV and a mixed gas (H_2 + 6 % Ar) pressure of 4 Torr. The total discharge current and the plasma current were measured with a Rogowski coil and a magnetic probe, respectively. The discharge current and its ringing frequency are 550 kA and 330 kHz when the bank is discharged at 60 kV. However, the current in the plasma column was less than 300 kA at its peak approximately.

2-2 Pinhole camera system

A soft X-ray pinhole camera with a quantitative image acquisition system is developed for soft X-ray image observation with time resolution.[4] It is intended to compose the system mainly employing devices which can be obtained easily in

commercial.

A pinhole image of the X-ray source is made on the MCP (microchannel plate, Hamamatsu Photonics, type F2223-11P) through a pinhole and Be and Ag foil filters (25 μm and 1 μm in thickness, respectively) which prevent the visible light also emitted from the source. The spectral response of the MCP system is described in a previous paper.[4] It was calculated with taking into account absorption by the Be + Ag filter and the detection efficiency for MCP. The combination of the filters and the MCP gives a pass band between 3.7 and 7Å ,which accepts Ar K-lines.

The photoelectrons produced by the X-rays on the MCP are multiplied by the MCP whose gain is a function of the applied voltage between the both sides of the MCP. Then they are accelerated onto the phosphor screen and an image of the visible light appears. The visible image is registered in an image memory board (PHOTRON FRM2-512) in 8 bits through a CCD camera (SONY XC-77). The image data can be stored both in the memory of the image memory board and on the floppy disk. The data are processed by the personal computer (NEC PC-9801RA2). A preferable data processing, such as the 3-D display, is possible by this system. The CCD camera was operated in a mode in which the response of the CCD was proportional to the luminosity of the object. The image memory board was modified to be operated in a single shot mode.

The electrons, which are emitted from the MCP and carrying image information, are measured as the phosphor screen current simultaneously. This allows not only to obtain a quantitative relationship between intensity of visible image and the electron number, but also to carry out an effective time resolved observation. Therefore, We can evaluate number of photons which pass through the pinhole after taking absorption by metal foil into account. This also allows to give the electron number which is collected on the phosphor screen after conversion of photons into electrons with the MCP. We can calibrate the phosphor current itself with same manner. This provides an analog measurement for the soft X-rays.

2-3 Auxiliary measurement

A Moire Schlieren method in framing mode was employed to observe the spatial distribution of electrons.[5] A N_2 laser whose pulse width was less than 1 ns was used as a light source. Soft X-ray emission was monitored by a scintillator-photomultiplier combination (Nuclear Enterprise NE-142 and Hamamatsu Photonics H1161).

The dynamic behavior of the plasma was monitored by an image converter camera in streak mode. Hard X-rays are also detected using a scintillator-photomultiplier combination at 6.5 m and at 90° with respect to the electrode axis.

§ 3 Experimental Results

3-1 Plasma evolution and soft X-ray emission

Observation was carried out with the tools mentioned above in the radial direction simultaneously. The current sheet reaches the end of the inner electrode, then collapses radially and forms a plasma column. At the maximum compression, the plasma radius was ~1 mm. Then the column was disrupted after a short stable phase (~ 15 ns) as demonstrated in Fig. 1 a).

In most discharge, the phosphor current consisted of two peaks as shown in Fig. 1 b). The first peak coincided to the disruption of the plasma column. The second one corresponded to the hard X-ray signal. The second is ascribed to the hard X-rays which is emitted from the electrode face bombarded by high energy electrons generated at the disruption. The first peak is responsible to the soft X-ray image observed at the plasma disruption as shown in Fig. 1 c). In the Moire Schlieren photograph taken at the disruption as shown in Fig.1 d), It is recognized that the region which emits the soft X-rays is very dense, because the N_2 laser light is interrupted by the Schlieren screen owing to a large gradient of the electron density. The duration of the spot was less than 15 nsec and its diameter was 0.5 ~ 1 mm. In this paper, evaluation of the x-ray intensity was carried out merely for the first one.

3-2 Processing of the soft X-ray image

The phosphor current, the soft X-ray signal and the x-ray image shown in Fig. 1 were taken simultaneously. The spots and the first peak in the phosphor current were

not recognized in the discharge at all without admixing Argon into hydrogen. It is, therefore, considered that the spots are the soft X-rays of Ar K-lines considering the spectral response of the pinhole camera.

After the image processing, we obtain a 3-D display as shown in Fig. 2. The maximum intensity observed in our experiment is 2×10^{13} (photons/(s•mm^2•(mrad)^2• 0.01%BW)), though the intensity showed the shot-to-shot variation of 50 %.

§ 4 Discussion

On the feature of the soft X-ray emission, there are significant difference between discharges with pure hydrogen or deuterium and with admixed impurity of high Z element. When the pure gas was embedded, soft X-rays are emitted at the maximum compression and the disruption by growth of macroscopic instabilities. The emission is recognized from the whole region of pinched plasma for each time. On the other hand, when 6 % of argon was admixed into hydrogen, for example, the soft X-ray which consisted mainly of K-lines was detected only at the disruption of the plasma column.

The effective Z equals two in the 6 % argon admixture, if we assume argon ions are fully stripped. This decreases the Pease-Braginskii current which is the criterion for the radiative collapse and ~1.3 MA for hydrogen, to a half.[6] However, the plasma current is much smaller than the reduced value in this experiment. In this plasma focus facility, generation of the ion-and electron beam were observed. The energy of the ion beam which was typically distributed from 100 to 700 keV with the maximum at ~200 keV in the down stream direction with respect to the discharge current was observed.[7] On the other hand, the electron beam energy was distributed up to nearly 1 MeV with the maximum of 400 keV.[8] The electron beam was directed to the upstream with respect to the discharge current.

In this experiment, it can, therefore, be concluded that the hot spots originate from the beam plasma interaction. There are two spots at both sides of the disrupted region of the plasma column as shown in Fig. 1 d). It is concluded that the spot far

from the electrode face is caused by the interaction between the ion beam and the turbulent plasma, and the nearer one is originated by the interaction with the electron beam. Choi et al ascribed the mechanism to the generation of the hot spots which is a direct result of the interaction of only an electron beam and very small, cold and dense region of plasma.[3]

From observation of transition lines of ArXVI and ArXVII, electron temperature is estimated higher than 3 ~ 5 keV by the calculated result of an electron temperature-ion state relationship.[9]

References

1 U. Cohen, M. Feldman, J. H. Schwartz and J. Underwood, J. Opt. Soc. Am. **58** 843 (1968)

2 V. V. Vikherev, V. V. Ivanov and K. N. Koshelev, Sov. J. Plasma Phys. **8** 688 (1982)

3 P. Choi, A. E. Dangor, C. Deeney and C. D. Challis, Rev. Sci Instrum. **57** 2162 (1986)

4 Y. Takahama, J. Du, T. Yanagidaira and K. Hirano, To be published in Rev. Sci. Instrum.

5 K. Hirano, C. Matsumoto, K. Shimoda and T. Yamamoto, Jpn. J. Appl. Phys. **24** 1518 (1985)

6 J. W. Shearer, Phys. Fluids **19** 1426 (1976)

7 T. Yamamoto, K. Ishii and K. Hirano, Jpn. J. Appl. Phys. **29** 1841 (1990)

8 K. Hirano, K. Asami, M. Shindo and T. Yamamoto, Jpn. J. Appl. Phys. **31** 2903 (1992)

9 M. Arnaud and R. Rothenflug, Astron. Astrophys. Suppl. Ser. **60** 425 (1985)

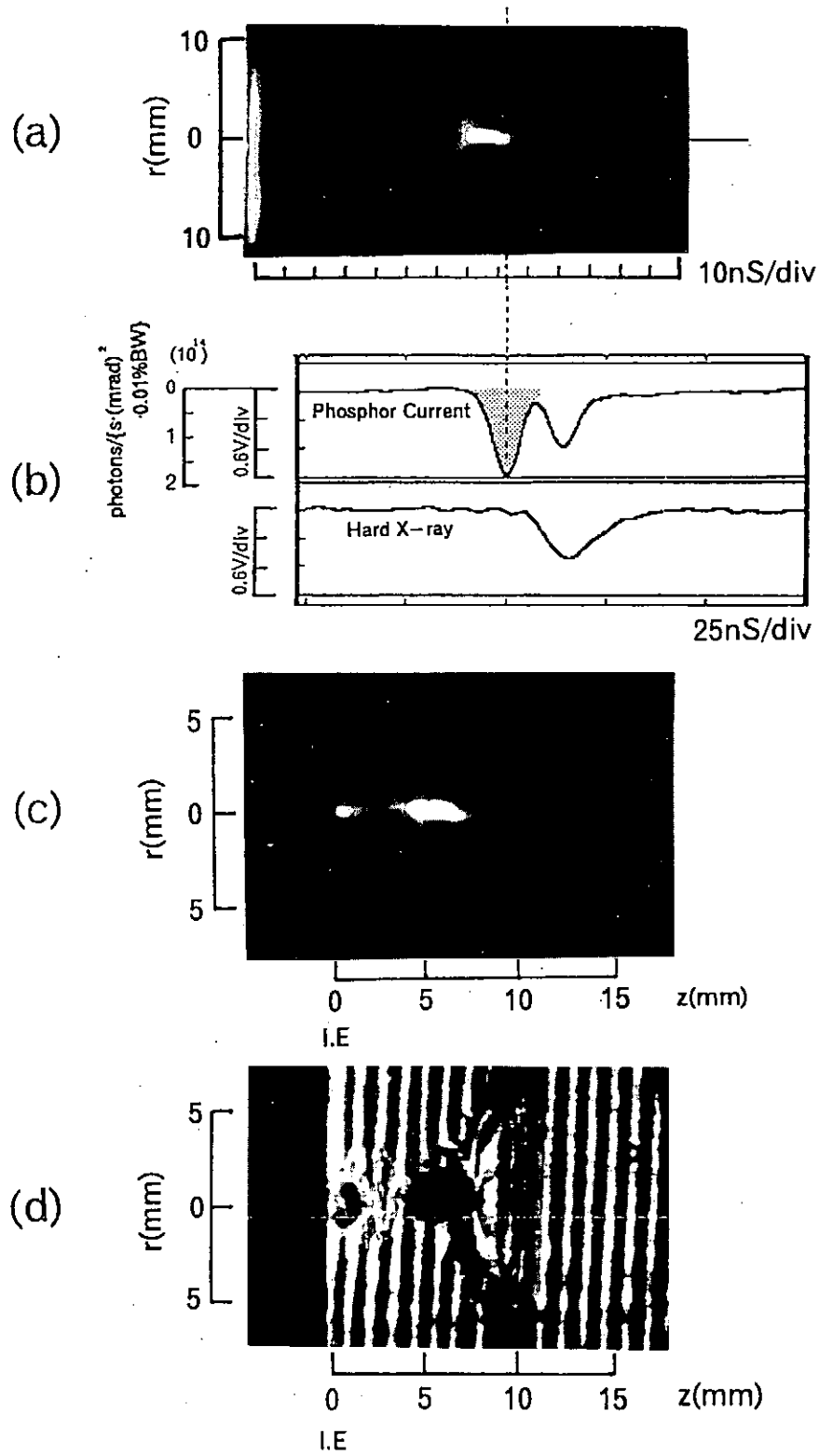

Fig.1 Example of simultaneous observation of hot spots. a); streak photograph, b);phosphor current of the pinhole camera and hard X-ray signal, c);Soft X-ray image by Ar-K lines, d);Moire Schlieren photograph.
I.E: Inner electrode

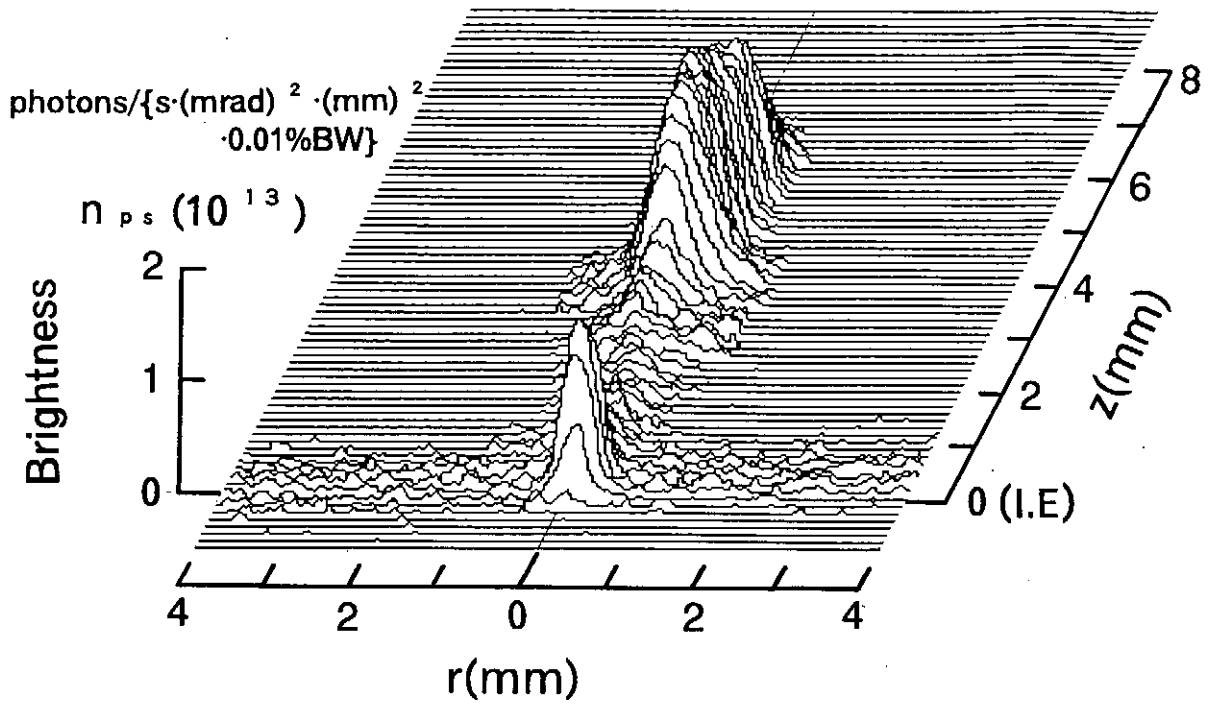

Fig.2 3−D display of soft X−ray image with calibrated intensity.

Observation of a soft x-ray emitting core in a dense plasma focus

A. Yoshida, K. Shimoda, H. Kitaoka and K. Hirano

Department of Electronic Engineering, Gunma University

Kiryu, Gunma 376, Japan

Synopsis

A filamentary core and hot spots with strong soft X-ray emission are observed in a medium size plasma focus facility of working gas of hydrogen with Ar admixture. Macroscopic plasma behavior and the brightness of the soft X-ray source, hot spots in plasma are observed with Moire Schlieren Technique and a filtered pinhole camera. it is recognized that the radium of the filamentary core is in sub-mm range in spite of the radius of the plasma column is several times greater than that of the core. The maximum brightness of the soft X-ray is in$\sim 10^{16}$(photons/(s • mm^2 • mrad^2 • 0.01%BW)).

§ 1. Introduction

The classical z-pinch experiments which were carried out nearly till 1960, showed a rapid growth of macroscopic instabilities such as m = 0 and m = 1 mode. Those experimental results were in agreement with the stability theories at that time which were based on the ideal MHD theory[1] There are much differences between the theory and recent experimental results in which pulsed power generators are used as the power source.

The plasma focus also gives almost same stability with the plasma produced by pulsed power generator. It is considered that the plasma is quasi-stable in these experiments, namely, the containment time of the plasma column is much longer than Alfven transit time through the plasma diameter. Recent experiment in Imperial College in London,[2] Los Alamos[3] and Naval Research Laboratory in Washington[4]

have shown remarkable stability.

In the plasma focus experiment, the plasma is carrying a heavy current at the beginning of the radial collapse already. This means that a rapid rising current is applied the collapsing column at the beginning of the collapse.

One of the most interesting phenomenon in the z-pinch or the plasma focus is generation of micropinches or hot spots. They are small region in the plasma column whose characteristic length is sub mm with several KeV range and have not recognized in the discharge with pure hydrogen or deuterium, but in gases admixed heavy elements into them. Radiation collapse or beam-plasma interaction may be acceptable explanation for the micropinch formation.

The radiation collapse, which is pointed out by Shearer[5] and Vikhrev[6] concerning on the plasma focus at the first, is well known that the plasma column is in a steady state when the current is equal to the Pease-Breginsky current, I_{PB}. This is the current when the Joule heating in the plasma is in balance with it radiation loss which mainly consists of Bremsstralung under assumption that the resistivity is entirely classical. When the discharge current exceeds I_{PB}, the plasma is extremely constricted and the density increases, till the plasma obtains a new steady state. The Bremsstrahlung loss increases with proportional to Z, the charge state of ions, admixture of high Z elements decreases I_{PB}. Therefore, I_{PB} is lower for high Z ions if they are not fully stripped. The radiation collapse is considered to obtain an ultra high energy density plasma for studying not only nuclear fusion but also a source for powerful pulsed soft X-rays.

In this paper, correlation between the dynamical behavior of the plasma and soft X-ray emission is described when Ar is admixed with the embedded hydrogen as a working gas. The results presented here require that near the axis of the pinched column emits fairly strong Ar K lines, in spite of the tens times of the radius observed through the spatial distribution of electrons obtained with the Moire Schlieren method.

§ 2. Apparatus

A Mather type plasma focus device with a squirrel cage outer electrode was employed to produce a high energy density plasma. A schematic diagram if the plasma focus facility and diagnostic tools is shown in Fig. 1. The diameters of coaxial are 50 and 100 mm. The lengths of outer-and inner electrode were 230 and 280 mm, respectively. A quartz insulator extended 100 mm along the inner electrode which was anode. The condenser bank consisted of 28 × 1.56 μ F, 80 kV capacitors. Each capacitor was switched by a pressurized air gap. The device was operated at the bank voltage of 45 kV and a mixed gas (H_2 + 2 % Ar) pressure of 6 Torr. Admixture more than this amount of Ar prevented pinch formation. The total discharge current and the plasma current were measured with a Rogowski coil and a magnetic probe, respectively. The peak discharge current and its ringing frequency are 1.3 MA and 120 kHz. An example of the current is shown in Fig. 2. When the bank is operated at 45 kV, the current in the plasma column was 0.8 MA at its peak approximately.

To observe the region of the plasma column which emits the soft X-rays, a filtered soft X-ray pinhole system was employed. The pinhole, 25 μ m in diameter, was filtered with 25 μ m Be and 1 μ m Ag foils. The pinhole camera accepted mainly the spectra band around 4.0 Å which includes Ar K-line. The spectral response of the pinhole camera is shown in Fig. 3.

The system consisted of a pinhole camera, a microchannel plate-phosphor screen combination, a CCD camera, an image memory board and a personal computer. To make a quantitative measurement of the soft X-ray intensity possible, the image processing and observation of the phosphor screen current are carried out in conjunction. Performance of the system is described in previous paper.[7] The time evolution of the plasma was observed with an image converter camera in streak mode. A part of the light was picked up as an analog signal through an optical fiber and supplied for a monitor signal. A Moire Schlieren method in framing mode was also employed to

obtain the spatial distribution of electrons. The soft X-ray emission was monitored with X-ray sensitive PIN diodes.[8)]

The brightness and the contrast of the Moire Schlieren photograph were subjected to the influence of reproducibility of the N_2 laser light intensity from shot to shot. To avoid the effect we processed the photograph with a method which we developed. Details of the method will be described elsewhere.

§ 3 Experimental results

3-1 Macroscopic behavior of plasma

A typical example of plasma evolution observed simultaneously with the Moire Schlieren method, the image converter camera in streak mode and soft X-ray PIN diode is shown in Fig. 4. In Fig. 4 a), we can recognize that the pinch velocity and the radius at the maximum compression are 5.0×10^7 cm/sec and 0.15 cm, respectively. In a duration of ~10 ns, that is a containment time, the plasma is disrupted, then emits a visible light after ~ 30 ns again. The field of view of the PIN diode includes the face of the inner electrode which might be a source of the characteristic X-rays of electrode material. Obviously, the soft X-ray signal consists of four part shown in Fig. 4 b), and the first and second peak coincide to the those of the visible emission in a) with a good reproducibility.

Figure 4 c) shows Moire Schlieren photographs which were taken at each timing pointed out in b). The Moire Schlieren photographs were chosen and aligned from a number of discharge with almost the same soft X-ray signal. It is recognized that the soft X-ray emission begins before the maximum compression. The first peak corresponds approximately to the maximum compression as seen from Fig. 4 c) ③. The second peak coincides to the time when the plasma column is disrupted in part by the growth of the m = 0 type instabilities in part, after expansion in the plasma radius. At the third peak the plasma column is almost distinguished and so the soft X-rays at

this instant is emitted from the inner electrode face that might be exited by electron beam generated with the disruption. The forth signal ascribed to metal vapor which is vaporized from the electrode by the discharge current. The minimum plasma diameter is greater than 3 mm.

3-2 Soft X-ray images

The filtered pinhole camera used in this experiment, is a time-integrated one. However, it is possible to operate as a time-resolved pinhole camera by measuring the phosphor current which used to form soft X-ray image on the phosphor screen. The current provides the shutter duration and timing if images are not overlapped.

The region emitting the X-rays is completely different from the case in which a pure H_2 or D_2 is employed. When pure H_2 or D_2 is embedded, the soft X-rays are emitted from the whole pinched region depending on the shape of the plasma column, even the plasma is at the maximum compression or in the unstable phase.[9] On the other hand, impurity gas, 2.5% of Ar in this case, is admixed to H_2, there are two categories according to the shapes of the soft X-ray signal. As shown in Fig. 5 a), first is that the one pulse appears in the signal. The second has two pulses. In the former, several soft X-ray emitting spots are spread as shown in Fig. 5 d). The spots coincide to the extremely constricted region caused by the m = 0 instabilities as recognized from Fig. 5 c).

In the latter, the soft X-ray emitting region which is narrow and nearly straight is occasionally observed in the duration of the emission is less than 8 ns. It is noted that the diameter of the plasma column was approximately 3 mm even in this case. The soft X-ray images shown in Figs. 5 d) and 6 c) are processed and calibrated by a method which was developed in our laboratory.[7] The results are displayed in Figs. 5 e) and 6 d). The intensity of the soft X-ray is two order higher than plasma focus facility whose bank energy is about one sixth of the present facility.

The confinement time of the plasma column is measured to be $\sim$10 ns. On the other hand the Alfven velocity in the plasma column is calculated to be 6×10^8 cm/s. Therefore, it is possible that the plasma is in a quash-steady state, because the ratio of the containment time to the Alfven transit time is estimated to be $\sim$0.5 ns. The 2.5 % of Ar admixture makes Z = 1.5 effectively. This decreases the I_{PB} to 2/3, and so required discharge current is 1 MA approximately. Therefore the current in the present experiment is not enough for the radiation collapse. It is, however, no doubt that a fairly intense cylindrical soft X-ray source is obtained in the present experiment.

References

1) J.P.Freidbrg, Rev. Mod. Phy.; 54 (1982) 801

2) I.H.Mitchell, J.M.Bayley, J.P.Chittenden, P.Choi, J.F.Worley, A.E.Dangor and M.G.Haines, Third International Conference on Dense Z-pinches (Imperial College, London, UK, 19-23 April 1993) p.A2

3) J.Hammel and D.W.Scudder, in Proceeding of the Fourteenth European Conference on Controlled Fusion and Plasma Physics(European Physical Society, Petit-Lancy, 1987), Pt.2, p.450

4) J.D.Sethian, A.E.Robson, K.A.Gerber and A.W.DeSilva, Phys. Rev. Lett.; 59 (1987) 892

5) J.W.Shearer: Phys.of Fluids; 19 (1976) 1426

6) V.V.Vikhrev,JETP Lett., 27 (1978) 95

7) Y.Takahama, J. Du, T.Yanagidaira and K.Hrano, to be published in Rev. Sci. Instrum.

8) K.Hirano, C.Matsumoto, K.Shimoda and T.Yamamoto, Jpn. J. Appl. Phys.; 24 (1985) 1518

9) K.Hirano, Y.Tagaya, K.Shimoda Y.Okabe and T.Yamamoto, J. Phys. Soc. Jpn.; 55 (1986) 2215

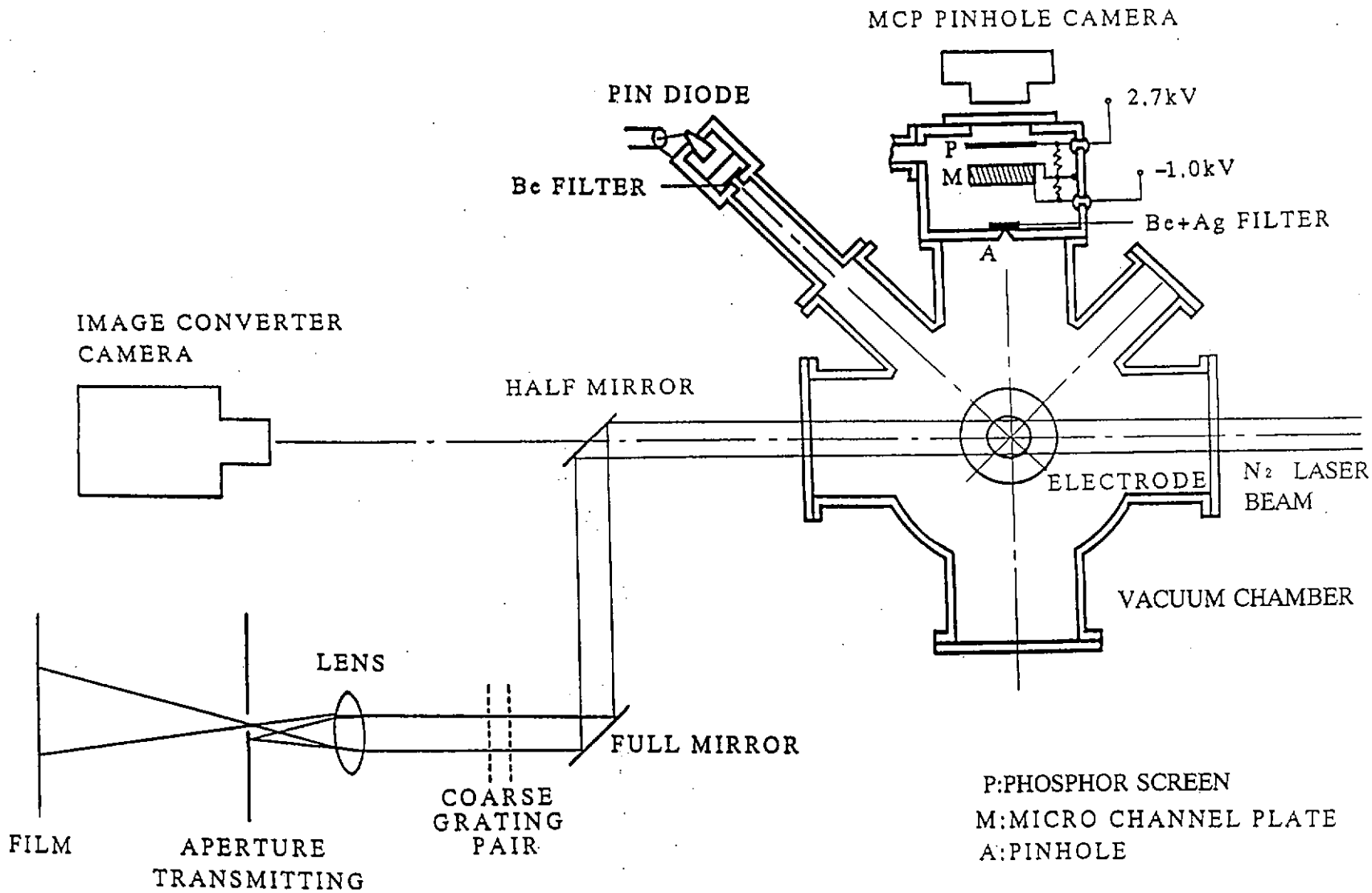

Fig. 1 Plasma focus facility and diagnostic tools

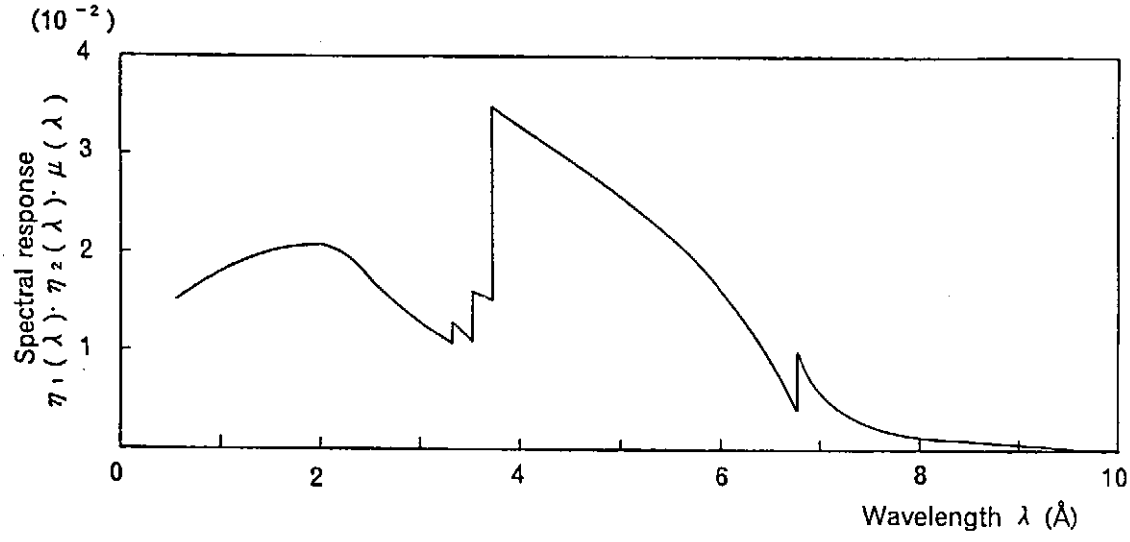

Fig. 2 Spectra response of the pinhole camera

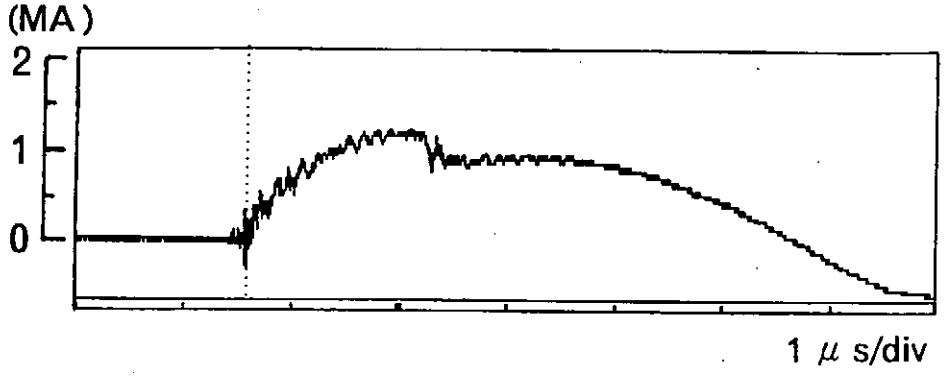

Fig. 3 Dicharge current

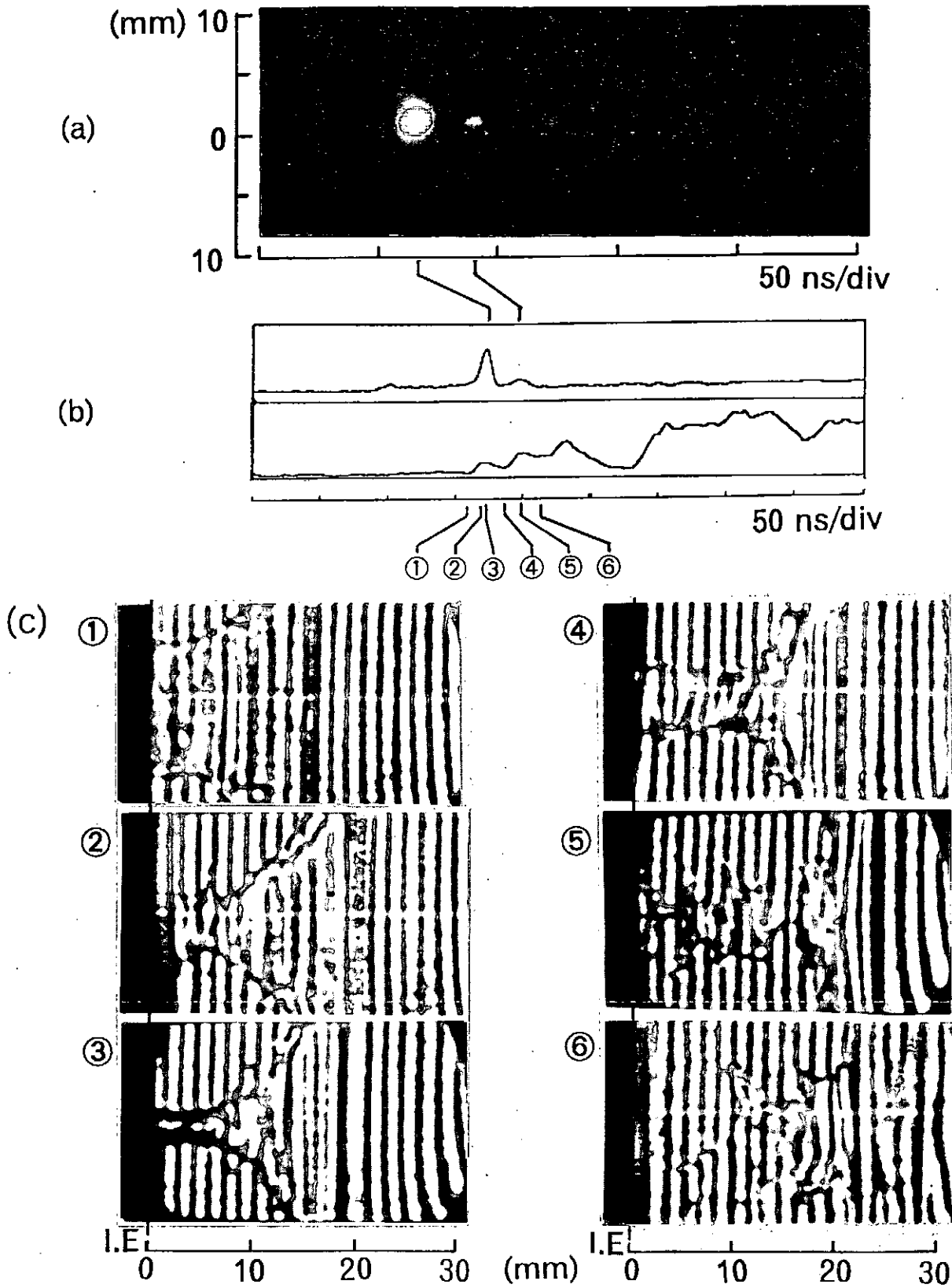

Fig. 4 Macroscopic behavior of the focused plasma
a) Streak photograph
b) Visible light and soft X-ray signal by PIN diodes
c) Moire Schlieren photographs
I.E.: Inner electrode

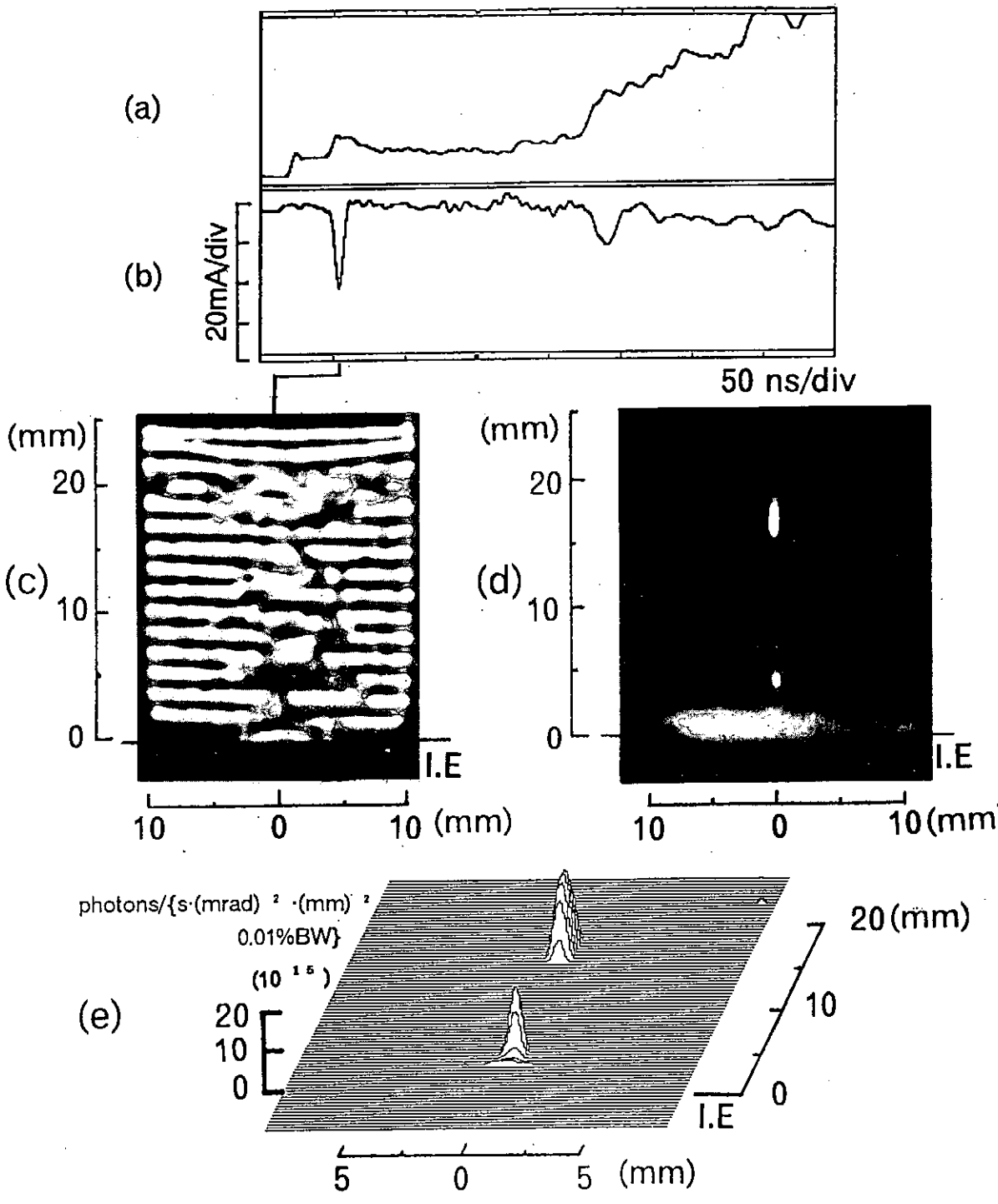

Fig. 5 Correlation between the macroscopic behavior of the plasma and soft X-ray emission

a) Soft X-ray signal b) Phosphor current in the pinhole camera system

c) Moire Schlieren photograph

d) Soft X-ray image taken by the pinhole camera system

e) Spatial distribution of intensity in 3D display

I.E.:Inner electrode

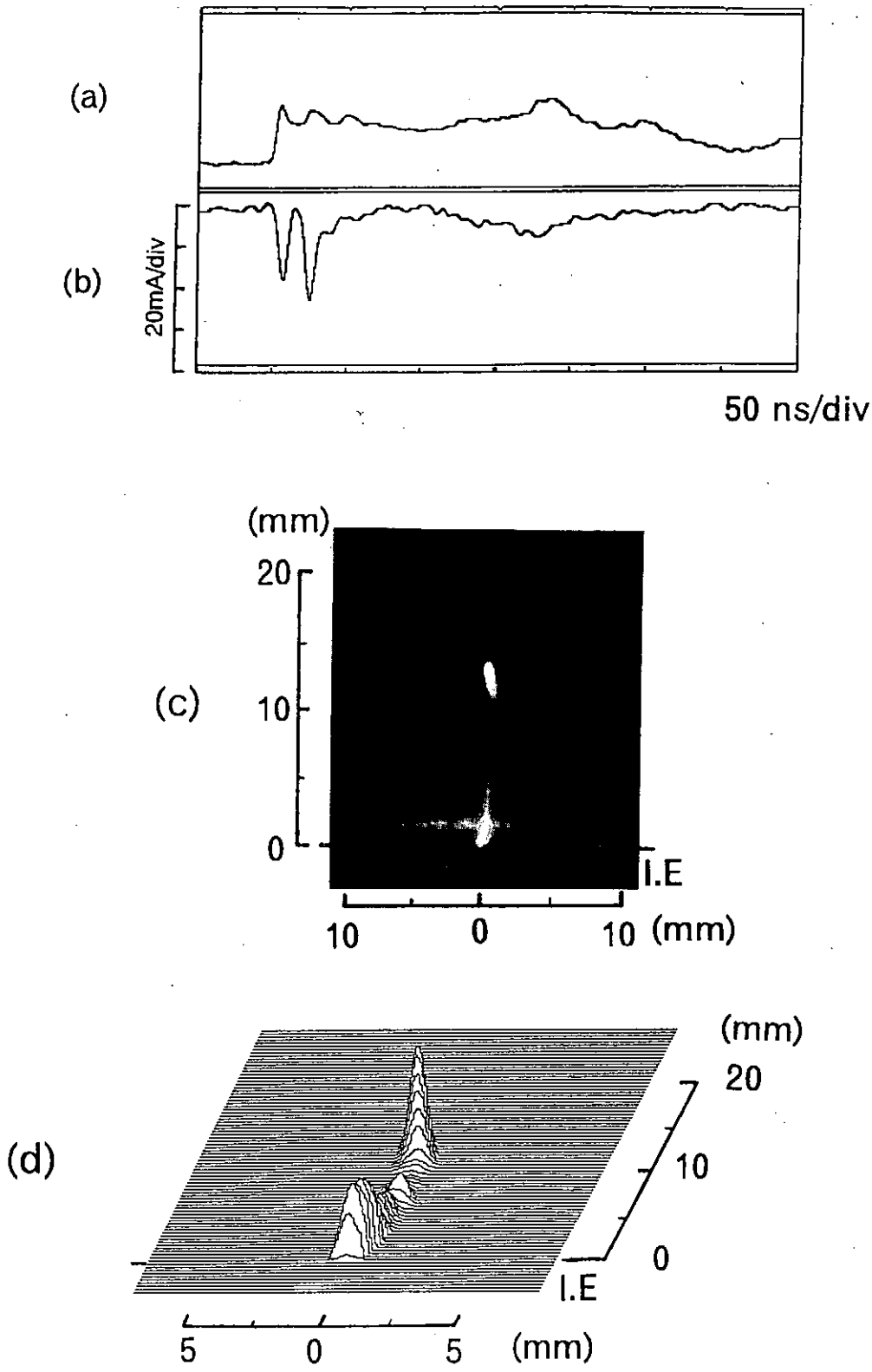

Fig. 6 Soft X-ray image and its 3D display
a) Soft X-ray signal b) Phosphor current in the pinhole camera system
c) Soft X-ray image taken by the pinhole camera system
d) Spatial distribution of soft X-ray intensity in 3D display
I.E.:Inner electrode

THE RESULTS OF THE STUDY OF COMPACT "GAS-PUFF" AND VACUUM SPARK PLASMA SOURCES OF SXR WITH GLASS-CAPILLARY CONVERTERS (GCC)

Alla Shlyaptseva , Victor Kantsyrev , Andrei Inozemtsev and Oleg Petrukhin

Scientific Research Institute of Technical Glass,
29 Krzhizanovsky street , 117218 Moscow, Russia

ABSTRACT

The results are presented dealing with the the working out and study of the SXR compact plasma source of new type . Experimental set up were compact new "gas-puff" source with parameters being better the traditional ones and new type of SXR source - low-inductance vacuum spark (LIVS) with glass-capillary converters (GCC) of SXR. Compact plasma "gas-puff" source had the high value of the $\eta \sim (1\text{-}2) \cdot 10^{-2}$ (conversion coefficient of initial energy supply into SXR) ; a little effective size of emission region and greater resource.

The characteristics of LIVS with GCC were studied . GCC consisting of about several hundreds of glass capillaries allowed to focus SXR, to change the cross section of SXR beams of plasma sources and to change SXR spectrum.

The possibility was shown of using of GCC in plasma diagnostics of powerful plasma devices ; for X-ray microscopy and to study the influence of SXR on the solid state surface.

§ 1. INTRODUCTION

The study and the working out of plasma sources of SXR based on the dense Z-pinches (for example, low-inductance vacuum spark , gas - puff) has besides the pure scientific

purposes the applied meaning [1]. By that the basic problem was to produce the maximal values of energy density E and flux density q of SXR impulse on the surface of pattern emitted. As the source of SXR we choose the low-inductance vacuum spark (LIVS), while this source had high value of the coefficient of conversion of energy flux of the source into SXR η - up to 0.01, the small effective size of emitted region (averaged during the series of impulses d) - few millimeters. This source is a compact one with rather simple construction. One of the directions of development of these sources is the creation of new types of compact sources of "gas-puff" configuration [2]. However, characteristics of all compact plasma source of SXR aren't sufficient good for practical applications. On practice the geometric coefficient of the use of this emission ξ doesn't exceed $\xi = 10^{-3}$. It is necessary to apply non-selective focusing systems for the spectral range λ = 1.0- 1.5 nm., as the plasma sources have wide spectrum. Among the recent X-ray optics of grazing incidence is progressive in this spectral range.

The possibility of transferring and focusing of SXR from laser plasma with glass capillaries were experimentally set in papers[3-5], later glass-capillary converter (GCC) was constructed from few hundreds capillaries [6]. The value $q = 10^5$ Wt/cm^2 (λ <1.2 nm) was reached in spot with 2 mm diameter. However, the density of SXR energy didn't exceed E = (2-3)$\cdot 10^{-3}$ J/cm^2, what didn't differ from the value of E for laser plasma at the distance 3...5 cm without focusing. The better results must be obtained using LIVS [7]. The purpose of our investigations was to work out the new type of SXR source, which posses the better parameters in comparison with traditional LIVS which are needed both for plasma studies and for X-ray micrography and X-ray lithography.

§ 2. EXPERIMENTAL SET UP

The experimental set up consists of new type "gas-puff" plasma source - gas plasma source (GPS) of SXR (Fig.1), low-inductance vacuum spark source (LIVS) of SXR (Fig.2) and X-ray diagnostic complex [8].

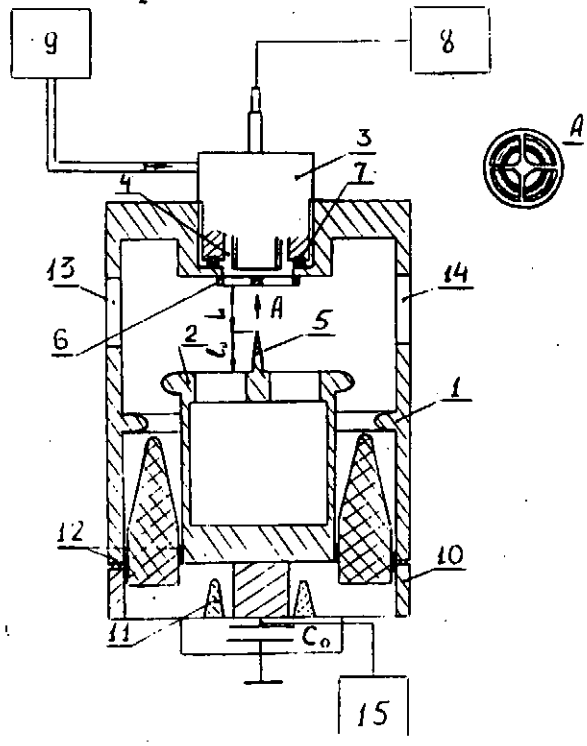

Fig. 1. The scheme of the GPS source .
1. Vacuum chamber ; 2. Anode; 3. Batcher of ionized gas liner; 4. Cycle nozzle; 5.Anode edge ; 6. Cathode ; 7, 12. Vacuum packing ;8. Control block ; 9. Gas block; 10. Conductor; 11. Low-inductance capacity; 13. Diagnostic window;14. Vacuum pumping; 15. Charge block.

GPS presents itself simplified modification of "gas-puff" set up with impulsive gas injection into vacuum chamber of poor ionized gas-like liner. This allowed to get rid of controlled intermediate discharger between anode and basic low-inductance capacity. Anode making as radial grazing was plane or had central edge similar with one in LIVS. The following material were used for anode : Al, Ti, Fe, Cu, Mo and W. Using impulsive batcher supersonic "hollow shape" weak ionized gas jet was created between electrodes which reserved discharge spacing

caused heavy-current discharge and provided formation of plasma rope in GPS. The duration of the injection front of gas-like liner wasn't greater than 50...100 mcsec. The volume of injected gas is equal to few cm^3 . The vacuum was created in GPS chamber by turbomolecular pump. The initial energy supply reaches 2.9-3 kJ at the capacity voltage equal up to 23 kV, an amplitude of discharge current Im=220 kA, discharge half-period - 2.6 mcsec.

LIVS was constructed in scheme using trigger ignition. The initial energy supply was up to 2.5 kJ , maximal discharge current was up to Im=250 kA, discharge half-period - 2 mcs.

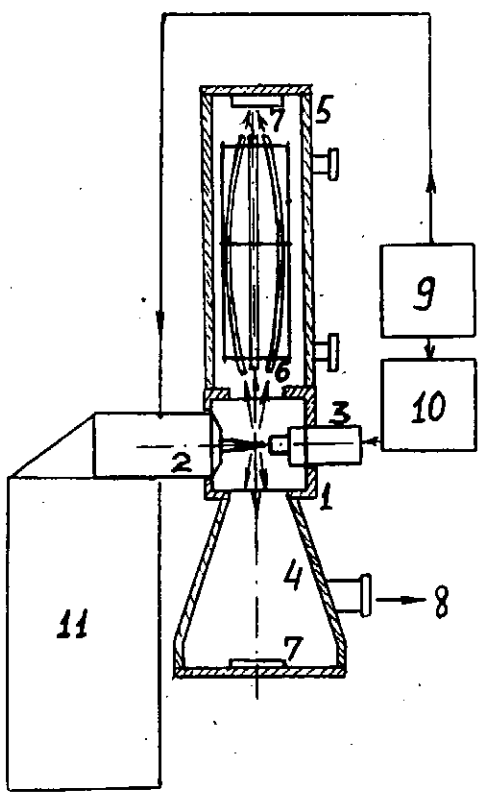

1. Vacuum chamber.
2. Anode.
3. Cathode knot.
4. Camera with diagnostic complex.
5. GCC camera.
6. GCC.
7. Emitted patterns and detectors.
8. Vacuum system.
9, 10. Blocks for control.
11. Low-inductance capacity.
12. Block of GCC protection.

Fig. 2. The scheme of the LIVS source with GCC .

The diagnostic complex includes[8] sensors with absorption filters (from Be, Al or mylar) and X-ray film UF-VR or UF-SHC, thermo-luminescence detectors (TLD), X-ray calorimeters, X-ray pin diodes, three-channel vacuum pinhole camera, two survey spectrographs with convex mica crystal (λ < 1.8 nm), Rogowsky coil or magnetic probe.

§ 3. THE RESULTS OF THE STUDY OF THE PECULIARITIES OF X-RAY EMISSION FROM GPS AND LIVS

During experimental study of the dependencies of γ , and spectra on the electrode geometry, composition and geometry of gas-like liner and the value of maximum discharge current Im the following was established:

1) The value γ decreases from 10^{-4} (for GPS with anode without edge) up to (1-2)$\cdot 10^{-2}$ (for GPS with anode with edge) in spectral range λ < 1.5 nm ;
2) The value d increases from 3-6 mm up to 2-3 mm (in correspondence with (1)) in the same spectral range.

It was observed that at the same time with weak brightness in SXR diffusion region with size of a few mm, two kinds of the small emitting formations (micropinches) were observed: subplasma points with size 500...1000 mcm and plasma points with size less than 200 mcm (lower limit - 30 mcm). By that plasma points were observed only for anode with edge but subplasma ones - in both cases (see Fig.3).The peculiarities on current waveforms were corresponding to plasma points formation were observed in 80-90% discharges.

Spectrum of GPS depended on composition of gas liner, the value of pressure in batcher and the presence of anode edge. Without edge spectrum contains intense spectral lines of multiply-charged ions of linear plasma (for example , He-like Ar) and sometimes weak lines of ions of anode (for example, Ne-like Cu). the presence of the edge caused the appearance of intense lines of anode plasma (see Fig. 4), which could exceed in intensity the lines emitted by gas-like liner.

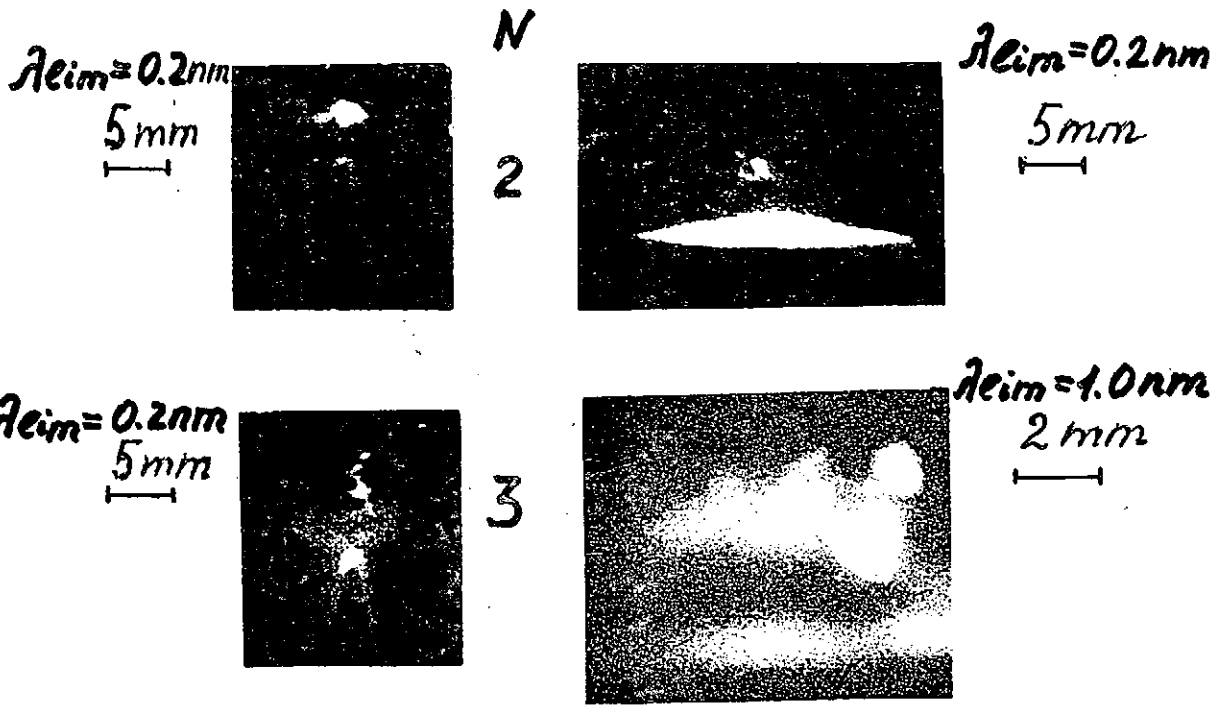

Fig.3. Pinhole photographs of heavy-current discharge in GPS. Anode - Fe, gas - Ar, Im= 200 kA (maximal discharge current); On the right - without central edge, on the left- with central edge. *N - number of impulses for one photo.*

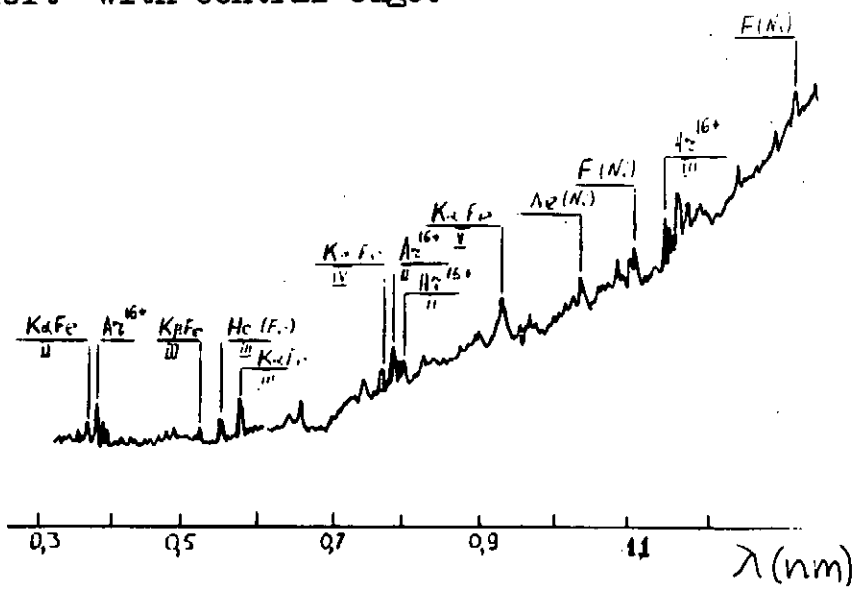

Fig.4. X-ray spectrum of GPS plasma.
Spectrum contains spectral line of gas-like liner plasma (gas - Ar) and spectral lines of plasma of anode material vapor (anode - style , with central edge). Maximal discharge current Im=220 kA.

Maximal intensity of emission was in the spectral range λ = 1.0 - 1.2 nm.

An explanation of phenomenons observed may be caused by the fact that there is mixed regime of micropinching which is realized : by which during the typical discharge there are consistently appeared both subplasmas points in plasma of injected cycle-like liner and the plasma points in plasma of anode material vapor when anode being with edge. This is pointed also on with the fact of weak dependence of η on discharge numbers N > 10000 and therefore on the small wear of anode edge. The later speaks about the improvement characteristics of GPS in comparison with LIVS: for LIVS the number of plasma points and value of η abruptly falls at N > 100 - 200 .

The striking peak dependence of η on Za for LIVS was experimentally observed[8] in the spectral SXR range λ < 1.5 nm (Fig.5) . The similar dependence η (Za) was observed for laser plasma [9-10]. As Te increases the peaks move to great Za.

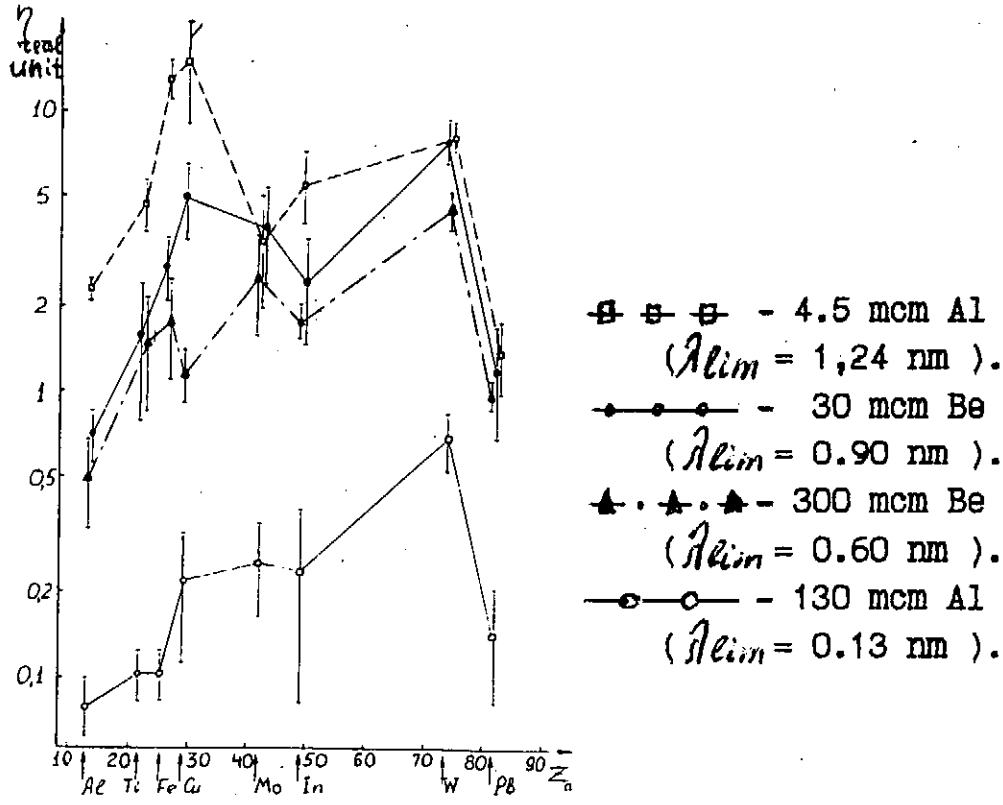

Fig. 5. The dependence of η (Za) for LIVS [8].

The analysis of spectra of multiply-charged ions (Fig. 6) and imagines of discharge spacing made using pin-hole camera has shown that the basic contribution into formation of dependence η (Za) and the total intensity of SXR was caused by linear radiation of multiply-charged ions of plasma points. The mechanism of formation of dependence η (Za) was analyzed in paper [9] and it is the same for all plasma sources.

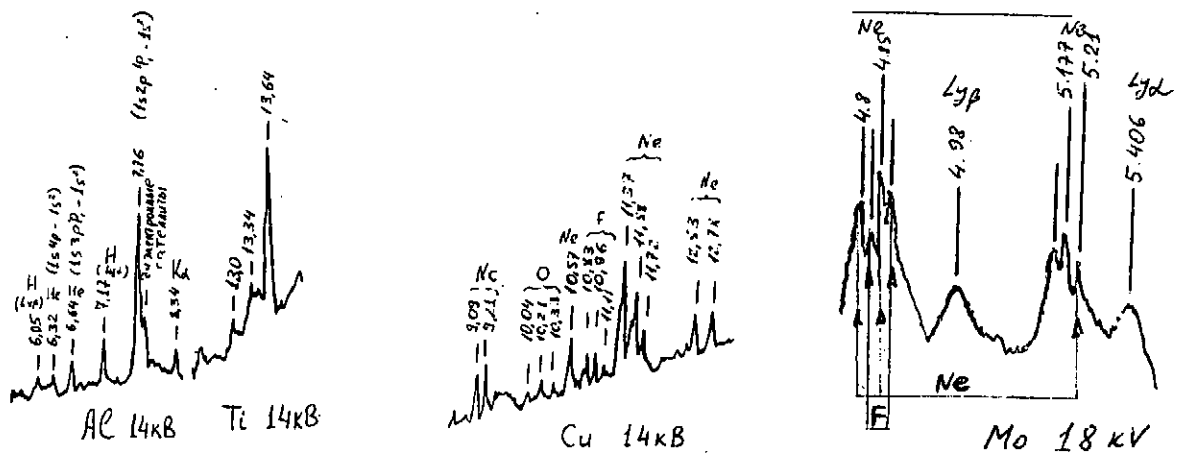

Fig. 6. X-ray spectra of multiply-charged ions of LIVS. The spectra of LIVS contain the lines of multiply-charged ions with nuclear charge up to Z_a=74 (W XXXXIY) and ionization potential up to 8 keV (Fe XXIV). The maximal value of η = 0.01, maximum number of plasma points in discharge (up to 4-5) and minimal size d (0.5 - 1.5 mm) were reached at the value of current Im = 150-230 kA and spacing between electrodes L=6-8 mm (for anodes from Fe and W) [11]. The most informative X-ray spectra were obtained using anode made from Mo. Using survey spectrograph we obtained X-ray spectrum emitted by Mo ions in spectral region beginning from 4.4 Å up to 5.4 Å containing more than 10 lines of X-ray multiply-charged ions. They belong to Ne-like ion (Mo XXXIII) and F-like ion (Mo XXXIV). Then using another focusing spectrograph we recorded narrow spectral region 4.8 - 5.2Å with improved brightness what allowed to resolve more number of lines.

§ 4. GLASS-CAPILLARY CONVERTER (GCC) AND NEW TYPE OF SXR SOURCE .

In the present paper we constructed GCC on the basis of GCC made in paper [6]. It consists from 450 glass capillaries with inner diameter - 400 mcm, outer diameter - 600 mcm, length - 500 mm (Figs. 2,7,8). In GCC the total reflection of SXR from the inner capillary walls by the grazing incidence of radiation. The focus of GCC was equal to 60 mm. The diameter of the smallest focusing spot was equal to 1.2 mm. On Fig.9 it is shown in what way SXR is transmitting along capillary.

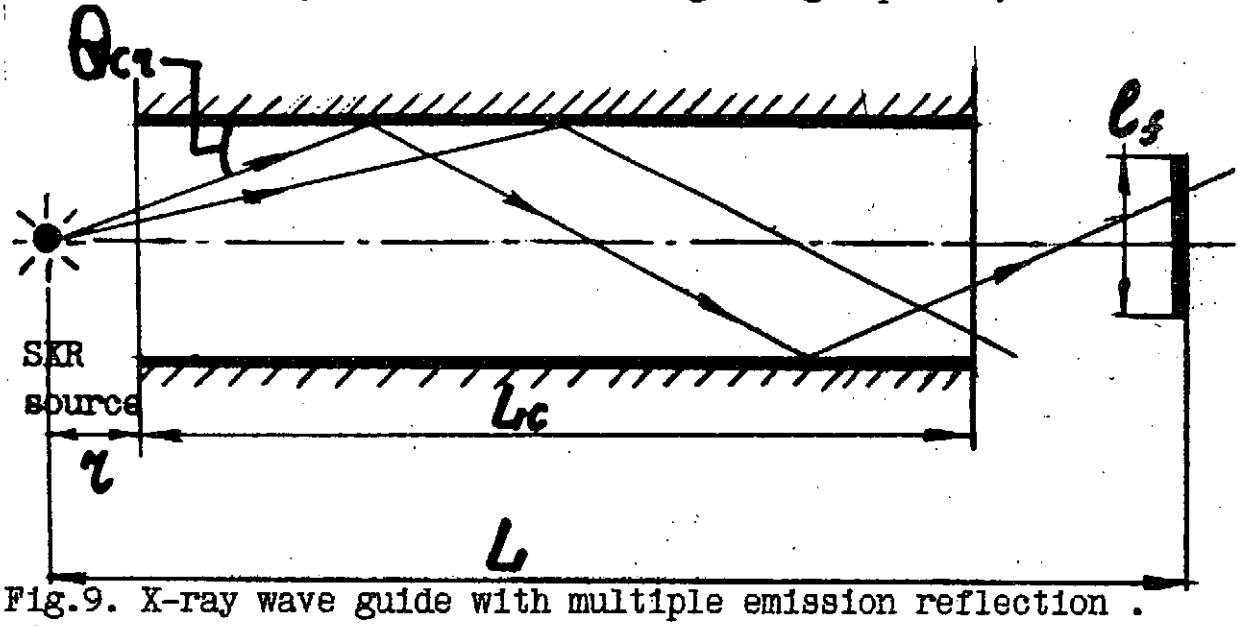

Fig.9. X-ray wave guide with multiple emission reflection . λ_{cr} - critical wavelength of SXR ; θ_{cr} - critical glancing angle.

The scheme of the one among first experiments dealing with focusing of laser plasma SXR is shown on Fig.10. The dependence of spectral transmission of single glass capillary is shown for various X-ray filters on Fig.11. It appears in our experiments to be possible to use GCC only in the spectral range 0.67 - 1.5 nm where protecting filters existed (Be-foils and mylar films). Using such filters the device was constructed for protection of entrance window of GCC. Than the combination of improved LIVS and GCC was achieved: the spectral transmission range of GCC corresponds to the maximum of spectral intensity of LIVS with Fe anode (coinciding to the maximum of η(Za) ; d is close to diameter of focusing spot of GCC.

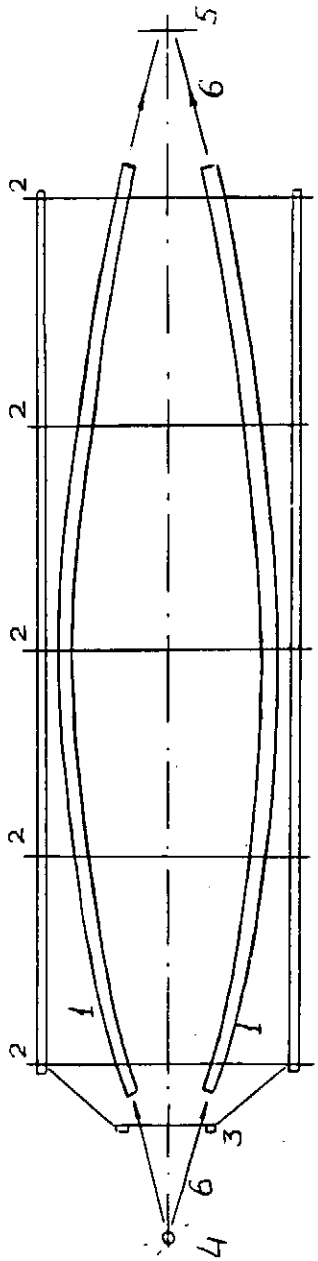

1. Glass capillary.
2. Supporting perforated membranes and bearing bars.
3. protective block.

Fig.7. Block scheme of GCC.

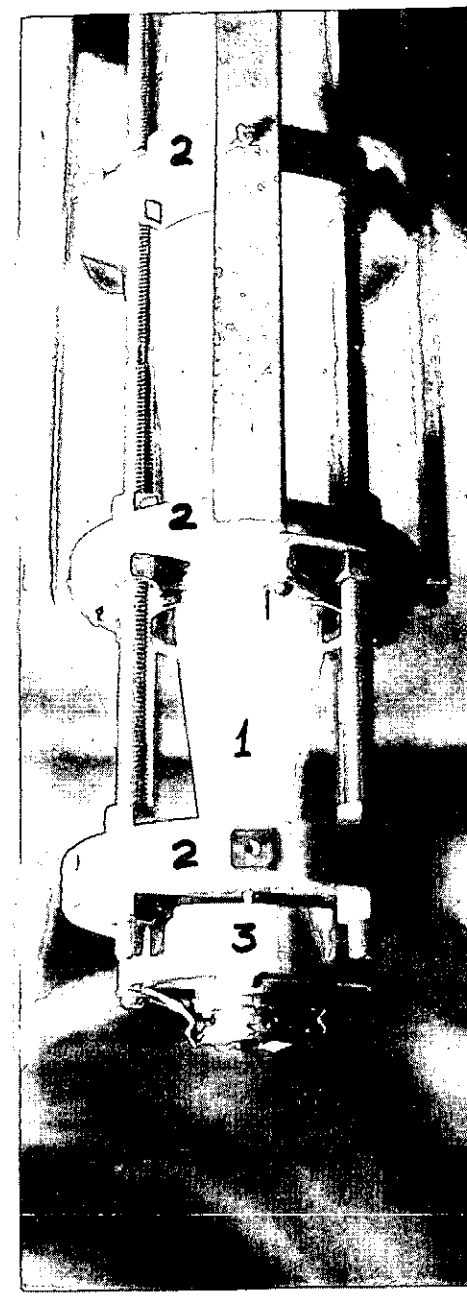

4. Hot plasma.
5. Detector of irradiated pattern.
6. SXR

Fig.8. The outside diameter of GCC.

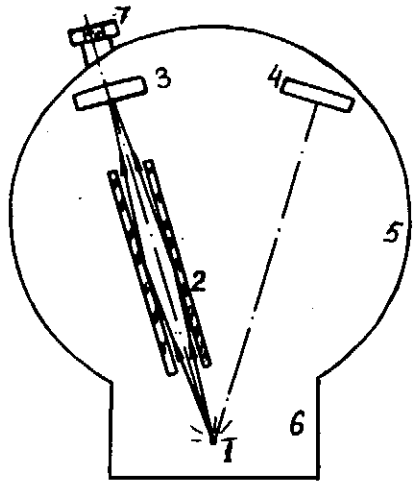

1. Laser plasma
2. Glass tube
3. Base cassette
4. Control cassette
5. Upper chamber
6. Lower chamber
7. Positioning window

Fig. 10. The scheme of the one among first experiments with focusing of SXR using a single glass capillary [4)]

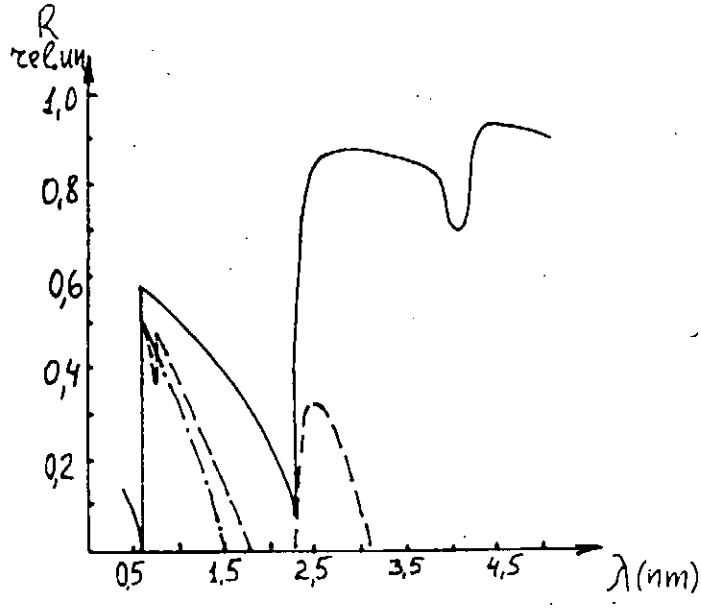

Fig. 11. The spectral transmission of GCC :
without filters (————)
and with protective filters :
from 1 mcm mylar (— — — —)
from 15 mcm Be (—·—·—·—).

5. EXPERIMENTAL RESULTS OF THE STUDY OF NEW COMPACT SOURCE OF SXR AND IT'S APPLICATIONS

The size of focusing spot was dependent on the spectral region of registration[7] (at λ lim= 0.9 nm up to 1.3 mm) (Fig.12).. The value of E , measured by TLD , varied from 15...30 up to 0.3 mJ/cm^2.The value of the coefficient of concentration - K (the ratio of energy density E in focusing spot to E at the same distance from plasma without focusing) reached to K=30 (Fig.13). The measuring of SXR impulse duration allowed to estimate the value of $q=10^6$ Wt/cm^2 [7] in comparison with 10^5 Wt/cm^2 in paper [6]. This coincides with estimations of calculations of radiation loading on the mylar film with width equal to 3 mcm which caused it's partial melting in focusing spot what was really observed in experiment. The values q and E obtained in the present paper are typical for experiments with synchrotrone sources.

The studied source of SXR was used in high- resolution biological microscopy of non-colored histological shears of liver and lung fabric with registration of the images on the X-ray film (Fig.14) or on the X-ray resist. The image resolution was achieved equal to 0.2 mcm.

The new source of SXR was also used in radiative physics of dielectric and semiconductors surfaces. At doze of SXR greater than 0.1...0.2 J/cm^2 it was observed the effects of the changing of coloring of electrochromic alkaline tungsten and niobium phosphate glasses and the changing of stecheometry of surface layers of chalcogenide glass-like semiconductors. The effects found could be used in technology of microcircuit and integral-optical circuits production. About the progress in GCC development: the flexibility of the glass-capillary focus system form gives an opportunity to concentrate SXR from not only point SXR sources but from ones with extended emitted region (for example, gas-puff). It is possible to change the form of cross-section of SXR beam. In the last case the system works as glass-capillary converter which can be applied for investigating of temporal behavior of space distribution of SXR of plasma. Such device is shown on Fig.15 .

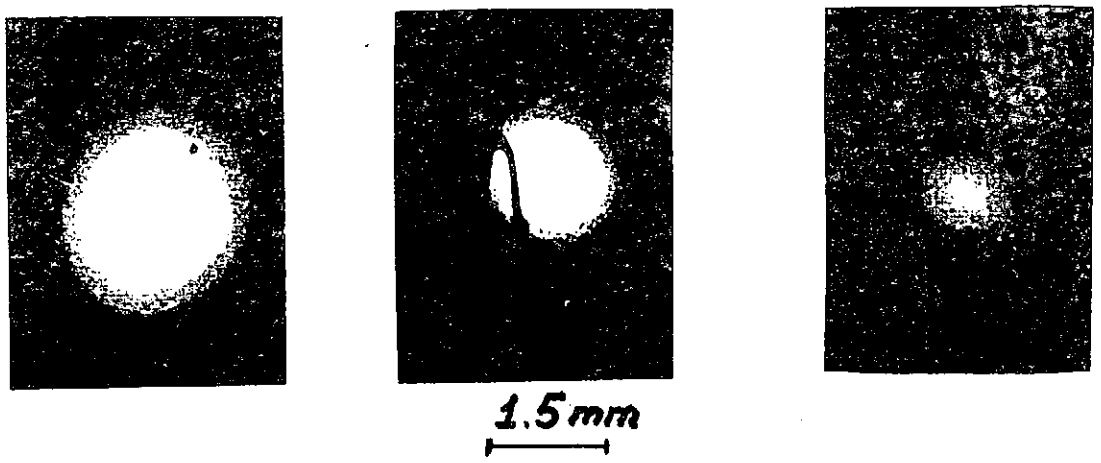

Fig. 12. Pictures of focusing spot of LIVS SXR for various value of λ_{eim} :
a) λ_{eim} = 0.9 nm ; b) λ_{eim} = 0.65 nm ; c) λ_{eim} = 0.53 nm
b) Picture was made through metal wire with thickness 100 mm.

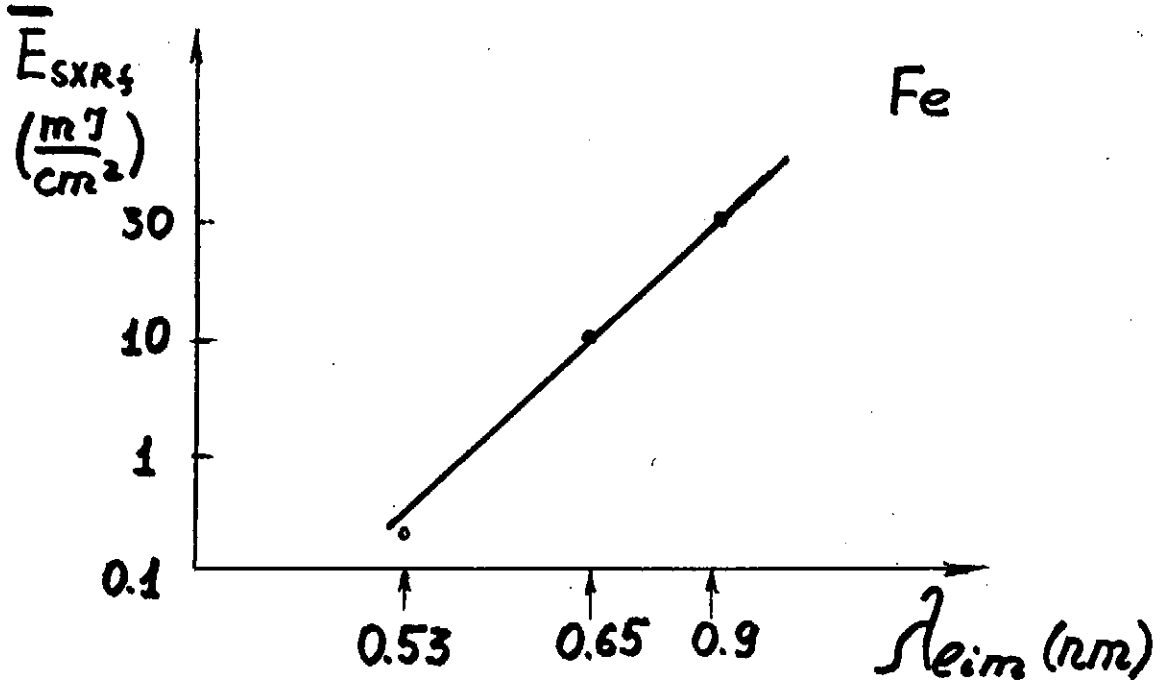

Fig. 13. Dependence of averaged energy density in impulse in focusing spot (E_{SXRf}) on wavelength cutted by filter λ_{eim}.

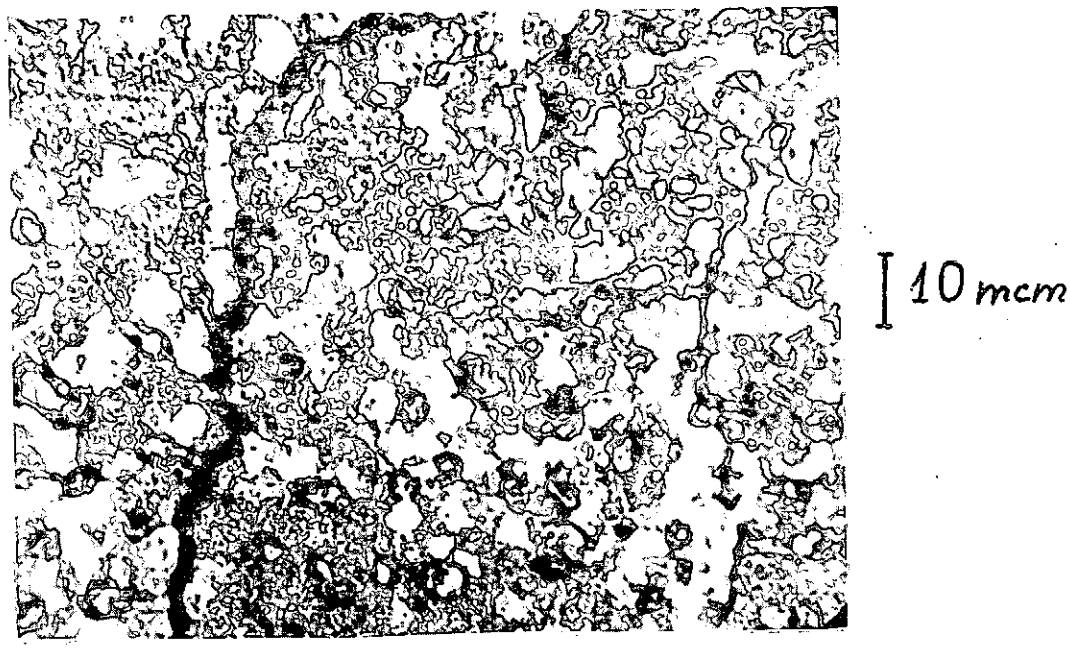

Fig.14 . Microroentgenograms made on X-ray films of non colored shears of liver . The thickness of the shear - 5-7 mcm; exposure - 1 *LIVS* shot.

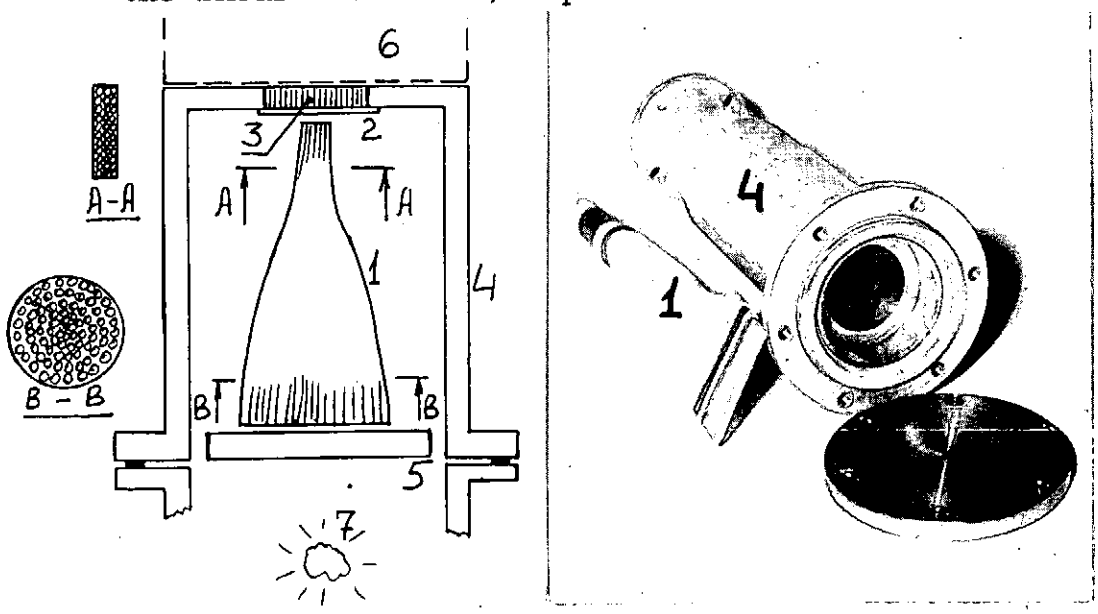

1. GCC.
2. Scintillator layer.
3. Fiber-optical disk.
4. Vacuum shell.
5. Protective block.
6. Image converter.
7. Plasma .

Fig.15 . The block scheme of transforming module made on the basis of small GCC.

The results of experiments of use GCC for powerful device

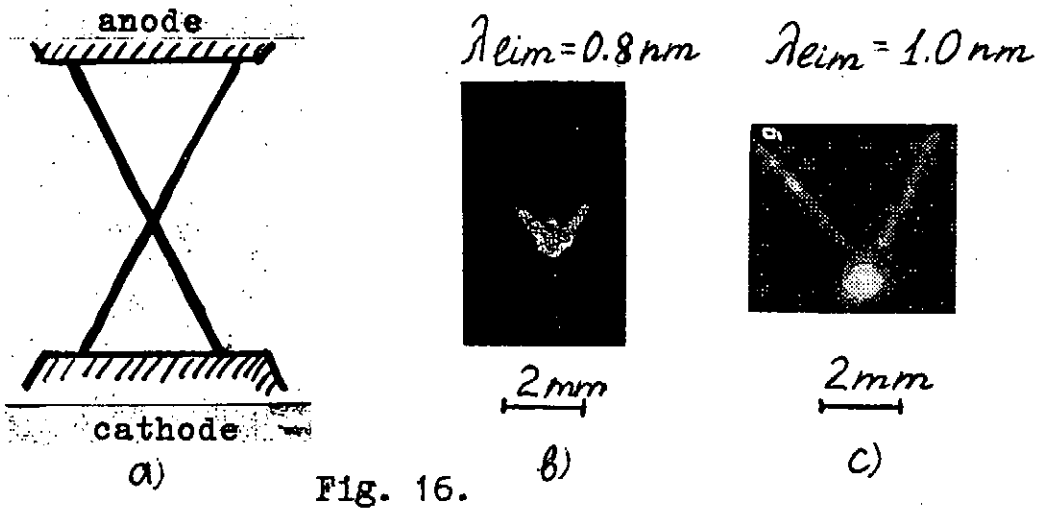

Fig. 16.

a) Scheme of wire anode from Pd-wire with thickness 20 mcm ;
b) Vacuum-pinhole photo of emitting region of discharge ;
c) Image in GCC focus.

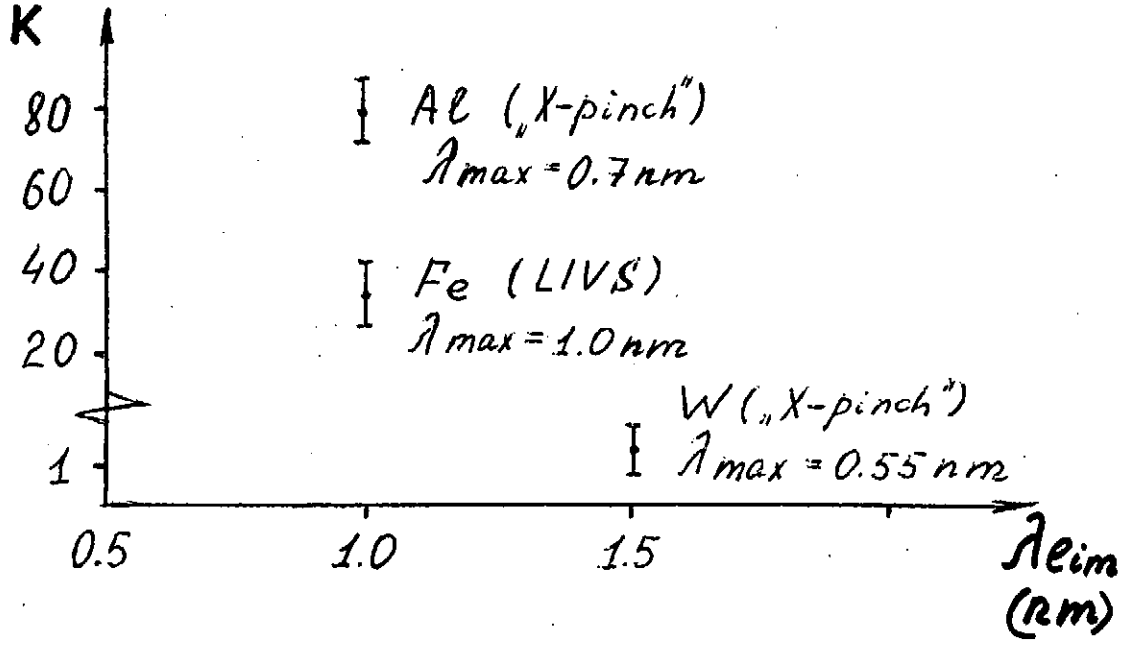

Fig.17. Dependence of the concentration coefficient K on value of wavelength cutted off by filters.
$K = E_{sxrf} / E_{sxr}$; E_{sxrf} - energy density in impulse in focusing spot , E_{sxrf} - energy density in impulse without focusing at the same distance;
λ_{max} - wavelength which corresponds to the maximum spectral distribution of the source..

It transforms SXR in visible emission at the entrance window of IC (image converter) and has the changing cross section.

In our work focusing GCC was used for study of emitting region structure of powerful Z-pinch source of X-pinch type[12] (Fig.16) from Physical Lebedev Institute. Energy on the wire X-loading (from Al, Cu, Pd, W) was up to 3 kJ, voltage was U < 300 kV, Imax= 250 kA, $\tau_{1/2}$~100 nsec. It was shown (Fig.17) that the value of concentration coefficient K can achieve 80 (when maximum of spectral distribution of source intensity and GCC transmission are at the same time).GCC worked as X-ray lens transmitting an image in the scale 1 : 1. On Fig.16 an image of X-pinch from Pd was observed with use of general pinhole camera and in focus of GCC. The presence of some details are observed on the images behind GCC which weren't seen on the traditional pinhole pictures.

The very important peculiarity of GCC for high-temperature plasma diagnostics is that GCC could work as filter of hard X-ray emission (λ < 0.1 - 0.01 A) and decreased it in 100 - 1000 times.

In our work some properties of simple GCC (without concentration of SXR) called by us as "rope" type GCC. These are GCC in the form of capillaries packet with changing cross section (Fig.15) and the "rope" type GCC with cycle cross section. The deflection of the "rope" type GCC is assumed over the angle up to 45-90 from axis, inner diameter is greater 40-50 mcm, outer diameter is greater 80-100 mcm, length is up to 1 - 1.5 m. The "rope" type GCC were studied with use of our compact plasma source - LIVS (Fig.2). It was founded that the number of x-ray quanta (during single LIVS shot) in spectral range λ < 0.7 nm at the GCC exit is sufficient for registration onto the special X-ray film of UF-VR and UF-SHC type that is the film luminescence is > 10^7 Q/cm^2. The divergency of SXR behind GCC was 5 10^{-2} Rad by the working with LIVS at the distance from GCC exit window ~ 120 mm.

Such characteristics allowed us to apply simple GCC of the "rope" type in plasma diagnostics for study plasma source

emitting region structure as the filter cutting off hard X-ray; for study temporal structure of SXR impulse . for example it can be used as cheep single-used filter for SXR sensors and spectrographs protecting them from destructive plasma action and hard X-ray in experiments with powerful plasma devices.

REFERENCES

1. N.G.Basov, Yu.A.Bykovsky, A.V.Vinogradov, V.L.Kantsyrev, Poverkhn. Fiz., Khim. Mekn., No 9, 5 (1985)
2. V.L.Kantsyrev, A.A.Kologrivov, K.I.Kopytok, A.S.Shlyaptseva. Proceedings of the Twelfth International Conference on Coherent and Nonlinear Optics (Kino' 91), Leningrad, (September 24-27, 1991, vol.1, 103-104.
3. P.J.Mallozzi et all, J.Appl.Phys.,45, 1891 (1974).
4 O.B.Ananyin, Yu.A.Bykovsky, V.L.Kantsyrev, Yu.P.Kozyrev. "Invertors certificate No 520863 ,October 15, 1974" Byull.Izobret.SSSR, N 11 , 229 (1979)
5 Yu.A.Bykovsky, V.L.Kantsyrev,Yu.P.Kozyrev. Reports of XIY Intern.Congress of Hih speed Photography, and photonic . Moskow, 630-635 (1980).
6. O.B.Ananyin, Yu.A.Bykovsky, A.A.Zhuravlev, V.A.Znamenskii, V.L.Kantsyrev, S.P.Frolov. Sov.Techn.Phys.Lett.,16,55 (1990).
7. O.B.Ananyin, Yu.A.Bykovsky, V.L.Kantsyrev, A.A.Kologrivov, K.I.Kopytok, A.S.Shlyaptseva, M.Ya.Yakovlev. Sov.Techn.Phys.Lett.,18, 331 (1992).
8. A.K.Zhverkov, V.L.Kantsyrev,A.A.Krivtsov, A.S.Shlyaptseva. J.Techn.Phys.,56, 975 (1987).(In Russian)
9. O.B.Ananyin, Yu.A.Bykovsky, V.L.Kantsyrev, Yu.P.Kozyrev, A.M.Raspopin. J.Quant.Elect.,4, 965 (1977).(In Russian)
10. Yu.A.Bykovsky, V.L.Kantsyrev,Yu.P.Kozyrev. J.Quant.Elect., 6, 414 (1979).(In Russian)
11. A.K.Zhverkov, V.L.Kantsyrev,A.A.Krivtsov, A.S.Shlyaptseva. Sov.J.Plasma Phys., 13 , 480 (1987).
12. V.L.Kantsyrev, N.L.Mingaliev, O.G.Petrukhin, S.A.Pikuz, V.M.Romanova, T.A.Shelkovenko, A.S.Shlyaptseva, A.Ya.Faenov. Sov.Techn.Phys.Lett., 19 ,42 (1993).

Common Understandings of Phenomena in Z-pinches

Keiichi Takasugi, Hideaki Suzuki,*

Kinya Moriyama† and Tetsu Miyamoto

Atomic Energy Research Institute, Nihon University

†College of Science and Technology, Nihon University

ABSTRACT

Common problems which are observed in gas-puff z-pinch experiments are discussed. The crowbar of plasma current is observed in z-pinches which automatically occurs due to shortcircuiting near the power feed. The emissivity of x-ray increases with Z of the operating gas. The higher the Z of the gas, the larger the input energy during the contraction.

I. INTRODUCTION

Contemporally z-pinches are characterized by the gas-puffing[1] and the use of pulsed power source[2]. Separation of plasma from the chamber wall provides less impurity invasion and easiness of its handling. And the use of pulsed power technology suppresses growth of instabilities and enables the efficient power injection.

Applications of z-pinch plasmas have been suggested for realization of thermo-nuclear fusion, intense x-ray and particle

* Present address : Mie Works, Fujitsu Limited.

source, generation of high magnetic field and electric devices. Among those applications the z-pinch is especially an efficient power converter into soft x-ray range of radiation.[3] Useful applications as x-ray sources are x-ray laser and x-ray microscope. A contact soft x-ray radiography has been demonstrated.[4]

Here some common observations which occur in z-pinches are presented. They contain important problems in view of the z-pinch application.

II. SNOWPLOW CALCULATION

The contraction process of the z-pinch plasma is well described by a simple one dimensional snowplow equation.

$$\frac{d}{dt}\left(M\frac{dr}{dt}\right) = -\frac{\mu_0 I^2}{4\pi r} \qquad (1)$$

where M is the mass collected, r is the plasma radius and I is the total plasma current. For simplicity the current I is set to constant. The characteristic time of the radial motion is

$$t_0 = \left(\frac{4\pi M_0}{\mu_0}\right)^{1/2}\frac{r_0}{I} \qquad (2)$$

where M_0 is the total mass and r_0 is the initial radius. Two extreme cases are compared, i) uniform gas distribution until the gas-puff radius and ii) initially fully ionized hollow plasma at the gas-puff radius. The pinch times t_p for both cases are calculated as i) $0.931t_0$ and ii) $1.253t_0$. The radial motions of these cases are shown in Fig.1. The gas-filled pinch shrinks at almost constant velocity at first. On the other hand the hollow pinch increases its velocity, then it surpasses the gas-

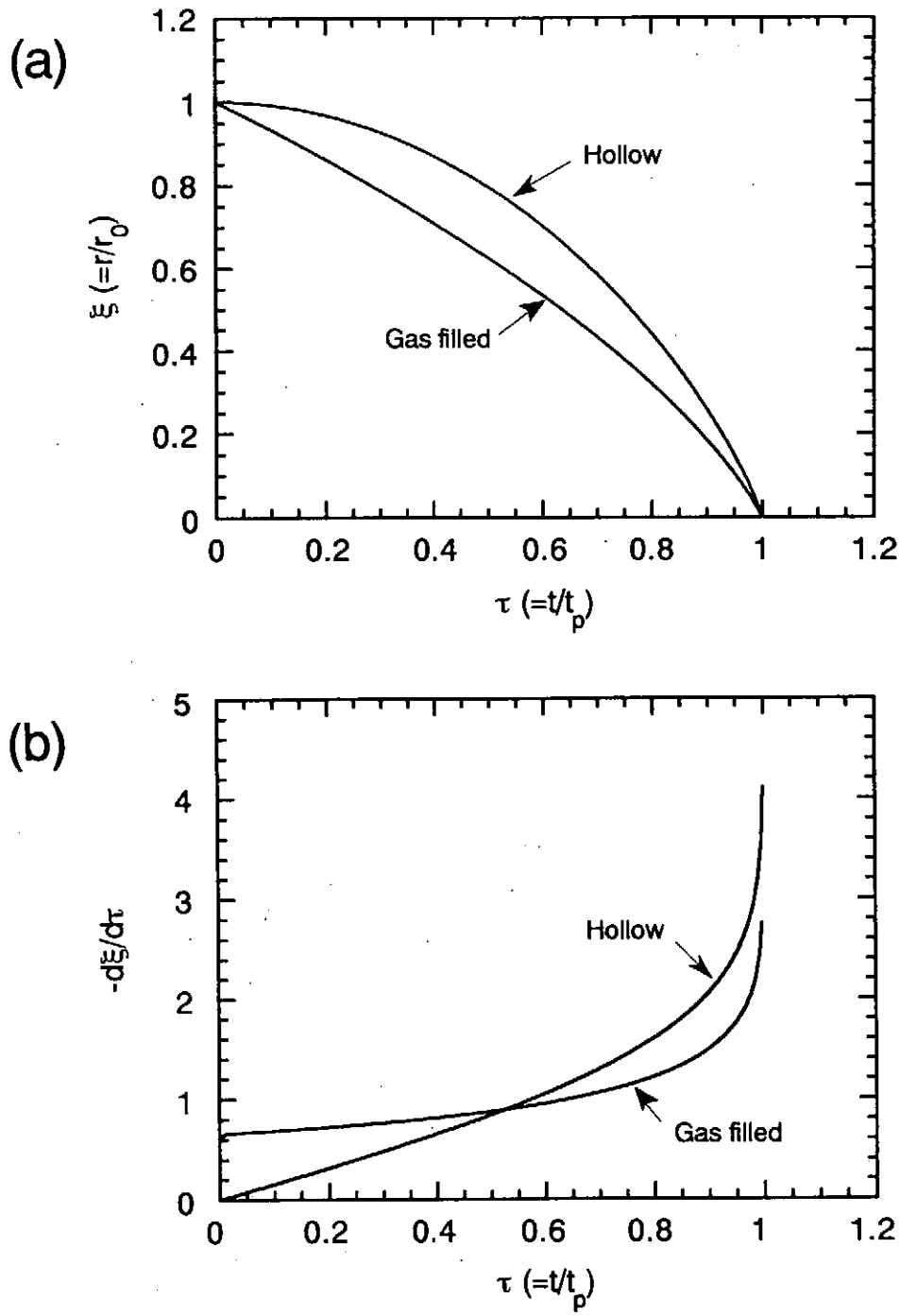

Fig. 1. (a) The radial motions of the gas-filled z-pinch and the hollow gas-puff z-pinch. (b) The radial velocities of them.

filled one and finally collapses stronger than that. In order to obtain higher final speed for a fixed final radius, the hollow gas-puff pinch is better than the gas-filled one.

III. Operating Region

The operating region of a gas-puff z-pinch is divided into three regions depending on the time of discharge t_d from the gas-puffing. Figure 2 shows the anode and the cathode currents of SHOTGUN z-pinch[5] measured at the maximum pinch (when x-ray signal peaked). In the region I the amount of gas is not enough to start discharge smoothly. This is vacuum-like discharge. The discharge itself is unstable and it delays randomly from the applied voltage pulse. The region II is normal z-pinch discharge between two electrodes. Both currents are almost the same at the maximum pinch. The pinch occurs within the increasing current accompanied by strong x-ray emission. After the maximum pinch current or maybe the zero-crossing voltage the crowbar occurs near the power feed. It is due to inductive energy storage into the plasma region. In the region III two currents are separated before the maximum pinch. This means that the crowbar occurs near the power feed before the pinch formation. This is the region of plasma focus-like discharge.

In the pulsed power z-pinch LIMAY-I a similar phenomenon was observed.[6] However the operating regions were complicated; (a) internal self-crowbar after the maximum pinch, (b) self-crowbar after the voltage pulse and (c) self-crowbar at the onset of the voltage pulse. The plasma in the region (a) may have a structure like spheromak. In the region (b) x-ray

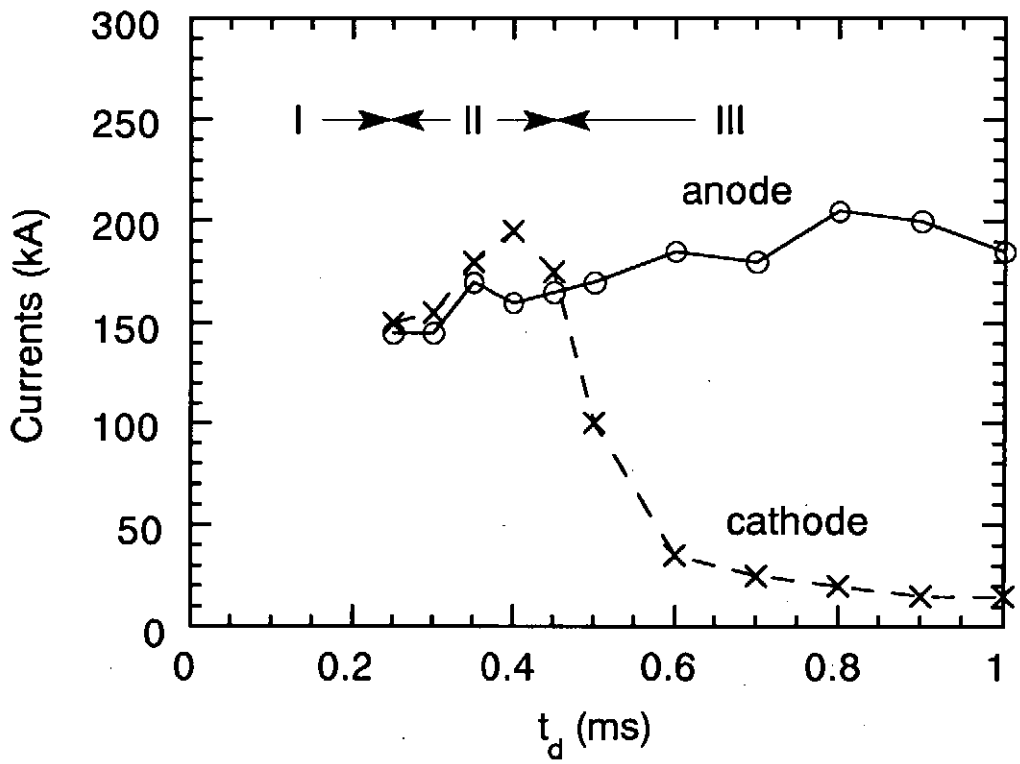

Fig. 2. Three operating regions of the SHOTGUN z-pinch are represented by the time of discharge t_d from the gas-puff detection.

emission followed by the maximum pinch was observed.[7]

IV. X-RAY EMISSION

Figure 3 shows x-ray photographs of Ne, Ar, Kr and Xe gas-puff z-pinch plasmas taken with four kinds of absorbing filters simultaneously. In the Ne pinch the x-ray image is seen in left two frames. It is seen in three frames in the Ar pinch, and it is seen in the right end frame in the Kr pinch. The hardest x-ray image becomes intense in the Xe pinch.

The x-ray emission intensities were compared in Fig.4 with two kinds of Al filters for Ne, Ar and Kr z-pinches. The data shows the effective radiation temperatures of the three z-pinches do not change so much, but the intensities apparently increase with Z of the operating gas.

V. POWER INPUT INTO Z-PINCH

A simple series circuit equation with a capacitance C, registance R and inductance L is shown as

$$\frac{d}{dt}(LI) + RI + \frac{1}{C}\int I dt \qquad (3)$$

Here I is the current through the circuit. The inductance L is composed of the external and the plasma inductances, and there is no mutual inductance between them. The voltage V of the capacitance is obtained from the current I as

$$V = -\frac{1}{C}\int I dt \qquad (4)$$

Then the net power and the energy inputs into tha plasma is calculated as

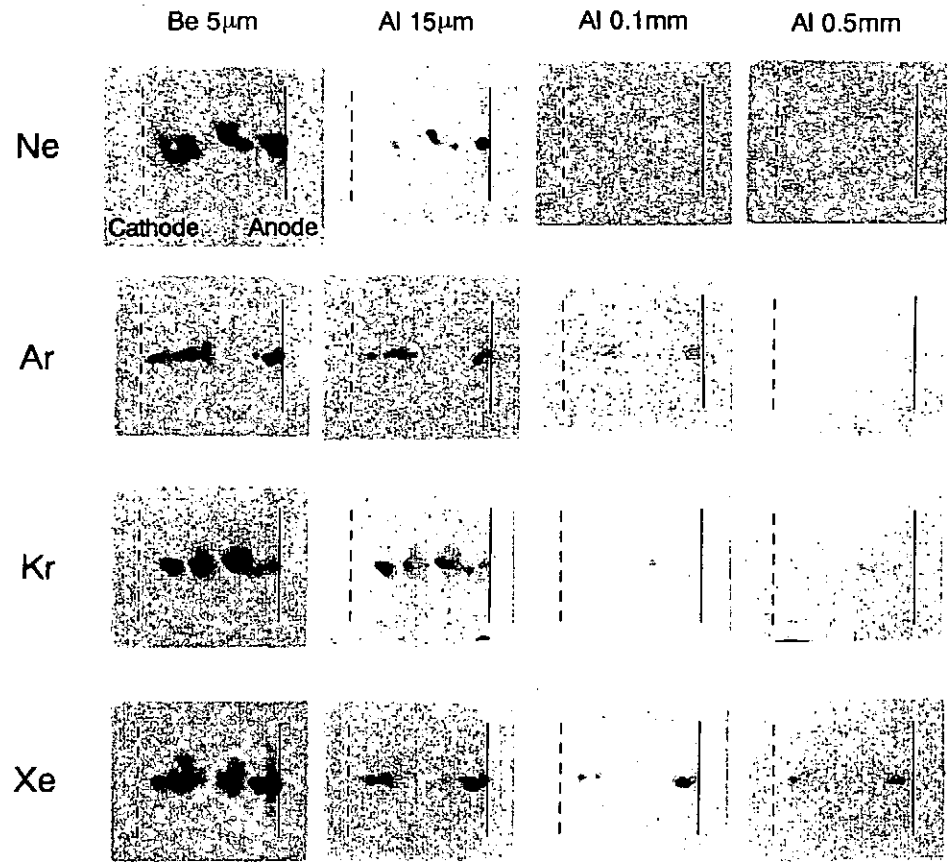

Fig. 3. X-ray pinhole photographs of Ne, Ar and Kr z-pinches taken with different x-ray filters.

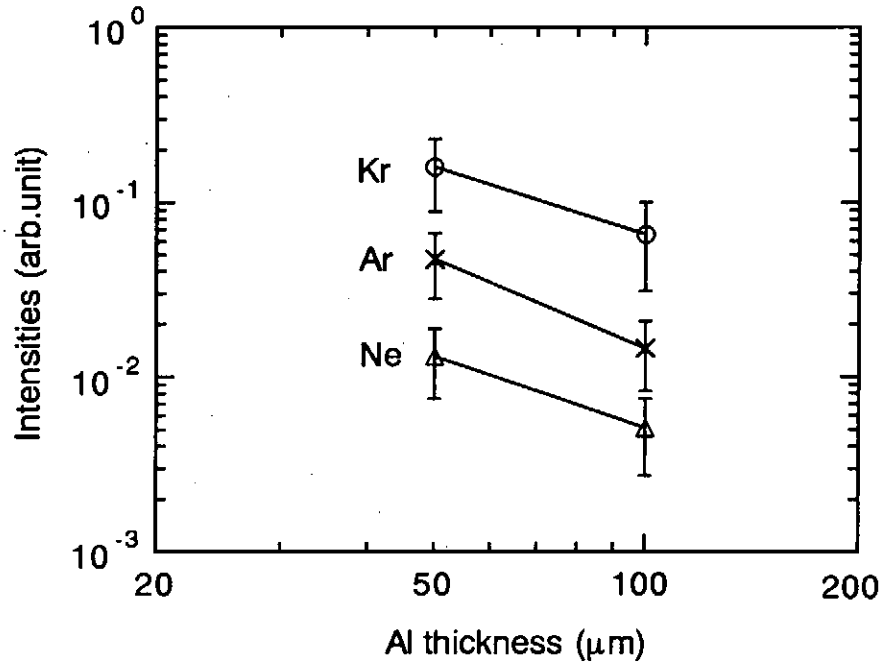

Fig. 4. X-ray emission intensities of Ne, Ar and Kr z-pinches measured by scintillation probes with Al filters.

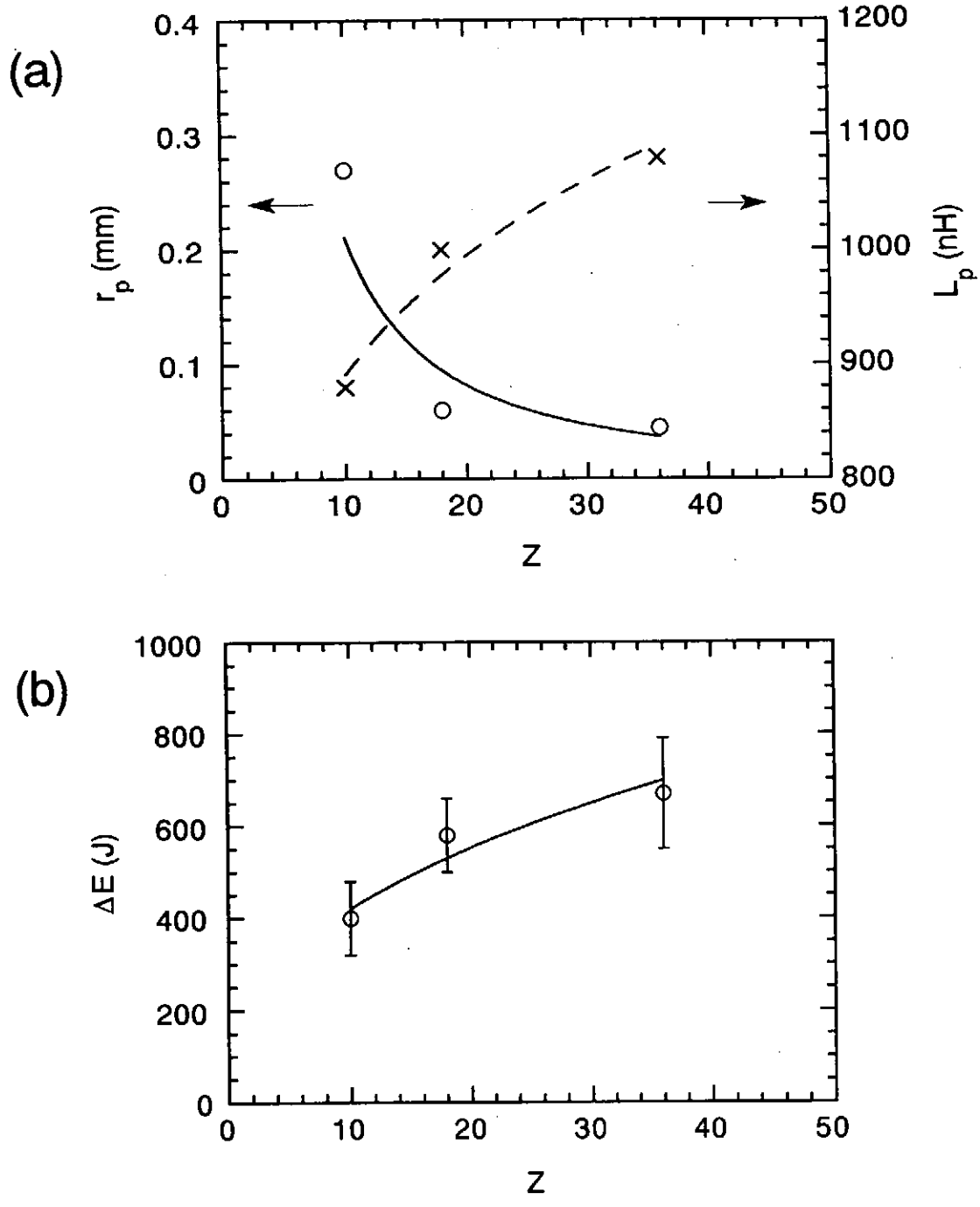

Fig. 5. (a) The maximum inductance L_p and the minimum pinch radius r_p as a function of Z of the gas. (b) The input energy ΔE.

$$P = VI - RI^2 \tag{5}$$

$$\Delta E = \int P dt - \frac{1}{2} L I^2 \tag{6}$$

Using the known values of R and $V(0)$, the temporal evolution of V, P and L are calculated from I. Figure 5 shows the maximum plasma inductance L_p, the minimum average plasma radius r_p calculated from L_p and the energy input ΔE as a function of Z of the gas. The energy ΔE increases with Z, which is a direct result of increasing L_p, hence decreasing r_p. One of the reason for this may be some stabilization effect acting on high Z z-pinch during contraction, and it makes possible of reaching a small pinch radius.

V. Summary

Depending on the time of discharge from the gas-puffing, the operating region is devided into several regions. The crowbar of plasma current occurs automatically after the maximum current or the voltage pulse is turned off. This is due to the shortcircuiting near the power feed.

The z-pinch plasma with higher Z contracts to a smaller radius on the average, and it gains more energy during the contraction. Then the emissivity of x-ray increases with Z of the operating gas.

References

[1] J. Shiloh, A. Fisher and N. Rostoker, Phys. Rev. Lett. 40, 515 (1978).

[2] J.D. Setian, A.E. Robson, K.A. Gerber and A.W. DeSilva, Phys. Rev. Lett. 59, 892 (1987).

[3] N.R. Pereira and J. Davis, J. Appl. Phys. 64, R1 (1988).

[4] J. Bailey, Y. Ettinger, A. Fisher and R. Feder, Appl. Phys. Lett. 40, 33 (1982).

[5] K. Takasugi, A. Takeuchi, H. Takada and T. Miyamoto, Jpn. J. Appl. Phys. 31, 1874 (1992).

[6] H. Akiyama, N. Shimomura, K. Takasugi, T. Miyamoto, M. Sato and T. Tazima, Rev. Sci. Instrum. 61, 1344 (1990).

[7] K. Takasugi, H. Akiyama, N. Shimomura, M. Sato and T. Tazima, Rev. Sci. Instrum. 64, 2403 (1993).

High Resolution Diagnostics of Intense Ion Diodes and Key Issues for Bright Light Ion Beam Generation

Kazuhiko HORIOKA

Department of Energy Sciences Tokyo Institute of Technology
Nagatsuta 4259, Midori-ku Yokohama 227, Japan

ABSTRACT

Progress in the diagnostic techniques of high power vacuum gaps has stimulated the development of analytical and numerical calculation of the diode physics. These developments have made clear the diode physics and key issues for bright light ion beam generation. In this report recent diagnostic techniques of the acceleration gaps are reviewed and those issues are briefly discussed.

1. INTRODUCTION

Until recently three types of diode configurations have been developed for high power ion beam generation. They are pinched electron beam diodes[1] reflex triodes[2] and applied-B[3],[4] diodes. In general intense self fiel in the acceleration gap of high power diode induces unstable diode behavior thereby severely degrades the ion beam quality.

The applied-B diodes are less sensitive to the induced self field because the diode insulation fields are supplied from controllable external circuits. Thus the applied-B diodes can produce most efficient and bright ion beams. Although they can be

operated at TW beam power level they still have some drawbacks; such as impedance collapse of the gap[5] and instability of cathode electron sheath[6].

2. Development of Diagnostic Techniques for High Power Diodes

Although we needed the understanding of the physics of applied-B diode it had not been understood exactly because of difficulty of the diagnostics. The acceleration gap is exposed to the high electric and magnetic field stress and the electrode plasma is localized and highly nonequilibrium. The equipotential surfaces (Virtual Cathode) are formed by electrons which drift along the magnetic fiel lines. Generally the electron cloud changes its distribution with nsec time scale. Thus the optical diagnostics are most suitable for the observation of the gap dynamics.They must have nsec-level temporal and mm-level spatial resolution with sufficient signal to noise ratio.

2-1 Spectroscopy

In order to estimate the parameters of anode plasma and the gap dynamics various spectroscopic techhniques are developed. They are the observation of the broadening (Stark or Doppler) and shift of the hydrogen balmer line the ion line emission of C++ or doped Al++.

The electron density,[7] temperature an expansion of the anode plasma was measured with the width and/or intensity ratio of those visible spectral lines. Measurements of electril field distribution in the gap[8] showed that the field-excluding anode plasma expands early in the pulse. This cause gap closure and temporal impedance collapse in the applied-B diodes with surface flashover passive ion source.[9]

The ion transverse-velocity distribution was measured by observing the Doppler broadened C++4647A or Al++3602A spectral line emission from the anode plasma or from the gap region.[10] The estimated divergence angle in the gap was significantly smaller than the value measured outside the diode gap. This fact suggests the beam

divergence induced by the instability of cathode electron sheath.

2-2 Laser Techniques

Laser-based diagnostics are developed for the investigation of the particle distribution in the diode gaps. A N2-Laser shadowgraphy a Ruby laser interferometry[11] a resonance interferometry and a resonance scattering method[12] were used for observation of the electrode plasma dynamics. The resonant interferometry detects the population difference and the resonance scattered light reflects the ratio of the population.These techniques could allow direct determination of the particle distribution in the vacuum acceleration gap.

Obtained results qualitatively support the anode plasma expansion mechanism induced by the energatic neutral particles in the gap.[12],[13],[14] So this fact suggests that to increase the operation range of the diode, a high flux capable of providing high current, neutral free and high purity plasma source must be supplied.

2-3 High Resolution Mass-Energy Spectroscopy

Formerely the beam composition and its energy spectrum had been measured in the drift region by use of Faraday caps placed at different distances from the diode or by a Thomson parabola mass spectrometer with CR-39 as a time integrated detecter.

A time resolved energy spectrum of extracted ion beams provides critical information on the dynamics of the diode gaps. A Rutherford scattered magnetic spectrometer measures energy-momentum history of the ion beam.[16] PIN detecters have given us a time-resolved divergence information. It provide experimental evidence for the existence of electromagnetic fluctuations. With a correlation of ion beam energy sprea and momentum in the PBFA-II diode, it was concluded that the wave particle interaction was a major source of the beam divergence.

The time resolved energy distribution of the extracted beams was measured by a

Thomson parabola mass-energy analyzer with modulated electric field[17] or MCP detecter.[18] An arrayed-[19] and a multi-[20] pinhole mass spectrometer are developed to measure the ion beam micro-divergence with spatial resolution. Those temporally and spatially resolved spectrum of the ion beams also clarified the cause of the beam divergence induced by the charge exchange process and the electromagnetic instability.

2-4 Estimated Physical Parameters of Diode Operation

Typical values of the diode physical parameters are summarize in Table.1. By the optical measurements a large amount of emission of neutral particles are observed in the initial phase of passive diode operation which severely degrade the diode characteristics. The total charge in the A-K gap must remain zero. Thus if unlimited ion supply is afforded from the anode plasma it brings bootstrap behavior in the gap ie, increase of the ion charge induces the electron buildup and the virtual cathode motion to the anode which further induces the ion emission. The movement of virtual cathode induced by the diamagnetil effect of the electron causes the rapid impedance collapse. The fluctuations and nonuniformity of the electron flow were measured using X-ray emission from the anode in a long pulse applied-B diode.[21] It was concluded that a low frequency instability induced by the cathode plasma filamentation caused the fluctuations.

In order to avoid the charge builup in the acceleration gap, active diodes with flux limited source plasma supply[22] and two-stage acceleration gaps[23]were developed and successfully operated.

Physical Parameter		Measured Values	Dianostics
Electron Density;	ne	10^{15}~$10^{16}$$_{cm}$$^{-3}$	Hα, Hβ Stark Broadening(7),(8),(9)
Temperature;	Te	2 ~ 8eV	Spectal Line Ratios, CRE-Model
Plasma Expansion;	VH,VD	2~3cm/μ sec	Resonant Interferometry(12) Spectral Line Emissions
Ion Temperature;	Ti	20~80eV	Doppler Broadening (10)
Transverse Velocity;	Vi	200eV(Vd~300kV)	Doppler Shift (10)
Neutral (Density);	Nn	10^{16}~$10^{17}$$_{cm}$$^{-3}$	Hook Method, CRE-Model (9)
H(n=2);		$10^{15}$$_{cm}$$^{-3}$	LIF (12)
Energy;	Eh	10^{2}~10^{3}eV	Mag. Detecter
Emmision;	Ne	10^{19}/Shot	Fast Ionigage
Surface Evaporeation;		10^{3}~10^{4} Layer	Pressure Jump
Electric Fieldd;	E	~MV/cm	Stark Shift (13)

Table.1 Typical Values of the Physical Parameters of High Power Applied-B Ion Diodes

3. Progress of the Analytical Understanding and Numerical Simulation of Diode Physics

The theoretical understanding of the physics of applied-B diodes has been rapidly improved. A 1-D electromagnetic PIC diode code combined with an external circuit was developed to simulate the impedance hystory of the diode.[24] A 3-D particle simulatio[25]and analytil theories[26]have provided a new insight into the physics of the diode gap.A new model based on a self-consistent calculation of the diamagnetic effect on the virtual cathode location appears to explain the previously discussed scaling laws of the diode impedance. These theory also enabled us the quantitative comparison of the results with experimental values of beam divergence. A qusi-linear stability analysis provided new insights into the physics governing low frequency beam divergence induced by ion streaming.[27]

All of the above analyses indicate that the suppression of electron buildup in the gap and higher insulation magnetic field are critical for suppression of impedance collapse and the harmful low frequency electromagnetic instability.

A schematic of the applied-B diode behavior is shown in Fig.1. A sufficiently strong axial magnetic fiel is applie to inhibit the electron flow across the gap. The diode impedance generally starts out very high. The E=0 surface (Virtual Cathode) is tie to the Ay(Vector Potential)=0 flux surface. Electromagnetic fluctuations[28] induce variations in the energy and momentum of the electrons thus allowing them to cross the insulation fiel lines. As the electron charge accumulates in the gap the virtual cathode position moves to the anode thereby the ion current increases and the impedance decreses rapidly. By considering total flux the position of virtual cathode is derived self-consistently.

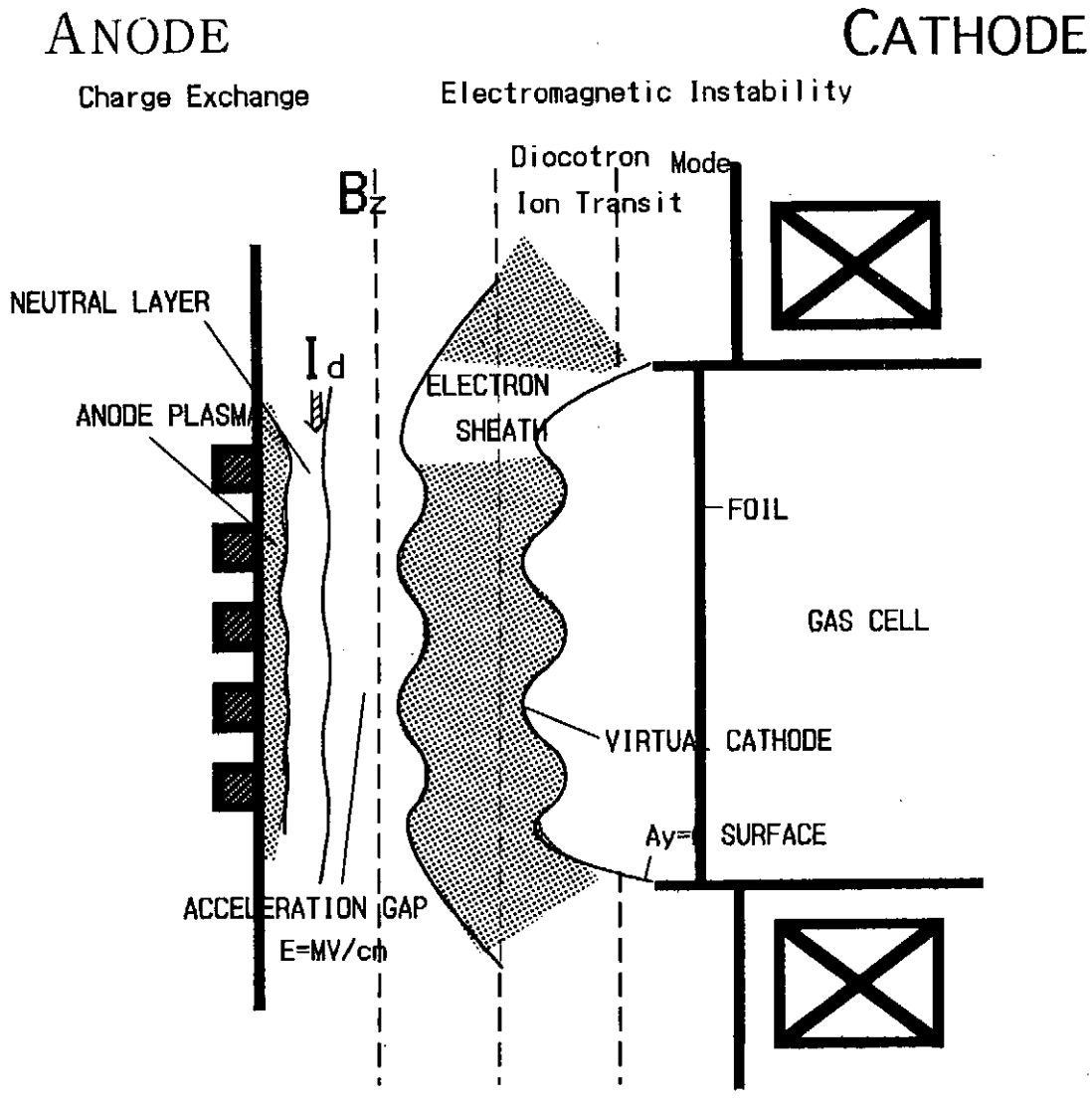

Fig.1 Schematic of Applied-B Diode Behavior

Eerly in the diode time a high frequency (diocotron) sheath instability is dominant, however this mode dose not produce large divergence because of its high frequency. The low frequency ion transit modes result in a dramatic increase in the ion divergence[23]

4. SUMMARY

Advances of diagnostic techniques and experimental evidence obtained by using those methods stimulate the developments of the analytical an the numerical analyses. Those developments seem to have promised us to generate $10^{13}W/cm^2$ level high power density light ion beams.

They predict that to control the impedance hystory and to suppress the beam divergence caused by the cathode sheath instability, a high purity, flux limited source plasma supply anhigh insulation field are critical factors.

From recently advanced experimental and theoretical results, we can make rather classical criterions for bright ion beam generation. They are,

1 limited supply of high purity ions from well controled anode plasma, and

2 to inhibit the charge accumulation by placing an electron limiter[29] by applying higher magnetic insulation field in the gap.

In fact it was reported that 0.8TW level proton beam extraction was possible with more than 90% ion current efficiency and 76% diode electrical efficiency by a preformed, limited supply, high purity ion source and high insulation field diode configuration.[30]

REFERENCES

(1) S.A.Goldstein and R.Lee Phys. Rev. Lett. Vol.35, p.1077 (1975)
(2) S.Humphries, Jr. et. al. Appl.Phys.Lett., Vol.25 p.20 (1974)
(3) R.N.Sudan and R.V.Lovelace Phys.Rev.Lett., Vol.31, p.1174 (1973)
(4) S.Humphries Jr. et. al. J. Appl.Phys., vol.48, p.273 (1977)
(5) P.A.Miller, J.Appl.Phys., Vol.61 p.527 (1985)
P.A.Miller and C.W.Mendel.Jr., Journal of Appl.Phys., Vol.61 p.531 (1987)
(6) J.Maenchen et. al. Proc. 6th Int.Conf.High Power Beams, Kobe, p.85 (1986)
(7) R.Pal and D.A.Hammer, Phys.Rev.Lett., Vol.50, p.732 (1983)
(8) C.Litwin and Y.Maron, Phys.Fluid, B1 p.(1989)
Y.Maron et.al., Phys.Rev.A, Vol.41, No.2 p.1074 (1990)
(9) K.Horioka et. al. IEEE Trans. Plasma Sci. Vol.17 No.5 (1989)
(10)Y.Maron et.el., J.Appl.Phys., Vol.61 p.4781 (1987)
(11)D.J.Johnson et.al., J.Appl.Phys., Vol.52, p.168 (1981)
(12)K.Horioka et. al. Rev. Sci. Instr. Vol.61 No.1 p.610 (1990)
(13)C.Litwin and Y.Maron, Phys. Fluids B1, p.670 (1989)
(14)T.D.Pointon, J. Appl. Phys., vol.66, p.2879 (1989)
(15)K.Horioka et. al. Proc. 8th Int. Conf.High Power Beams, P.R03, vol.2, p.822 (1990)
(16)R.J.Leeper et.al., Rev.Sci.Inst., Vol.57 p.1700 (1988)
R.J.Leeper et. al. Proc. 8th Int.Conf.High Power Beams, C.A05, Vol.1, p.173 (1990)
(17)H.Yoneda et.al., Rev.Sci.Instr., Vol.59, p.457 (1988)
(18)K.Yatsui et.al., Laser & Particle Beams, Vol.5, p.415 (1987)
(19)K.Yasuike S.Miyamoto et. al. Proc. 9th Int. Conf.High Power Beams, p.1403 (1992)
(20)K.Yatsui et. al. Res. Rep.Inst.Electrical Eng.Japan, EP-93-31, p.67 (1993)
(21)Y.Nakagawa and T.Enomoto, J. Appl. Phys., Vol.59, (11) p.3716 (1986)
(22)Y.Saitoet. al. NIFS Report (1991)
(23)S.Miyamotoet. al. Proc. Int. Conf. High Power Beams, C.A07, Vol.1, p.190 (1990)
(24)T.Aoki and K.Niu, NIFS-Proc 5, (1990)
(25)J.P.Quintenz et. al. Proceedings of the IEEE, Vol.80, No.6 p.971 (1992)
(26)M.P.Desjarlais Phys. Rev. Lett. Vol.59 No.20 p.2295 (1987)
M.P.Desjarlais, Phys.Fluids B, Vol.1 p.1707 (1989)
(27)R.N.Sudan and D.W.Longcope, Phys.Fluids B5, p.1614 (1993)
(28)C.L.Chang, et. al., Phys. Fluids Vol.29, p.1258 (1986)
(29)S.A.Slutz, et. al., J. Appl. Phys., Vol.62, p.16 (1987)
(30)H.Bluhm et. al., Proceedings of the IEEE, Vol.80, No.6 (1992)

BEHAVIORS OF PLASMA ARMATURE IN THE AUGMENTED RAILGUN USING A PERMANENT MAGNET

S. Katsuki, H. Akiyama, S. Maeda

Department of Electrical Engineering and Computer Science
Kumamoto University

ABSTRACT

Augmentation of the magnetic field for electromagnetic railguns is a quite effective method to suppress the ablation of bore materials since it allows to decrease the plasma armature current without a decrease of the Lorentz force for the acceleration. Another constructive effect of the augmentation on a plasma armature was observed in our experiment, that is to say, an external magnetic field for the augmentation compresses the plasma armature in the axial direction and suppresses the broadening of the plasma armature. In this paper, the behavior of plasma armature in the augmented railgun using a permanent magnet is investigated in comparison with that in the railgun without the augmentation.

§1. INTRODUCTION

Ablation of bore materials due to an energy flux from a plasma armature[1] is one of serious problems that must be solved in order to increase the projectile velocity and achieve repetitive operations of plasma armature railguns. Augmentation[1)-3)] of the magnetic field for electromagnetic railguns is a quite effective method to suppress the ablation of bore materials, since it allows to decrease the plasma armature current without a decrease of the Lorentz force for the acceleration. Generally, an augmented railgun is composed of rails and a several turned coil along the rails. The coil is electrically connected to the rails in series, and therefore the magnetic field between rails is augmented automatically. A superconducting coil[3] has been used for augmentation.

A permanent magnet can be used as the augmentation device for the railgun driven by a relatively small current in the range of 10 kA, for instance, for a pellet injector[4)-6)] of the magnetically confined fusion reactor. Using a permanent magnet has the following advantages in comparison with using augmentation coils: 1) the efficiency of system increases, 2) since the magnetic field is constant, a larger Lorentz force can be generated even when the current is small, namely, during the rising or decaying phase of current, 3) the system becomes simple and compact because a power supply and a timing apparatus are not used for making the additional magnetic field.

We have developed an augmented railgun using the permanent magnet, which has a 5 mm square bore and is 50 cm in length. The magnetic field in a space between rails, which is produced by the permanent magnet, is 0.53 T and uniform. Also we made another railgun without the augmentation, which has the same dimension as the augmented railgun. Both railguns use the Plasma Initiation Separated from the Projectile (PISP method)[7),8)] instead of any preaccelerators to decrease the ablation of bore materials in the initial phase. From comparisons between two kinds of railguns, the performance of the augmented railgun using a permanent magnet is much superior to that of the conventional railgun without an augmentation in terms of the achieved projectile velocity, the erosion of the rail surface and the reproducibility of operation, even though the same maximum Lorentz force is used for both railguns. Another constructive effect of the augmentation on the plasma armature was observed in our experiment, that is to say, the plasma armature was compressed in the axial direction and the broadening of the plasma armature was suppressed in the case of the augmented railgun using the permanent magnet.

In this paper, the behavior of the plasma armature in an augmented railgun using a permanent magnet is investigated and compared with that in the railgun without the augmentation. In order to investigate the influence of the external magnetic field applied by the permanent magnet on a plasma armature, the current density distributions are calculated from the experimental signals of B-dot probes. The Jansson's method[8),9)] is used to deconvolve the signals of B-dot probes to determine the current density distribution in plasma armature.

§2. AUGMENTED RAILGUN USING PERMANENT MAGNET

In conventional railguns, the Lorentz force due to a driving current, I, is given by

$$F = \frac{1}{2} L' I^2, \tag{1}$$

where L' is the inductance per unit length of the rail pair. Though the decrease of driving current flowing through the plasma armature seems to decrease the ablation of bore materials, the acceleration of the projectile by the Lorentz force decreases with the square of the driving current, simultaneously. Therefore, a decrease of the driving current would degrade the performance of railgun.

Figure 1 shows the schematic configuration of an augmented railgun. In the augmented railgun, the Lorentz force, F_{arg}, is expressed as

$$F_{arg} = \frac{1}{2} L' I^2 + I B_e d, \tag{2}$$

where B_e is the external magnetic field in the space between rails using an external magnetic device and d is the separation between the rails. The external magnetic field allows a decrease of the driving current without de-creasing the Lorentz force. As a result, a decrease of the ablation can be expected by using the external magnetic field. If the propulsive pressure is limited to a critical value, P_c, then the Lorentz force, F_{arg}, is limited and a critical driving current, I_c, is obtained from Eq. (2), such as

$$I_c = \frac{d}{L'}\left(-B_e + \sqrt{B_e^2 + 2L'P_c}\right), \tag{3}$$

Figure 2 shows the dependence of the critical driving current on the external magnetic field for L'=0.48 μH/m and d=5 mm. The limiting pressure, P_c, due to the yield strength of hydrogen pellets might be 6 MPa.[6] It is clear that the larger the external magnetic field for the augmentation, the smaller is the current required to drive the railgun.

Figure 3 shows a comparison of the driving current and the calculated Lorentz force for a conventional railgun and an augmented railgun using a permanent magnet. If the external magnetic field supplied by a permanent magnet is 0.53 T, maximum driving currents of the

railguns without and with a permanent magnet have to be set to 25 kA and 20 kA, respectively, so that the maximum magnetic pressure in each case corresponds to 6 MPa.

§3. EXPERIMENTAL SETUP AND PROCEDURES

Two kinds of railguns are used to investigate the influence of the magnetic field augmented by a permanent magnet on the plasma armature. One is the conventional railgun, which is composed of copper rails and insulating rail spacers made of polycarbonate, without an augmentation of magnetic field. Total length of the railgun is 50 cm and the bore is 5 mm square section. Since the projectile is placed 10 cm from the breech, the effective length of the railgun for the acceleration is 40 cm. The other is the augmented railgun using a permanent magnet, of which cross section is shown in Fig. 4. The acceleration tube is the same size and materials as the conventional railgun. The "C" type of magnetic circuit is assembled to supply a constant magnetic field to the space between rails. The average magnetic flux density is 0.53 T in the cross section of the acceleration tube and uniform along the direction of acceleration.

Low density square wood coated by resin is used as a projectile to simulate the hydrogen isotope pellet for a pellet injection of magnetically confined fusion reactors. The projectile mass and length are 30 mg and 2.5 mm, respectively.

Figure 5 shows a schematic diagram of the experimental setup. The power supply consists of a capacitor bank with the maximum stored energy of 10.8 kJ and a capacitance of 872 μF, a coil with the inductance of 11.0 μH, a thyristor (SF1500GX21, Toshiba) as the main switch and a diode (2500GXD21, Toshiba) as the crowbar switch. This power supply is able to be operated with a repetition frequency of 2 pps. The maximum driving currents for the conventional railgun without an augmentation and the augmented railgun using a permanent magnet must be 25 kA and 20 kA, respectively, so that both railguns have the same maximum Lorentz force. In this case, the primary stored energies of capacitor bank are 4.8 kJ and 2.9 kJ, respectively. The railguns are set in a vacuum chamber evacuated to less than 1.4 Pa.

The current flowing into the railgun is measured by a Rogowski coil, and the plasma behavior is observed by five B-dot probes placed along the rails. Since the B-dot probes are placed so as to pick up the magnetic flux due to only the rail currents, output signals from the B-dot probes indicate the differential of rail currents theoretically.[11] The final projectile velocity is measured by two wire screens placed 5 cm apart and placed about 20 cm away from the muzzle.

The signals obtained by B-dot probes are stored in the digitizing oscilloscope and computed later. The sampling rate in this experiment is 5×10^6 samples per second. In order to determine the current density profile in a plasma armature in the axial direction, the B-dot signals are deconvolved using Jansson's method[9),10)]. It is assumed in the deconvolutions that the armature and rail currents have no thickness in the direction of the external magnetic field, and all the current in the plasma armature flows in the perpendicular direction to the rail. The obtained current distributions are compared between the two kinds of railguns, which are the conventional railgun and the augmented railgun using a permanent magnet.

§4. EXPERIMENTAL RESULTS AND DISCUSSIONS

Figures 6 and 7 show typical waveforms of driving current and signals from five B-dot probes, which are placed at different positions of z=0, 10, 20, 30, 35 cm along the rails. The projectile is placed at z=0 cm. The marks of * show the positions of wire screens and times when the projectile breaks wire screens placed about 25 cm apart from the muzzle. The marks of Δ show the time when the projectile just exits out of the railgun, which is calculated from the velocity obtained from the wire screens.

Typical experimental results in the case of the conventional railgun without augmentation are shown in Fig. 6 (#1270). The final projectile velocity measured by wire screens was 1.19 km/s in this shot. The efficiency of the system, defined as the ratio of the kinetic energy of a projectile to the stored energy in the capacitor bank, is only 0.45 %. Each signal from all the B-dot probes became noisy after the plasma armature passed through each position of the B-dot probes.

Typical results in the case of the augmented railgun using a permanent magnet are shown in Fig. 7 (#1306). All the driving current from the power supply seems to flow into the main plasma armature when the plasma armature passes through the position of z=10 cm. The final projectile velocity measured by wire screens was 1.64 km/s in spite of the lower primary energy stored in the capacitor. The efficiency of system is 1.4 % which is more than 3 times as large as that of #1270 using the railgun without augmentation.

Figures 8 shows the signals from the B-dot probe placed at z=10 cm (upper), the deconvolved waves of the B-dot signals (middle) and the B-dot signals restored by the convolution of the deconvolved waves (lower) in the cases of the railguns using a permanent magnet. The correspondence of profiles between the original and restored B-dot signals indicates the validity of the deconvolved wave, which shows the increment of current passing through a position of z, dI/dt. Assuming that the flow velocity of plasma armature is constant and the current distribution does not alter for a period of 200 μs, the current distribution is obtained by multiplying the horizontal axis of the deconvolved wave by the flow velocity of plasma armature, v_a, and by dividing the vertical axis by v_a. Figs. 9 (a) and (b) show the current distributions around plasma armatures in the railguns without and with a permanent magnet, respectively. The current profiles are not uniform. The profile of the current flowing through the main plasma armature in the augmented railgun with a permanent magnet is obviously steeper than that in the conventional railgun without a permanent magnet. Two reasons why the driving current concentrates in the main plasma armature and the B-dot signals become steeper in the augmented railgun with a permanent magnet are considered. Firstly, the decrease of the ablation of bore materials due to the decrease of the driving current might suppress the separation of plasma armature. Since the Lorentz force acting on the plasma armature in the railgun with a permanent magnet is larger than that in the railgun without a permanent magnet in spite of smaller current as shown in Figs. 2 and 3, the mass ablated from the bore surface and then flowing into the plasma armature becomes smaller. Secondly, the constriction of armature plasma by the external magnetic field might occur since the density of armature plasma is generally high. The constriction suppresses the separation of plasma armature and makes the behavior of plasma armature stable.

Figure 10 shows the history of the current distribution in the plasma armature for #1306. This is typical operation of the augmented railgun using a permanent magnet. Figs. 10 (a), (b) and (c) are the current distributions around the times when the plasma armature passed through different positions of z=10, 20, and 30 cm, respectively. The separation of plasma armature was already observed when the plasma armature passed through the position of z=10 cm. A series of the waves indicates the current distribution spreads gradually, and finally the length of plasma armature becomes more than 10 cm. This behavior might be caused by the increase of the mass of plasma armature and the decrease of the Lorentz force due to the decay of driving current. Since a large quantity of vapors due to the ablation of bore materials is generated and a part of vapors flows into the plasma armature, the mass of plasma armature increases with its propagation. On the other hand, since the magnetic pressure behind a plasma armature due to a driving current had begun to decay when the plasma armature passed through the position of z=10 cm, the plasma armature with a large mass spreads in the axial direction by the plasma pressure and the drag force that is proportional to the square of velocity.

§5. CONCLUSIONS

Behaviors of plasma armatures in railguns were investigated using two kinds of railguns, a conventional railgun and an augmented railgun using a permanent magnet. The current from a power supply distributes broadly in the axial direction in the case of the conventional railgun. On the other hand, the current concentrates in the main plasma armature in the case of the railgun using a permanent magnet because of the decrease of the ablation of bore materials that is caused by the decrease of driving current and the increase of the Lorentz force in the initial phase of the acceleration. However, spreading of the plasma armature occurs later even in the augmented railgun using a permanent magnet. This spread of the plasma armature might be caused by the increase of the mass of plasma armature and the decay of the driving current.

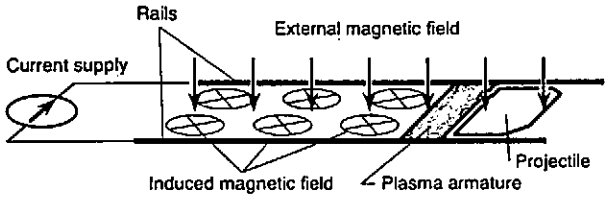

Figure 1 Augmented railgun.

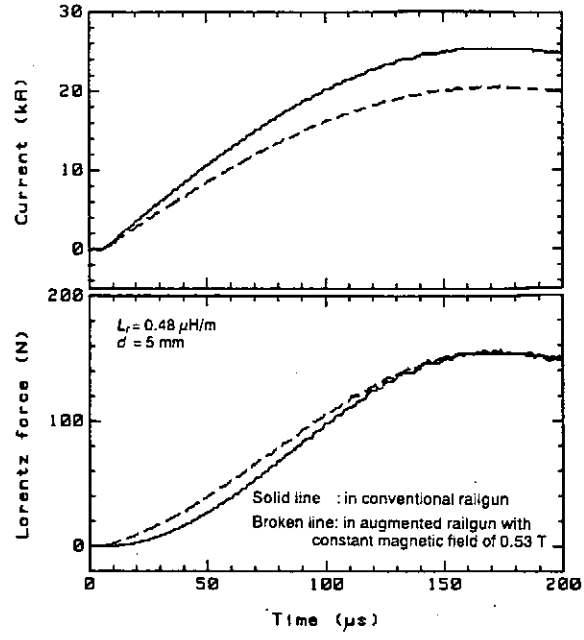

Figure 3 Comparison of the driving current and the Lorentz force between railguns with and without an external magnetic field. Maximum driving currents are adjusted so that the maximum propulsive pressures in each railgun correspond to 6 MPa.

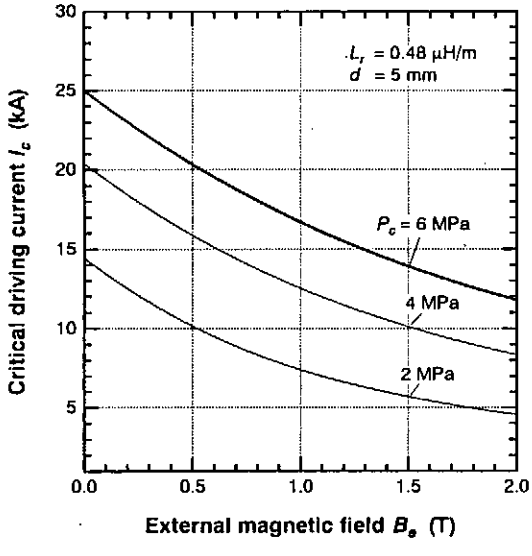

Figure 2 Dependence of the critical driving force on the external magnetic field in the case of the limited propulsive pressure.

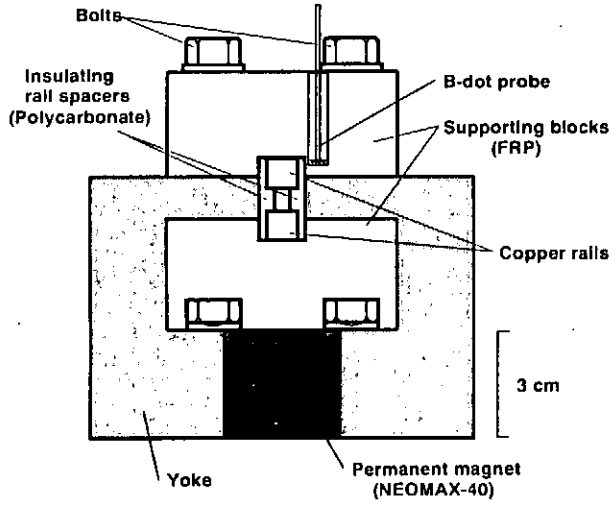

Figure 4 Cross section of the augmented railgun using permanent magnet.

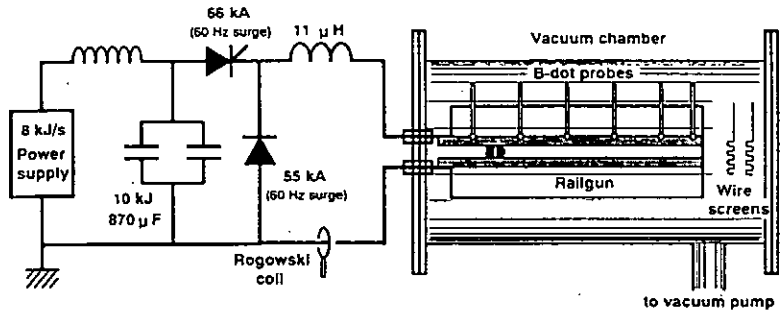

Figure 5 Experimental setup.

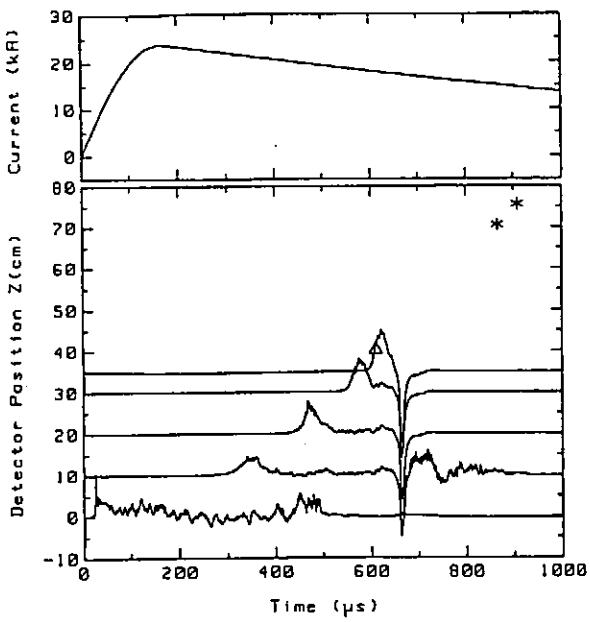

Figure 6 Typical operation of the conventional railgun.

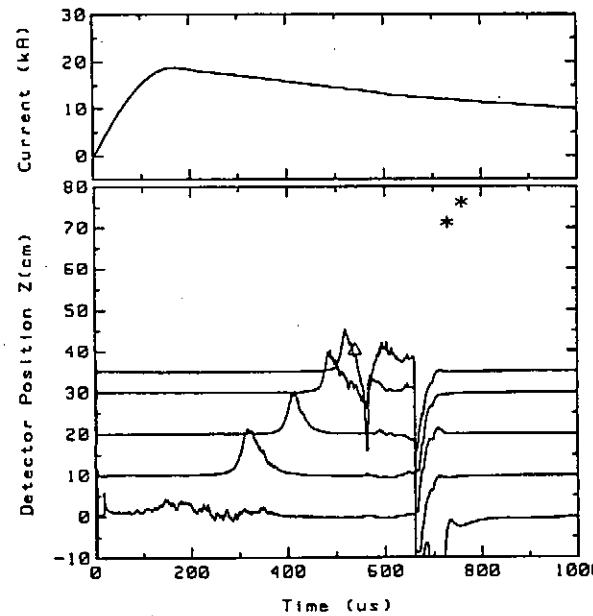

Figure 7 Typical operation of the augmented railgun using permanent magnet.

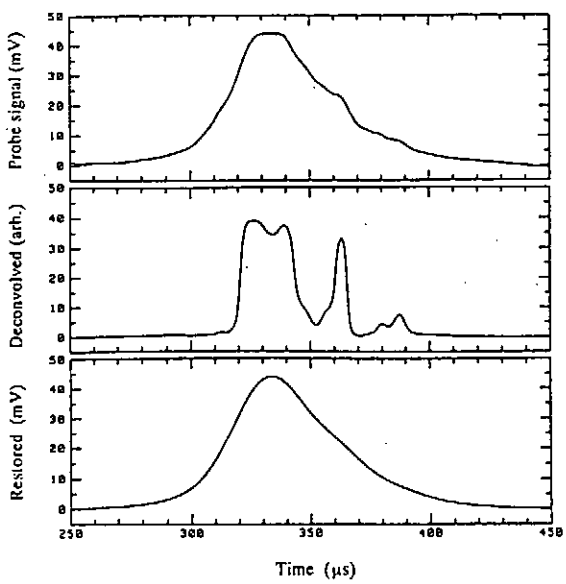

Figure 8 Signals from the B-dot probe placed at z=10 cm (upper), the deconvolved wave of the B-dot signal (middle) and the B-dot signal restored by the convolution of the deconvolved wave (lower) in the case of the augmented railgun using the permanent magnet.

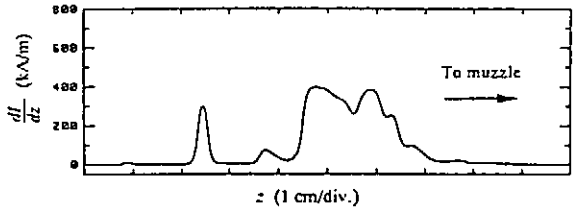

(a) In the conventional railgun.

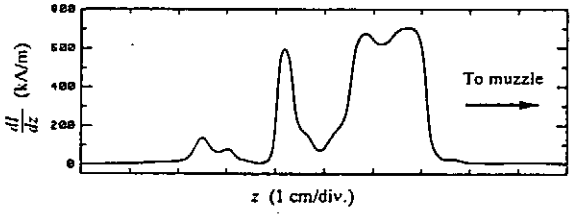

(b) In the augmented railgun using the permanent magnet.

Figure 9 Comparison of current distribution in the plasma armature between (a) the conventional railgun and (b) the augmented railgun using permanent magnet.

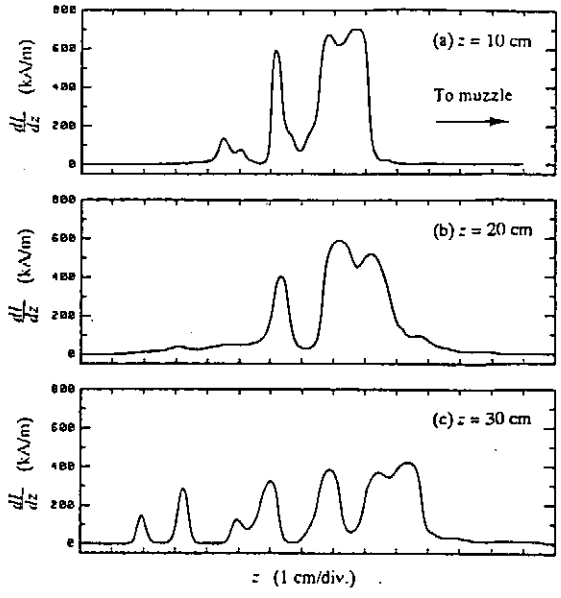

Figure 10 History of the current distribution in #1306 which is in the augmented railgun using permanent magnet.

REFERENCES

1) J. V. Parker, IEEE Trans. Magnetics, vol. 25, no. 1, pp. 418-424, 1989.

2) D. A. Fiske, et. al., vol. 27, no. 1, pp. 176-180, 1991.

3) C. G. Homan, C. E. Cummings and C. M. Fowler, *Megagauss Technology and Pulsed Power Applications*, New York: Plenum, 1987, pp. 829-837.

4) R. S. Hawke, J. Vac. Sci. Technol. A, vol. 1, no. 2, pp. 969-973, 1983.

5) S. L. Milora, J. Vac. Sci. Technol. A, vol. 7, no. 3, pp. 925-937, 1989.

6) K. Kim and J. Honig, Fusion Technol., vol. 6, pp. 372-377, 1984.

7) S. Katsuki, H. Akiyama, et. al., IEEE Trans. Plasma Sci., vol. 21, no. 6, pp. 755-759, 1993.

8) S. Katsuki, H. Akiyama, et. al., *Proc. of 9 th International Pulsed Power Conf.*, Albuquerque, NM, 1993, (in print).

9) B. J. Evans and L. Montgomery Smith, IEEE Trans. Plasma Sci., vol. 20, no. 4, pp. 432-438, 1992.

10) P. B. Crilly, IEEE Trans. Instrumentation and Measurement, vol. 40, no. 3, 1991.

11) J. V. Parker, IEEE Trans. Plasma Sci., vol. 17, no. 3, pp. 487-500, 1989.

Strong Beam-Plasma Turbulence

M. Masuzaki, R. Ando, M. Yoshikawa, K. Kobayashi,
H. Koguchi, D. Yamada and K. Kamada

Faculty of Science, Department of Physics, Kanazawa University

Abstract

High-power broadband microwave radiation was observed when an intense relativistic electron beam was injected into an unmagnetized gun-produced plasma. From spectroscopic measurements of hf strong electric fields in the plasma, it was found that our beam-plasma system is in the strong Langmuir turbulent state. A preliminary result indicating relation between the radiation and the turbulence is shown.

§1 Introduction

Recent theoretical and computational works[1,2] have shown that when a fast electron beam is injected into a plasma, the plasma becomes a strong Langmuir turbulent state, in which formation, collapse and burnout of cavitons, i.e., spatially localized volumes with density depletion in which large amplitude electrostatic waves are trapped, are repeated. Such a state is sustained by the local nucleation process.[3-6] For such turbulence, the dimensionless electrostatic wave energy density $W = \varepsilon_0 \langle E^2 \rangle / 2 n_p T_e$ should be larger than $(k_0 \lambda_D)^2$. Here k_0 is the resonance wave number ω_{pe} / v_b , ω_{pe} and v_b being the plasma frequency and the beam velocity, respectively, n_p is the plasma density and λ_D is the Debye length.

A number of groups have carried out experiments on interaction of an intense relativistic electron beam (IREB) with a plasma which are closely connected with strong Langmuir turbulence.[7-18]

We observed high-power broadband microwave radiation emitted from interaction between an IREB of 1.2 MeV and 30 ns and a gun-produced carbon plasma.[15,16] In order to know the mechanism of this emission, we measured strong high frequency electric fields originating from the IREB-plasma interaction in the same experimental setup as used for observation of high-power microwave radiation.

§2 Experimental Apparatus

The experimental apparatus consisted of an IREB generator, drift chamber, plasma guns, and measurement systems. The measurement systems included a 5-channel microwave spectrometer and an 8-channel spectroscopic system.

The IREB generator used was a modified Pulserad 110A produced by Physics International, which can generate an IREB of 1.5 MeV, 27 kA, 30 ns pulse in a conventional diode. In this work we used two kinds of diodes as shown in Fig. 1. One was a foilless diode [Fig. 1(a)], which consisted of a cathode made of a 3 mm-diam. tungsten rod and a carbon anode with a 2 cm-diam. aperture in the axis, the A-K distance being about 9 mm. The other was a foil diode [Fig. 1(b)], which consisted of a carbon cathode of 3.6 cm-diam. and a titanium foil anode of 20 mm thick with the A-K distance of 3 cm. Figure 2 shows typical waveforms of the diode voltage V_d and the diode current I_d.

The drift chamber was of stainless-steel and 16 cm in diameter and 46~60 cm in length. Its inner wall surface was covered with sheets of electromagnetic wave absorber (ECCOSORB AN) to eliminate spurious reflections of microwaves. It had two observation ports at z = 17.5 cm, z being the distance from the downstream side of the anode. The base pressure was kept below 5×10^{-5} Torr. In the case of the spectroscopic measurements of hf electric fields, helium gas of about 20 mTorr was introduced into the drift chamber.

A carbon plasma was produced by two rail-type plasma guns set opposite to each other.[16] The produced plasma was time decaying one and had an axial density gradient. Figure 3 shows the plasma densities measured by a Langmuir probe at three points in the axis as a function of the delay time τ of the IREB injection after the firing time of the plasma guns. In the case with helium gas the plasma density somewhat changed.

The net current and the beam current were measured separately using the same Rogowski coil set just at the position of the observation port. For beam current measurement titanium foil of 20 μm thick was attached in front of the Rogowski coil and the beam collector was attached at its backside. For net current measurement they were removed. In order to obtain the beam density, the beam profile was measured using a target-phosphor combination which intercepted the beam. Open photograph of the phosphor was taken. A mini-Faraday cup array was also used for beam profile measurement. Both results agreed well. The ratio of the beam density to the plasma density was from 0.001 to 0.4.

The electron temperature T_e when the IREB was injected into the plasma was obtained from the intensity ratio of HeI 4921.9 Å (singlet) to HeI 4713.1 Å (triplet) when helium gas was introduced into the drift chamber. We used relations between the intensity ratio and the temperature obtained from newly developed collisional radiative model.[19] The measured T_e varied from 10 to 50 eV.

§3 High-power Broadband Microwave Radiation from IREB-Plasma Interaction

Figure 4 shows a schematic diagram of the microwave spectrometer used in this work. A detail of the spectrometer is given in Ref. 15.

Figure 5 shows microwave spectra which were obtained when the foil diode was used.The delay timeτ was taken as a parameter. The ratio of the beam density to the plasma density at each τ is also shown. The spectra are broadband above the plasma frequency, which is shown in the parentheses in each figure, in a certain range of τ. Figure 6 shows relations among the several measured quantities, i.e., the plasma density, the beam density, the beam diameter, the beam current and the total power from 18 to 40 GHz. All quantities are plotted as a function of τ. One of remarkable features is that there are two peaks in the microwave radiation. The peak value is several hundreds w/cm^{-2}. We notice relation between the ratio of the beam density to the plasma density and the total microwave power. In this case the total microwave power has peaks at the density ratio of about 0.01. We also measured the radiation emitted forward direction. As shown in Fig. 7, the forward radiation was several tens times higher than the radial radiation when the horns were set at z = 29 cm.

Thinking that such high-power broadband microwave radiation is concerned with the strong Langmuir turbulence originating from the IREB-plasma interaction, we have spectroscopically investigated whether our beam-plasma system is in the strong Langmuir turbulent state or not.

§4 Spectroscopic Measurements of Turbulent Electric Fields

Figure 8 shows a schematic diagram of the 8-channel spectroscopic system.[17] Quadratic Stark systems in singlet He, such as 3^1P_1 and 3^1D_2 levels, were used for Stark shift measurements. The 5015.7 Å line ($3^1P_1 \rightarrow 2^1S_0$) shifts to the blue side and the 6678.2 Å line ($3^1D_2 \rightarrow 2^1P_1$) shifts to the red side when rapidly oscillating electric fields exist in the plasma. Using the original data compiled by Ryde,[20] the dependence of the shifts on the rms electric field can be calculated for the electric field up to 150 kV/cm. The relation between the energy shift and the rms electric field is

$$\Delta\varepsilon\,[\,\mathrm{cm^{-1}}\,] = (\,4.5 \pm 1.2\,) \times 10^{-4} \times (\,E\,[\,\mathrm{kV/cm}\,]\,)^2$$

for the 5015.7 Å line, and

$$\Delta\varepsilon\,[\,\mathrm{cm^{-1}}\,] = (\,4.2 \pm 0.6\,) \times 10^{-4} \times (\,E\,[\,\mathrm{kV/cm}\,]\,)^2$$

for the 6678.2 Å line. Here $\Delta\varepsilon$ is the energy shift made by the electric field in cm^{-1}. Then the relative shifts of wavelength becomes as follows,

$$\Delta\lambda\,[\text{Å}] = \lambda_0 - \frac{10^8}{n(\varepsilon_0 - \Delta\varepsilon)}$$

Here n is the refractive index of the air corresponding to λ_0, ε_0 is the energy gap of the allowed transition in cm^{-1}, and λ_0 is the wavelength in Å corresponding to ε_0. Each channel of the 8-channel spectrometer has an electric field range ΔE which is due to the spectral resolution of the spectrometer. Using these shift-field relations, we get the field ranges for each wavelength channel as tabulated in Table 1; (a) for the 5015.7 Å line and (b) for the 6678.2 Å line.

Table. 1 (a)

Channel	Wavelength [Å]	Energy shifts e [cm^{-1}]	Erms [kV/cm]	Field range ΔE [kV/cm]
Ch. 5	5015.7 Å	0 ~ 0.712	0 ~ 40	40
Ch. 4	5015.3 Å	0.712 ~ 2.302	40 ~ 72	32
Ch. 3	5014.9 Å	2.302 ~ 3.892	72 ~ 93	21
Ch. 2	5014.5 A	3.892 ~ 5.482	93 ~ 110	17
Ch. 1	5014.1 Å	5.482 ~ 7.073	110 ~ 125	15

Table. 1 (b)

Channel	Wavelength [Å]	Energy shifts [cm^{-1}]	Erms [kV/cm]	Field range ΔE [kV/cm]
Ch. 4	6678.2 Å	0 ~ 0.347	0 ~ 29	29
Ch. 5	6678.6 Å	0.347 ~ 1.243	29 ~ 54	25
Ch. 6	6679.0 Å	1.243 ~ 2.140	54 ~ 71	17
Ch. 7	6679.4 A	2.140 ~ 3.036	71 ~ 85	14
Ch. 8	6679.8 Å	3.036 ~ 3.932	85 ~ 96	11

Before observing emissions from the IREB-plasma interactions, we set, using a helium discharge lamp, the channel-5 of the spectrometer for the 5015.7 Å line for the case of the blue shift measurement, and set the channel-4 for the 6678.2 Å for the case of the red shift measurement. Figure 9 shows typical photomultiplier traces of 5015.7 Å line in a single shot. The fluorescence signals with spiky features last about one microsecond. Spike voltage of 10 mV corresponds to detection of about one photon.

Figure 10 shows typical spectral profiles of the 5015.7 Å (a) and the 6678.2 Å (b) at τ = 10 μsec, which was obtained by counting all spikes in 900 ns after the IREB injection. The foilless diode was used for this case, and an IREB of 1.2 MV and 10 kA was injected into the plasma. Data from 20 shots were gathered to obtain each profile. In order to remove non-Stark shift effects such as instrumental broadening, Doppler broadening and Stark broadening, we fitted the Voigt distribution function to the experimental points on the non-shifted side of the profile and extended it to the shifted side (solid lines in the figure), and then subtracted its value from the observed value at each channel. The figure shows clear Stark shifts. In order to obtain the normalized population of the electric field, we divided the difference between the experimentally obtained intensity and the intensity given by the Voigt distribution by the electric field range ΔE for each channel. Figure 11 shows the normalized population as a function of the

rms electric field for the case of 5015.7 Å. A curve $P(E) \propto \exp(-E^2/E_s^2)$, with E_s = 96 kV/cm, is the best fit.

We applied the plasma satellite method proposed by Baranger and Mozer,[21] too, to measure the oscillating electric field in the plasma. We measured spectra in the vicinity of the HeI 4471.5 Å ($4^3D \rightarrow 2^3P$) and 4921.9 Å ($4^1D \rightarrow 2^1P$) lines. Both have forbidden lines near them, 4469.9 Å ($4^3F \rightarrow 2^3P$) for the former and 4920.4 Å ($4^1F \rightarrow 2^1P$) for the latter.[22] When helium atoms are under the influence of the oscillating electric fields with the plasma frequency, two plasma satellite lines appear on either side of the forbidden line with frequency separation of the plasma frequency. From the measurement of the intensity ratio of the satellite line to the allowed line we can obtain the rms electric field. The relation between the rms electric field and the intensity ratio is given by

$$S^{\pm} = \frac{h^2 \langle E_p^2 \rangle R_{ll'}}{24\pi^2 m^2 e^2 (\Delta \pm \Omega)^2}.$$

Here Ω is the oscillation frequency, Δ is the splitting (in angular frequency units) between the allowed and the forbidden line, $\langle E_p^2 \rangle$ is the time average of plasma field squared, and $R_{ll'}$ is a dimensionless radial integral given by Baranger and Mozer. For $\Omega \ll \Delta$, the two satellites merge into a single forbidden line. Then, the relative intensity ratio is given by the above equation multiplied by 2.[21,23] Figure 12 shows the profiles of the HeI 4471.5 Å line (a) and HeI 4921.9 Å line (b) at τ = 10 μs. Data were gathered from 20 shots for each line. To obtain the intensity of the forbidden line, we must subtract the tail component from the measured value at the line. We fitted a Voigt distribution function to the experimental points of the allowed line and subtract its value at the forbidden line from the measured value. The rms electric field E_{ps} obtained were 5 kV/cm for the HeI 4471.5 Å line and 7.5 kV/cm for the HeI 4921.9 Å line, respectively.

The dimensionless electrostatic energy density $W \sim 1.3$ in the case of E_s = 96 kV/cm, $n_p = 4 \times 10^{13}$ cm^{-3} and T_e = 30 eV. An assumption of Zakharov equations[24] on which strong turbulence theories and simulations are based on, is $W \ll 1$. However, Newman *et al.*[25] showed that the numerical simulation results were expected to be correct within a factor of order unity for $W \lesssim 1$. So we think that our experiment is in the strong Langmuir turbulence regime.

We tentatively analyzed our experimental results according to Robinson and Newman[2] and obtained the final scale size of the caviton $l_f = 22\lambda_D$. The volume fraction of the cavitons are given by $(E_{ps}/E_s)^2$. It was about 0.006 for the case of τ = 10 μs, as E_{ps} = 7.5 kV/cm and E_s = 96 kV/cm. However, it seems reasonable to assume that cavitons distribute in the beam volume. Then the volume fraction becomes $(r_p/r_b)^2$ times higher. The plasma radius was 4 cm and the beam radius was 1.5 cm. So the volume fraction becomes 0.04, and the mean electric field in the beam volume becomes 20 kV/cm. Time evolution of the 5015.7 Å line profile was

obtained with 100 ns step after the IREB injection at each τ. Figure 13 shows the time evolution of the rms electric field of IREB-Plasma interaction region obtained from the best fits curves for each time step for the foilless diode. The turbulent state lasted for about one microsecond, about thirty times as long as the IREB duration.

§5 Concluding Remarks

From the spectroscopic measurements of the hf electric fields in our IREB-plasma system, it has been found that the system is in a strong Langmuir turbulent state. Simultaneous measurement of the turbulent electric fields and the microwave radiation is now going on with helium gas introduced in the drift chamber. Although the aspect of microwave radiation in the case with helium gas is somewhat different against the case without helium gas, we think we can obtain common relation between the turbulence and the microwave radiation. Figure 14 shows one of recent results; a relation between the Ka-band total output power and the hf electric field obtained from Stark shift measurement for the case of foil diode. This relation indicates that when microwave radiation is observed, the plasma is in a strong Langmuir turbulent state. Further studies will reveal more detailed connection between the turbulence and the microwave radiation.

Part of this work was supported by a Grant-in-Aid for Scientific Research from the Ministry of Education, Science and Culture.

References

1) P. A. Robinson and D. L. Newman: Phys. Fluids **B 1**(1989) 2319.
2) P. A. Robinson and D. L. Newman: Phys. Fluids **B 2** (1990) 3120.
3) G. D. Doolen, D. F. DuBois and H. A. Rose: Phys. Rev. Lett. **54** (1985) 804.
4) D. Russel, D. F. DuBois and H. A. Rose: Phys. Rev. Lett. **56** (1986) 838.
5) D. Russel, D. F. DuBois and H. A. Rose: Phys. Rev. Lett. **60** (1988) 581.
6) D. F. DuBois, H. A. Rose and D. Russel: Phys. Rev. Lett. **61** (1988) 2209.
7) G. C. A. M. Janssen, E. H. A. Granneman and H. J. Hopman: Phys. Fluids: **27** (1984) 736
8) H. J. Hopman and G. C. A. M. Janssen: Phys. Rev. Lett. **52** (1984) 1613.
9) D. Levron, G. Benford and D. Tzach: Phys. Rev. Lett. **58** (1987) 1336.
10) G. Benford, X. Zhai and D. Levron: Phys. Fluids **B 3** (1991) 560.
11) D. Levron, G. Benford, A. Ben-Amar Baranga and J. Means: Phys. Fluids **31** (1988) 2026.
12) A. Dovrat and G. Benford: Phys. Fluids **B 1** (1989) 2488.
13) K. G. Kato, G. Benford and D. Tzach: Phys. Fluids **26** (1983) 3636.
14) W. Main and G. Benford: Phys. Fluids **B 1** (1989) 2479.
15) M. Masuzaki, R. Ando, A. Yoshimoto, M. Ishikawa, M. Yoshikawa, K. Kitawada, H. Morita and K. Kamada: *Proceedings of the 8th International Conference on High-Power Particle Beams*, edited by B. N. Breizman and B. A. Knyazev (World Scientific, Singapore, 1991), Vol. 2, p. 683.
16) M. Masuzaki, R. Ando, M. Yoshikawa, H. Morita, J. Yasuoka and K. Kamada: *Proceedings of the 9th International Conference on High-Power Particle Beams*, edited by D. Mosher and G. Cooperstein (Washington, DC.,1992), Vol. 2, p. 1227.
17) M. Yoshikawa, R. Ando and M. Masuzaki: Jpn. J. Appl. Phys. **32** (1993) 969.

18) K. Koláček, M. Řípa, J. Ullschmied, K. Jungwirth and P. Šunka: *Proceedings of the 9th International Conference on High-Power Particle Beams*, edited by D. Mosher and G. Cooperstein (Washington, DC.,1992), Vol. 2, p. 1337.
19) S. Sasaki: private communication. (1994)
20) N. Ryde: *Atoms and Molecules in Electric Fields* (Almquist & Wiksell International, Stockholm, 1976).
21) M. Baranger and B. Mozer: Phys. Rev. **123** (1961) 25.
22) S. Bashkin and J. O. Stoner, Jr.: *Atomic Energy Levels and Grotrian Diagrams* (North-Holland, Amsterdam and Oxford, 1975), Vol.1.
23) T. Ohgo: J. Phys. Soc. Jpn. **52** (1983) 867.
24) V. E. Zakharov: Sov. Phys. JETP, **35** (1972) 908.
25) D. L. Newman, R. M. Winglee, P. A. Robinson, J. Glanz and M. V. Goldman: Phys. Fluids, **B2** (1990) 2600.

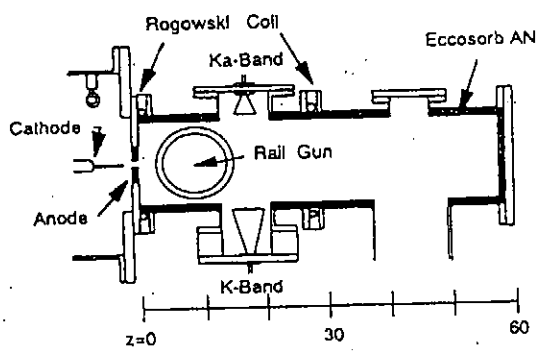

(a)

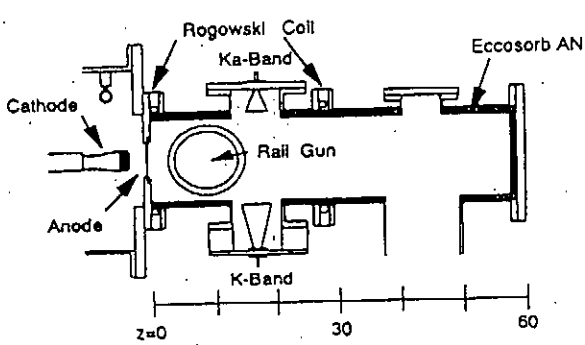

(b)

Fig. 1

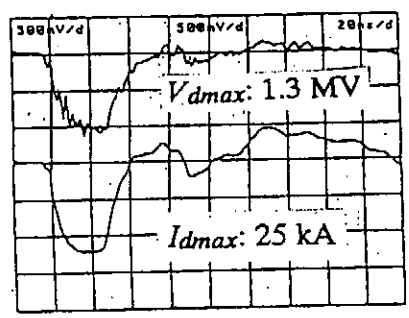

Fig. 2

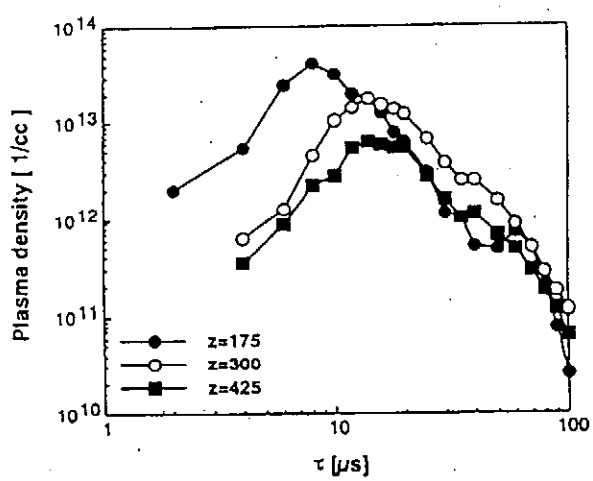

Fig. 3

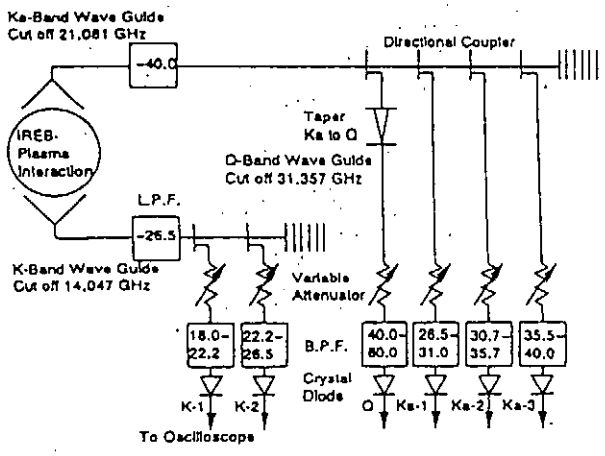

Fig. 4

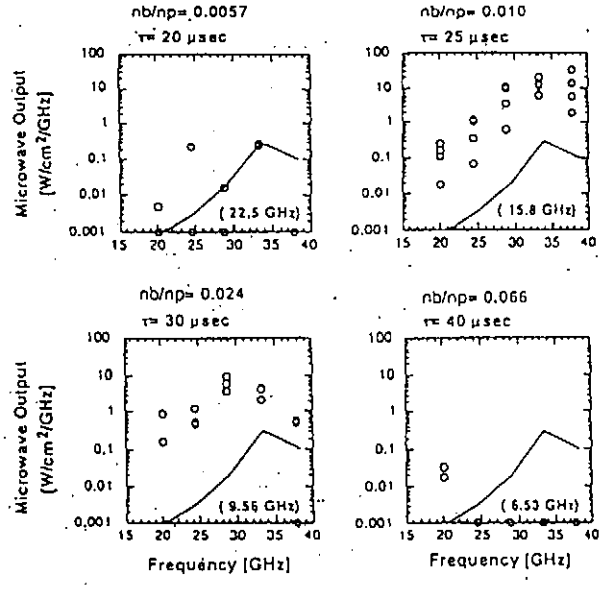

Fig. 5

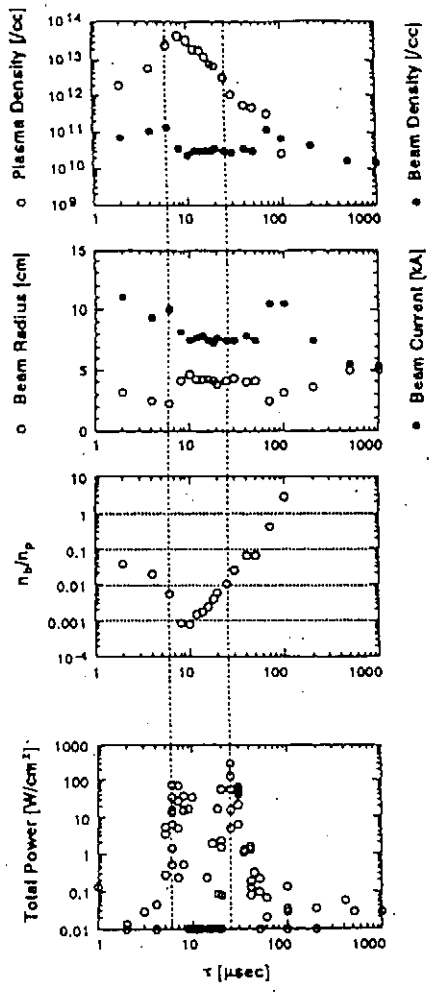

Fig. 6

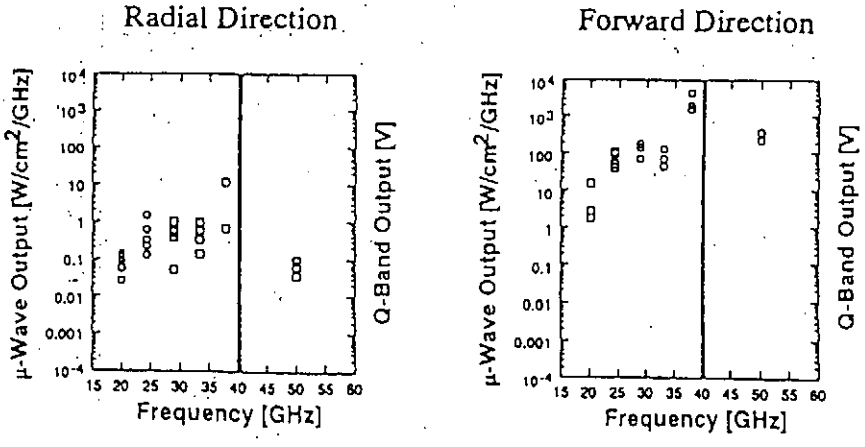

Fig. 7

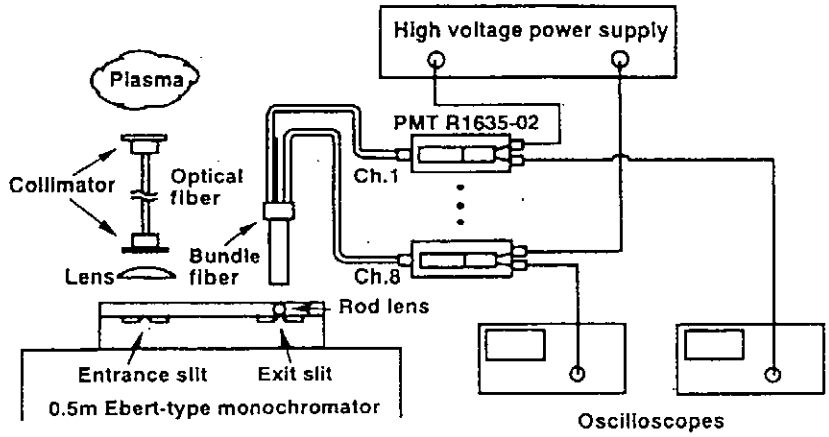

Fig. 8

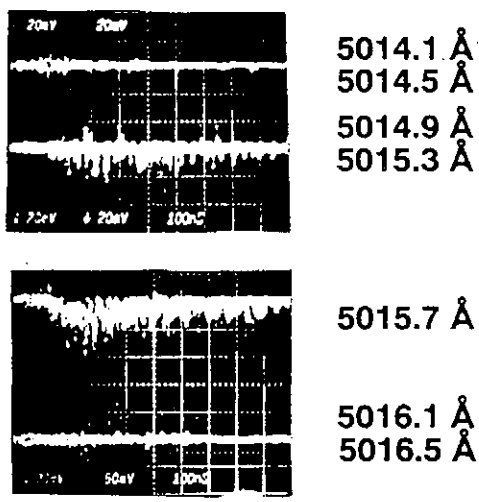

Fig. 9

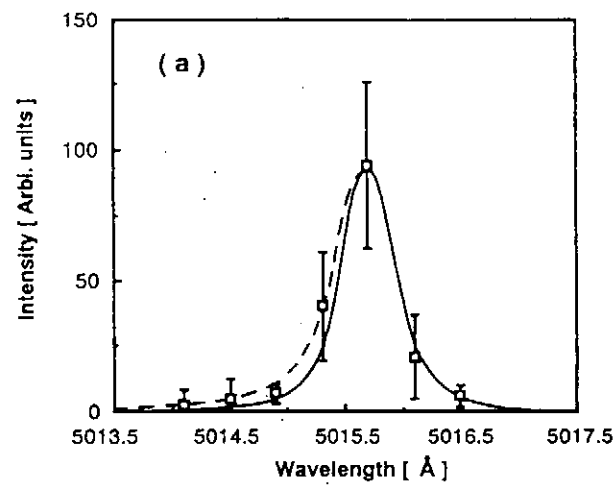

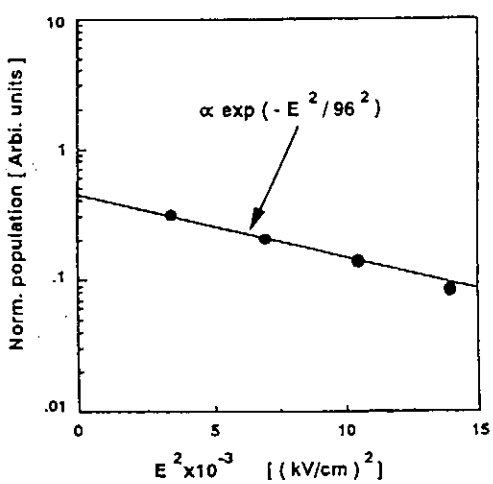

Fig. 11

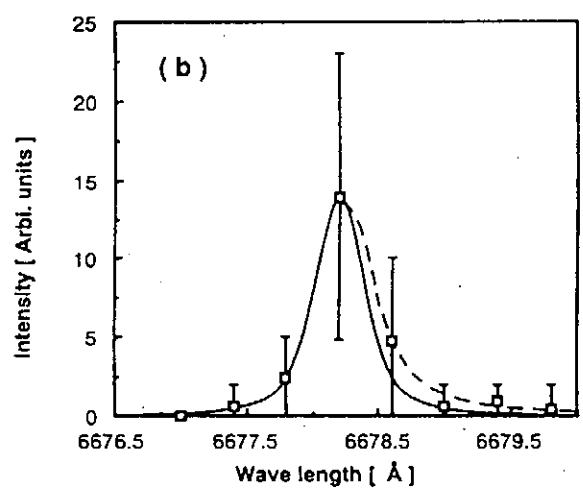

Fig. 10

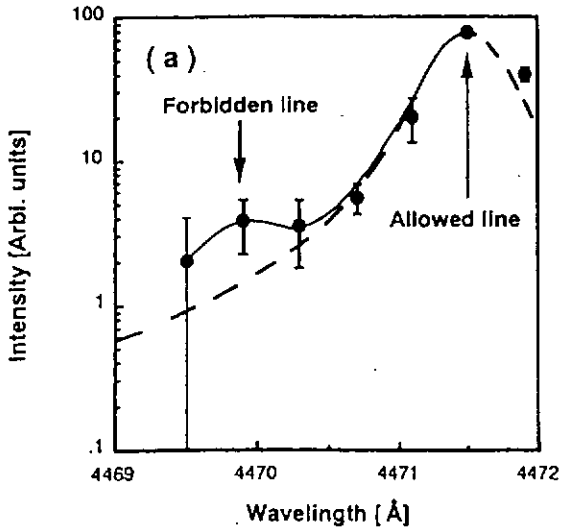

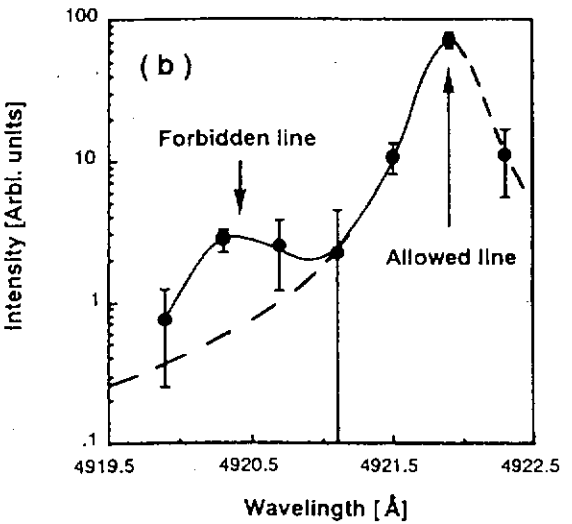

Fig. 12

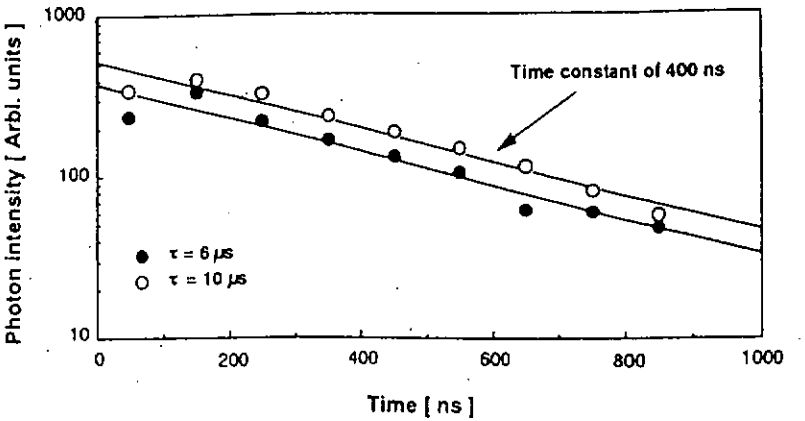

Fig. 13

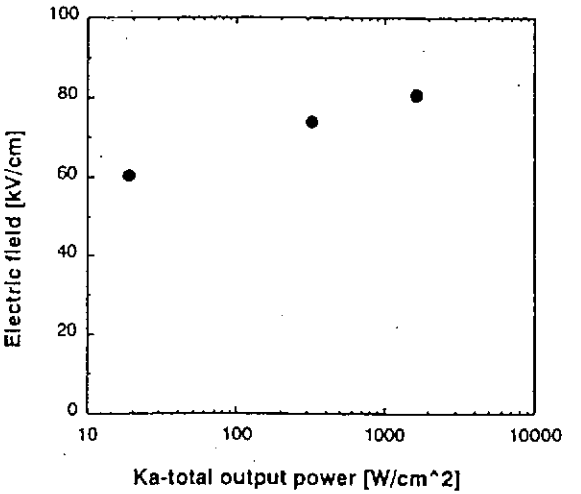

Fig. 14

Plasma Opening Switch by Laser-Produced Plasma with different kinds of Ion Species

Satoshi Ihara*, Hidenori Akiyama**, Susumu Kohno**, Sunao Katsuki**,
Sadao Maeda** and Chobei Yamabe*

* Department of Electrical Engineering,
Faculty of School of Science and Engineering, Saga University

** Department of Electrical Engineering and Computer Science,
Faculty of Engineering, Kumamoto University

ABSTRACT

We have already proposed using laser-produced plasma as plasma sources of the plasma opening switch (POS). A POS using laser-produced plasma has a possibility to be operated repeatedly by focusing the laser light on the target surface repeatedly. Other advantages are that the parameters of plasmas are kept constant for many shots, and the kinds of ion species can be changed easily by changing the targets for plasma production. In this paper, the operation of POS using the laser-produced plasma is experimentally investigated by changing the target materials (Al, Cu, W) as plasma sources.

1. INTRODUCTION

Pulsed power generator with an inductive energy storage, which can be made compact and light-weight, would be of benefit for many pulsed power applications. The opening switch is the key element in developing such a system. The requirements of the opening switches are as follows:

① A large current can be conducted and interrupted rapidly.

② It is possible to be operated repeatedly without maintenance.

The plasma opening switch (POS) [1]-[5] is one of the opening switches that are expected to satisfy these requirements. Plasma guns[6] and flashboards[7] sprayed with carbon have been used as plasma sources. However, the lifetimes of these sources are limited to tens of shots because the carbon decreases with each shot. Moreover, the parameters of the plasmas produced by plasma guns and flashboards change somewhat with every shot. Plasma sources which can produce plasmas with the same parameters repeatedly for many shots are required to make the POS practical. The POS using a laser-produced plasma, which has the capability of being operated repeatedly without maintenance, was proposed[8]. The plasma is produced by focusing a laser on a solid target which can be rotated slightly before each shot, and therefore the plasma which has same parameter for each shot can be produced repeatedly. If the diameters of the target and laser beam are 5cm and 100μm, respectively, and the laser beam is focused only once on a particular spot, plasmas can be produced up to 250000 times[8]. The laser produced plasmas have other more advantages as follows:

① The different kinds of ion species can be used easily by changing the target material.

② The plasmas produced by lasers do not have impurities such as electrode materials that are found in those produced by plasma guns and flashboards.

From above two things, the POS using laser-produced plasma is advantageous on understanding the physics of POS operation .

In this paper, experiments of POS operation are carried out with different kinds of target materials, aluminum, copper, tungsten. The reappearance of plasma parameters is confirmed by observing the ion current in plasma, and also the time of flight for ions is measured and its results are compared with the experimental results of POS operation.

2. EXPERIMENTAL APPARATUS AND METHOD

A schematic diagram of the experimental apparatus of the POS and its equivalent circuit are shown in Fig. 1. The apparatus is in a coaxial configuration with the inner conductor being the cathode. The components of the experimental apparatus include (from bottom to top) capacitors, a triggered spark gap (TSG), the POS as an opening switch, and a load. In these experiments, the load is short-circuit load. The storage inductance L_S is 400nH, the total capacitance C is 1.2 μF, and the load inductance L_l is 36nH. The polarity of the inner conductor is negative, and the charging voltage V_0 of 25kV was used in the experiments. The diameters of outer and inner conductors are 22mm and 3mm, respectively, and the outer conductor in the POS switch region is made of a stainless mesh with 97.5% transparency.

The laser for the plasma production is the Q-switched ruby laser (NEC SLG2018) with the peak power and FWHM of 5MW and 20ns, respectively. The laser light is focused on the target surface by a lens placed outside the vacuum chamber, and the produced plasma enters into the switch region from only one direction. Aluminum, copper and tungsten materials are used as the targets. The distance between the target and the surface of the inner conductor is 19.5mm. The target is rotated after several shots. The first shot is not used as data, since the plasmas of the contamination on the target surface are included.

The TSG was triggered after the laser was fired. The delay time Δt, from the time when the laser begins to oscillate until the time when the source current I_g, begins to flow, is varied in the experiments. The load current I_l and the source current I_g are measured with Rogowski coils, and the laser light is observed with a photomultiplier tube and a calorimeter, which are placed outside of the vacuum chamber. The pressure in the vacuum chamber is about 5×10^{-5}Torr.

The ion current I_i of the laser-produced plasmas is measured by a biased Faraday cup. The distance between the target and Faraday cup is 81mm. To remove any contaminations such as pump oil or water from the target surface, the laser is fired once before POS operation to clean the surface and then fired again at same point on above experiments.

3. EXPERIMENTAL RESULTS AND DISCUSSIONS

Figs. 2 (a)-(b) show the waveforms of I_i, which are measured with Faraday cup at 19.5mm away from the targets of aluminum, copper and tungsten, respectively. Each figure has four waveforms to show the variation of I_i from shot to shot. Laser light is focused on a target at t=0. Though the values of ion current slightly change from shot to shot from comparison of the four waveforms, the times when two peaks (first and second peaks) occur are nearly equal, and also these waveforms are analogous with each other. It is found that the plasmas produced by laser light have approximately same parameters for each shot.

Fig. 3 shows the time when the first peak occur versus the square root of mass number. If the ion kinetic energy is same for each target materials, the time should be proportional to the square root of mass number of target materials. Since the time for the first peak is proportional to the square root of mass number, it is found that these ions have approximately the same kinetic energy (=360 ev).

Fig. 4 shows the typical waveforms of the generator current I_g and the load current I_l at Δt=1.18μs in the case of aluminum target. In Table I, the value of T_c, dI_l/dt and I_{sw} are summarized in the cases of aluminum, copper, and tungsten targets, where T_c is the time when the load current begins to increase rapidly after beginning of the generator currents, dI_l/dt is the maximum rate of change in I_l, I_{sw} is the maximum value of switch current flowing through the plasma. Since the maximum value of I_g is 55kA and the quarter period is 800ns, the rate of change in I_g at beginning of conduction phase is about 1.1×10^{11}A/s. The value of dI_l/dt is 11 times as large as dI_g/dt. It is clear from these results that aluminum, copper and tungsten plasmas can be used as the plasmas of the POS. Figs. 5 (a)-(c) show the dependence of the conduction time T_c on Δt in the cases of aluminum, copper and tungsten targets, respectively. The minimum values Δt_s of Δt, in which the plasma is operated as the opening switch, are 0.4μs, 0.6μs, 1.0μs, in the cases of aluminum, copper, tungsten targets, respectively, and the maximum values Δt_m of Δt are 1.0μs, 1.5μs, 1.6μs. Fig. 6 shows Δt_m and Δt_s versus the square root of mass number of each target material. Since Δt_s is

proportional to the square root of mass number, it is found that the kinetic energy of each ion produced from different target materials is nearly equal to about 350ev.

4. SUMMARY

The experiments of POS using laser-produced plasmas were carried out by changing the target materials (Al, Cu, W) as plasma sources. The obtained results are summarized as follows:

① The different kinds of plasmas (Al, Cu, W) were operated as opening switches.

② The kinetic energy of each ion produced by different target materials is nearly equal to about 350ev.

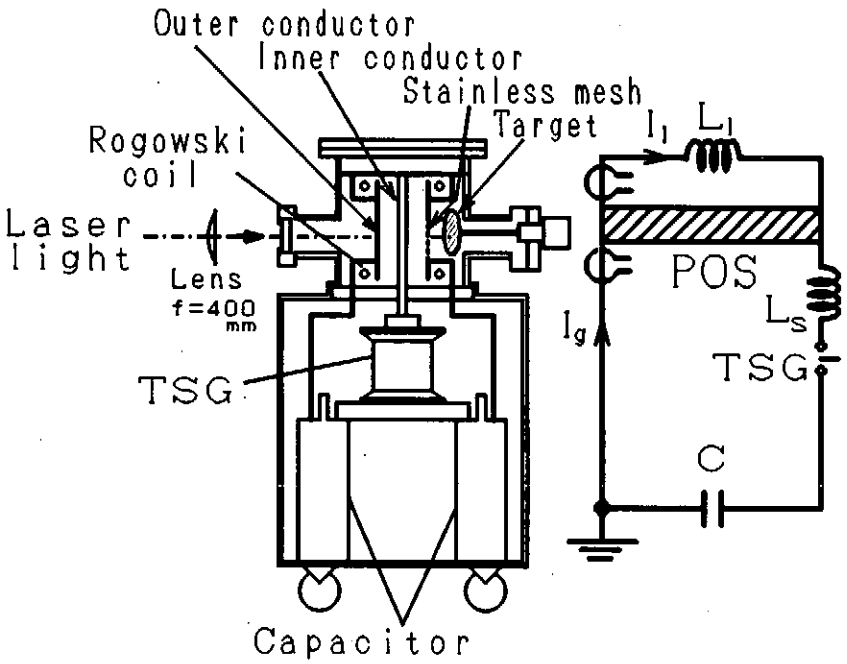

Fig. 1. Schematic diagram of experimental apparatus and its equivalent circuit.

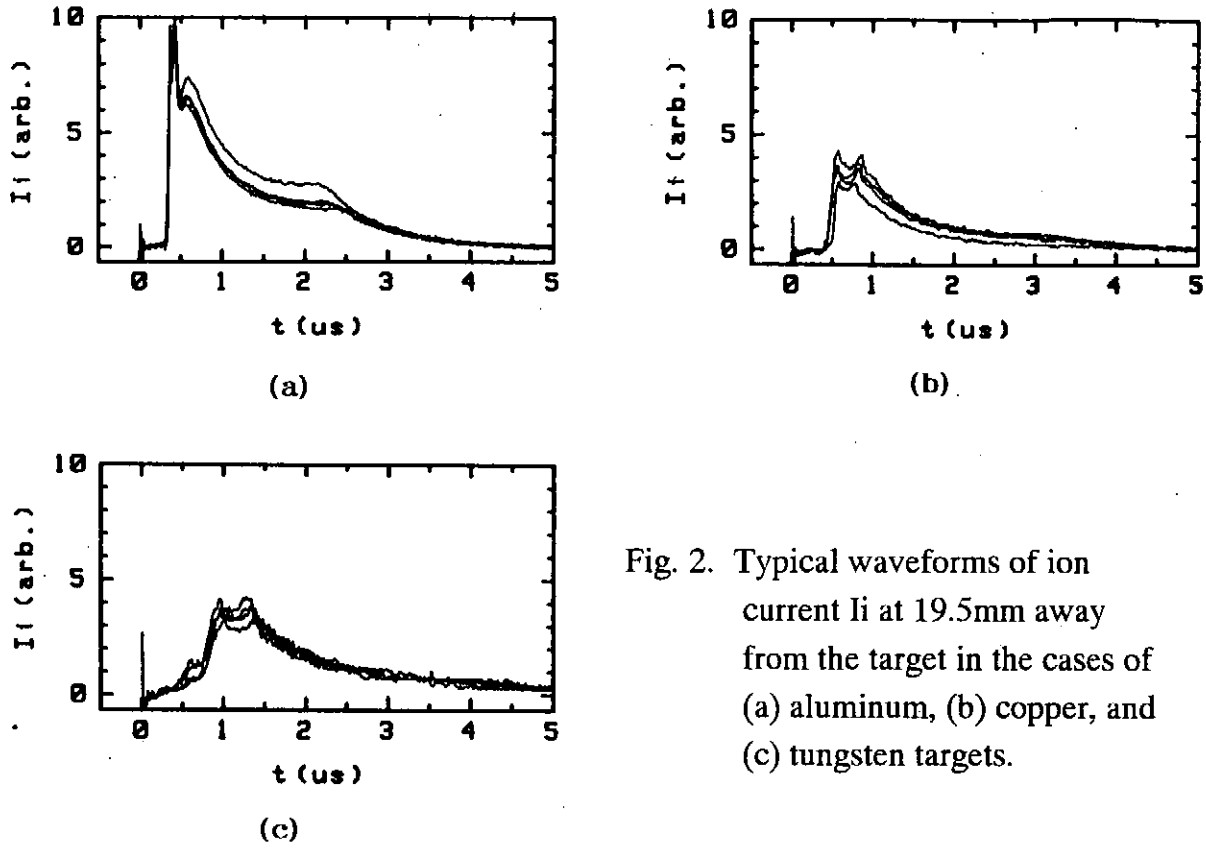

Fig. 2. Typical waveforms of ion current Ii at 19.5mm away from the target in the cases of (a) aluminum, (b) copper, and (c) tungsten targets.

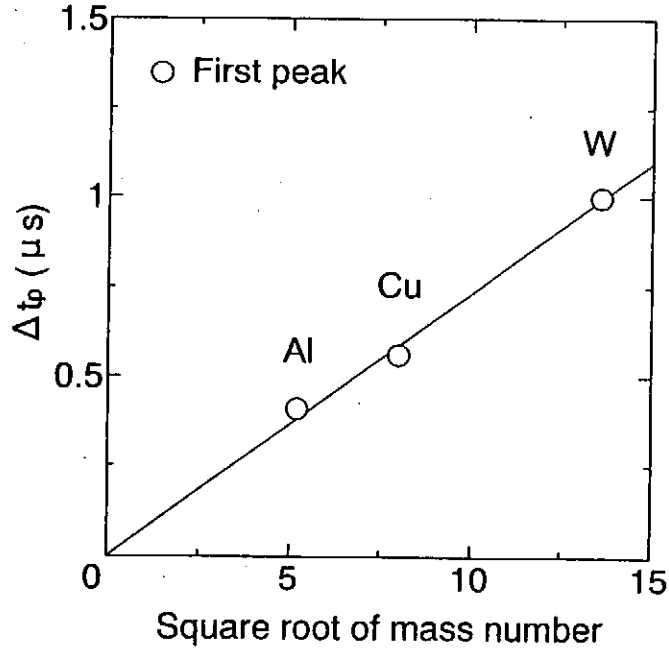

Fig. 3. Dependence of the time when the first peak occur on the square root of mass number.

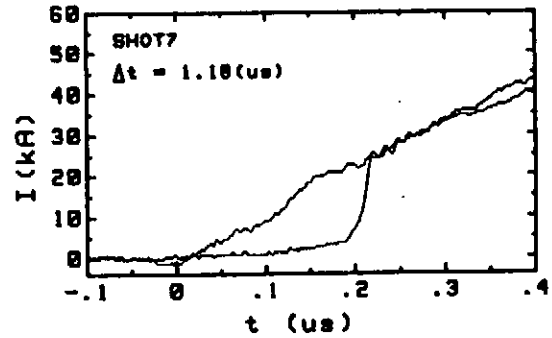

Fig. 4. Typical waveforms of generator current I_g and load current I_l in the case of aluminum target.

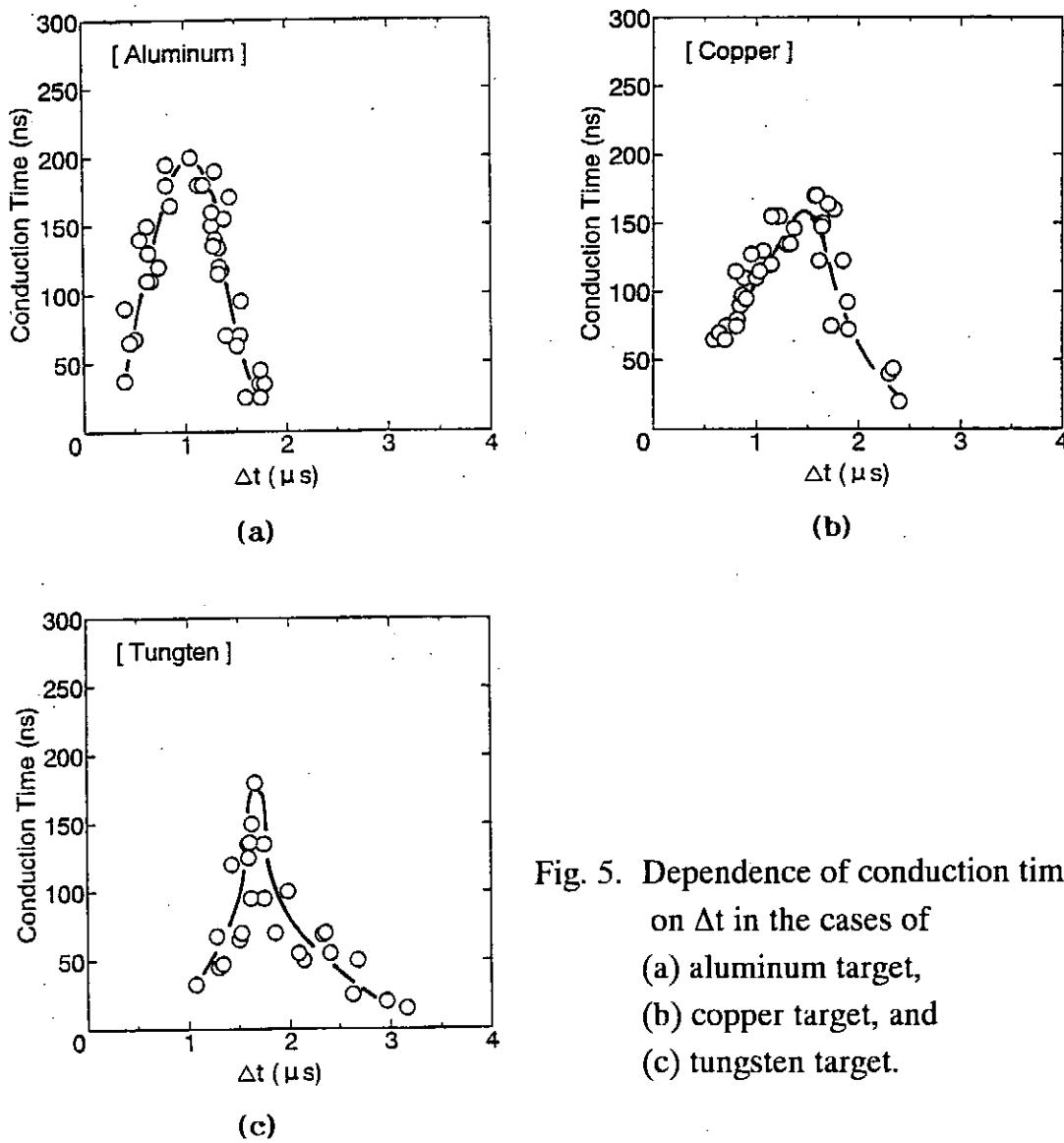

Fig. 5. Dependence of conduction time T_c on Δt in the cases of
(a) aluminum target,
(b) copper target, and
(c) tungsten target.

Table I. Typical parameters of POS.

	T_e (ns)	dI_i/dt (A/s)	I_{sw} (kA)	Δt (μs)
Aluminum	180	14×10^{11}	19	1.18
Copper	170	11×10^{11}	17	1.57
Tungsten	180	12×10^{11}	17	1.67

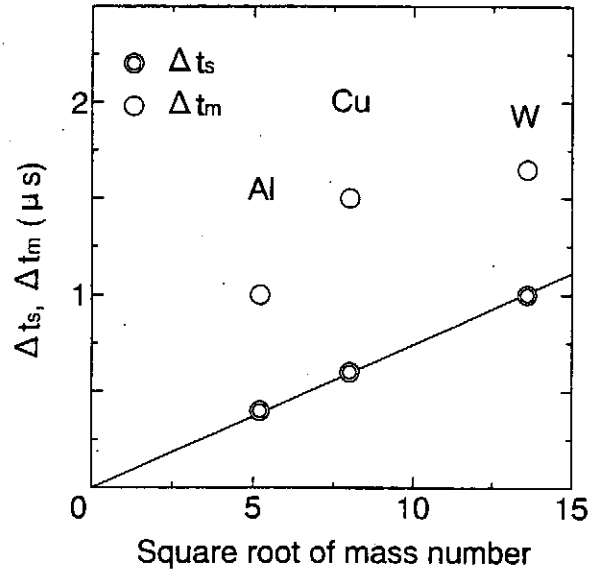

Fig. 6. Dependences of Δt_S and Δt_m on square root of mass number of target material.

REFERENCES

[1] B. V. Weber, R. J. Commisso, P. J. Goodrich, J. M. Grossmann, D. D. Hinshelwood, J. C. Kellogg, and P. F. Ottinger, "Investigation of Plasma Opening Switch Conduction and Opening Mechanism,"
IEEE Trans. Plasma Sci., Vol. 19, No. 5, pp. 757-766, 1991.

[2] N. Shimomura, H. Akiyama and S. Maeda, "Compact Pulsed Power Generator by an Inductive Energy Storage System with Two-Staged Opening Switches," IEEE Trans. Plasma Sci., Vol. 19, No. 6, pp. 1220-1227, 1991.

[3] J. R. Goyer, "A Conduction Model for PEOS Operation Incorporating Simplified Cathode Sheath Effects," IEEE Trans. Plasma Sci., Vol. 19, No. 5, pp. 920-925, 1991.

[4] B. V. Weber, R. J. Commisso, G. Cooperstein, J. M. Grossmann, D. D. Hinshelwood, D. Mosher, J. M. Neri, P. F. Ottinger, and S. J. Stephanakis, "Plasma Erosion Opening Switch Research at NRL" IEEE Trans. Plasma Sci., Vol. 15, No. 6, pp. 635-648, 1987.

[5] V. M. Bystritskii, Ya. E. Krasik, I. V. Lisitsyn, and A. A. Sinebryukhov, "Experimental Investigation of the Conduction Phase of the Microsecond Plasma Opening Switch," IEEE Trans. Plasma Sci., Vol. 19, No. 4, pp. 607-611, 1991.

[6] C. W. Model, Jr, D. M. Zagar, G. S. Mills, S. Humphries, Jr., and S. A. Goldstein, "Carbon plasma gun," Rev. Sci. Instrum., Vol. 51, No. 12, pp. 1641-1644, 1980.

[7] T. J. Renk, "Flashboards as a plasma source for plasma opening switch applications," J. Appl. Phys., Vol. 65, No. 7, pp. 2652-2663, 1989.

[8] T. Fukuzawa, S. Ihara, S. Maeda and H. Akiyama, "Plasma Erosion Opening Switch Using Laser-Produced Plasma," IEEE Trans. Plasma Sci., Vol. 20, No. 4, pp. 447-451, 1992.

Publication List of NIFS-PROC Series

NIFS-PROC-1 *U.S.-Japan on Comparison of Theoretical and Experimental Transport in Toroidal Systems Oct. 23-27, 1989* Mar. 1990

NIFS-PROC-2 *Structures in Confined Plasmas –Proceedings of Workshop of US-Japan Joint Institute for Fusion Theory Program–* ; Mar. 1990

NIFS-PROC-3 *Proceedings of the First International Toki Conference on Plasma Physics and Controlled Nuclear Fusion –Next Generation Experiments in Helical Systems– Dec. 4-7, 1989* Mar. 1990

NIFS-PROC-4 *Plasma Spectroscopy and Atomic Processes –Proceedings of the Workshop at Data & Planning Center in NIFS–*; Sep. 1990

NIFS-PROC-5 *Symposium on Development of Intensed Pulsed Particle Beams and Its Applications February 20 1990*; Oct. 1990

NIFS-PROC-6 *Proceedings of the Second International TOKI Conference on Plasma Physics and Controlled Nuclear Fusion , Nonlinear Phenomena in Fusion Plasmas -Theory and Computer Simulation-;* Apr. 1991

NIFS-PROC-7 *Proceedings of Workshop on Emissions from Heavy Current Carrying High Density Plasma and Diagnostics;* May 1991

NIFS-PROC-8 *Symposium on Development and Applications of Intense Pulsed Particle Beams, December 6 - 7, 1990*; June 1991

NIFS-PROC-9 *X-ray Radiation from Hot Dense Plasmas and Atomic Processes*; Oct. 1991

NIFS-PROC-10 *U.S.-Japan Workshop on "RF Heating and Current Drive in Confinement Systems Tokamaks" Nov. 18-21, 1991*, Jan. 1992

NIFS-PROC-11 *Plasma-Based and Novel Accelerators (Proceedings of Workshop on Plasma-Based and Novel Accelerators) Nagoya, Japan, Dec. 1991*; May 1992

NIFS-PROC-12 *Proceedings of Japan-U.S. Workshop P-196 on High Heat Flux Components and Plasma Surface Interactions for Next Devices*; Mar. 1993

NIFS-PROC-13 『NIFS シンポジウム
「核燃焼プラズマの研究を考える－現状と今後の取り組み方」
1992年 7月 15日、核融合科学研究所』
1993年 7月
NIFS Symposium
"Toward the Research of Fusion Burning Plasmas -Present status and Future strategy-", 1992 July 15, National Institute for Fusion Science; July 1993
(in Japanese)

NIFS-PROC-14 *Physics and Application of High Density Z-pinches,*
July 1993

NIFS-PROC-15 岡本正雄、講義「プラズマ物理の基礎」
平成5年度 総合大学院大学
1994年 2月
M. Okamoto,
"Lecture Note on the Bases of Plasma Pysics"
Graduate University for Advanced Studies
Feb. 1994
(in Japanese)

NIFS-PROC-16 代表者 河合良信
平成5年度 核融合科学研究所共同研究
研究会報告書
「プラズマ中のカオス現象」
"Interdisciplinary Graduate School of Engineering Sciences"
Report of the meeting on Chaotic Phenomena in Plasma
Apr. 1994
(in Japanese)

NIFS-PROC-17 平成5年度NIFSシンオジウム報告書
「核融合炉開発研究のアセスメント」
平成5年11月29日-30日 於 核融合科学研究所
"Assessment of Fusion Reactor Development"
Proceedings of NIFS Symposium held on November 29-30, 1993 at National Insitute for Fusion Science
Apr. 1994
(in Japanese)